



THÈSE DE DOCTORAT

Advanced Cellular Network Modelling and Optimization for Unmanned Aerial Vehicles

Matteo BERNABÈ

*A thesis submitted in fulfillment of the requirements
for the degree of Doctor of Philosophy*

in the

École Doctorale Informatique, Télécommunications et Electronique
Sorbonne Université (ED130) - EDITE de Paris
EURECOM Département Systèmes de Communication

Jury

David Gesbert	EURECOM	Directeur de thèse
Symeon Chatzinotas	Université du Luxembourg	Rapporteur
Marco Giordani	Università di Padova	Rapporteur
Michela Meo	Politecnico di Torino	Examinatrice
Lorenzo Galati Giordano	Nokia Bell Labs	Examineur
Adlen Ksentini	EURECOM	Président du jury

Invited

David López-Pérez	Universitat Politècnica de València	Co-encadrant
Nicola Piovesan	Huawei Research	Co-encadrant Industriel

“What I cannot create, I do not understand.”

Richard Feynman

ÉCOLE DOCTORALE INFORMATIQUE, TÉLÉCOMMUNICATIONS ET
ELECTRONIQUE

Abstract

Sorbonne Université (ED130) - EDITE de Paris

Doctor of Philosophy

Advanced Cellular Network Modelling and Optimization for Unmanned Aerial Vehicles

by Matteo BERNABÈ

Remotely piloted drones, also known as unmanned aerial vehicles (UAVs), have become increasingly important in recent years, making a notable impact on different applications, such as surveillance, precision agriculture, and parcel delivery. As interest in UAVs operating within urban environments continues to grow, the use of UAVs in populated areas presents a significant challenge. Aerial highways (AHs) are emerging as a promising solution for enabling optimal management of UAVs traffic and secure urban operations. Like terrestrial highways, AHs are predefined lanes in the sky that UAVs must adhere to when navigating in the urban sky.

Owing to their ability to navigate 3D space, due to the typical line of sight (LoS) condition, UAVs experience favourable channel gains across multiple cells within urban cellular networks. Although this permits UAVs to perceive sufficient reference signal received powers (RSRPs), it also results in comparable signal power from multiple neighbouring cells, leading to high interference and reduced signal quality. Moreover, the inherited high channel correlation due to LoS and the proximity of UAVs along AHs pose significant challenges when adopting massive multiple-input multiple-output (mMIMO) systems.

In this thesis, we investigate, from a system-level network perspective, how the prior information of the planned AHs can be leveraged by network operators to optimize their deployed terrestrial cellular network to provide connectivity along AHs while maintaining unchanged ground service.

Specifically, we first focus on legacy 4G long term evolution (LTE) networks can be optimized to maintain minimum connectivity along the AHs. To achieve this, we propose a gradient-based optimization framework that leverages AH information and adjust the vertical tilt of terrestrial LTE sectors, ensuring optimal power distribution and meeting coverage requirements along the AH.

Then, moving towards 5G new radio (NR), we investigate how multi-antenna systems can be leveraged, together with the information of the planned AHs, to provide enhanced coverage. Therefore, we propose an optimization framework that utilizes gradient computations to design optimal coverage beams from surrounding

network cells, identifying the most critical beams while configuring the remaining according to legacy configuration designed primarily for ground service.

Acknowledging that optimizing solely coverage is insufficient to enhance the UAVs data rate effectively, we propose then a solution capable of merging coverage and capacity optimization. Specifically, we envision that UAVs performances along the AHs can be optimized by solely controlling UAVs serving cells. Therefore, we propose a novel solution to optimally plan 5G NR coverage beams across the network to strategically control the UAVs cell association and, in turn, maximize UAVs data rate without affecting ground users. This solution can increase the final UAVs data rate along the AH by adjusting the network solely at its planning stage, allowing the network to remain unchanged regardless of instantaneous conditions. To solve the problem, we propose a heuristic solution based on a novel metric that captures the multiplexing capability, average channel quality gain, and interference. Leveraging this metric, we introduce a two-stage framework in which, first, we optimally split the AH into multiple segments and identify the corresponding set of optimal serving cells. Secondly, we define the optimal set of transmitted NR coverage beams from the identified cell set to maximize their coverage.

ÉCOLE DOCTORALE INFORMATIQUE, TÉLÉCOMMUNICATIONS ET
ELECTRONIQUE

Résumé

Sorbonne Université (ED130) - EDITE de Paris

Doctor of Philosophy

Advanced Cellular Network Modelling and Optimization for Unmanned Aerial Vehicles

by Matteo BERNABÈ

Les drones télépilotés, unmanned aerial vehicles (UAVs), ont acquis une importance croissante ces dernières années, impactant diverses applications comme la surveillance, l'agriculture de précision et la livraison de colis. Bien que l'intérêt pour les UAVs en environnements urbains augmente, leur utilisation dans les zones peuplées pose des défis. Les aerial highways (AHs) émergent comme une solution prometteuse pour une gestion optimale du trafic des UAVs et des opérations urbaines sécurisées. Similaires aux autoroutes terrestres, les AHs sont des voies prédéfinies dans le ciel que les UAVs doivent suivre dans l'espace aérien urbain.

Grâce à leur capacité à naviguer dans l'espace 3D, en raison de la condition typique de line of sights (LoSs), les UAV bénéficient de gains de canal favorables à travers plusieurs cellules dans les réseaux cellulaires urbains. Cependant, bien que les UAVs reçoivent des puissances de signal suffisantes *reference signal received power* (RSRP) de plusieurs cellules, cela engendre des interférences élevées et une qualité de signal réduite. De plus, la forte corrélation de canal due au LoS et à la proximité des UAVs le long des AHs pose des défis pour l'adoption des systèmes massive multiple-input multiple-output (mMIMO).

Dans cette thèse, nous étudions comment les informations préalables des AHs peuvent être exploitées par les opérateurs pour optimiser les réseaux cellulaires terrestres, afin de fournir une connectivité le long des AHs tout en maintenant le service au sol.

Nous nous concentrons d'abord sur l'optimisation des réseaux 4G long term evolution (LTE) existants pour maintenir une connectivité minimale le long des AHs. Nous proposons un cadre d'optimisation basé sur le gradient qui utilise les informations des AHs et ajuste l'inclinaison verticale des secteurs LTE, assurant une distribution de puissance optimale pour répondre aux exigences de couverture le long des AHs.

En nous tournant vers la 5G new radio (NR), nous explorons comment les systèmes multi-antennes peuvent être exploités avec les informations des AHs pour

améliorer la couverture. Nous proposons un cadre d'optimisation utilisant des calculs de gradient pour concevoir des faisceaux de couverture optimaux à partir des cellules environnantes, en identifiant les faisceaux critiques tout en maintenant la configuration existante pour le service au sol.

Reconnaissant que l'optimisation de la seule couverture est insuffisante pour améliorer le débit des UAV, nous proposons une solution fusionnant l'optimisation de la couverture et de la capacité. Nous envisageons d'optimiser les performances des UAVs en contrôlant uniquement les cellules de desserte. Nous proposons donc une nouvelle solution pour planifier de manière optimale les faisceaux de couverture 5G NR, contrôlant stratégiquement l'association des cellules pour maximiser le débit des UAVs sans affecter les utilisateurs au sol. Cette solution peut augmenter le débit des UAVs le long des AHs en ajustant le réseau uniquement lors de la planification, le réseau restant inchangé malgré les conditions instantanées. Pour résoudre ce problème, nous proposons une solution heuristique basée sur une nouvelle métrique capturant la capacité de multiplexage, le gain moyen de qualité de canal et les interférences. En exploitant cette métrique, nous introduisons un cadre en deux étapes : premièrement, nous divisons de manière optimale les AHs en segments et identifions les cellules de desserte optimales; deuxièmement, nous définissons l'ensemble optimal de faisceaux de couverture NR émis par ces cellules pour maximiser leur couverture.

Acknowledgements

First of all, I would like to thank my supervisors, David Gesbert, David López Pérez, and Nicola Piovesan, for their continuous support, patience, motivation and for being admirable mentors. A sincere thank you for all the good moments and for encouraging me to keep going even when the road got tough.

Another big thank you goes to all the people with whom I have been able to collaborate and have interesting discussions. In particular, I would like to thank the entire NetOp Team at Huawei Paris—Antonio De Domenico, Nicola Piovesan, Fadhel Ayed, Wenjie Li, and Tareq Si Salem—with whom I have shared all these years. Another thank you also goes to Ali Maatouk and Adrian Garcia Rodriguez for the professional discussions and even more for the non-professional ones. Another big thank you also goes to Giovanni Geraci for his teachings and help.

A sincere thank you goes to my office and desk-mate, Henri Alam, for listening to all my complaints, all my “Italian reactions” to code that wouldn’t compile, and especially for all the fun moments we’ve shared over these years together. Also, thank you for answering all my phone calls in French and being my personal translator, saving me from unpleasant situations. Another special thank you goes to Giulia Milan, Alberto Rech, and Gianpietro Consolaro for sharing these years at Huawei with me and for quickly becoming important people in my life. Similarly, a special thank you goes to Alessandro Aimi, almost a fellow countryman and PhD student in Paris, whom I randomly met in Rio de Janeiro, and who has also become one of the most important people who have marked this journey.

A big thank you goes to all my dear friends from “L’Isola Delle Rosole” and in particular to the sub-group “Sportello Psicologico”—Sapo, Buba, and Jack—for the mutual sharing of the difficult times during PhD life and continuous mutual support. Thanks to Mohamed Benzaghta and Masoud Sadeghian for the good times in Barcelona and to all my friends from EURECOM—Giuseppe Serra, Reza Deylam Salehi, Alireza Mohammadi, Carlos Mateo Risma Carletti, Ilias Chatzistefanidis, Pouya Agheli, and honorary member Eduard Tulbure—with whom I have shared beautiful and important moments.

A truly thank you goes to Riccardo Marini, Giampaolo Cuzzo, Marco Skocaj, Mario Minardi, Leonardo Boldrini, and Giovanni Calabrese, my dear university friends with whom we are continuing this journey together, even though we’re in different countries.

Finally, a special thank you to my parents, Riccardo Bernabè and Novella Balzi, for always being by my side and supporting me in so many different ways on this adventure. And last but not least, a special thank you to all the people and friends I’ve met on this journey who have made it all unique and incredible. Thank you all.

Contents

Abstract	v
Résumé	vii
Acknowledgements	ix
1 Introduction	1
1.1 Related Work	2
1.2 Motivation	5
1.2.1 Research Directions	6
1.3 Our Contributions	9
1.3.1 4G LTE Vertical Tilt Optimization	9
1.3.2 5G NR SSB Beam Coverage Optimization	9
1.3.3 Aerial Highway Segmentation and SSB Beam Planning for UAVs Rate Maximization	10
2 System Models	15
2.1 Network Cell Layout	16
2.1.1 Evaluation Points	17
2.1.2 UEs Distribution	17
2.2 Antenna Sector Array	21
2.2.1 LTE ULA Panel	21
2.2.2 NR UPA Panel	21
2.3 Channel Model	22
2.3.1 Line of Sight Probability and Path Loss	23
2.3.2 Shadow Fading Gain	23
2.3.3 Multi-Path Fading	24
2.4 Antenna Element Gain and Beamforming Gain	24
2.4.1 Beamforming Gain	25
2.5 Network Initial Access	26
2.5.1 LTE Initial Access	26
2.5.2 LTE Serving Cell Association	27
2.5.3 Enhanced NR Initial Access	28
2.5.4 NR Serving Cell Selection	30
2.6 Data Performance Metric	31
2.6.1 LTE Data SINR and Achievable Data Rate	31

2.6.2	NR Data Precoding	32
2.6.3	NR Data SINR and Achievable Data Rate	33
3	Aerial Highways LTE Vertical Tilt Optimization	35
3.1	Introduction	35
3.2	Problem Formulation	36
3.3	LTE Vertical Tilt Gradient Based Solution	37
3.3.1	Objective Scalar Function	37
3.3.2	ADAM Optimizer	39
3.3.3	Optimization Framework	40
3.3.4	Time Complexity	41
3.4	LTE Vertical Tilt Optimization Setup and Solution	42
3.5	Resulting LTE Coverage SINR	48
3.5.1	Out of Coverage Rate	49
3.5.2	Coverage Serving Power and Interference	57
3.6	LTE Achievable Data Rate	59
3.6.1	Minimum PRBs required for C&C	60
3.7	Conclusion	68
4	Aerial Highways NR Coverage SSB Beams Optimization	69
4.1	Introduction	69
4.2	Problem Formulation	70
4.3	NR Coverage SSB Beams Gradient Based Solution	71
4.3.1	Optimization Variables and Objective Scalar Function	71
	Objective Scalar Function	72
4.3.2	ADAM Optimizer	73
4.3.3	Optimization Framework	75
4.3.4	Time Complexity	77
4.4	Optimization Setup and Solution	79
4.5	NR Coverage SINR	85
4.5.1	Coverage Serving Power and Interference	95
4.6	NR Data SINR and Achievable Data Rate	99
4.7	Conclusion	101
5	Aerial Highway Segmentation and SSB Beam Planning for UAVs Rate Maximization	103
5.1	Introduction	103
5.2	Problem Formulation	105
5.3	MAMA - An Aerial Highway Serving Cell Metric	107
5.3.1	MAMA Metric	107
	Average Channel Gain	108
	Channel Diversity Assessment	108
	Inter Cell Interference Assessment	109

Aerial Segment Serving Cell Selection	110
5.3.2 Illustrative Example	110
5.4 Two Stage solution: Aerial Highway Split and SSB Beam Selection . . .	112
5.4.1 Split and Segment-to-cell Association Problem	112
5.4.2 Aerial Highway Split Algorithm	113
Outer Split Algorithm	113
PAHSS Algorithm	113
5.4.3 SSB Codebook Beams and Transmit Power Selection Problem .	117
5.4.4 Extended SSB Codebook	118
5.4.5 Beam And Power Selection Genetic algorithm	119
5.4.6 Time Complexity	122
5.5 Optimization Setup	123
5.6 Two Stage Solution Resulting UAV Data Results	125
5.6.1 SSB Codeword Beam Selection Limitation	127
5.7 MAMA Coverage SSB Beam Continuous Solution	128
5.7.1 Two Stage with Beam Coverage Optimization Data Results . .	130
5.8 Type-A Data Precoder and Simulation Results	132
5.8.1 UAV Data SINR and Achievable Data Rate	134
UAV Traffic Analysis	141
Ground UEs Analysis	148
6 Conclusion	151
6.1 Future Research Directions	154
A NR Multi Antenna Transmission	155
B Line of Sight Probability and Path Loss	159
B.1 UMa Ground Segment	159
B.1.1 Line of Sight Probability	159
B.1.2 Path Loss Gain	159
B.2 UMi Ground Segment	160
B.2.1 Line of Sight Probability	160
B.2.2 Path Loss Gain	160
B.3 UMa Aerial Segment	161
B.3.1 Line of Sight Probability	161
B.3.2 Path loss Gain	161
B.4 UMi Aerial Segment	161
B.4.1 Line of Sight Probability	162
B.4.2 Path Loss Gain	162
C Optimization Problem Concavity	163
C.1 LTE Vertical Tilt Concavity	163
C.2 NR Coverage SSB Beam Concavity	165

List of Figures

1.1	Illustration of a cellular network with base station providing coverage on the ground and the aerial highways.	2
1.2	UAV communication research road map.	7
1.3	Example of UAVs along an aerial highway supported by the terrestrial network and generated interference.	8
1.4	Illustration of optimal 5G NR coverage beams planning for serving multiple aerial highway segments.	11
2.1	Adopted global reference system.	16
2.2	2D different network layouts.	19
2.3	2D different aerial highways configurations.	20
2.4	UPA antenna panel considered within NR networks.	21
2.5	LTE initial access frame structure.	27
2.6	Example of transmitted LTE beam.	27
2.7	NR SSB initial access frame structure.	29
2.8	NR SSB beams beamforming gain.	29
2.9	Example of NR SSB beam sweeping	30
2.10	Illustration of <i>Type-I</i> CSI/RS reporting.	32
3.1	Block diagram for the ADAM LTE vertical tilt optimizer.	39
3.2	Block diagram for the LTE vertical tilt optimization framework.	40
3.3	LTE vertical tilt utility function and obtained tilt for different aerial highway configurations in UMa.	45
3.4	LTE vertical tilt utility function and obtained tilt for different aerial highway configurations in UMi.	46
3.5	LTE vertical tilt utility function and obtained tilt for different aerial highway configurations in URD.	47
3.6	LTE obtained out of coverage rates for different network and aerial highways configurations.	50
3.7	LTE obtained SINR CDF for different aerial highways configurations and ground evaluation points in UMa.	51
3.8	LTE obtained SINR CDF for different aerial highways configurations and ground evaluation points in UMi.	53
3.9	LTE obtained SINR CDF for different aerial highways configurations and ground evaluation points in URD.	55

3.10	LTE obtained serving RSRP and interference CDF for different aerial highway altitudes.	58
3.11	LTE vertical tilt minimum required PRBs for C&C channels for different network and aerial highway configurations.	61
3.12	LTE obtained achievable UAVs and gUEs data rate CDF for different aerial highways configurations in UMa.	62
3.13	LTE obtained achievable UAVs and gUEs data rate CDF for different aerial highways configurations in UMi.	64
3.14	LTE obtained achievable UAVs and gUEs data rate CDF for different aerial highways configurations in URD.	66
4.1	Block diagram for the ADAM NR SSB beam codeword optimizer.	74
4.2	Block diagram for the NR SSB beam codeword optimization framework.	75
4.3	NR coverage SSB beams optimization utility function and activation values for different aerial highway configurations in UMa.	82
4.4	NR coverage SSB beams optimization utility function and activation values for different aerial highway configurations in UMi.	83
4.5	NR coverage SSB beams optimization utility function and activation values for different aerial highway configurations in URD.	84
4.6	NR coverage SSB beam SINR CDF for different aerial highways configurations in UMa.	87
4.7	NR coverage SSB beam SINR CDF for different aerial highways configurations in UMi.	89
4.8	NR coverage SSB beam SINR CDF for different aerial highways configurations in URD.	91
4.9	NR coverage SSB beam summary of obtained SINR gains for different network and aerial highways configurations.	93
4.10	Distribution of 5%-tile and mean NR SSB coverage considering all network and aerial highways configurations.	94
4.11	NR coverage SSB beam serving RSRP and interference for different aerial highway configurations in UMa.	96
4.12	NR coverage SSB beam serving RSRP and interference for different aerial highway configurations in UMi.	97
4.13	NR coverage SSB beam serving RSRP and interference for different aerial highway configurations in URD.	98
4.14	UAVs NR data SINR and achievable data rate CDF obtained after NR SSB beam optimization.	100
5.1	Simplified 2D network layout	110
5.2	UAV NR data SINR and rate CDF considering MAMA association metric in the simplified layout.	111
5.3	PAHSS and eGA algorithm utility functions.	124

5.4	UAVs NR data SINR and rate CDF obtained for the two-stage proposed solution with codebook coverage beams selection	126
5.5	UAVs accuracy association to MAMA serving cells considering coverage beam codebook selection at 150 m.	127
5.6	UAVs accuracy association to MAMA serving cells considering coverage beam codebook selection at 100 m.	128
5.7	Block diagram for the MAMA ADAM NR SSB beam optimizer.	130
5.8	Block diagram for the NR MAMA SSB beams optimization framework.	130
5.9	Utility function NR MAMA SSB beams optimization and obtained UAVs accuracy association to MAMA serving cells	131
5.10	UAVs NR data SINR and rate CDF obtained for aerial highway split and different coverage beams design methods.	132
5.11	UAVs NR data SINR and rate for different optimization schemes and precoders for a Curved aerial highway.	137
5.12	UAVs NR data SINR and rate for different optimization schemes and precoders for a Straight Centre aerial highway.	138
5.13	UAVs NR data SINR and rate for different optimization schemes and precoders for a Straight Edge aerial highway.	139
5.14	UAVs 5%-tile data SINR in a Curved aerial highways for different traffic conditions and optimization schemes.	142
5.15	UAVs 5%-tile data rate in a Curved aerial highways for different traffic conditions and optimization schemes.	143
5.16	UAVs 5%-tile data SINR in a Straight Centre aerial highways for different traffic conditions and optimization schemes.	144
5.17	UAVs 5%-tile data rate in a Straight Centre aerial highways for different traffic conditions and optimization schemes.	145
5.18	UAVs 5%-tile data SINR in a Straight Edge aerial highways for different traffic conditions and optimization schemes.	146
5.19	UAVs 5%-tile data rate in a Straight Edge aerial highways for different traffic conditions and optimization schemes.	147
5.20	gUEs NR data SINR and rate obtained for different for different aerial highways optimization schemes.	148
C.1	Percentage of concavity instance for the LTE vertical tilt optimization problem.	164
C.2	Percentage of concavity instance for the NR coverage beam optimization problem.	166

List of Tables

1.1	3GPP release 15 UAVs connectivity requirements.	5
1.2	3GPP release 19 UAVs connectivity requirements.	6
2.1	Summary of shadow fading standard deviation.	23
2.2	Antenna model parameters.	25
2.3	LTE sector antenna beamforming model parameters.	26
3.1	LTE vertical tilt optimization layout summary.	44
3.2	LTE vertical tilt optimization hyperparameters summary.	44
3.3	LTE obtained SINR statistics for different aerial highways configurations and ground evaluation points in UMa.	52
3.4	LTE obtained out of coverage rates for different aerial highways configurations and ground evaluation points in UMa.	52
3.5	LTE obtained SINR statistics for different aerial highways configurations and ground evaluation points in UMi.	54
3.6	LTE obtained out of coverage rates for different aerial highways configurations and ground evaluation points in UMi.	54
3.7	LTE obtained SINR statistics for different aerial highways configurations and ground evaluation points in URD.	56
3.8	LTE obtained out of coverage rates for different aerial highways configurations and ground evaluation points in URD.	56
3.9	LTE obtained serving RSRP and interference statistics for a Curved aerial highways in UMa.	57
3.10	LTE obtained UAVs and gUEs achievable data rate statistics for different aerial highways configurations in UMa.	63
3.11	LTE obtained UAVs minimum PRBs required for C&C channel for different aerial highways configurations in UMa.	63
3.12	LTE obtained UAVs and gUEs achievable data rate statistics for different aerial highways configurations in UMi.	65
3.13	LTE obtained UAVs minimum PRBs required for C&C channel for different aerial highways configurations in UMi.	65
3.14	LTE obtained UAVs and gUEs achievable data rate statistics for different aerial highways configurations in URD.	67
3.15	LTE obtained UAVs minimum PRBs required for C&C channel for different aerial highways configurations in URD.	67

4.1	NR coverage SSB beam optimization layout summary	81
4.2	NR Coverage SSB beams optimization hyperparameters summary.	81
4.3	NR SSB beams coverage SINR statistics for different aerial highways configuration in UMa.	88
4.4	NR SSB beams coverage SINR statistics for different aerial highways configuration in UMi.	90
4.5	NR SSB beams coverage SINR statistics for different aerial highways configuration in URD.	92
4.6	UAVs NR data SINR and achievable data rate statistic obtained after NR SSB beam optimization.	100
5.1	UAV NR data SINR and rate statistic considering MAMA association metric.	111
5.2	Summary of PAHSS and eGA hyperparameters.	124
5.3	UAVs NR data SINR and rate statistics obtained for the two-stage pro- posed solution with codebook coverage beams selection.	126
5.4	UAVs NR data SINR and rate statistics obtained for the two-stage pro- posed solution and different coverage beams design methods.	133
5.5	UAVs NR data SINR and rate for different optimization schemes and different aerial highways configurations.	140

To my parents, family, and all the friends I met on this journey...

Chapter 1

Introduction

WHAT will the future look like? The emergence of drones, also known as unmanned aerial vehicles (UAVs), has been foretold by experts and enthusiasts alike, envisioning a future where these flying marvels become an integral part of our society. This is no longer a distant vision, but a tangible reality. Fueled by their cost-effectiveness, and a remarkable ability to operate seamlessly in diverse and challenging conditions, drones have gathered significant attention [1–11]. To quantify their ascending trajectory, recent reports have projected the value of the civil drone market at 5.1 billion U.S. dollars by 2028 [12].

Although success depends on efficiently providing well-defined services, such as imaging, agriculture, and search & rescue [13, 14], urban environments pose a unique challenge, attracting only a few ventures so far. Amazon stands out as a pioneering force, launching its groundbreaking last-mile delivery service—Amazon Prime Air—in California in June 2022 [15]. Notably, Amazon’s strategic move to extend this service to Italy and the United Kingdom by the end of 2024 [16, 17] signals a shift towards conquering urban spaces.

Building upon this burgeoning interest in UAVs within urban landscapes, the growth in drone utilization within human-inhabited spaces poses a critical challenge: developing regulations for optimal management and safety in urban skies [18]. To tackle this concern, regulatory bodies and industries are collaboratively working to establish what can be deemed as the “highways of the sky” or simply aerial highways (AHs). Analogous to terrestrial highways, these designated airspace zones—often also referred to as “Drone Corridors”—are poised to play a pivotal role in drone transportation, providing predefined routes for UAV flights [19–21]. In this context, communication coverage will not be the primary design principle. Instead, regulators will focus on making the routes efficient, safe, and conducive to both human and business needs. Communication issues will be addressed at a later stage once AHs are established. So, as traffic controllers plan AHs in accordance with specific and varying regulations for UAVs flights, network operators aiming to support beyond visual line of sight (BVLoS) services must adapt and optimize their networks to ensure reliable connectivity along these designated flight zones—akin to the deployment of communication networks for terrestrial highways. Precisely, BVLoS operation refers to the ability of UAVs to operate outside the direct visual range of

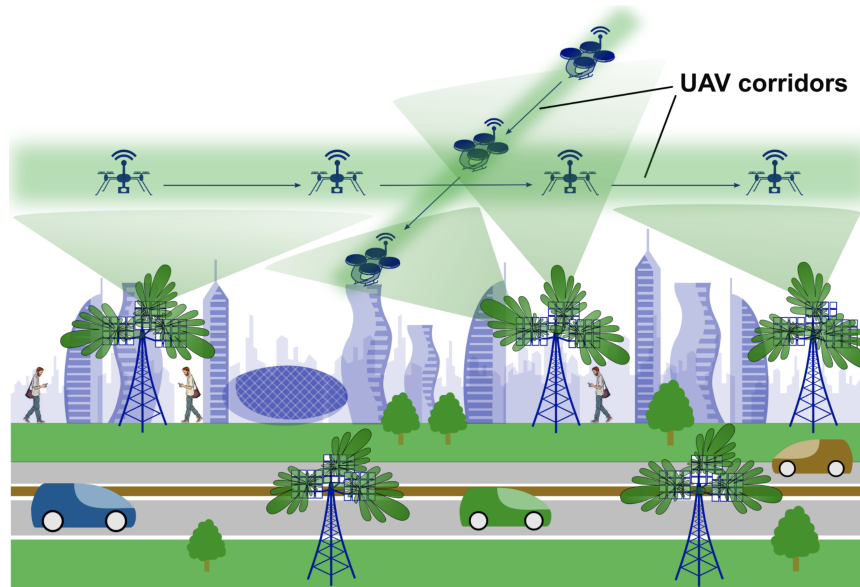


FIGURE 1.1: Illustration of a cellular network with down-tilted and up-tilted base stations providing coverage to ground users as well as UAVs flying along aerial highways (blurred green) [34].

the pilot, with a traffic control entity remotely monitoring and managing the UAVs movements to ensure safe and coordinated airspace operations.

The high-speed, low-latency capabilities of cellular networks, and in particular 5G, make it a prime contender to support the dynamic and data-intensive needs of AHs, ensuring seamless and efficient communication for urban drone navigation BVLoS [22–27]. However, cellular networks are optimized to serve ground user equipments (gUEs), and thus providing service to UAVs in general, and AHs in particular, comes with a series of significant challenges [28]. Overall, the radio propagation characteristics for UAVs differ significantly from conventional gUEs. Operating at considerable altitudes above the clutter of human-made structures inherently leads to favourable line of sight (LoS) conditions across potentially many cells. This unique scenario may result in UAVs receiving comparable signal power from multiple cells, introducing complexities in determining the optimal serving cell, and potentially disruptive interference for both downlink and uplink transmissions. As most networks operate multiple-input multiple-output (MIMO) today, the high spatio-temporal correlation among the complex channels of nearby UAVs in an AH may also significantly affect the overall drone performance [29–33]. Thus, bearing in mind these unique characteristics, current and future cellular networks require new solutions to be integrated to provision UAVs communications optimally.

1.1 Related Work

From a communication perspective, UAVs application can be classified into two categories: *i)* UAVs-aided network, where UAVs are acting as flying base stations

(BSs) to provide communication services in different use cases, such as disaster recovery, enhanced coverage for flash-crowd events or data harvesting in internet of thing (IoT) scenarios, and *ii*) cellular connected unmanned aerial vehicles (CCUAVs), where UAV acts as flying user equipments (UEs) and connect to cellular networks.

Although extraordinary work has been devoted to analyze, optimize and implement flying UAVs-BS systems [35–45], understanding how to optimally integrate CCUAVs within complex, large-scale cellular networks remains a topic that has not been fully explored. Therefore, within this thesis, we aim to tackle this research gap. Moreover, since we consider only CCUAVs, we will refer to them simply as UAVs for the remainder of the manuscript.

To address the intricate challenges of navigating UAVs in diverse environments, the research community has primarily focused on optimizing decisions and actions on the UAV side. Two notable solution categories have emerged. Generally speaking, the first involves UAV trajectory planning that maximizes UAV coverage, and/or rate, while simultaneously minimizing the impact on gUE performance due to resource sharing [46–50]. The second explores methods to enhance the robustness of UAV communications, primarily through optimal UAV association and multi-connectivity, optimizing the selection of serving cells and/or some of their transmit characteristics [51–53].

Yet, these autonomous, network-aware decision-making processes do not account for the challenges posed by AHs, and may lead to extended travel times, increased onboard complexity, and higher energy consumption. Additionally, the scalability of autonomous navigation plans is challenged by the increasing UAVs number, potentially conflicting with forthcoming safety regulations.

From our perspective, AHs demand a distinct approach. Rather than adapting UAV behaviours, AHs require optimizing existing or to-be-deployed networks to meet the UAVs' unique needs. However, research in this direction remains limited. Despite that, the research community has begun to adopt such a complementary approach, with few pioneering works investigating how aerial highways and the predetermined UAVs trajectories can enable different optimization frameworks. As an example, the work in [54] marked a milestone by investigating the optimal number and positions of millimetre wave (mmWave) cells with up-tilted antenna arrays required to serve AHs in an urban environment. From this work, we learnt two fundamental lessons: by leveraging AH information, it is possible to effectively derive the minimum number of BSs needed for communication service, as well as the efficacy of the use of mmWave cells, as the predominant LoS conditions help to avoid significant blockages. Then, building upon this, the authors of [55] extended their work by analyzing the benefits of non-orthogonal multiple access (NOMA) for up-link transmissions UAVs swarm in aerial corridors as well as optimizing their trajectory to jointly minimize interference and maximize efficiency. Focusing on the sub-6 GHz band, the studies proposed in [56,57] examined the advantages of deploying additional base stations for serving AHs. Importantly, these studies also provide an

analytical framework to assess coverage outages under specific assumptions. These works have shown, first, how leveraging the information regarding planned AH can enable optimal planning of terrestrial infrastructure, and second, the effectiveness of redistributing power in the sky to ensure reliable cellular coverage for UAVs operating within AHs. Then, to further investigate optimal deployment of infrastructure in [58], the authors proposed to integrate a new set of co-channel uptilted antennas to serve both UEs on the ground and UAVs over AH. Moreover, they proposed a solution based on genetic algorithm (GA) to optimally tune the tilt of the newly deployed antennas, while also analyzing the interference generated towards the ground and introducing an interference mitigation technique based on enhanced inter-cell interference coordination (eICIC). This work showed the potential of using GAs to address these problems as well as demonstrating the efficacy of deploying a set of antennas that radiate towards the AHs and, more importantly, underscores how integrating co-channel solutions for UAVs and gUE can significantly impact the latter; therefore, highlighting the need for solutions which mitigate the performance loss on the ground.

In the context of 4G long term evolution (LTE) networks, breaking new ground in [34,59], researchers pioneered a novel approach to tackle the intricacies of practical networks serving AHs. Instead of emphasizing the deployment of new uptilted infrastructure, the authors introduced a sophisticated mathematical framework based on quantization theory to optimize the downlink signal-to-interference-plus-noise ratio (SINR) for both terrestrial and aerial UEs. This optimization involved fine-tuning the downtilt and transmit power of already deployed base stations. With a similar motivation, the authors of [60] recently introduced a methodology based on machine learning (ML) and bayesian optimization (BO) for adjusting the sectors' electrical tilt and power, learning from the environment, with the final goal of maximizing the downlink SINR for both terrestrial and aerial UEs. These studies demonstrate that leveraging planning information of AHs permits the re-use of terrestrial LTE networks to provide reliable and robust coverage for UAVs.

Moving towards to the next generation of cellular networks, given its powerful precoding capabilities, massive multiple-input multiple-output (mMIMO) has become a key physical layer technology for 5G, and is expected to remain a cornerstone in the 6G era. In recent years, several studies have underscored the advantages of mMIMO in enhancing UAVs data connectivity [61–66]. Notably, beamforming has proven to be especially valuable in managing interference to and from UAVs, while spatial multiplexing capabilities have played a pivotal role in enhancing UEs data rates. However, despite their fundamental contributions, these studies have largely focused on scenarios involving sparsely located, hovering UAVs, overlooking the complexities of downlink data transmission and the complex challenges of operating 5G networks for UAVs in dense, dynamic environments like AHs, particularly in the context of prevalent mMIMO technology.

TABLE 1.1: 3GPP downlink requirements for UAVs connectivity services defined in release 15.

Items		Value
DL Data Rate	C&C	60–100 kbps
	Application Data	up to 50 Mbps
C&C Reliability	Up to 10^{-3} Packet Error Loss Rate	

1.2 Motivation

With the growth of the UAVs market and the emergence of new businesses, we believe that AHs will be primarily designed for the secure and safe management of in-sky applications. Additionally, we expect that these aerial lanes will be deployed based on governmental and aerospace standards rather than focusing solely on connectivity requirements. As a result, we believe that the adoption of AHs, along with their role in optimizing terrestrial cellular networks, will be key to achieving reliable, robust, and ubiquitous connectivity.

In terms of terrestrial cellular network support for UAVs communications, the 3rd Generation Partnership Project (3GPP) is actively advancing into defining requirements for accommodating aerial services. Specification for UAVs terrestrial supports have been defined within release 15 in technical report TR36.777 [67]. Precisely, Table 1.1 summarize the defined requirement in terms of command and control (C&C) and application rate. Although providing a minimum data rate for applications like video streaming, imaging, and sensor data is essential, the 3GPP places greater emphasis on setting minimum standards for C&C transmissions. These transmissions are critical for parameters such as telemetry, waypoint updates, real-time piloting, identification, and authorization in UAVs operations. Notably, the 3GPP specifies a required data rate between 60 and 100 kbps for these operations, with three nines reliability regarding packet error loss rate.

Moving towards the next generation of cellular networks, within the last few months,¹ the 3GPP is actively working on defining requirements for the incoming cellular networks within release 19. Specifically, within technical study TS22.125 [68] 3GPP identifies the requirements for operation of UAVs via 3GPP systems, including those regarding security, public safety, remote identification and communication key performance indicators (KPIs).

When focusing on C&C communication to enable BVLoS operations, 3GPP identify three operation modes to support it, specifically:

1. **D2D Mode:** In this mode, a UAV operates as a controller, establishing a direct link to other UAVs for control purposes.
2. **Network-Assisted Mode:** Here, a UAV acts as a controller but does not directly link to other UAVs. Instead, both UAVs connect to the terrestrial cellular network, which is responsible for providing reliable routing between them.

¹at the time of writing this manuscript.

TABLE 1.2: 3GPP data rate requirements for different UAVs application connectivity services for release 19.

Application	Data Rate	Altitude	Scenario
8K video live broadcast	100 Mbps (UL)	<100 m	Urban
	600 Kbps (DL)		
Laser mapping/HD patrol	120 Mbps (UL)	30–300 m	Urban, rural
	300 Kbps (DL)		
4×4K AI surveillance	120 Mbps (UL) 50 Mbps (DL)	<200 m	Urban, Rural
Remote UAV controller through HD video	≥25 Mbps (UL)	<300 m	Urban, Rural
	300 Kbps (DL)		

3. **Network-Controller Mode:** In this mode, control resides within the terrestrial cellular network. The UAVs are provided with pre-scheduled flight plans for autonomous operation and must establish reliable communication to periodically transmit flight status updates.

Among these operational modes, as anticipated, we identify the latter (the semi-autonomous method network-controller mode) as the most efficient method, as the use of AHs as pre-scheduled flight plans has the potential to enhance security, energy management and mission lifetime significantly. It is important to note that both mission lifetime and UAV energy consumption fall outside the scope of this thesis, as these aspects are assumed to be independently analyzed and optimized by dedicated flight controllers. In terms of data rate constraints and reliability, requirements for the C&C communication remain defined as in Table 1.1. Then, regarding data communication KPIs requirements, they identify minimum rates for different applications. Table 1.2 summarize requirements specified within 3GPP TS22.215 [68].

It should be noted that within the envisioned 3GPP ecosystems, despite the C&C operation modes discussed above, data transmission is always made by direct links within mobile networks. Thereby highlighting the need for cellular network solutions capable of efficiently integrating reliable UAVs while accounting for the coexistence of traditional terrestrial mobile services.

1.2.1 Research Directions

Despite the pioneering works introduced in Section 1.1, works in literature mainly focused UAVs-aided network solutions within research in the direction of cellular-connected UAVs, especially in the context of AHs quite limited. Therefore, our objective is to address this gap by exploring efficient solutions that can be seamlessly integrated to support communication for UAVs systems while ensuring compliance with the 3GPP requirements outlined in the previous section.

As illustrated in our research road map depicted in Figure 1.2, starting from the general UAVs communication optimization and moving towards optimization for cellular-connected UAVs, as anticipated, we envision that AHs will be essential

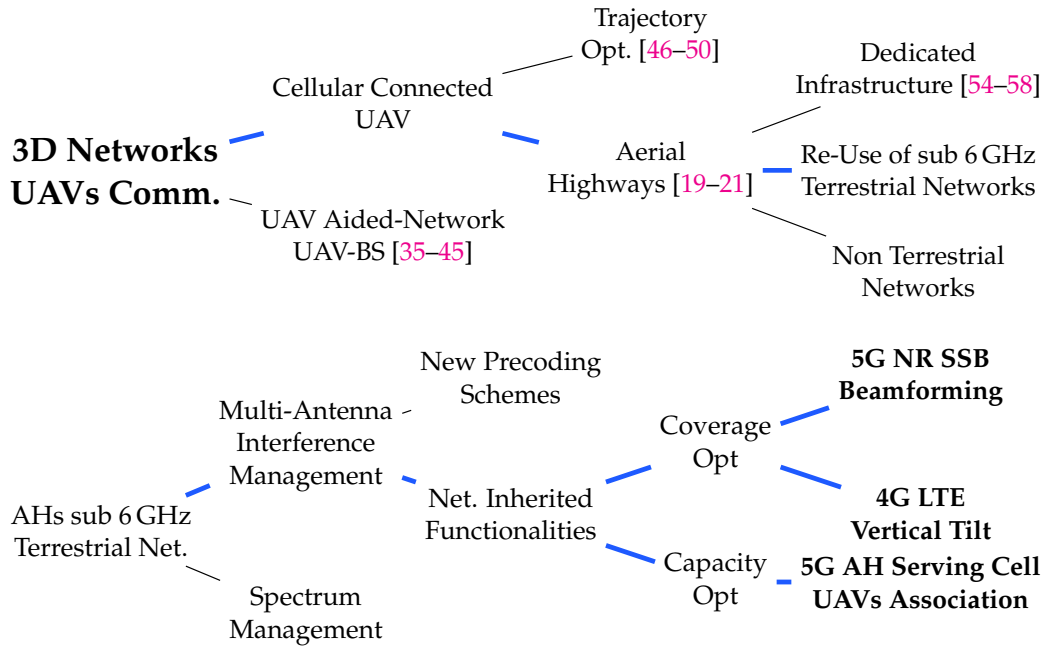


FIGURE 1.2: 3D networks UAVs communication research taxonomy.

for secure UAVs operations, as highlighted by some operational modes defined by 3GPP. However, research in this direction remains limited. In particular, we aim to provide an answer to the research question: “How to use the information regarding the planned AH, and thereby the trajectory that UAVs have to follow to optimize communication?”. As discussed in Section 1.1, a few pioneering works investigated how to support connectivity from cellular networks, specifically by focusing on deploying dedicated infrastructure. However, despite the important contribution of these works, relying on dedicated infrastructure, both terrestrial or non terrestrial networks (NTNs), an important drawback arises: the high cost of dedicated deployment, maintenance, and the capability to rapidly adapt to network variation and new configurations of AHs; as the last may change on relatively short time scale for meeting new business and management constraints. We believe that the solution to these practical challenges lies in fully re-using sub-6GHz terrestrial networks, which are currently the most widespread. Following that, our research question refines into: “How to use the information regarding the planned AH to **optimize deployed** terrestrial cellular network to jointly serve gUEs on the ground and UAVs over AHs?”

Current cellular networks are characterized by large complexity and high interplay of system parameters, which turn into numerous potential approaches for improving UAVs connectivity. Reserving specific spectrum portions or resource sets for UAVs communication, despite its effectiveness, would most likely cause disruption to legacy networks, drastically reducing KPIs for gUEs. Within this research, we target solutions that result in minimal loss on terrestrial networks, thereby allowing a perfect coexistence of legacy gUEs and cellular connected UAVs. Following that,

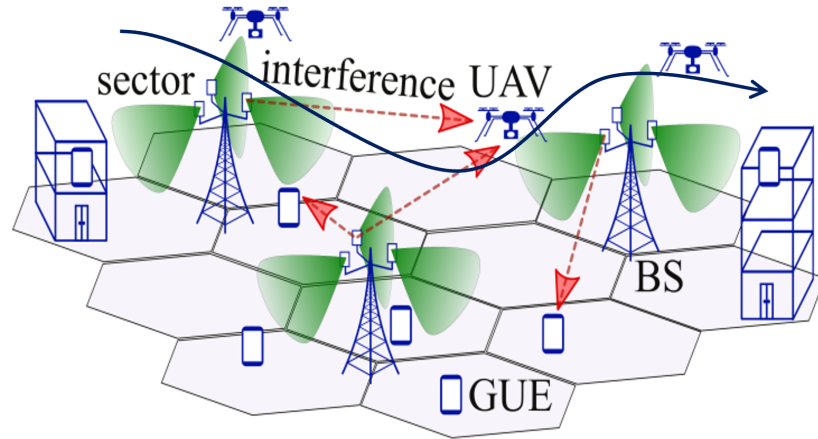


FIGURE 1.3: Example of UAVs along an AH supported by the terrestrial network and generated interference [63].

and inspired by the promising results achieved in literature for UAVs supported by mMIMO [61–66], we address how multi-antenna systems can be leveraged, together with the information of the planned AHs, to provide robust and enhanced aerial cellular connectivity on those.

When addressing mMIMO, most of the studies in the literature have focused on a scenario with sparsely distributed UAVs and on the design of optimal precoders for maximizing UAVs data performances. To the best of the author’s knowledge, no existing works in literature directly address AH systems and their inherent challenges, such as strong correlation and LoS predominance, nor explore the prior information of the planned AHs to derive optimal precoders.

Moreover, despite the expected large benefits introduced by designing ad-hoc precoders for UAVs, it is important to note that practical challenges, such as the need for highly accurate channel state information, real-time management of dedicated transmission schemes, and their integration into complex network procedures, impose significant constraints on the immediate deployment in current cellular networks. In this thesis, we believe that the most effective way to integrate UAVs lies in leveraging existing network functionalities. Specifically, we focus on approaches that avoid ad-hoc solutions or real-time processes for optimizing UAVs communication. Instead, our target is on the optimal planning of terrestrial networks, offering efficient and practical solutions that network operators can integrate into current or future cellular networks to immediately integrate AHs communication and provision desired UAVs services. Finally, but most importantly, we investigate solutions that ideally do not provide any loss on legacy gUEs.

With this in mind, our research question ultimately becomes: **“How to use the information regarding the planned AH to optimize deployed terrestrial cellular network at their planning stage, such that optimal service can be provisioned to UAVs without affecting ground performance?”**

1.3 Our Contributions

To tackle the research question discussed above, within this thesis we aim to target, from a system-level network perspective, two essential aspects of cellular 4G LTE and 5G new radio (NR) cellular networks optimization for AH: coverage optimization and capacity optimization.

Our contribution are summarized within the following sections.

1.3.1 4G LTE Vertical Tilt Optimization

With 5G NR deployments still in progress² and 4G LTE networks being the most prevalent today, we first investigate how network operators can use the information leveraged by the planned AH to adjust their 4G LTEs cellular networks and provide UAVs connectivity while maintaining continuous and unchanged service on the ground. As UAVs operate in the 3D space at altitudes up to a few hundred meters, they typically perceive favourable channel conditions across multiple network cells. This condition results at the UAVs in comparable signal power from both its serving cell and the neighbouring ones, thereby resulting in strong interference and, consequently, low signal quality. To address this problem, we propose a gradient-based vertical tilt framework for the 4G LTEs sectors, which, leveraging the knowledge of the AH, re-distribute the power along the AH to meet minimum constraints while also accounting for the coverage holes introduced by uptilted cells. Through comprehensive simulation results, we demonstrate the benefits and effectiveness of the proposed method in meeting 3GPP requirements, as well as highlighting the limitations of this proposed approach. Thus, we devise recommendations for network operators which aim to plan AH in their network and aim to provide service through 4G LTE networks.

Parts of the results presented in this chapter have been published in the following conference and journal:

- M. Bernabè, D. Lopez-Perez, D. Gesbert and H. Bao, "On the Optimization of Cellular Networks for UAV Aerial Corridor Support," GLOBECOM 2022 - 2022 IEEE Global Communications Conference, Rio de Janeiro, Brazil, 2022, pp. 2969-2974, doi: 10.1109/GLOBECOM48099.2022.10001469 [69].
- M. Bernabè, D. López-Pérez, N. Piovesan, and D. Gesbert, "Gradient-Based Optimization of Terrestrial Cellular Networks for Aerial Highways" (under submission in IEEE Transaction on Vehicular Technology).

1.3.2 5G NR SSB Beam Coverage Optimization

Moving towards the next generation of cellular networks, we focus on 5G NR systems and how to leverage their enhanced multi-antenna system capability to further

²at the start of this research work.

improve network coverage along AHs, addressing and overcoming the key limitation of 4G LTE networks. A key advancement of 5G NR, in terms of coverage, is its ability to perform beamforming also during the transmission of the signals controlling initial access. As later discussed in Chapter 2, 5G NR utilizes multiple directional beams to cover each cell's designated area. Therefore, building up and extending the previously discussed gradient-based method for LTE, we propose an optimization framework that uses the planned trajectory information to determine the optimal set of coverage beams across all network cells. The obtained results demonstrate the efficacy of the proposed methods, showing how the proposed methods permit the achievement of enhanced coverage of the AH within each scenario and overcome the limitation from 4G LTE networks.

Nevertheless, it should be noted that our simulation results obtained for final data rate transmission, with multiple gUEs and UAVs flying along the AHs, highlight the main limitation of the proposed optimization framework: re-optimizing terrestrial network to optimal provision coverage along the AH does not create any benefit in terms of final AH capacity, but actually can reduce it. Therefore, to tackle this issue, we investigate a novel approach to bridge together AH capacity and coverage optimization.

Parts of the results presented in this chapter have been published in the following journal:

- M. Bernabè, D. López-Pérez, N. Piovesan, and D. Gesbert, "Gradient-Based Optimization of Terrestrial Cellular Networks for Aerial Highways" (under submission in IEEE Transaction on Vehicular Technology).

1.3.3 Aerial Highway Segmentation and SSB Beam Planning for UAVs Rate Maximization

As UAVs traffic in AHs increases, the close proximity of UAVs and the dominance of LoS channel condition, lead to higher channel correlation, posing significant challenges for mMIMO systems. Here, we identify two critical research gaps: the lack of research on optimal UAVs cell associations under practical mMIMO configurations, and a scarcity of studies on large-scale downlink mMIMO optimization in 5G sub-6 GHz networks, especially in scenarios incorporating UAVs and AHs. Therefore, we propose a novel solution that leverages the knowledge of the AH to plan 5G coverage beams optimally. This strategy aims to control UAVs cell associations to maximise their capacity along the AH without impacting terrestrial users.

Specifically, we envision that the key to optimizing UAVs within AHs data rates without the need for additional complexity lies in their optimal cell association. Therefore, we formulate an optimization problem to select optimal coverage beams, along with their transmit power for each cell throughout the network, with the final goal of maximizing UAVs data rates while maintaining unchanged gUEs one.

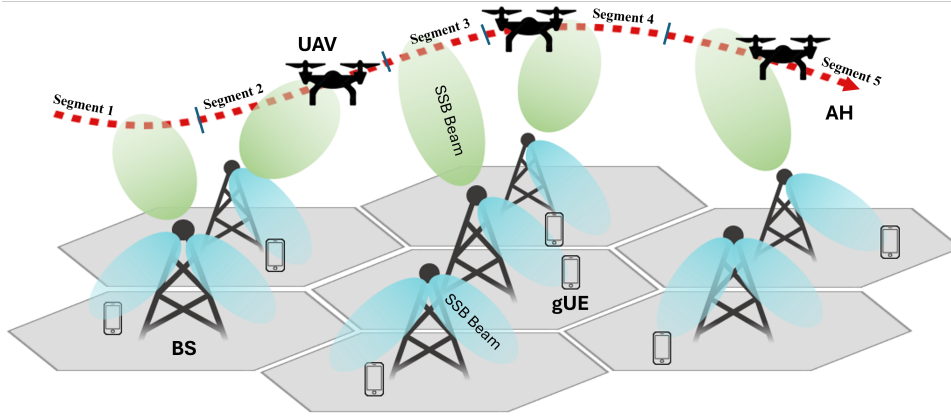


FIGURE 1.4: Illustration of optimal 5G NR coverage beams planning for serving multiple AH segments.

Then, to tackle the complex problem, we introduce a novel heuristic metric, named mMIMO-Aerial-Metric-Association (MAMA), for optimally identifying AH serving cells by jointly merging together information regarding multiplexing capability, average channel gain, and interference of each cell within the network. This metric leverages the information of the planned AH and enables the optimal and efficient definition of the set of serving cells aimed at provision coverage. Following that, we formulate a two-stage heuristic optimization framework to tackle the 5G NR beams planning problem. First, leveraging our proposed MAMAs metric, we define a problem to optimal split the AH in multiple segments of different lengths and define the optimal serving cell of each; then, we propose a particle swarm optimization (PSO)-based algorithm to solve the problem. Secondly, to enable the association of UAVs with their respective segments and designated serving cells—and acknowledging that network operators typically rely on discrete beam sets for network planning—we formulate an optimization problem to determine the optimal coverage beams from a discrete codebook with the final goal of maximize coverage from the identified set of AH serving cells. To solve the resulting mixed-integer non-convex problem, we design a GA solution.

Then, having identified the limitations of the previous codebook-based beam transmission, we define an optimization problem for precise beam design at the set of identified serving cells. In particular, we propose a continuous optimization problem to define, from the continuous vector space of complex numbers, the set of amplitude and phase shifters of cells representing the transmitted beams. Harnessing the methodology presented in Chapter 4 we propose a gradient-based method to solve the problem. Then, finally, through simulation results, we demonstrate the efficacy of our proposed methods, showing how adopting our proposed metric to optimally define the set of AHs serving cells, and in turn, provide optimal coverage from those, permits to enhance final UAVs data rate over the AH.

It should be noted that, in contrast with the related studies referenced previously in Chapter 1, our work presents the following distinctive characteristics:

1. To enhance final UAVs data rate, this work explores solutions within terrestrial networks rather than focusing on UAVs actions, such as trajectory planning and transmission schemes. As a result, it does not introduce additional complexity or payload on-board, which is crucial for UAVs efficiency and security.
2. Unlike works that rely on UAVs supported by dedicated terrestrial infrastructure, this study focuses on reusing existing networks. This approach minimizes the need to invest in additional high-cost dedicated infrastructure.
3. While existing literature on the optimization of already deployed networks for UAVs often only focuses on reusing 4G LTE infrastructure, this thesis targets 4G LTE and 5G NR mMIMO scenarios, where the last are characterized by high complexity and significant interplay among numerous system parameters.
4. While the literature has established mMIMO as a pivotal technology for enhancing aerial communications, those studies typically focus on a few sparsely located UAVs within the network. In contrast, this work is grounded in the forthcoming regulations that will govern air traffic through AHs. It considers several UAVs densely packed in small area (i.e., AH) and addresses the resultant challenges, including the high channel correlation due to typical LoS conditions, which severely limits spatial multiplexing capabilities.
5. This work focuses focus on showcasing the potential in adopting AHs to derive efficient optimization tools for maximizing aerial coverage and, indeed, maximizing UAVs achievable data rates on AHs from both 4G LTE and 5G NR terrestrial cellular networks.
6. When considering 5G NR system and maximization of in AH UAVs data rates, this work focuses solely on optimizing the UAVs cell association to enhance connectivity through the optimal panning of the coverage beams. And, to the best of the author's knowledge, this has never been attempted before.
7. Moreover, this work is also the first to present a scalar metric for defining, at the stage of network planning, the set of serving cells aimed at serving the AH, and a two-stage evolutionary algorithm that combines PSO and an GA to optimally segment the AH, identify the set of serving cells for each AH' segment, and determine the optimal configuration of coverage beams from those cells.
8. Finally, but most significantly, this work operates under realistic and practical assumptions. When considering final UAVs data rate maximization, we do not aim neither to provide real-time solutions nor optimize optimize coverage in real-time to meet instantaneous communication needs. Instead, with the final goal of enhancing the UAVs data rate, we focus on providing the best coverage over precise segments of the AH from a precise set of identified serving cells.

Parts of the results presented in this chapter have been published in the following conferences and journal:

- M. Bernabè, D. López-Pérez, N. Piovesan, G. Geraci and D. Gesbert, “A Novel Metric for mMIMO Base Station Association for Aerial Highway Systems,” 2023 IEEE International Conference on Communications Workshops (ICC Workshops), Rome, Italy, 2023, pp. 1063-1068 [70].
- M. Bernabè, D. López-Pérez, N. Piovesan, G. Geraci and D. Gesbert, “Massive MIMO for Aerial Highways: Enhancing Cell Selection via SSB Beams Optimization,” in IEEE Open Journal of the Communications Society, vol. 5, pp. 3975-3996, 2024 [71].
- M. Bernabè, D. López-Pérez, N. Piovesan, G. Geraci and D. Gesbert, “Optimal SSB Beam Planning and UAV Cell Selection for 5G Connectivity on Aerial Highways,” GLOBECOM 2024 - 2024 IEEE Global Communications Conference, Cape Town, Sour Africa, 2024 [72].

Finally, the rest of the thesis is organized as follows, Chapter 2 presents the models used to represent the networks, Chapter 3 introduces and discusses simulation results for the LTE vertical tilt optimization framework designed to efficiently optimize the terrestrial 4G LTE network to ensure cellular connectivity over AHs while maintaining continuous service over the ground. Chapter 4 introduces the optimization framework and the proposed gradient-based method devised to effectively leverage the knowledge of AHs and the enhanced multi-antenna capabilities of 5G NR systems to maximize cellular coverage along the AH. Additionally, it presents the simulation results, showcasing the improved coverage performance compared to 4G LTE. Moving towards optimization of capacity for AH systems, Chapter 5 motivates and introduces the new proposed metric for selecting the set of AHs serving cells and the two-stage proposed solution for AH segmentation and coverage beam selection/design. Finally, it introduces a dedicated transmission scheme tailored to the set of beams used for coverage control and discusses the simulation results, highlighting the advantages and benefits of our proposed approach. Finally, Chapter 6 concludes the work by summarizing the benefits and limitations of the proposed solutions, along with providing recommendations for network operators which aim to integrate and support AHs connectivity within their actual or future cellular networks.

Chapter 2

System Models

In this chapter, we introduce the models adopted in this work to represent the network. In the following, we first aim to present the commonly used models and then present the main characteristics of the two network generations under consideration in this research work: 4G LTE and 5G NR cellular networks. As, at the time of starting this research work, 4G LTE was the most widely adopted, with 5G NR networks deployments still ongoing.

It should be noted that in this work, we mainly focus on outdoor downlink (DL) network aspects, with the cellular network operating carrier frequency f_c in the sub-6 GHz spectrum frequency range 1 (FR1), as it is nowadays the most used portion of the available licensed spectrum. Precisely, we consider a LTE network working at 2.6 GHz and a NR network operating at 3.5 GHz.

We assume full frequency reuse among all the considered network cells, and, in addition, we assume equal long-term resource allocation among UEs within the network, as typically done by round-robin schedulers. Then, we consider a total available band B_0 at each cell.

To derive insights that are directly applicable to real-world urban deployments, we adhere to the stochastic channel modelling guidelines and specifications outlined by the 3GPP. The following documents are primarily considered:

1. 3GPP TR 38.901 [73]: “Study on Channel Model for Frequencies from 0.5 to 100 GHz”. This document is used to define the network layout, model antennas and panels, and address all channel aspects concerning terrestrial UE.
2. 3GPP TR 36.777 [67]: “Study on Enhanced LTE Support for Aerial Vehicles”. This document is used to extend the models considered in [73] and accommodate aerial vehicles.
3. 3GPP TR 36.814 [74]: “Further Advancements for E-UTRA Physical Layer Aspects”. This document is utilized for modelling LTE macro cellular sectors.
4. 3GPP TR 38.214 [75]: “Physical Layer Procedures for Data” and 3GPP TR 38.211 [76] “Physical Channels and Modulation”. These documents are used for NR UEs data reporting and precoding.

Finally, we adopt the coordinate references system outlined by 3GPP in [73, Section 7.1] and represented in Figure 2.1

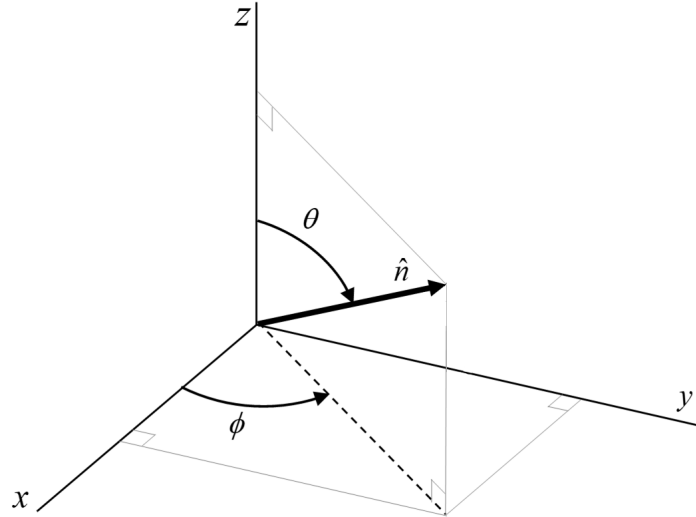


FIGURE 2.1: Adopted global reference system.

2.1 Network Cell Layout

To evaluate how various network layout may impact performances and also to demonstrate the effectiveness of our proposed solutions, this research focuses on three different outdoor urban scenarios. Each scenario comprises N_{site} base station sites, characterized by different geometric layout configurations.

In more detail, we take into account the following scenarios:

- Urban macro (UMa), where base station sites are arranged in a 2-tiers hexagonal grid with inter-site distance (ISD) d_{ISD} set to 500 m and height h_{BS} set to 25 m.
- Urban micro (UMi), where base station sites are arranged in a 2-tiers hexagonal grid with ISD d_{ISD} set to 200 m and height h_{BS} set to 10 m.
- Urban random distributed (URD), where base station sites are uniformly randomly distributed within the whole network area in the interval $[-1000, 1000]$ m for both X and Y-coordinates. Moreover, within this configuration, it is ensured a minimum 200 m distance between neighbouring sites and constant height h_{BS} of 25 m

Within each network layout configuration, each site hosts three sectors with bore-sight directions evenly spaced with 120° intervals to ensure consistent orientations across the network. Then, it should be noted that for the remaining part of the thesis, terms “sector” and “cell” will be used as synonyms.

Finally, we denote with \mathcal{B} the set of all cells within the network and with N_{BS} its cardinality.

2.1.1 Evaluation Points

To systematically study the average ground coverage signal quality within our network, we employ an approach involving a regular two-tier hexagonal grid of ground evaluation points. These points are spaced at an inter-grid distance (IGD) denoted as d_{IGD} ; we consider IGD set to 25 m, in accordance with the coherent spatial distances outlined in [73]. This grid spans the entirety of the network layout at a specified altitude h_g . The height of the ground grid is set to $h_g=1.5$ m, as reference height specified by 3GPP for gUEs. We refer to this set of evaluation ground points with \mathcal{E}_g and with N_g^e to its cardinality.

Within the sky, for each AH of length L_a that stretches over several cell centres and edges, we consider a series of consecutive aerial evaluation points at fixed altitude h_a . These points will impose positions in which, later on, UAVs must navigate through while traversing the network. All of these points have a fix inter-highway distance (IHD), denoted as d_{IHD} , and, to ensure high precision in evaluating final performance, this distance is set to 1 m. We denote this set of points with \mathcal{E}_a and its cardinality with N_a^e .

In this work, we consider three different configurations of aerial highways: *Curved*, *Straight Edge* and *Straight Centre* (see Figure 2.3). The first trajectory traces a curved path from south to north, navigating cell edges and centres, emulating potential operator routes that bypass certain coordinates. The *Straight Edge* and *Straight Centre* trajectories, in contrast, represent direct straight paths between two points (e.g., an AH connecting two warehouses); however, the first, *Edge*, consistently crosses cell edges, while the second, *Centre*, mainly passes through cell centres. Thereby tackling different network conditions.

Finally, we denote with $\mathcal{E} = \mathcal{E}_g \cup \mathcal{E}_a$ the set of all evaluation points in the network and with $N_e = N_g^e + N_a^e$ its cardinality.

2.1.2 UEs Distribution

To assess the final network data performance, we consider a fully loaded scenario with outdoor single antenna UEs deployed within the network. We consider two distinct types of UEs in our analysis: gUEs located on the ground portion of the network and cellular connected UAVs flying along the considered AH. In this work, we focus exclusively on CCUAVs and we do not consider other scenarios involving drones; therefore, we refer to CCUAVs simply as UAVs.

Within the network, we randomly deploy N_g gUEs on the ground at altitude h_g , as for the ground evaluation grid points, i.e., at 1.5 m. We denote with \mathcal{G} the set of gUEs.

More precisely, assuming consistent traffic across all network cells, we uniformly random deploy N_g^{cell} gUE within each network cell; therefore, for each network realization i , the x-y coordinates of each gUEs g of the N_g^{cell} w.r.t. to cell b , are computed

as follows,

$$\begin{bmatrix} x_g \\ y_g \end{bmatrix} = \begin{bmatrix} r_{g,b} \cos(\varphi_{g,b}) \\ r_{g,b} \sin(\varphi_{g,b}) \end{bmatrix}, \quad (2.1)$$

with

$$r_{g,b} \sim U(d_{\min}^g, d_{\max}^g), \quad \varphi_{g,b} \sim U(-60^\circ + \phi_b^{\text{bst}}, +60^\circ + \phi_b^{\text{bst}}), \quad (2.2)$$

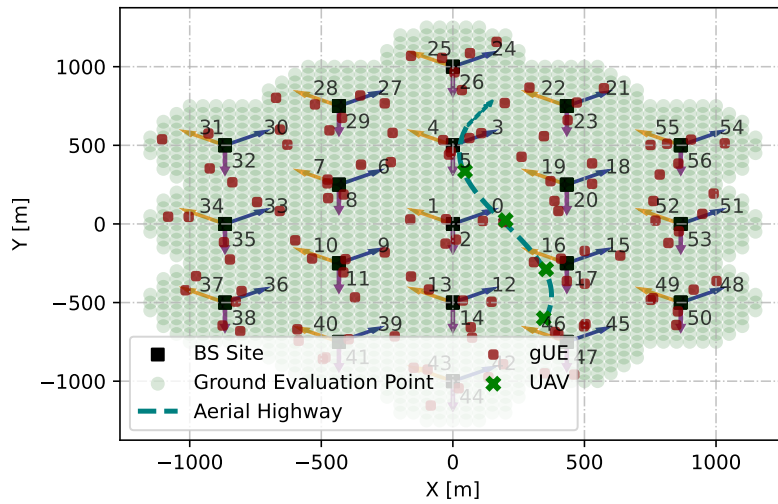
where we recall ϕ_b^{bst} being the boresight direction of cell b , then d_{\min}^g is the minimum distance between gUE and cell b and it is set to 35 m, according to [73], and, similarly, d_{\max}^g is the maximum distance set to $d_{\text{ISD}}/2$.

The random deployment of gUEs across the network at each network realization ensures a realistic simulation of gUEs distribution and mobility within urban environments.

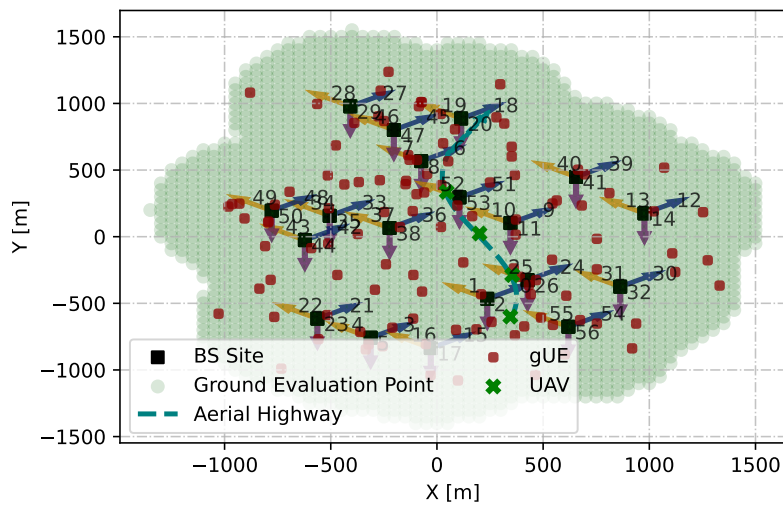
Within the aerial part of the network, a total number of N_{uav} UAVs are located along the AH at fixed altitude h_a . We denote with \mathcal{A} the set of UAVs in the network. Along the AH UAVs evenly spaced with a fixed inter-UAV distance (IUD) d_{IUD} , where reference values for secure collision avoidance can be found in recently published works [77, 78]. Within this configuration, UAVs move collectively along the AH, therefore maintaining the same d_{IUD} . Moreover, maintain a continuous consistent traffic condition, at each network iteration, if a UAV exits the AH, a new one immediately enters.

We denote as \mathcal{U} the set of all UEs, comprising both gUEs and UAVs; we denote with $N_u = N_g + N_{\text{uav}}$ the cardinality of this set.

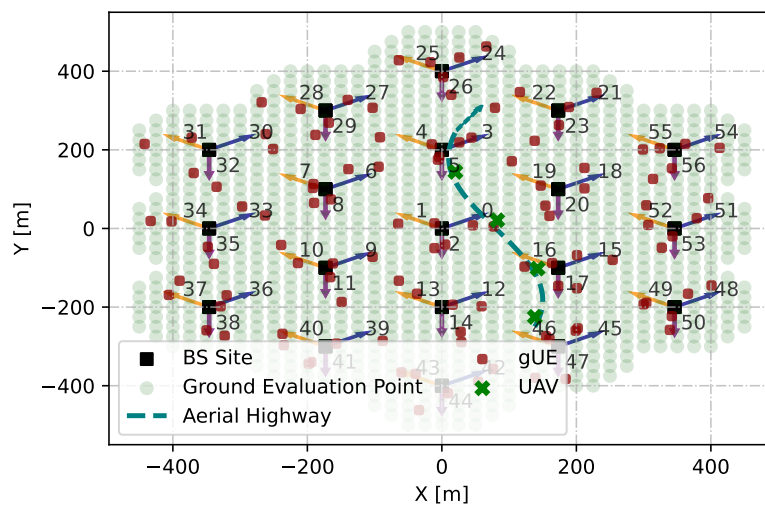
Finally, Figure 2.2 shows the three different network cell layout configurations, i.e., UMa, URD and UMi, as well as the set of located evaluation ground points \mathcal{E}_g and aerial highways. Then, Figure 2.3 shows the three considered AH configurations within a UMa network layout.



(a) UMa Scenario

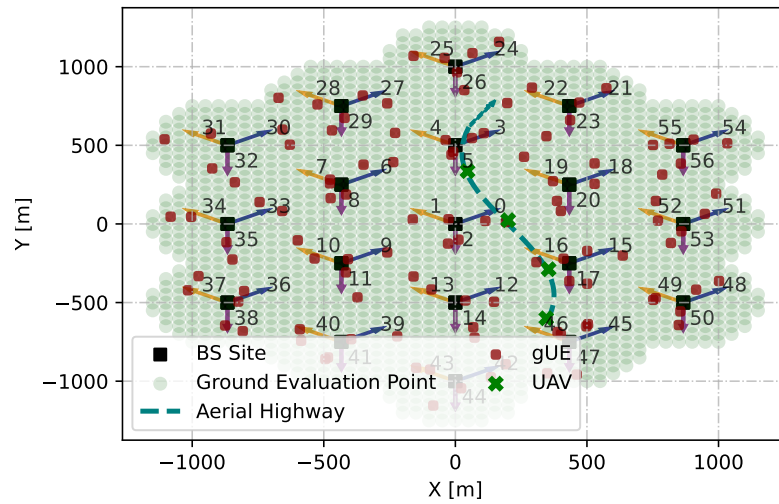


(b) URD Scenario

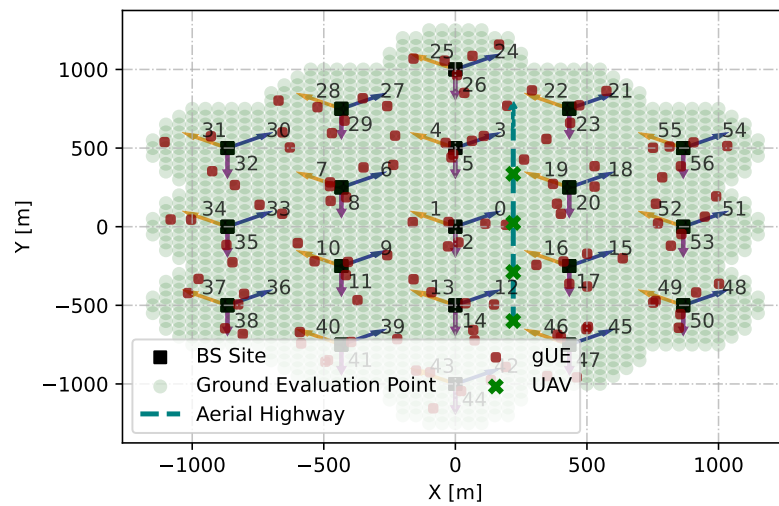


(c) UMi Scenario

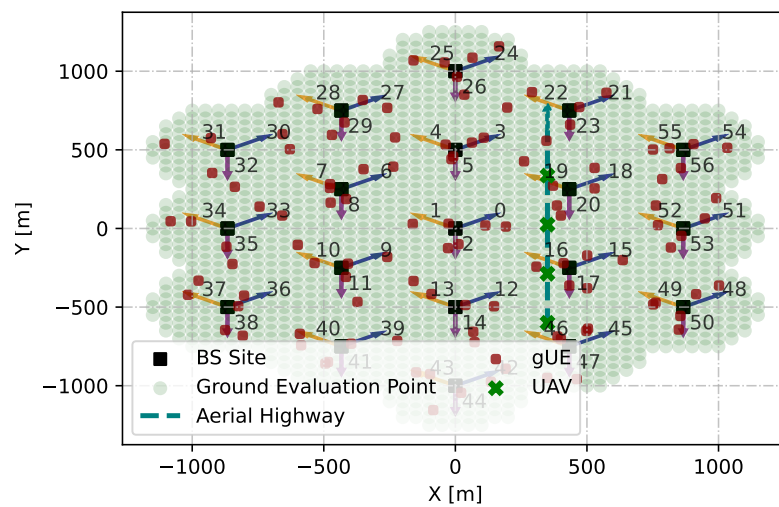
FIGURE 2.2: 2D different network layouts with ground evaluation points, random gUEs and example of aerial highway with UAVs.



(a) Curved



(b) Straight Edge



(c) Straight Centre

FIGURE 2.3: 2D UMA network layout with different configurations for the aerial highway.

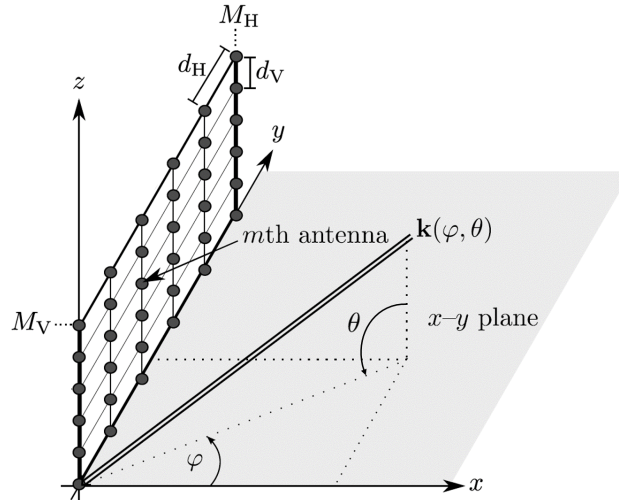


FIGURE 2.4: UPA antenna panel considered within NR network cells consisting of M_v vertical and M_h horizontal antenna elements equalising spaced [79].

2.2 Antenna Sector Array

Within this research work, we focus on two different cellular network generations: 4G LTE and 5G NR. In the following, we introduce models for both the LTE and NR panel structures.

2.2.1 LTE ULA Panel

Within the LTE network, we assume each cell b is equipped with a vertical uniform linear array (ULA) antenna panel consisting of N single vertically polarized antenna elements.

4G LTE network involves panels with all antennas connected to a single digital transceiver. As a result, the transmitted beam from these antennas is fixed and steered in the boresight direction on the azimuth plane, with a vertical tilt controlled by the transceiver which introduces a constant phase shift across the connected antennas.

2.2.2 NR UPA Panel

When considering NR networks, we assume each cell b is equipped with a vertical uniform planar array (UPA) antenna panel consisting of M single vertically polarized antenna elements arranged in M_v rows and M_h columns, as represented in Figure 2.4. However, in contrast to what was presented for LTE networks to embrace the enhanced beamforming capability introduced with NR and thereby enable full-dimensional MIMO, we consider each antenna element connected to a digital transceiver.

For each UPA panel at each cell, both vertical and horizontal spaces d_v and d_h between adjacent antenna elements are set to $\lambda_p/2$, where λ_p is the panel design

wavelength, determined according to the operating frequency f_c . Then, for each cell b , \mathbf{V}_b represents the matrix containing the Cartesian coordinate of each antenna element relative to the panel centre, defined as follows,

$$\begin{aligned} \mathbf{V}_b &= \begin{bmatrix} v_{0,b}^x & \cdots & v_{m,b}^x & \cdots & v_{M-1,b}^x \\ v_{0,b}^y & \cdots & v_{m,b}^y & \cdots & v_{M-1,b}^y \\ v_{0,b}^z & \cdots & v_{m,b}^z & \cdots & v_{M-1,b}^z \end{bmatrix} = \mathbf{R}_{xy}(\phi_b^{\text{bst}}) \mathbf{R}_{zy}(\theta_b^{\text{tilt}}) \mathbf{R}_{zx}(\gamma_b^{\text{slt}}) \mathbf{U} = \quad (2.3) \\ &= \mathbf{R}_{xy}(\phi_b^{\text{bst}}) \mathbf{R}_{zy}(\theta_b^{\text{tilt}}) \mathbf{R}_{zx}(\gamma_b^{\text{slt}}) \begin{bmatrix} u_0^x & \cdots & u_m^x & \cdots & u_M^x \\ u_0^y & \cdots & u_m^y & \cdots & u_M^y \\ u_0^z & \cdots & u_m^z & \cdots & u_M^z \end{bmatrix}, \end{aligned}$$

where \mathbf{U} represents the cartesian coordinate for the reference panel. The Cartesian coordinates of each antenna m is defined as follows,

$$\begin{bmatrix} u_m^x \\ u_m^y \\ u_m^z \end{bmatrix} = \begin{bmatrix} 0 \\ \text{mod}\left(\frac{m}{M_H}\right) \frac{\lambda}{2} - \text{mod}\left(\frac{M}{M_H}\right) \frac{\lambda}{2} \\ \lfloor \frac{m}{M_H} \rfloor \frac{\lambda}{2} - \frac{\lambda}{2} \lfloor \frac{M}{M_H} \rfloor \end{bmatrix}. \quad (2.4)$$

Then, to accommodate each panel at each cell with the correct boresight, tilt and slant angles, the three rotation matrices $\mathbf{R}_{xy}(\phi_b^{\text{bst}})$, $\mathbf{R}_{zy}(\theta_b^{\text{tilt}})$, $\mathbf{R}_{zx}(\gamma_b^{\text{slt}})$ are applied to \mathbf{U} . The three rotation matrices are defined as follows,

$$\mathbf{R}_{xy}(\phi_b^{\text{bst}}) = \begin{bmatrix} \cos(\phi_b^{\text{bst}}) & -\sin(\phi_b^{\text{bst}}) & 0 \\ \sin(\phi_b^{\text{bst}}) & \cos(\phi_b^{\text{bst}}) & 0 \\ 0 & 0 & 1 \end{bmatrix} \quad (2.5)$$

$$\mathbf{R}_{zy}(\theta_b^{\text{tilt}}) = \begin{bmatrix} \cos(\theta_b^{\text{tilt}}) & 0 & -\sin(\theta_b^{\text{tilt}}) \\ 0 & 1 & 0 \\ \sin(\theta_b^{\text{tilt}}) & 0 & \cos(\theta_b^{\text{tilt}}) \end{bmatrix} \quad (2.6)$$

$$\mathbf{R}_{zx}(\gamma_b^{\text{slt}}) = \begin{bmatrix} 1 & 0 & 0 \\ 0 & \cos(\gamma_b^{\text{slt}}) & -\sin(\gamma_b^{\text{slt}}) \\ 0 & \sin(\gamma_b^{\text{slt}}) & \cos(\gamma_b^{\text{slt}}) \end{bmatrix}. \quad (2.7)$$

It should be noted that for both LTE and NR we consider each panel downtilted at 150° .

2.3 Channel Model

In this section, we provide an overview of the channel models adopted in this work. In more detail, we rely on 3GPP's channel models as the widely adopted, standardized and referenced models for characterizing cellular networks. Specifically, for gUEs we adopt model outlined in document [73], while, its extension presented in [67] is used for aerials. For the sake of completeness, we report here recent works

that focused on channel measurements and modelling for UAVs communications. These studies analyze not only ground-to-air segments but also air-to-ground and air-to-air scenarios [80–82].

In this work, we consider at each UEs (i.e., both legacy gUE and UAVs) a noise figure F_{ue} equals to 9 dB and a spectral noise density \bar{N}_0 equals to -174 dBm/Hz. Then, we refer with N_0 to the UE spectral noise density computed as $N_0 = F_{\text{ue}}^{\text{lin}} \bar{N}_0^{\text{lin}}$.

In the remaining part of the section, we introduce the large-scale channel components, such as LoS probability, path loss, shadowing, and the complex representation of the fast-fading, characterizing the channel between each outdoor UE u and network cell b .

2.3.1 Line of Sight Probability and Path Loss

In this work we adopts models outlined by 3GPP in [73, Section 7.4] and [67, Section A.1] to compute the LoS probability $P_{u,b}^{\text{LoS}}$ and the path loss gain $\rho_{u,b}$ for each UE u and each cell b . Specifically, the employed models consider both UMa and UMi scenarios and differentiate between gUEs located on the ground segment and UAVs located on the aerial one. A detailed description of these models is provided in Appendix B.

2.3.2 Shadow Fading Gain

In this work, we model the stochastic shadow fading gain $\tau_{u,b}$, between each UE u and cell b , as a zero mean log-normal random variable, with standard deviation values outlined by 3GPP in [73, Table 7.5-6 Part-1] and [67, Table B-3]. As described in [67], for aerial UE, i.e., UAVs, shadow fading standard deviation values under LoS conditions depend on the altitude. Specifically, standard deviation values are computed as,

$$\sigma_{\text{SF}}^{\text{UAV-UMa-LoS}} = 4.64e^{-0.0066h_{\text{AH}}}, \quad (2.8)$$

$$\sigma_{\text{SF}}^{\text{UAV-UMi-LoS}} = \max\left(5e^{-0.01h_{\text{AH}}}, 2\right). \quad (2.9)$$

The standard deviation values in dB are summarized in Table 2.1.

TABLE 2.1: Summary of shadow fading standard deviation.

UMa				UMi			
Ground		Aerial		Ground		Aerial	
LoS	NLoS	LoS	NLoS	LoS	NLoS	LoS	NLoS
4	6	eq. (2.8)	6	4	7.82	eq. (2.9)	8

Moreover, we embrace 2D spatial correlation among the realization of the log-normal shadow fading; specifically, shadow fading maps generated for each network configuration are generated using a proprietary tool which is baed on the work presented in [83].

2.3.3 Multi-Path Fading

In the following, we introduce the small-scale fading capturing the multi-path nature of the link between each UE u and the M antennas of each sector b . Specifically, we model the small-scale fading as a Rician fading. Embracing the plane wave approximation [73, 79], the resulting downlink small-scale channel $\mathbf{h}_{u,b}^{\text{dl}} \in \mathbb{C}^{1 \times M}$ is modeled as follows:

$$\mathbf{h}_{u,b}^{\text{dl}} = \sqrt{\frac{K}{1+K}} \mathbf{h}_{u,b}^{\text{LoS}} + \sqrt{\frac{1}{1+K}} \mathbf{h}_{u,b}^{\text{NLoS}}, \quad (2.10)$$

with

$$\mathbf{h}_{u,b}^{\text{LoS}} = e^{-j\frac{2\pi}{\lambda_c} d_{u,b}^{\text{3D}}} e^{j\frac{2\pi}{\lambda_c} \mathbf{k}_{u,b}^T(\phi_{u,b}, \theta_{u,b}) \mathbf{V}_b} \quad (2.11)$$

and

$$\mathbf{h}_{u,b}^{\text{NLoS}} \sim \text{CN}(\mathbf{0}, \mathbf{I}_M), \quad (2.12)$$

where we recall $d_{u,b}^{\text{3D}}$ being the 3D distance between UE u and the cell's b panel centre, then, $\phi_{u,b}$ and $\theta_{u,b}$ are their relative azimuth and zenith angles, respectively¹. Then, K is the Rician factor that characterizes the trade-off between the LoS and not line of sight (NLoS) component of the channel, with values outlined in [67, 73].

The wave vector $\mathbf{k}_{u,b}(\cdot, \cdot)$ represents the phase variation of a plane wave in 3D-orthogonal directions, defined as follows:

$$\mathbf{k}_{u,b}(\phi_{u,b}, \theta_{u,b}) = \begin{bmatrix} \cos(\phi_{u,b}) \cos(\theta_{u,b}) \\ \sin(\phi_{u,b}) \cos(\theta_{u,b}) \\ \sin(\theta_{u,b}) \end{bmatrix}, \quad (2.13)$$

and we recall \mathbf{V}_b as the matrix containing the Cartesian coordinates of each antenna element w.r.t. the panel centre.

2.4 Antenna Element Gain and Beamforming Gain

In the following, we present models outlined by 3GPP in [73, Table 7.3-1] for the single antenna element gain. Specifically between each UE u and cell b the antenna element gain $g_{u,b}$ is defined as follows,

$$g_{u,b} = 10^{\frac{g_{u,b}|_{\text{dB}}}{10}}, \quad (2.14)$$

with $g_{u,b}|_{\text{dB}}$ representing the gain in dB and defined, following 3GPP models as,

$$g_{u,b}|_{\text{dB}} = G_0 - \min\left(-\left(G_{u,b}^V + G_{u,v}^H\right), A_m\right). \quad (2.15)$$

¹Note that the reference zenith angle $\theta_{u,b} = 0$ points towards the sky.

Where G_0 is the antenna maximum directional gain and $G_{u,b}^V$ and $G_{u,b}^H$ are, respectively, the vertical and horizontal offset gain defined as,

$$G_{u,b}^V = -\min \left(12 \left(\frac{\theta_{u,b} - \theta_b^{\text{tilt}}}{\theta_{3\text{dB}}} \right)^2, \text{SLA}_v \right), \quad (2.16)$$

$$G_{u,b}^H = -\min \left(12 \left(\frac{\phi_{u,b} - \phi_b^{\text{bst}}}{\phi_{3\text{dB}}} \right)^2, A_m \right). \quad (2.17)$$

where $\phi_{u,b}$ and $\theta_{u,b}$ represent the azimuth and zenith angles, respectively, between UE u and sector b . ϕ_b^{bst} and θ_b^{tilt} denote the boresight and vertical tilt directions of cell b , respectively. Then, $\phi_{3\text{dB}}$ and $\theta_{3\text{dB}}$ are the 3 dB beamwidths in the horizontal and vertical directions, respectively. And finally, SLA_v and A_m are the side-lobe attenuation in the vertical and horizontal planes.

Parameters for the antenna element gain modelling are summarized in Table 2.2

Parameter	G_0	A_m	SLA_v	$\phi_{3\text{dB}}$	$\theta_{3\text{dB}}$
Value	8 dBi	30	30	65°	65°

TABLE 2.2: Antenna model parameters.

2.4.1 Beamforming Gain

When considering LTE networks we model the resulting ULA beamforming gain according to what outlined by 3GPP in [74, Table A.2.1.1-2]. Specifically, the antenna beamforming gain $g_{u,b}^{\text{lte}}$ in between each UE u and each cell b is computed as follows,

$$g_{u,b}^{\text{lte}} = 10^{\frac{g_{u,b}^{\text{lte}}|_{\text{dB}}}{10}}, \quad (2.18)$$

with $g_{u,b}^{\text{lte}}|_{\text{dB}}$ representing the gain in dB and defined as,

$$g_{u,b}^{\text{lte}}|_{\text{dB}} = G_0^{\text{lte}} - \min \left(- \left(G_{u,b}^{V,\text{lte}} + G_{u,b}^{H,\text{lte}} \right), A_m^{\text{lte}} \right). \quad (2.19)$$

In the above formulation G_0^{lte} is the maximum directional beamforming gain and $G_{u,b}^V$ and $G_{u,b}^H$ are, respectively, the vertical and horizontal offset gains defined as,

$$G_{u,b}^{V,\text{lte}} = -\min \left(12 \left(\frac{\theta_{u,b} - \theta_b^{\text{tilt,lte}}}{\theta_{3\text{dB}}^{\text{lte}}} \right)^2, \text{SLA}_v^{\text{lte}} \right), \quad (2.20)$$

$$G_{u,b}^{H,\text{lte}} = -\min \left(12 \left(\frac{\phi_{u,b} - \phi_b^{\text{bst}}}{\phi_{3\text{dB}}^{\text{lte}}} \right)^2, A_m^{\text{lte}} \right). \quad (2.21)$$

it should be noted that models in eqs. (2.19), (2.20) and (2.21), together within their specific parameters outlined in [74, Table A.2.1.1-2] and summarized in Table 2.3, incorporate both the single antenna gain and the beamforming effects.

Parameter	G_0^{lte}	A_m^{lte}	SLA_v^{lte}	$\phi_{3\text{dB}}^{\text{lte}}$	$\theta_{3\text{dB}}^{\text{lte}}$
Value	14 dB	25	20	70°	10°

TABLE 2.3: LTE sector antenna beamforming model parameters.

Within NR networks, leveraging the multi-antenna panel’s capability of actively control the phase shift at each antenna, the resulting beamforming gain $\delta_{u,b}^{\text{nr}}$ between each UE u and each cell b is defined as follows,

$$\delta_{u,b}^{\text{nr}} = \left| \mathbf{h}_{u,b}^{\text{dl}} \mathbf{w}_{u,b} \right|^2, \quad (2.22)$$

where $\mathbf{w}_{u,b} \in \mathbb{C}^{M \times 1}$ is a complex codeword representing each antenna amplitude and phase shift.

2.5 Network Initial Access

In both LTE and NR networks, during the initial phase of cell discovery and access, each cell b transmits multiple signals, such as common reference signal (CRS), primary synchronization signal (PSS), secondary synchronization signal (SSS) and physical broadcast channel (PBCH), all across the designated coverage area. Those signals allow UEs to properly synchronize with the network, conduct measurements, select the serving cell, report to the serving cell information and establish a connection for data transmission [84].

Our objective in this work is not to delve into the specifics of those signals. Rather, we concentrate on system-level considerations and problems, including achieving sufficient coverage SINR for decoding reference signals.

2.5.1 LTE Initial Access

The primary focus of LTE macro cellular networks has been on extensive macro networks and relatively large serving areas. A cornerstone of LTE are the cell-specific reference signals, which are continuously transmitted following the transmitting beam pattern described in Section 2.2.1. It should be noted that this large beam, as shown in the frame structure in Figure 2.5, is used both to transmit reference signals for cell discovery and initialization, as well as transmitting data.

The reference signals, moreover, are continuously transmitted, regardless of whether there is downlink data to transmit or not; for these reasons, LTE reference signals are often referred to as “always-on” signalling.

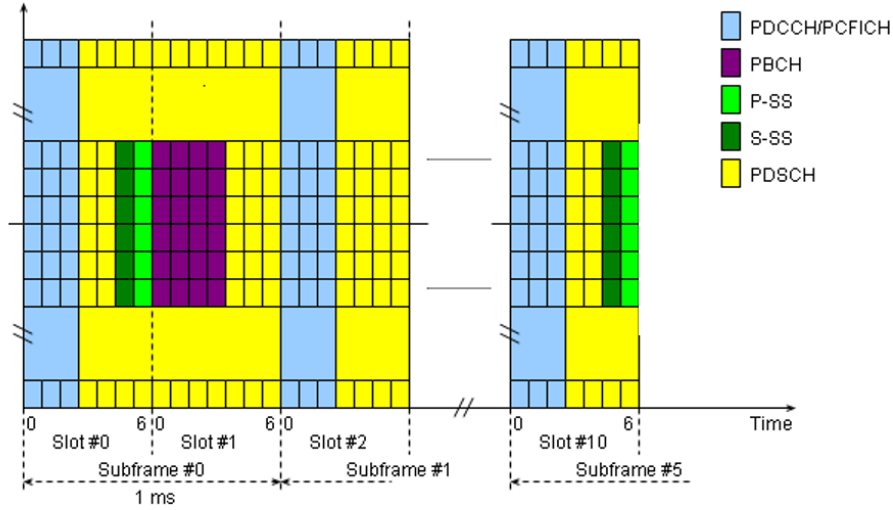


FIGURE 2.5: LTE initial access frame structure.

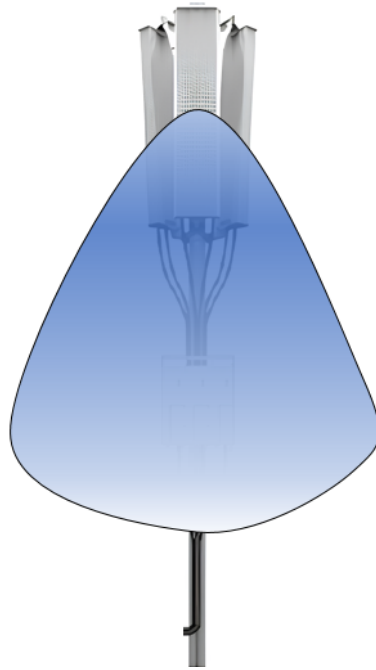


FIGURE 2.6: Example of transmitted LTE beam.

2.5.2 LTE Serving Cell Association

Within 4G LTE networks, signals controlling initial access are continuously transmitted by each cell, i.e., always-on signals, following the sector beam pattern discussed and described in Section 2.2.1. To determine its serving cell, each UE measures the reference signal received power (RSRP) from each cell within the network and selects the serving cell \hat{b}_u that provides the highest value, as follows,

$$\text{rsrp}_{u,b}^{\text{lte}} = \mathbb{E}_{\mathbf{h}_{u,b}^{\text{dl}}} \left\{ \rho_{u,b} \tau_{u,b} \left| \mathbf{h}_{u,b}^{\text{dl}} \right|^2 g_{u,b}^{\text{lte}} p_b \right\} = \rho_{u,b} \tau_{u,b} g_{u,b}^{\text{lte}} p_b \quad (2.23)$$

and

$$\hat{b}_u = \underset{b}{\operatorname{argmax}} \left\{ \operatorname{rsrp}_{u,b}^{\text{lte}} \right\}, \quad (2.24)$$

where p_b is the transmitted power of cell b , and we recall $\rho_{u,b}$, $\tau_{u,b}$, $\mathbf{h}_{u,b}^{\text{dl}}$ and $\mathcal{G}_{u,b}^{\text{lte}}$, being respectively the path loss gain, the shadow fading gain, the downlink fast-fading complex channel and beamforming gain between cell b and UE u .

Due to the complexity of the system and all the possible configurations of LTE cells and their transmitting reference signals, realizing a practical and tractable model for the resulting coverage SINR is very challenging. Therefore, within the scenario described above, to understand and quantify the quality of the received signals controlling the initial access and thereby coverage, we define the following quantity $\gamma_u^{\text{lte-cov}}$ as, Due to the complexity of the system and the numerous possible configurations of LTE cells and their transmitting reference signals, modelling the resulting coverage SINR in a practical and tractable way is highly challenging. Therefore, within the scenario described above, to quantify and understand the quality of the received signals controlling initial access and thereby coverage, we define the following quantity, $\gamma_u^{\text{lte-cov}}$, as:

$$\gamma_u^{\text{lte-cov}} = \frac{\rho_{u,b} \tau_{u,b} \mathcal{G}_{u,b}^{\text{lte}} p_b}{\rho_{u,\hat{b}_u} \tau_{u,\hat{b}_u} \mathcal{G}_{u,\hat{b}_u}^{\text{lte}} p_{\hat{b}_u} + B_0 N_0}, \quad (2.25)$$

where N_0 is the thermal noise spectral density, and B_0 is the bandwidth of the system. For the sake of reference, we will refer to this quantity as LTE coverage SINR.

2.5.3 Enhanced NR Initial Access

Although MIMO technology has already been introduced in LTE, its capabilities are quite limited.

Moving towards the next generation of cellular networks, one of the main differences concerning the cell discovery phase in NR, with respect to the previous in LTE, is the enhanced capability of beamforming the aforementioned signals in various spatial directions, thereby improving signal strength, interference management, flexibility and efficiency in covering the designed area. In NR terminology, the cell reference signals PSS, SSS and PBCH are transmitted together within the so-called synchronization signal block (SSB) as represented in the NR frame depicted in Figure 2.7. We refer to the beam transmitting those signals with SSB beam.

It is important to note that variations in these signals, such as waveform design, numerology, and sub-frame structures, are present. However, delving into the physical details of these signals and frames is beyond the scope of this research.

As specified by 3GPP standards [75, 76], each cell can transmit up to N_{ssb} SSB beams, with this number limited to 8 in case of network operating in the sub-6 GHz band. It is important to note that SSB beams are not transmitted simultaneously, but

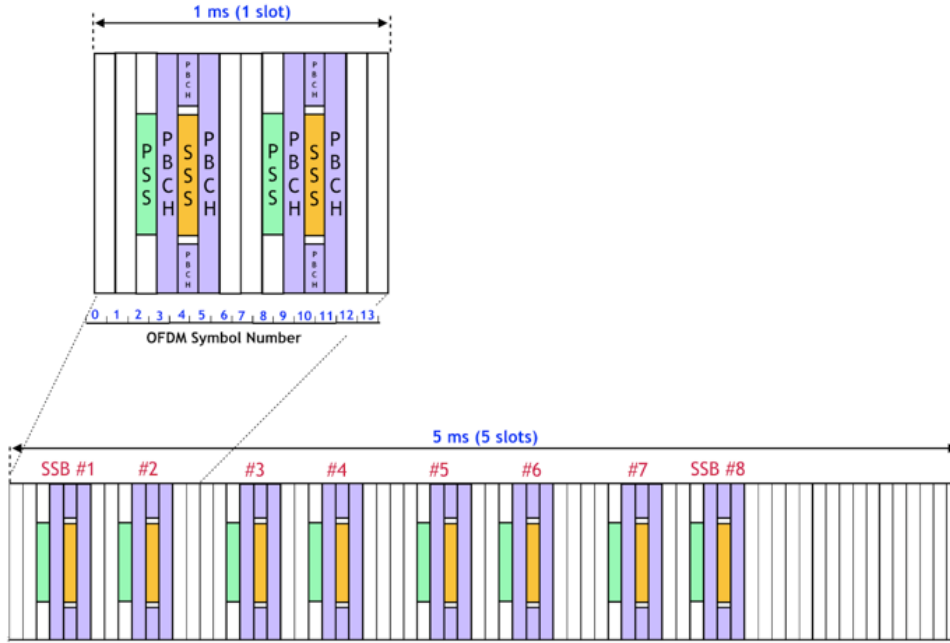


FIGURE 2.7: NR SSB initial access frame structure.

each cell performs a process known as beam sweeping, where beams, each associated with a beam sweep index i_s^{ssb} , are transmitted sequentially over time according to a predefined sweeping pattern. (See Figure 2.9).

In this work, we assume each transmitted SSB beam represented by a specific complex codeword $\mathbf{w}_{s,b}^{ssb} \in \mathbb{C}^{M \times 1}$ from a fixed codebook \mathcal{W}^{ssb} generated via two dimensional discrete Fourier transform (2D-DFT) precoding; we denote with N_{CB} the total number of available codewords. Figure 2.8 illustrates the resulting SSB beam beamforming gain resulting on the azimuth plane considering 8 transmitted SSB beams.

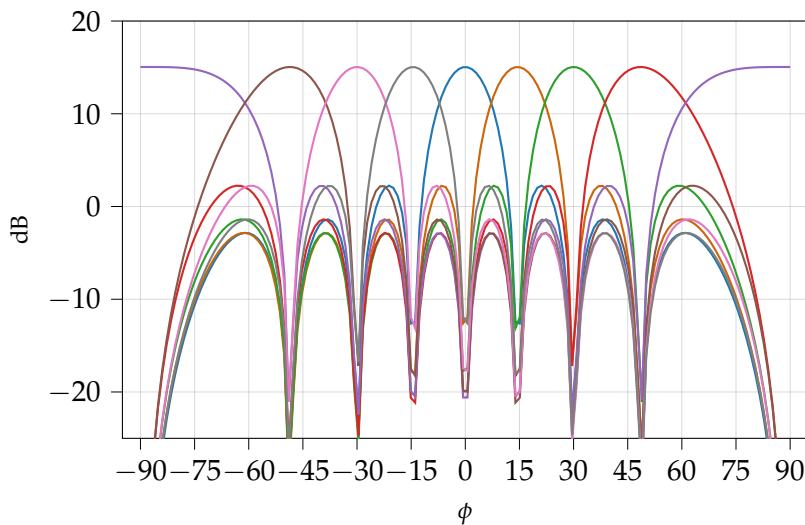


FIGURE 2.8: NR SSB beams beamforming gain.

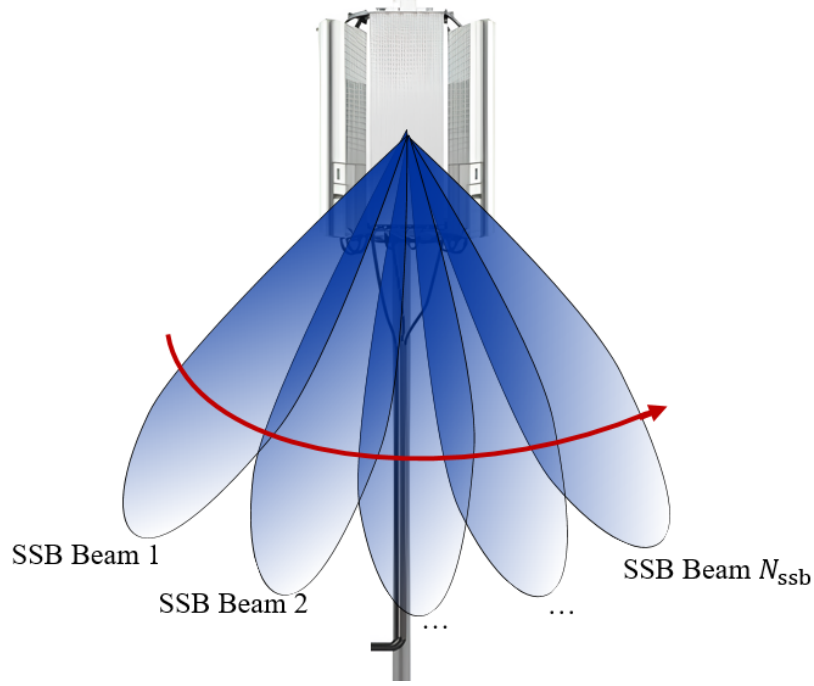


FIGURE 2.9: Example of NR SSB beam sweeping.

We represent with $\mathbf{W}_b^{\text{ssb}} \in \mathbb{C}^{M \times N_{\text{ssb}}}$ the matrix containing the transmitted SSB beams at cell b , defined as follows,

$$\mathbf{W}_b^{\text{ssb}} = \left[\mathbf{w}_{0,b}^{\text{ssb}}, \dots, \mathbf{w}_{s,b}^{\text{ssb}}, \dots, \mathbf{w}_{N_{\text{ssb}}-1,b}^{\text{ssb}} \right]. \quad (2.26)$$

Finally, to represent from a whole network perspective the set of SSB beams transmitted we introduce the binary matrix $\mathbf{X} \in \{0, 1\}^{N_{\text{CB}} \times N_{\text{BS}}}$, with values $x_{s,b}$ equal to one if beam/codeword s is transmitted at cell b .

2.5.4 NR Serving Cell Selection

Leveraging the introduced beamforming capabilities during the coverage/initial access phase, as discussed in Section 2.5.3, within NR network, to select its serving cell, each UE u measures the RSRP received from each of the transmitted SSB beams and selects as serving beam and cell, \hat{s}_u and \hat{b}_u , the ones that provide the highest RSRP value, as follows,

$$\begin{aligned} \text{rsrp}_{u,s,b}^{\text{ssb}} &= \mathbb{E} \left\{ \rho_{u,b} \tau_{u,b} \left| \mathbf{h}_{u,b}^{\text{dl}} \mathbf{w}_{s,b}^{\text{ssb}} \right|^2 g_{u,b} p_{s,b} \right\}, \\ &= \mathbb{E} \left\{ \beta_{u,b} \left| \mathbf{h}_{u,b}^{\text{dl}} \mathbf{w}_{s,b}^{\text{ssb}} \right|^2 p_{s,b} \right\}, \end{aligned} \quad (2.27)$$

and

$$\hat{s}_u, \hat{b}_u = \underset{s,b}{\text{argmax}} \left\{ x_{s,b} \text{rsrp}_{u,s,b}^{\text{ssb}} \right\}, \quad (2.28)$$

with $x_{s,b} \in \mathbf{X}$, where \mathbf{X} being the binary matrix \mathbf{X} describing the set of transmitted beams in the whole network. Moreover $\beta_{u,b}$ is defined as the large-scale gain between cell b and UE u as follows,

$$\beta_{u,b} = \rho_{u,b} \tau_{u,b} g_{u,b}. \quad (2.29)$$

Similar to what was discussed for LTE in Section 2.5.2, in the following, we aim to define a metric to quantify and evaluate the resulting SSB beam coverage SINR. Specifically, for each UE u from the chosen serving cell \hat{b} and SSB beam \hat{s}_u we define quantity γ_u^{ssb} as follows,

$$\gamma_u^{\text{nr-cov}} = \frac{\text{rsrp}_{u,\hat{s}_u,\hat{b}_u}^{\text{ssb}}}{\sum_{b \in \mathcal{B} \setminus \hat{b}_u} \sum_s x_{s,b} \text{rsrp}_{u,s,b}^{\text{ssb}} \delta(i_{\hat{s}_u}^{\text{ssb}}, i_s^{\text{ssb}})} + B_0 N_0}, \quad (2.30)$$

with

$$\delta(i, j) = \begin{cases} 1, & \text{If } i = j \\ 0, & \text{Otherwise} \end{cases}. \quad (2.31)$$

Let $\delta(\cdot, \cdot)$ denote the Kronecker delta function computed for the pair of SSB beam indices, since, as a result of the temporal beam sweeping mechanism, only beams associated with the same index i^{ssb} interfere with one another.

For the sake of reference, in this work we refer to this quantity as NR coverage SINR.

2.6 Data Performance Metric

In this section, we introduce the metric adopted to assess the data performance of UE and thereby assess the benefits of our proposed solutions. In particular, within this research work, we focus on the downlink data SINR and achievable data rate.

For both LTE and NR networks, we assume a total bandwidth B_0 available at each cell $b \in \mathcal{B}$ equally divided into $N_{\text{PRB}}^{\text{tot}}$ physical resource blocks (PRBs) each of B_{PRB} bandwidth each. Precisely, for both LTE and NR networks, we consider a total of 100 PRB of 180 KHz each.

2.6.1 LTE Data SINR and Achievable Data Rate

Within the considered LTE network, after each UE u is associated with its serving cell b , the cell begins transmitting to its set of connected UEs \mathcal{U}_b using the transmitting beam as discuss in Section 2.5.1. Each cell b multiplexes its connected UEs on different PRBs in order to orthogonally serve them. To assess the performance of

each UEs, we define the LTE data SINR γ_u^{lte} as follows,

$$\gamma_u^{\text{lte}} = \frac{\rho_{u,\hat{b}_u} \tau_{u,\hat{b}_u} \left| \mathbf{h}_{u,\hat{b}_u}^{\text{dl}} \right|^2 g_{u,\hat{b}_u}^{\text{lte}} p_{\hat{b}_u}}{\sum_{b \in \mathcal{B} \setminus \hat{b}_u} \rho_{u,b} \tau_{u,b} \left| \mathbf{h}_{u,b}^{\text{dl}} \right|^2 g_{u,b}^{\text{lte}} p_b + \frac{B_{\text{PRB}} N_{\text{PRB}}^{\text{tot}}}{N_{\hat{b}_u}} N_0}, \quad (2.32)$$

where $N_{\hat{b}_u}$ is the cardinality of set \mathcal{U}_b , thus representing.

Finally, define the LTE achievable data rate R_u^{lte} as follows,

$$R_u^{\text{lte}} = \frac{B_{\text{PRB}} N_{\text{PRB}}^{\text{tot}}}{N_{\hat{b}_u}} \log_2 \left(1 + \gamma_u^{\text{lte}} \right). \quad (2.33)$$

2.6.2 NR Data Precoding

To harness mMIMO beamforming and multiplexing capabilities, we mainly focus on a *Type I channel state information (CSI)* multi-antenna reporting and precoding designed for handling high-mobility scenarios, with more details provided in Appendix A.

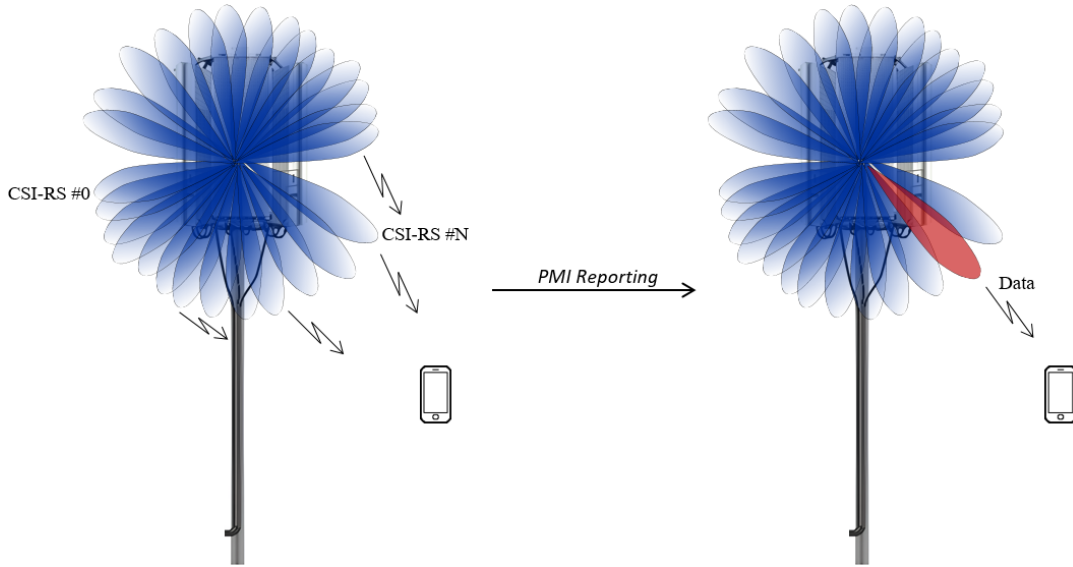


FIGURE 2.10: Illustration of a NR *Type-I* channel state information-reference signal (CSI-RS) multi-antenna reporting, and transmitting beam data selection.

In this mode of operation, the cell configures multiple CSI-RS beams, and instructs each UE to report a set of indices characterizing the channel conditions via a *Type I CSI* report. More in detail, as represented in Figure 2.10, each transmitted CSI-RS is precoded with a codeword selected from a 2D-DFT CSI-RS codebook here defined with $\mathbf{W}_b^{\text{csi-rs}}$; in accordance with 3GPP standards [75,76], each cell can transmit up to 32 distinct CSI-RS beams. UEs are then instructed to measure the received power from each CSI-RS beam and then to report indices to the serving cell, including the rank indicator (RI), precoding matrix indicator (PMI), and channel quality indicator (CQI), encapsulated within the *Type I CSI* report, as further discussed in

$$\gamma_u^{\text{nr}} = \frac{\beta_{u,\hat{b}_u} \left| \mathbf{h}_{u,\hat{b}_u}^{\text{dl}} \mathbf{w}_{u,\hat{b}_u}^{\text{dl}} \right|^2 p_{u,\hat{b}_u}^{\text{dl}}}{\beta_{u,\hat{b}_u} \sum_{p \in \mathcal{U}_{\hat{b}_u} \setminus u} \left(1 - \delta \left(\mathbf{w}_{u,\hat{b}_u}^{\text{dl}}, \mathbf{w}_{p,\hat{b}_u}^{\text{dl}} \right) \right) \left| \mathbf{h}_{u,\hat{b}_u}^{\text{dl}} \mathbf{w}_{p,\hat{b}_u}^{\text{dl}} \right|^2 p_{p,\hat{b}_u}^{\text{dl}} + \sum_{b \in B \setminus \hat{b}_u} \sum_{i \in \mathcal{U}_b} \beta_{u,b} \left| \mathbf{h}_{u,b}^{\text{dl}} \mathbf{w}_{i,b}^{\text{dl}} \right|^2 p_{i,b}^{\text{dl}} + \frac{B_{\text{PRB}} N_{\text{PRB}}^{\text{tot}}}{N_{\mathbf{w}_{u,\hat{b}_u}^{\text{dl}}}} N_0} \quad (2.35)$$

Appendix A. Through the PMI, UEs report the index of the codeword that provided the highest received power, i.e., the largest CSI-RS RSRP. The cell then uses this UE-reported codeword $\mathbf{w}_{\text{pmi}}^{\text{csi-rs}}$ as transmitting precoder/beam $\mathbf{w}_{u,\hat{b}_u}^{\text{dl}}$ for the UE data downlink.

According to the adopted *Type-I* reporting and precoding scheme described above, the data precoding vector for each UE u served by cell \hat{b}_u is defined as follows:

$$\mathbf{w}_{u,\hat{b}_u}^{\text{dl}} = \mathbf{w}_{\text{pmi}}^{\text{csi-rs}} = \underset{\mathbf{w}_{\text{pmi}}^{\text{csi-rs}} \in \mathbf{W}_{\hat{b}_u}^{\text{csi-rs}}}{\text{argmax}} \left\{ \beta_{u,\hat{b}_u} \left| \mathbf{h}_{u,\hat{b}_u}^{\text{dl}} \mathbf{w}_{\text{pmi}}^{\text{csi-rs}} \right|^2 \right\}. \quad (2.34)$$

Note that in this configuration, each UE does not estimate and report channel coefficients. Instead, it only reports indices related to the measured CSI-RS beam received power, enhancing robustness against channel estimation errors.

2.6.3 NR Data SINR and Achievable Data Rate

To assess the data transmission quality of each UE associated with its serving cell \hat{b}_u , we define the NR data SINR γ_u^{nr} as in eq. (2.35), where term $\mathcal{U}_{\hat{b}_u} \subseteq \mathcal{U}$ denotes the subset of UEs connected to cell \hat{b}_u . Then, $\mathbf{w}_{u,b}^{\text{dl}} \in \mathbb{C}^{M \times 1}$ and $p_{u,b}^{\text{dl}}$ are the downlink precoding vector and transmit power used at cell b to serve UE u , respectively. In this work, we consider equal data power transmission for all UEs. It should be noted that when a pair of UEs, denoted as u and p , select identical precoding codewords, the cell ensures orthogonal transmission by allocating distinct PRBs to them. Thus, the Kronecker delta function $\delta(\cdot, \cdot)$ reflects this network characteristic in the computation of the intra-cell interference and term $N_{\mathbf{w}_{u,\hat{b}_u}^{\text{dl}}}$ represent the number of UEs within the same cell that are served by the same beam/precoder as UE u .

Finally, we define for each UE u the NR achievable data R_u^{nr} as follows,

$$R_u^{\text{nr}} = \frac{B_{\text{PRB}} N_{\text{PRB}}^{\text{tot}}}{N_{\mathbf{w}_{u,\hat{b}_u}^{\text{dl}}}} \log_2 (1 + \gamma_u). \quad (2.36)$$

It is important to note that, although the formulation of eq. (2.36) resembles eq. (2.33), they differ substantially: in the LTE case, as outlined in eq. (2.33), all the UEs are allocated on different PRBs, thus the total band is split among the connected UEs. Differently, in the NRs scenarios, as showed in eq. (2.36), the total band is split only among UEs sharing the same transmitting beam; thereby increasing the transmitting band for each UEs, at the cost of accommodating intra-cell interference.

Chapter 3

Aerial Highways LTE Vertical Tilt Optimization

3.1 Introduction

Guaranteeing secure management of UAVs operations is essential for safe navigation within urban airspace and enabling next applications such as air delivery services and urban air mobility [81, 85, 86]. For this reason, relying on AHs systems and mirroring traditional ground highways infrastructure offers a change in the paradigm of air mobility, offering a clear pathway for optimizing control from air traffic controllers and thereby ensuring robust security and safety measures [19, 87].

Ensuring robust and reliable connectivity in the sky is a must for enabling BVLoS operations. However, within this paradigm shift, relying on solutions proposed in recent years for optimal trajectory planning [46–50] results impossible, as we envision that trajectories, represented by AHs, will be fixed according to business, security and control criteria.

Since 5G NR deployments are still ramping up, and because 4G LTE ones are the most widespread as of today, in this chapter, we assess which solution network operators can adopt to optimize their 4G LTE cellular network to provide reliable 3D aerial highway connectivity while having a minimum impact on its ground performance.

Due to their ability to navigate 3D space, UAVs often experience favourable channel gains from multiple network cells. Although this condition permits to perceive—almost always—sufficient RSRP from the serving cells, it also allows comparable signal power to be received from multiple neighbouring cells, leading to high interference and reduced signal quality. This issue is common in UAVs communication supported by terrestrial cellular systems, as they are primarily optimized for ground services only [8, 11, 26, 63, 88].

To account for these issues, in the following, we introduce an optimization framework that leverages the knowledge of AH to adjust the vertical sector tilt of cells within 4G LTE networks. Specifically, we aim to show how the a-priori information about the AH trajectory, i.e., the planned trajectory for UAVs, can be leveraged to enable optimization processes to provide highly reliable connectivity along those.

We envision that AHs enables optimal distribution of power in the sky and that this approach is the key to boosting UAV performance without requiring the allocation of specific physical resources, thereby enabling optimal integration of UAVs within AH in existing deployed LTE networks. In more detail, in the rest of the chapter, given the prior knowledge of the AH, we devise a gradient-based solution to determine the optimal configuration that maximizes overall average network coverage while ensuring a minimum SINR for UAVs flying along the AH.

Parts of the results presented in this chapter have been published in the following conference and journal:

- M. Bernabè, D. Lopez-Perez, D. Gesbert and H. Bao, “On the Optimization of Cellular Networks for UAV Aerial Corridor Support,” GLOBECOM 2022 - 2022 IEEE Global Communications Conference, Rio de Janeiro, Brazil, 2022, pp. 2969-2974, doi: 10.1109/GLOBECOM48099.2022.10001469 [69].
- M. Bernabè, D. López-Pérez, N. Piovesan, and D. Gesbert, “Gradient-Based Optimization of Terrestrial Cellular Networks for Aerial Highways” (under submission in IEEE Transaction on Vehicular Technology).

Finally, it should be noted that, as discussed in Section 1.1, in recent years, few studies have concluded that re-using and optimising terrestrial networks is the key to enabling optimal UAVs and AHs integration. Among them, we highlight the optimization framework presented in (Benzaghta M., 2023) [60] in which they proposed a methodology based on ML and BO for adjusting the sectors tilt and power in LTE networks. As well as the work presented in (Karimi-Bidhendi S., 2024) [59] in which they introduce a sophisticated mathematical framework based on quantization theory for fine-tuning of sectors tilt and power.

3.2 Problem Formulation

In the following, we formulate a maximization problem for the stochastic network spectral efficiency constrained by coverage requirements for LTE SINR along the AH.

Notably, in this work, we do not assume any specific distribution or knowledge about UE positions, except for UAVs, which are known to continuously traverse the AH and explore all evaluation points \mathcal{E}_a . We recall from Chapter 2 Section 2.1.1 the set of evaluation points \mathcal{E} , defined by the union of both ground and aerial points, respectively represented by \mathcal{E}_g and \mathcal{E}_a .

The optimization process aims to enhance the stochastic spectral efficiency across all considered evaluation points \mathcal{E} , by tuning tilt angles of all network cells, here represented as,

$$\boldsymbol{\theta}^{\text{tilt}} = \left[\theta_0^{\text{tilt}}, \dots, \theta_b^{\text{tilt}}, \dots, \theta_{N_{\text{BS}}-1}^{\text{tilt}} \right]^T ; \quad (3.1)$$

thereby controlling the resulting beamforming gain $g_{e,b}^{\text{lte}}(\theta_b^{\text{tilt}})$ between each evaluation point e and each cell b , as defined by eqs. (2.18).

Leveraging models presented for the LTE coverage SINR $\gamma^{\text{lte-cov}}$ (see eq. (2.25)) defined in Chapter 2, the constrained optimization problem is formulated as follows,

Problem 1. LTE Vertical Tilt Optimization

$$\begin{aligned} \max_{\boldsymbol{\theta}^{\text{tilt}}} \quad & \mathbb{E}_{\tau, \mathbf{h}^{\text{dl}}} \left\{ \sum_{e \in \mathcal{E}} \log \left(\log_2 \left(1 + \frac{\rho_{e, \hat{b}_e} \tau_{e, \hat{b}_e} p_b g_{e, \hat{b}_e}^{\text{lte}}(\theta_{\hat{b}_e}^{\text{tilt}})}{\sum_{b \in \mathcal{B} \setminus \hat{b}_e} \rho_{e, b} \tau_{e, b} p_b g_{e, b}^{\text{lte}}(\theta_b^{\text{tilt}}) + B_0 N_0} \right) \right) \right\} \\ \text{s.t.} \quad & \mathbb{E}_{\tau, \mathbf{h}^{\text{dl}}} \left\{ \frac{\rho_{a, \hat{b}_a} \tau_{a, \hat{b}_a} p_b g_{a, \hat{b}_a}^{\text{lte}}(\theta_{\hat{b}_a}^{\text{tilt}})}{\sum_{b \in \mathcal{B} \setminus \hat{b}_a} \rho_{a, b} \tau_{a, b} p_b g_{a, b}^{\text{lte}}(\theta_b^{\text{tilt}}) + B_0 N_0} \right\} \geq \gamma_{\text{th}}, \quad \forall a \in \mathcal{E}_a \quad (\text{C1.1}), \\ & \theta_b \in [0, \pi], \quad \forall \theta_b \in \boldsymbol{\theta}^{\text{tilt}} \quad (\text{C1.2}). \end{aligned}$$

The objective function in Problem (1) represents the average network sum spectral efficiency across the set of evaluation points, where the logarithm of the spectral efficiency is adopted into the summation to ensure fairness and mitigate cases of points with extreme high or low performance.

To guarantee a minimum SINR performance for UAVs along the AH, solution of Problem (1) must adhere to constraints C1.1, which impose a minimum SINR value of γ_{th} for each AH point a .

Problem (1) is a non-concave problem characterized by non-linearities, inherent stochasticity and a strong interplay of the optimization variables. Therefore, in the remaining part of the chapter, we propose a gradient-based solution to tackle this constrained optimization problem and solve this complex problem.

The non-concavity of the problem is discussed in Appendix C Section C.1.

3.3 LTE Vertical Tilt Gradient Based Solution

We observe that the objective function in Problem (1) is a real, continuous, and differentiable function with respect to $\boldsymbol{\theta}^{\text{tilt}}$. Therefore, we propose a robust gradient-based method to solve Problem (1). Specifically, we first devise a scalar function z^{lte} that embraces the objective function and guides the solver into the feasible domain defined by constraint C1.1. Then, we introduce an algorithm that leverages gradient-based computations to find the optimal vertical tilt angles $\boldsymbol{\theta}^{\text{tilt}}$ for the network cells.

3.3.1 Objective Scalar Function

To drive our optimization process and find robust solutions against different stochastic representations of the network, we define a scalar utility function z^{lte} to maximize.

Following an empirical risk approach, we define the utility function \bar{z}^{lte} as,

$$\begin{aligned} \bar{z}^{\text{lte}}(\boldsymbol{\theta}^{\text{tilt}}) &= \mathbb{E}_{\tau, \mathbf{h}^{\text{dl}}} \left\{ z^{\text{lte}}(\boldsymbol{\theta}^{\text{tilt}}) \right\} = \\ &= \frac{1}{N_{\text{real}}} \sum_i^{N_{\text{real}}} \left(\sum_{e \in \mathcal{E}} {}^i f_e(\boldsymbol{\theta}^{\text{tilt}}) - \lambda^{\text{lte}} \sum_{a \in \mathcal{E}_a} {}^i g_a(\boldsymbol{\theta}^{\text{tilt}}) \right), \end{aligned} \quad (3.2)$$

where N_{real} is the total number of stochastic realizations of the network random variables, e.g., channels, UEs locations.

For each stochastic realization i function ${}^i f_e$ is designed to mirror the objective in Problem (1) and defined as follows,

$$\begin{aligned} {}^i f_e(\boldsymbol{\theta}^{\text{tilt}}) &= \log \left(\log_2 \left(1 + {}^i \gamma_e^{\text{lte-cov}}(\boldsymbol{\theta}^{\text{tilt}}) \right) \right) = \\ &= \log \left(\log_2 \left(1 + \frac{\rho_{e, \hat{b}_e} {}^i \tau_{e, \hat{b}_e} p_b \mathcal{G}_{e, \hat{b}_e}^{\text{lte}}(\boldsymbol{\theta}_{\hat{b}_e}^{\text{tilt}})}{\sum_{b \in \mathcal{B} \setminus \hat{b}_e} \rho_{e, b} {}^i \tau_{e, \hat{b}_e} p_b \mathcal{G}_{e, b}^{\text{lte}}(\boldsymbol{\theta}_b^{\text{tilt}}) + B_0 N_0} \right) \right). \end{aligned} \quad (3.3)$$

Function ${}^i g_a$ serves as a penalty function to reshape the optimization surface and steer the solution away from infeasible areas defined by constraints C1.1, and is defined as follows

$$\begin{aligned} {}^i g_a(\boldsymbol{\theta}^{\text{tilt}}) &= \text{ReLu} \left(\gamma_{\text{th}} - {}^i \gamma_a^{\text{lte-cov}}(\boldsymbol{\theta}^{\text{tilt}}) \right) = \\ &= \text{ReLu} \left(\gamma_{\text{th}} - \frac{\rho_{a, \hat{b}_a} {}^i \tau_{a, \hat{b}_a} p_b \mathcal{G}_{a, \hat{b}_a}^{\text{lte}}(\boldsymbol{\theta}_{\hat{b}_a}^{\text{tilt}})}{\sum_{b \in \mathcal{B} \setminus \hat{b}_a} \rho_{a, b} {}^i \tau_{a, \hat{b}_a} p_b \mathcal{G}_{a, b}^{\text{lte}}(\boldsymbol{\theta}_b^{\text{tilt}}) + B_0 N_0} \right), \end{aligned} \quad (3.4)$$

where the ReLu function is defined as

$$\text{ReLu}(x) = \begin{cases} x, & \text{If } x \geq 0 \\ 0, & \text{Otherwise} \end{cases}. \quad (3.5)$$

To clarify the structure of the utility function \bar{z}^{lte} defined in eq.(3.2), we consider the following two scenarios:

1. $\exists a \in \mathcal{E}_a : \mathbb{E}_{\tau, \mathbf{h}^{\text{dl}}} \{ \gamma_a^{\text{lte-cov}} \} < \gamma_{\text{th}}$: In this scenario, there is at least one AH point that fails to meet the minimum SINR requirement. Consequently, the penalty function, amplified by λ^{lte} , will be greater than zero, and it will steer the solution towards a configuration that avoids this condition.
2. $\forall a \in \mathcal{E}_a, \mathbb{E}_{\tau, \mathbf{h}^{\text{dl}}} \{ \gamma_a^{\text{lte-cov}} \} \geq \gamma_{\text{th}}$: In this scenario, all penalty functions are zero, leading the optimizer to seek a solution that maximizes the log sum spectral efficiency for all points in the network (i.e., $\forall e \in \mathcal{E} = \mathcal{E}_g \cup \mathcal{E}_a$).

Note that this formulation pushes neighbouring cells to compensate for any coverage hole introduced by the uptilted cells, therefore minimizing the ground losses.

3.3.2 ADAM Optimizer

In the following, we present the ADAM optimizer designed to find the optimal configuration of vertical tilt angle θ^{tilt} that maximizes the utility \bar{z}^{lte} .

ADAPtive Moment estimation (ADAM) is an effective first-order gradient method tailored for stochastic functions, introduced in [89]. Due to its low computational requirements and efficient memory utilization, ADAM is widely adopted for gradient-based optimization, especially in the domains of machine learning, neural network training and parameters optimization, where efficient gradient operations are crucial [90–92].

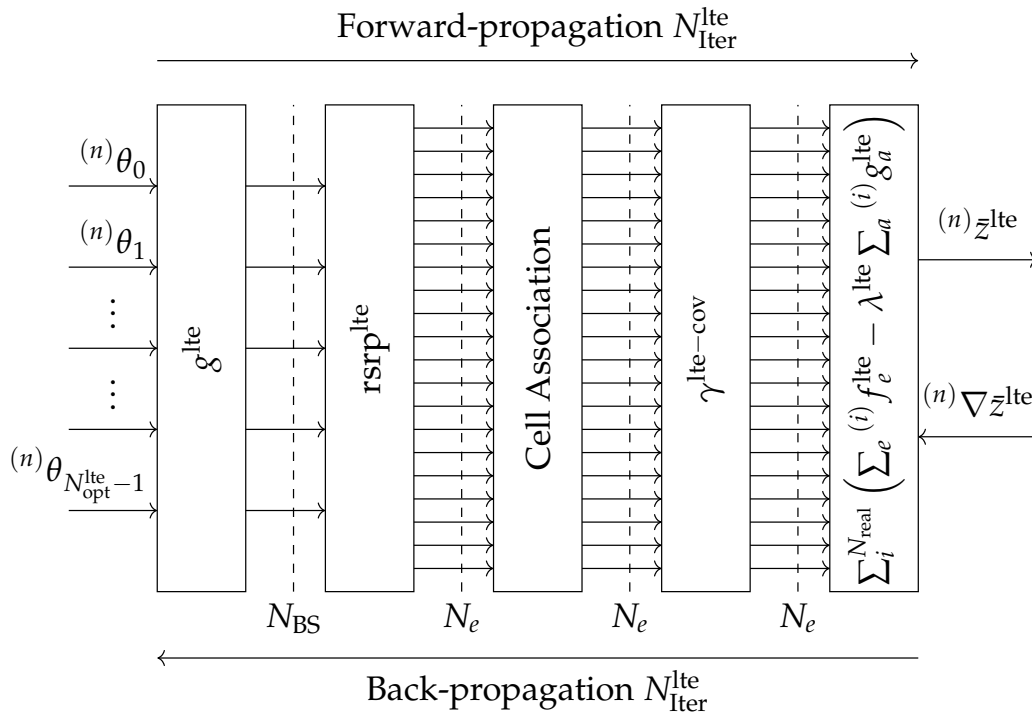


FIGURE 3.1: Block diagram for the ADAM LTE vertical tilt optimizer.

As illustrated in the block diagram in Figure 3.1, the optimization process proceeds iteratively. Given a configuration for the set of vertical tilt angle θ^{tilt} , represented in Figure 3.1 as the set of input, the resulting LTE beamforming gains, LTE coverage SINR and other functions described in Chapters 2 are computed for each evaluation point e with the final goal of calculating the utility function \bar{z}^{lte} according to eqs.(3.2), (3.3) and (3.4). All of these functions needed for the computation of the output are represented as consecutive and concatenate blocks in Figure 3.1. We refer to the process of passing sequentially through each block and culminating in the final output as “Forward Propagation”.

Using ADAM, we then compute the gradients and “back propagate” them to the input to obtain the set of gradients $\nabla_{\theta^{\text{tilt}}} \bar{z}^{\text{lte}}$ computed with respect to the input vectors θ^{tilt} .

At each iteration n of the total $N_{\text{iter}}^{\text{lte}}$, we update the set of angles θ^{tilt} as follows,

$${}^{(n+1)}\theta^{\text{tilt}} \leftarrow {}^{(n)}\theta^{\text{tilt}} - \mu^{\text{lte}} \nabla_{\theta^{\text{tilt}}} z^{\text{lte}} \left({}^{(n)}\theta^{\text{tilt}} \right), \quad (3.6)$$

where μ^{lte} is the learning rate.

3.3.3 Optimization Framework

In this section, leveraging the ADAM optimizer block and its utility function, we present the designed optimization framework. As depicted in Figure 3.2, the framework is composed of five main blocks:

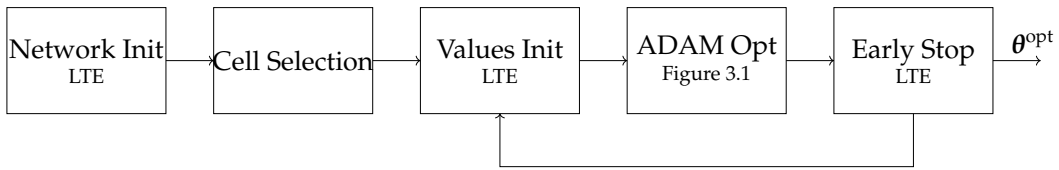


FIGURE 3.2: Block diagram for the LTE vertical tilt optimization framework.

1. **Network Init:** we initialize the network by deploying all network cells, as well as the set of ground evaluation points and AH, realizing all important variables. Every system variable is set up as if the network were deployed specifically to serve gUEs.
2. **Cell Selection:** we implement a cell selection process to reduce the complexity of the optimization problem and limit deviations from the initial configuration designed for ground coverage. This process, based on the location of points \mathcal{E}_a defining the AH and geometry calculations, reduces the set of cells to be adjusted, focusing on those facing the AH. This approach not only reduces the complexity but also allows for a more localized objective function with a smoother shape, enhancing the performance of the ADAM optimizer. Specifically, we denote the selected set of cells as $\mathcal{B}_{\text{inOpt}}^{\text{lte}}$, with cardinality $N_{\text{opt}}^{\text{lte}}$, defined as,

$$\mathcal{B}_{\text{inOpt}}^{\text{lte}} = \left\{ b \mid \exists a \in \mathcal{E}_a : \left(\phi_a - \phi_b^{\text{bst}} \right) \in [-90, 90] \right\}. \quad (3.7)$$
3. **Values Init:** for the selected cells, the initial value for the tilt angles vector (see (3.1)) for the optimization process is set to 105° , as per [74]. This choice is based on the assumption that this value is optimal to serve only gUEs. ¹
4. **ADAM Opt:** we employ the ADAM optimizer presented in Section 3.3.2 and represented in Figure 3.1.

¹We verified the validity of this value through separate simulation and optimization processes.

5. **Early Stop:** this block implements an early stop mechanism that, by monitoring the state of the utility function and related gradients, may halt the optimization process. It accounts for two aspects: i) stopping the optimization process when the utility function does not improve to avoid unnecessary iterations, and ii) addressing a gradient vanishing problem, as for certain configurations of AHs, multiple aerial evaluation point angles may result out of the main lobe of network cells, thereby resulting in poor gradient values.

Specifically, it halts the operations if the introduced enhancement is less than $\Delta_{z^{\text{lte}}}$ for $N_{\text{stop}}^{\text{lte}}$ consecutive iterations.

To address the gradient vanishing problem, upon detection, the early stop saves the results and, only once, resets the optimization process by initializing the vertical tilt values to 90° (i.e., directly pointing towards the horizon). Since there are no guarantees regarding the actual improvement, the final solution of the algorithm is chosen between the saved one and the last one obtained.

Finally, it should be noted that although this approach solves the problem, it may further deviate from the optimal configuration intended solely for ground coverage, as it introduces a big step in the uptilt of all the $N_{\text{opt}}^{\text{lte}}$ cells.

3.3.4 Time Complexity

In the following, we discuss the time complexity of the proposed LTE vertical tilt optimization framework, in which the driven component is the ADAM optimizer, whose time complexity scales with the number of inputs and the complexity of the utility and penalty functions computation.

The total time complexity, denoted as C^{lte} , can be expressed as the summation of one of each singular block depicted in Figure 3.2. In more detail, the considered complexity scales as,

$$\begin{aligned}
C^{\text{lte}} &\equiv O\left(2N_{\text{BS}} + N_{\text{iter}}^{\text{lte}} \left(C_{\text{Forward}}^{\text{lte}} + C_{\text{Back}}^{\text{lte}}\right)\right) = & (3.8) \\
&= O\left(N_{\text{BS}} + N_{\text{BS}}N_{\text{iter}}^{\text{lte}} \left(N_{\text{real}} \left(N_{\text{BS}}N_e + N_e + N_a\right) + N_{\text{opt}}^{\text{lte}}\right)\right) \leq \\
&\leq O\left(2N_{\text{BS}} + N_{\text{iter}}^{\text{lte}} \left(N_{\text{real}} \left(N_{\text{BS}}N_e + N_e + N_a\right) + N_{\text{BS}}\right)\right) \equiv \\
&\equiv O\left(N_{\text{BS}} + N_{\text{iter}}^{\text{lte}} \left(N_{\text{real}} \left(N_{\text{BS}}N_e + N_e + N_a\right) + N_{\text{BS}}\right)\right),
\end{aligned}$$

where the complexity of the ADAM optimizer scales with the sum of the forward and backward propagation complexities over the total number of iterations $N_{\text{iter}}^{\text{lte}}$. In the forward pass, for each of the N_{real} iterations, the terms $N_{\text{BS}}N_e + N_e$ and N_a represent the complexity of computing the utility function (eq. (3.3)) and the penalty

functions (eq. (3.4)), respectively. While the backward propagation complexity scales with the number of inputs, here equal to $N_{\text{opt}}^{\text{lte}} \leq N_{\text{BS}}$.

It is important to emphasize that the complexity scales linearly with the variables characterizing the system and optimizer. In particular, the dependence on the number of network realizations illustrates how increasing robustness in searching for the solution linearly affects the problem. Similarly, the dependence on the number of evaluation points demonstrates how enhancing accuracy and precision in assessing the resulting performance (i.e., high density of evaluation points) linearly impacts the problem. The number of considered cells shows as the time complexity scales linearly with the network size.

3.4 LTE Vertical Tilt Optimization Setup and Solution

To analyze the resulting final performance, we leverage the network layout, evaluation points and models described in Chapter 2 regarding LTE specification. Specifically, we show the evolution of the utility function for different scenarios as well the resulting optimized configuration for all the network cells by considering the UMa, UMi, URD urban scenario discussed in Section 2.1 and represented in Figure 2.2. Then, for each of them, we consider the three different AH configurations presented in Section 2.1 and illustrated in Figure 2.3, placed at three different altitudes: 50 m, 100 m and 150 m.

Within both UMa and URD scenarios AHs with a total length of 1250 m are considered; while, within the UMi, and in order to maintain a coherent scale factor, an AH of 500 m is considered. Then, to accurately study performance evolution along those, we place a sequence of consecutive aerial evaluation points with IHD of 1 m; which together define the set \mathcal{E}_a . Finally, to analyze the resulting ground performance, we consider a total of 6780, 2495, and 1110 ground evaluation points for the UMa, URD, and UMi scenarios, respectively. All these points are evenly spaced with an IGD of 25 m and constitute the \mathcal{E}_g set.

In the problem formulation presented in Section 3.2, the objective is to ensure a minimum SINR value along the AH. Specifically, considering reliability constraints we aim to achieve values greater than the outage threshold of -6 dB at each aerial points; thereby eliminating out coverage condition along the AH. Through extensive search and tuning of the hyperparameter γ_{th} , we have determined that setting γ_{th} to 1 (i.e., 0 dB) is optimal for enhancing aerial performance and maximizing the gap above the outage threshold. Then, we set the ADAM learning rate μ^{lte} equal to 0.1 and the total number of iterations equal to $N_{\text{iter}}^{\text{lte}}$ 1000; with $\Delta_{z^{\text{lte}}}$ and $N_{\text{stop}}^{\text{lte}}$, for the early stop mechanism set to 0.004 and 100, respectively. To ensure a robust and reliable solution across various environmental channel conditions, we consider a total number of N_{real} realizations for the stochastic variables characterizing the channels at each iteration; specifically, this value is set to 100. Finally, Table 3.1 summarizes

the adopted network layout and evaluation points parameters and Table 3.2 the optimization ones.

By analyzing the obtained curves illustrated in Figure 3.3, 3.4 and 3.5 that depict the evolution of the proposed utility function across various network configurations during the optimization process, we can draw the following conclusions:

- The early step mechanism discussed in Section 3.3.3 is essential for escaping conditions where vanishing gradients occur. Without this mechanism, vertical tilt values remain unchanged, leading to constant utility values across multiple iterations. This phenomenon is evident in the first 100 iterations for the 100 m case depicted in Figure 3.3a. This adjustment allows for exploring different initial solutions and identifying cells previously overlooked due to gradient vanishing issues, such as angles falling outside the main lobe of a few cells (see Section 2.2.1).
- Within all scenarios, the optimization process effectively converges in ~ 500 iterations upon the action of the early stop mechanism.² Considering the UMa, i.e., the largest in terms of number of evaluation points N_e and thereby the most time-challenging scenario (see Section 3.3.4), each iteration takes an average of 20 sec on a PC with a 11th Gen Intel(R) Core(TM) i7-1165G7 @ 2.80GHz, 2803 MHz, 4 cores, 8 logical processor; therefore resulting in a converge time of approximately 2 h 48 min.

Considering the obtained vertical tilt configuration for different altitudes in all considered urban scenarios (see right column of Figures 3.3, 3.5 and 3.4) the optimization process results in a few cells being completely uptilted to serve the AH, while the majority slightly deviate from the baseline configuration (vertical tilt set equal to 105°)³, here referred as “Baseline LTE”. This is a result of the formulation of the devised utility function z^{lte} , which embraces both aerial and ground evaluation points, driving the optimizer to also take care of the coverage holes introduced by the uptilted sectors.

Finally, it should be noted that for each analyzed network layout configuration, there is not a clear trend between the operating AH altitude and the final value reached for the utility function upon convergence.

In a similar way, can we notice that in the resulting tilt configurations, higher altitudes do not always correspond to higher vertical tilts for the cells. As an example, observing the UMa Curved scenario shown in Figure 3.3b, the 150 m scenario has the fewest uptilted cells, and, moreover, in most cases, these cells are not the most uptilted. This is a consequence of the high interplay and complexity of the system’s variables: while it is true that a higher altitude increases the LoS probability with more interfering cells, it is also true that individual interferers are more attenuated, and additionally uptilting just a few cells can be sufficient to counteract interference,

²Here, it should be noted that more iterations are considered for representation.

³We recall that in our reference system, the zero point is oriented towards the sky.

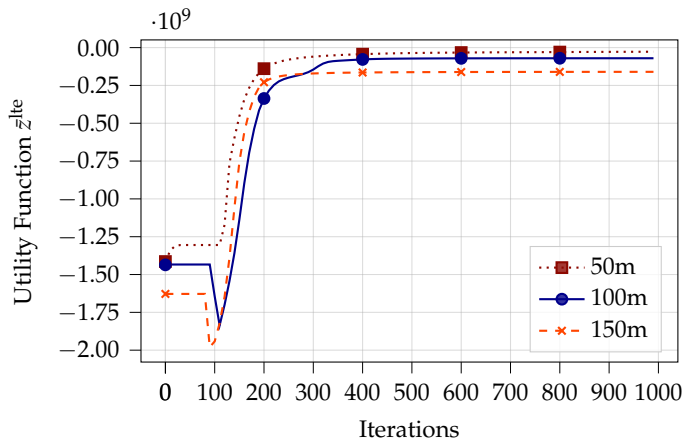
as the higher altitudes allow a single cell to cover a larger portion of the AH, since the illuminated area increases with altitude due to the geometry of solid angles.

TABLE 3.1: LTE vertical tilt optimization network layout and evaluation point configuration summary.

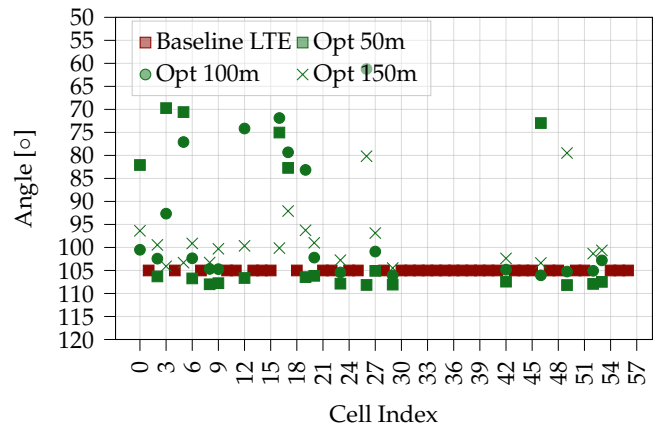
Network Layout	AH Altitude	AH Configuration	IGD	IHD	N_g	N_a	N_e	N_{BS}
UMa	50m, 100m, 150m	Curved, Straight Centre, Straight Edge	25	1	6780	1250	8030	57
URD	50m, 100m, 150m	Curved, Straight Centre, Straight Edge	25	1	2495	1250	1545	57
UMi	50m, 100m, 150m	Curved, Straight Centre, Straight Edge	25	1	1110	500	1610	57

TABLE 3.2: LTE vertical tilt optimization hyperparameters summary.

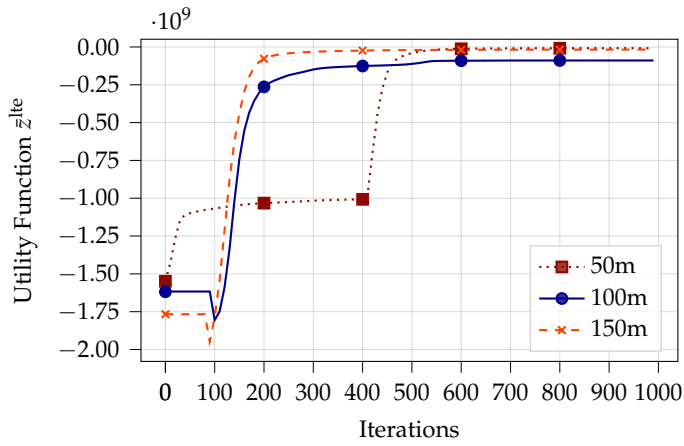
γ_{th} [dB]	λ^{lte}	μ^{lte}	N_{iter}^{lte}	N_{real}	$\Delta_{z^{lte}}$	N_{stop}^{lte}
0	10^6	0.1	1000	100	0.004	100



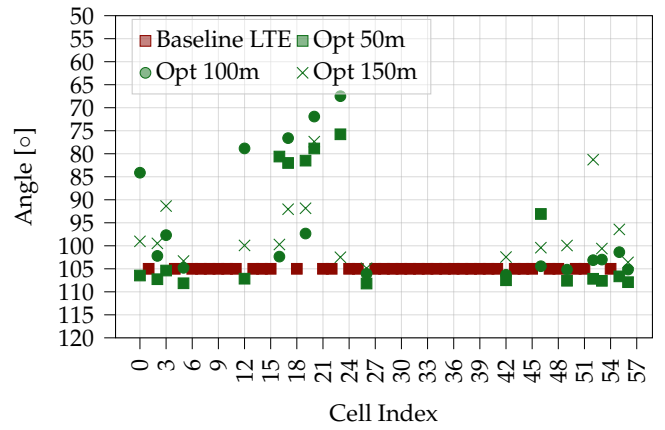
(a) Utility Function evolution for a Curved aerial highway.



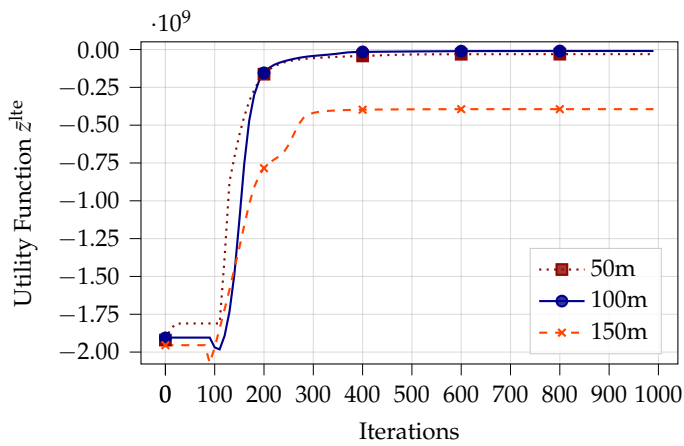
(b) Obtained Vertical Tilt Network Configuration for a Curved aerial highway.



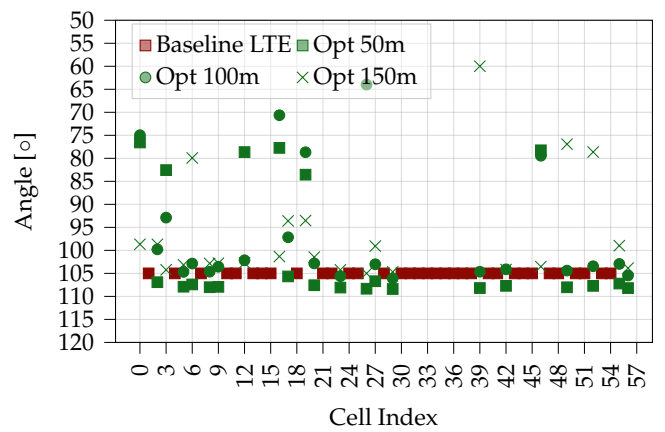
(c) Utility Function evolution for a Straight Centre aerial highway.



(d) Obtained Vertical Tilt Network Configuration for a Straight Centre aerial highway.

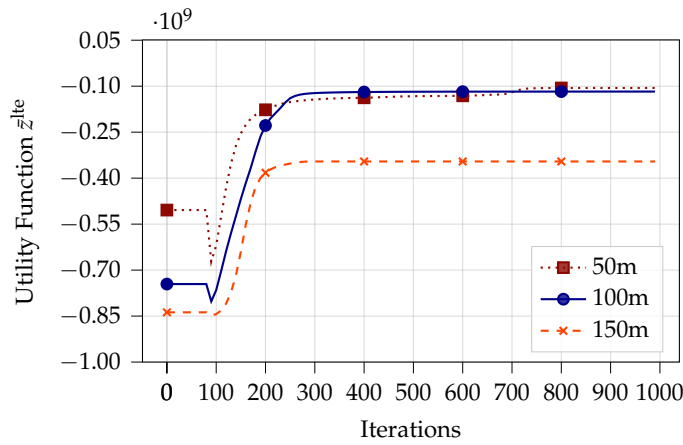


(e) Utility Function evolution for a Straight Edge aerial highway.

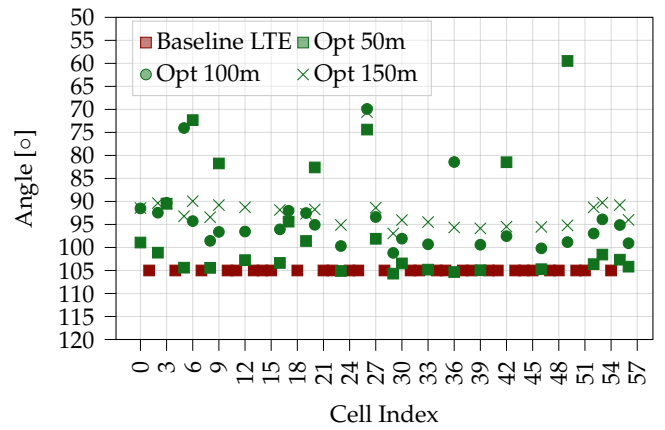


(f) Obtained Vertical Tilt Network Configuration for a Straight Edge aerial highway.

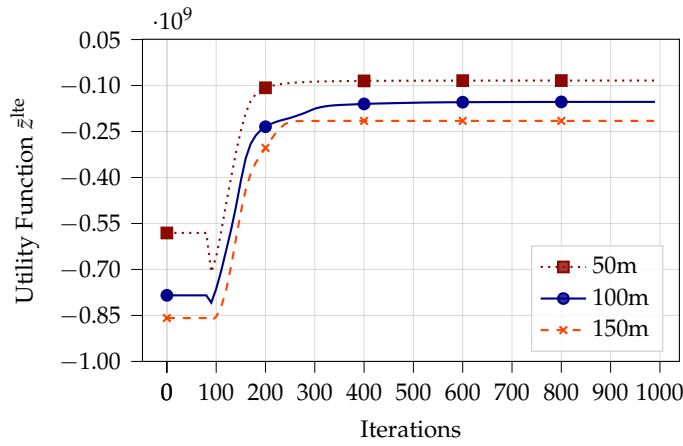
FIGURE 3.3: LTE vertical tilt ADAM utility function evolution (left column) and obtained vertical tilt network configuration (right column), considering different configurations for a 1250 m aerial highway at different altitudes in a UMa scenario.



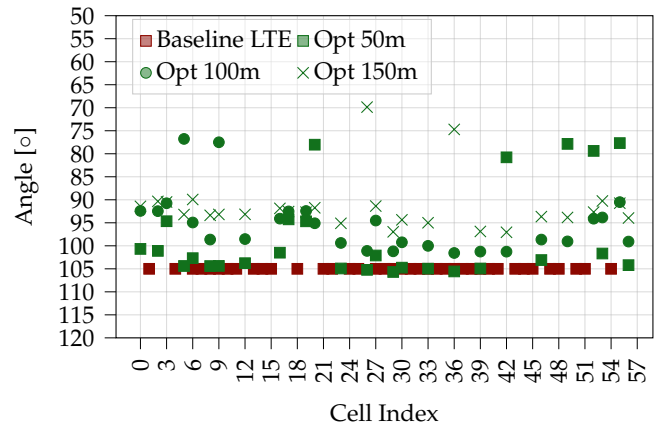
(a) Utility Function evolution for a Curved aerial highway.



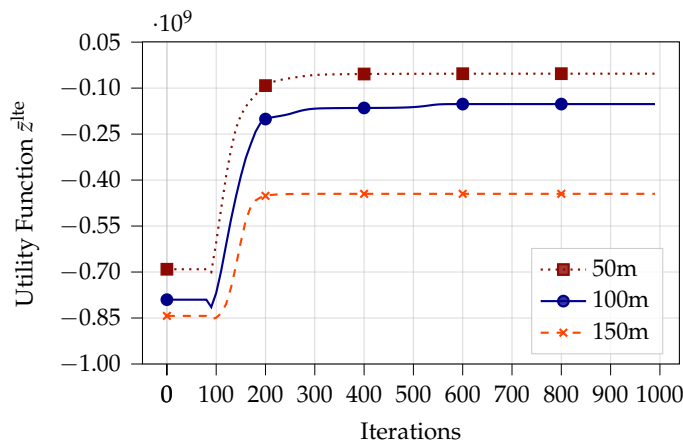
(b) Obtained Vertical Tilt Network Configuration for a Curved aerial highway.



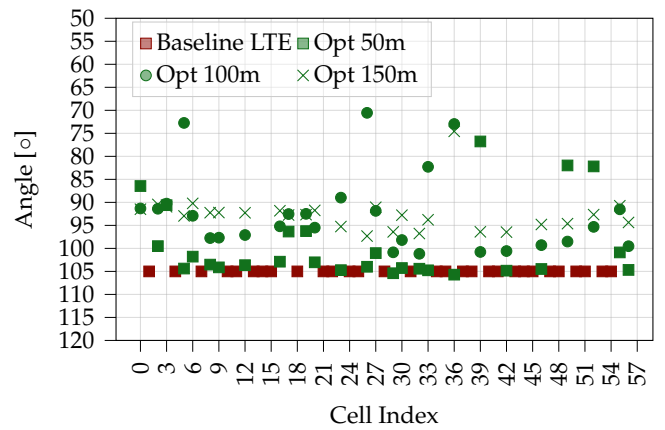
(c) Utility Function evolution for a Straight Centre aerial highway.



(d) Obtained Vertical Tilt Network Configuration for a Straight Centre aerial highway.

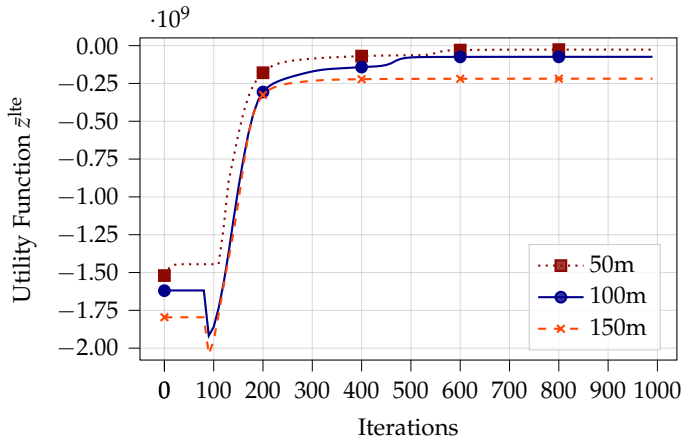


(e) Utility Function evolution for a Straight Edge aerial highway.

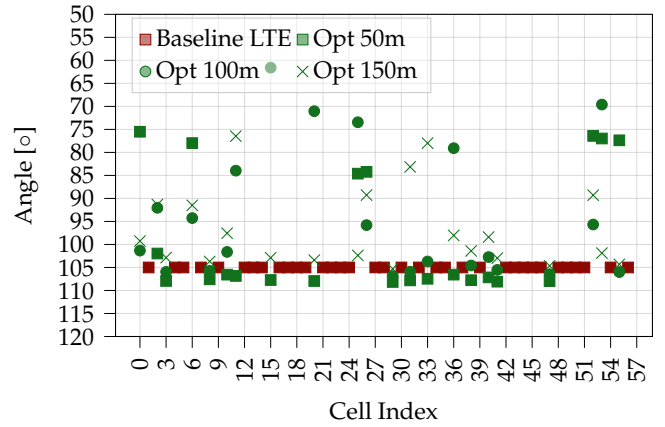


(f) Obtained Vertical Tilt Network Configuration for a Straight Edge aerial highway.

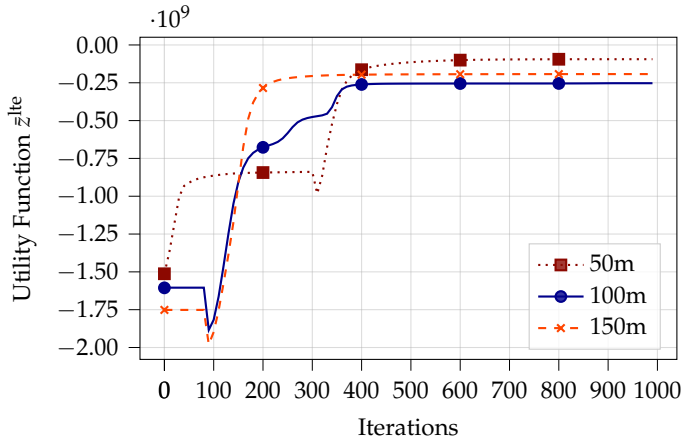
FIGURE 3.4: LTE vertical tilt ADAM utility function evolution (left column) and obtained vertical tilt network configuration (right column), considering different configurations for a 500 m aerial highway at different altitudes in a UMi scenario.



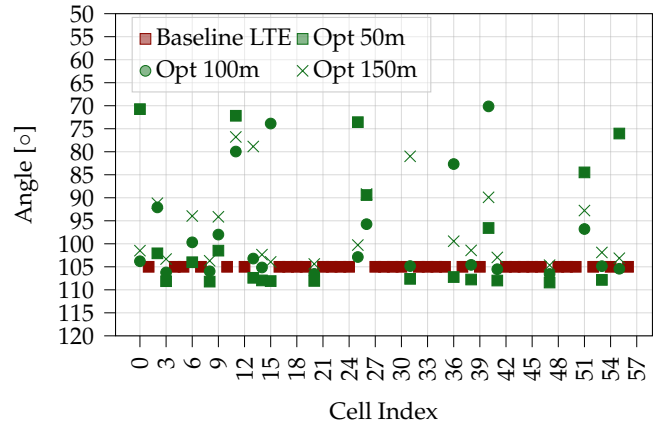
(a) Utility Function evolution for a Curved aerial highway.



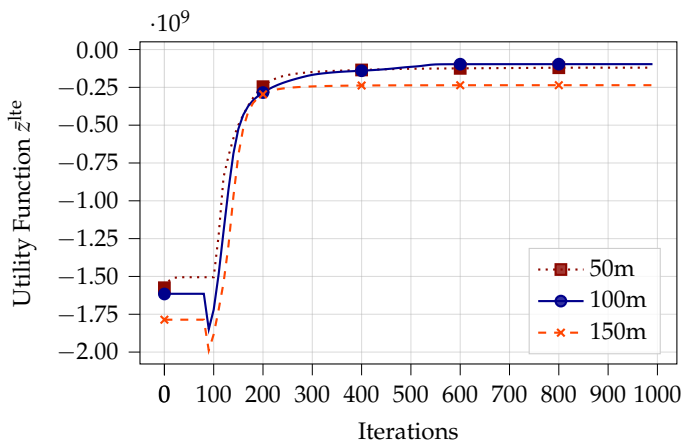
(b) Obtained Vertical Tilt Network Configuration for a Curved aerial highway.



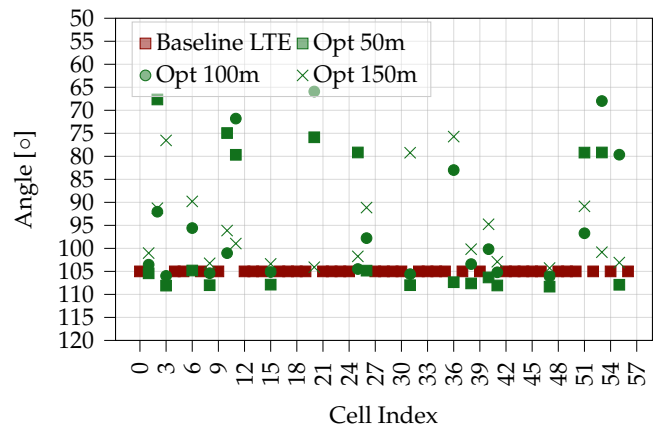
(c) Utility Function evolution for a Straight Centre aerial highway.



(d) Obtained Vertical Tilt Network Configuration for a Straight Centre aerial highway.



(e) Utility Function evolution for a Straight Edge aerial highway.



(f) Obtained Vertical Tilt Network Configuration for a Straight Edge aerial highway.

FIGURE 3.5: LTE vertical tilt ADAM utility function evolution (left column) and obtained vertical tilt network configuration (right column), considering different configurations for a 1250 m aerial highway at different altitudes in a URD scenario.

3.5 Resulting LTE Coverage SINR

To further analyze and understand the benefits of the proposed solution, in the following, we present and discuss the results obtained in terms of LTE coverage SINR (See Section 2.5.2 and eq (2.25)).

Figures 3.7, 3.8 and 3.9 show the coverage SINR cumulative distribution functions (CDFs) obtained for the three different network layout configurations and the three different aerial highway configurations at different altitudes. In each figure, the left column depicts the distribution of the coverage SINR of the considered aerial evaluation points, i.e., resulting AH coverage, while the right column reports the obtained coverage on the ground.

Then, for all scenarios, results obtained within the network configured solely for ground coverage, i.e., all network cells downtilted at 105° , are denoted as “Baseline”, while those resulting from our optimization process are denoted with “Opt”. Finally, for each considered network layout results on the obtained statistics are summarized, in Tables 3.3, 3.5, and 3.7.

Our results show evident benefits within all the considered scenarios, which gains up to 9 dB for the 5%-tile and up to 12 dB for the mean values; Thus, in the following, we discuss these results, and we provide useful insights to network operator, which aim to introduce and integrate AH systems with their already deployed LTE networks.

Starting from the baseline results, we observe a clear trend: as altitude increases, the aerial CDFs shifts to the left; thereby indicating a decrease in overall performance with higher highway altitudes. The primary causes are the consequent increased path loss and a higher likelihood of falling outside the main lobe of the sector, which together reduce the received serving RSRP. Moreover, it should be noted that altitude affects interference too; although higher path loss reduces received interference, this is somewhat mitigated by the introduction of new interfering cells, as higher altitudes increase the probability of being in LoS with distant cells.

Instead, when examining the results derived from our proposed solution, we observe a notable mitigation of the aforementioned trend across most scenarios, particularly concerning the tail and median components of the obtained curves. Nevertheless, this condition is not always present; rather than being an intrinsic physical condition of the system, our findings suggest that this behaviour is a result of the surrounding environment (e.g., UMa instead of UMi or URD) and depends on the location of the AH. Thereby further highlighting the complexity and intricate interactions within these systems. This is particularly evident in the results obtained within the UMa scenario, as presented in Figure 3.7 and Table 3.3; here, the optimal altitude is contingent on the specific configuration, and, even a slight shift of a few hundred meters in the AH location, therefore passing from the *Straight Centre* to the *Straight Edge* (see to Figure 2.3) case, can significantly alter the consideration regarding optimal altitude. However, it's important to note that this behaviour does not

manifest within the URD network layout in Figure 3.9; the URD consistently shows a trend between altitude and performance, although it shares all models and cell configurations with the UMa. The two scenarios differ only in the cell position, and the UMa can be potentially seen as a specific realization of a more generic random URD, thus suggesting that there may exist configurations for which the altitude-performance relationship breaks down.

Moving into UMi scenario, as shown in Figure 3.9 and summarize in Table 3.5, coverage SINR performances drastically reduce when considering higher altitudes. This occurs as a direct consequence of the UMi network cells, characterized by lower sector heights (see Section 2.1), for which steering up while maintaining ground service results more challenging. As a consequence, cells need to be steered up entirely, creating ground coverage gaps that neighboring cells find difficult to cover. This is an important aspect to note as it should be borne in mind the whole optimization process has been designed to safeguard the performance on the ground while feeding the AH. Moreover, within UMi networks, we can notice a slope change in the CDF (see Figure 3.8f as example); this occurs due to the presence of points in NLoS with some cells; in fact, it should be noted that a peculiarity of this scenario is the not zero probability of being in NLoS with different cells at different altitudes, therefore resulting in different performances distributions. So, our results suggest that network operators which target UMi scenarios for AH displacement should carefully study the surrounding environment and thereby integrate further techniques, such as the deployment of dedicated infrastructure as the only terrestrial network re-use may not be sufficient to provide reliable connectivity. In addition to the all previous considerations, it should be highlighted that across all the studied scenarios and regardless of the network layout and AH configuration, positioning the AH at an altitude of 50 m appears to be always the best choice to maximize not only the tail of the coverage SINR CDF, but also the mean and the peak performances; bringing aerial points to slightly achieve the ground ones. Therefore, our findings suggest that overall the 50 m results to be the preferable altitudes for optimal integration of AH within already deployed LTE network; a result that should be kept in mind by network operators if the final goal is not only providing minimum reliable connectivity, but also maximizing peak performance.

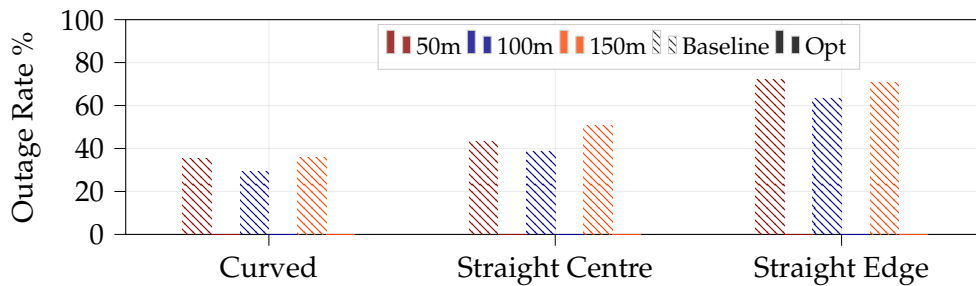
3.5.1 Out of Coverage Rate

Finally, in the following, we present and discuss results obtained in terms of out of coverage rate. As previously discussed, the goal of the optimization process is not maximizing overall aerial coverage SINR performance but instead providing minimum but reliable coverage along the AH.

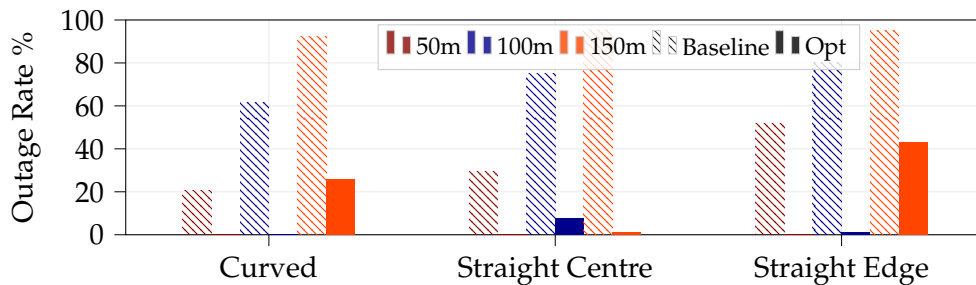
In this work, we consider an out of coverage SINR threshold of -6 dB. Then, through simulation results, we analyze the rate at which each aerial evaluation point along the AH experiences SINR values below this threshold.

To highlight the benefits of our proposed solution, Figure 3.6 shows the obtained out of coverage rates for all the considered scenarios, and Tables 3.4, 3.4, and 3.4 summarize those. It is important to remark that within the UMa and URD scenarios, when leveraging network setup solely optimized for the ground, i.e., baseline, the out of coverage rates fall in the range [40%, 60%], while, when relying on our proposed solution, those values drastically drops to 0. However, similar consideration may not apply for UMi cases, for which, although the introduced improvements, our proposed solution results in not negligible values for those rates, thereby highlighting once again the need for further actions within this scenario.

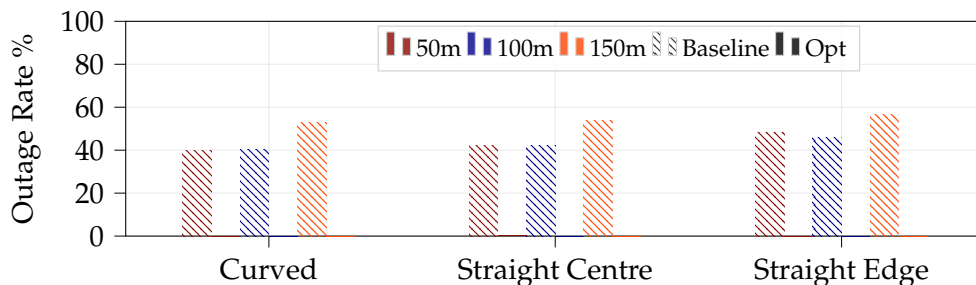
Finally, bearing in mind that our proposed solution has been designed to minimize the loss on the ground, it should be noted that the high gain in the AH SINR, with values up to 9 dB for the 5%-tile and up to 12 dB for the mean, comes at the minimum cost for the ground, -0.6 dB for the 5%-tile and up to -1.30 dB for the mean.



(a) UMa network layout considering 1250 m aerial highways.

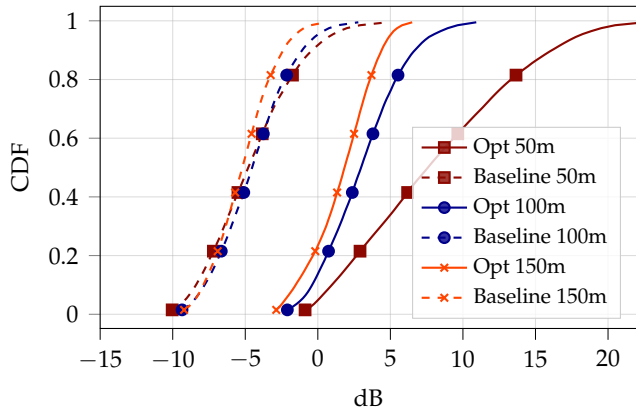


(b) UMi network layout considering 500 m aerial highways.

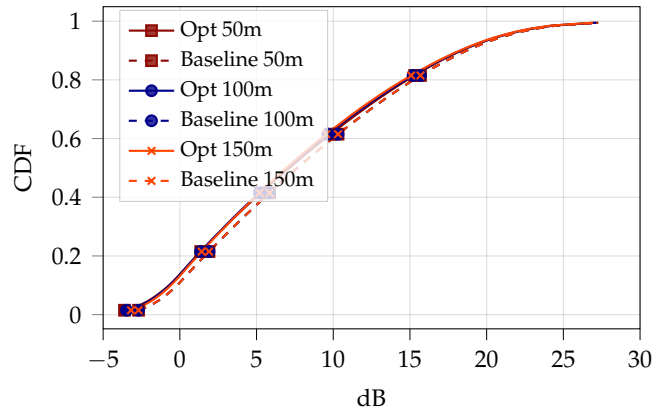


(c) URD network layout considering 1250 m aerial highways.

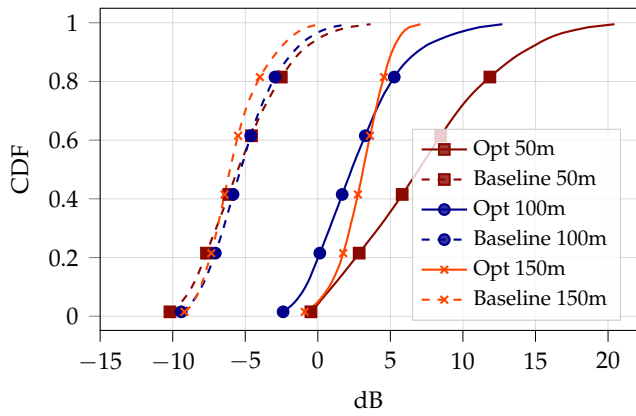
FIGURE 3.6: LTE vertical tilt aerial highway out of coverage rates, considering different configurations for aerial highways at different altitudes in different network layouts.



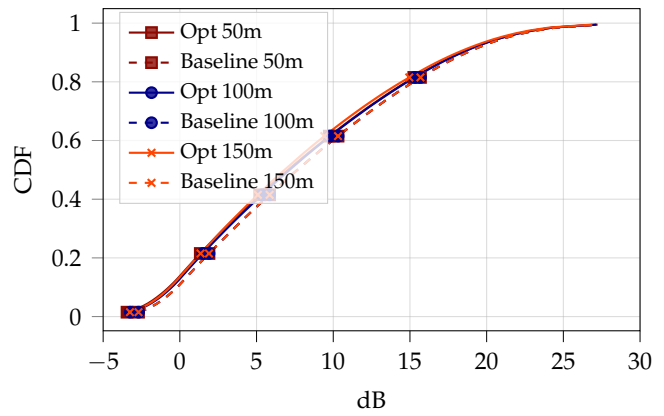
(a) Curved AH, Aerial Evaluation Points SINR.



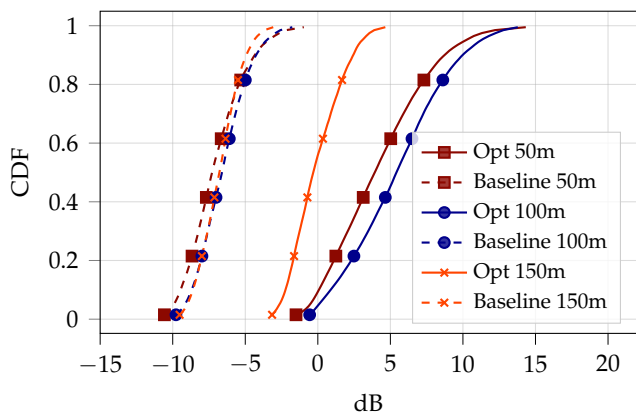
(b) Curved AH, Ground Evaluation Point SINR.



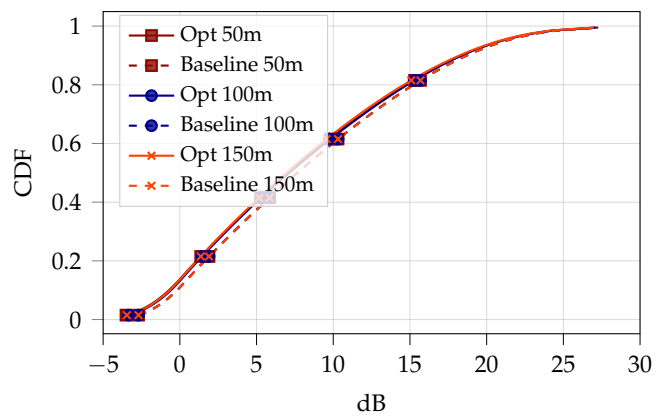
(c) Straight Centre AH, Aerial Evaluation Points SINR.



(d) Straight Centre AH, Ground Evaluation Point SINR.



(e) Straight Edge AH, Aerial Evaluation Points SINR.



(f) Straight Edge AH, Ground Evaluation Point SINR.

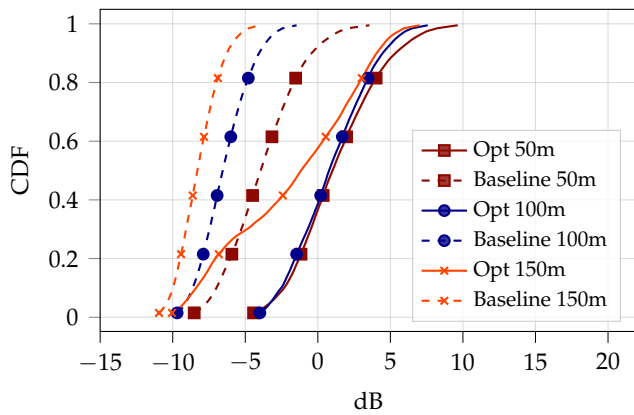
FIGURE 3.7: LTE vertical tilt coverage SINR CDFs on aerial highway's evaluation points (left column) and on ground evaluation points (right column), considering different configurations for a 1250 m aerial highway at different altitudes in a UMa scenario.

TABLE 3.3: Summary of LTE vertical tilt coverage SINR statistics, considering different configurations for a 1250 m aerial highway at different altitudes in a UMa scenario.

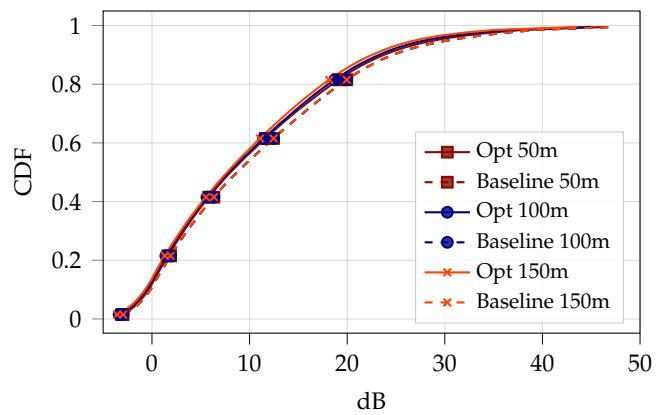
		UMa Cov. SINR Statistics					
		Aerial			Ground		
		Baseline	Opt	Gain	Baseline	Opt	Gain
		[dB]	[dB]	[dB]	[dB]	[dB]	[dB]
		Curved					
50m	5%-tile	-9.12	0.04	9.16	-1.32	-1.97	-0.65
	Mean	-4.56	8.13	12.69	8.53	8.04	-0.49
100m	5%-tile	-8.50	-1.12	7.38	-1.32	-1.90	-0.58
	Mean	-4.47	3.09	7.56	8.53	7.97	-0.56
150m	5%-tile	-8.46	-2.24	6.22	-1.32	-1.75	-0.43
	Mean	-5.16	1.66	6.82	8.53	7.95	-0.58
		Straight Centre					
50m	5%-tile	-9.36	0.15	9.51	-1.32	-1.92	-0.60
	Mean	-5.17	7.29	12.46	8.53	8.00	-0.53
100m	5%-tile	-8.63	-1.55	7.08	-1.32	-1.72	-0.40
	Mean	-5.08	2.72	7.80	8.53	8.11	-0.42
150m	5%-tile	-8.56	0.02	8.58	-1.32	-1.81	-0.49
	Mean	-5.75	3.03	8.78	8.53	7.85	-0.68
		Straight Edge					
50m	5%-tile	-9.92	-0.54	9.38	-1.32	-1.94	-0.62
	Mean	-7.05	4.21	11.26	8.53	8.04	-0.49
100m	5%-tile	-9.16	0.07	9.23	-1.32	-1.79	-0.47
	Mean	-6.54	5.46	12.00	8.53	8.06	-0.47
150m	5%-tile	-9.00	-2.65	6.35	-1.32	-1.87	-0.55
	Mean	-6.78	0.08	6.86	8.53	7.92	-0.61

TABLE 3.4: LTE vertical tilt aerial highway out of coverage rate, considering different configurations for a 1250 m aerial highway at different altitudes in a UMa scenario.

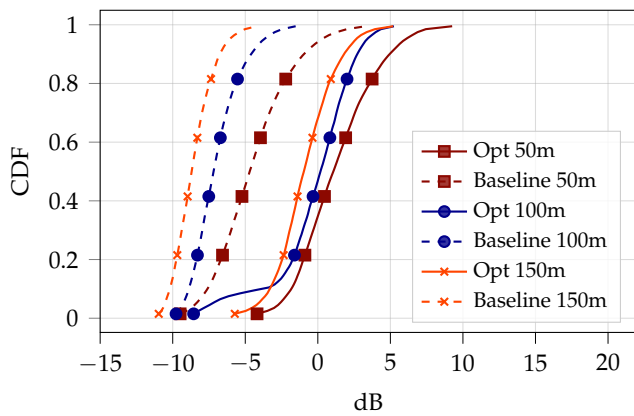
UMa - Aerial Highway Cov. Outage Rate						
	Curved		Straight Centre		Straight Edge	
	Baseline	Opt	Baseline	Opt	Baseline	Opt
50m	35.50%	0.00%	43.38%	0.00%	72.36%	0.00%
100m	29.43%	0.00%	38.65%	0.00%	63.49%	0.00%
150m	35.94%	0.00%	50.62%	0.00%	70.56%	0.00%



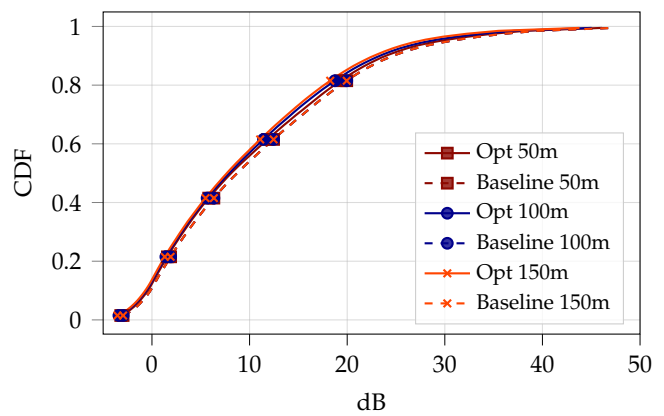
(a) Curved AH, Aerial Evaluation Points SINR.



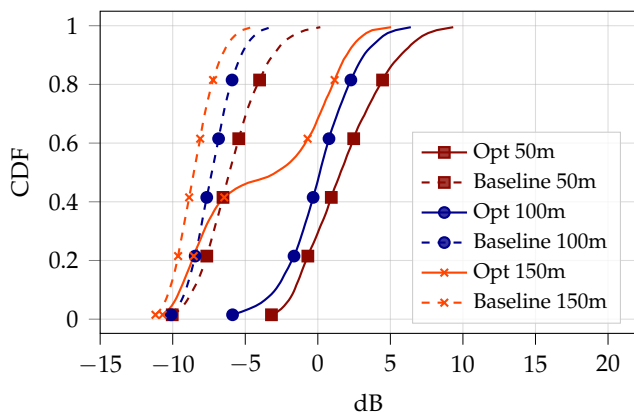
(b) Curved AH, Ground Evaluation Point SINR.



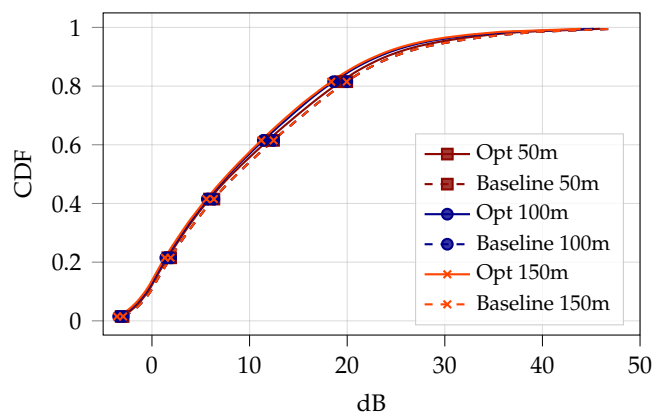
(c) Straight Centre AH, Aerial Evaluation Points SINR.



(d) Straight Centre AH, Ground Evaluation Point SINR.



(e) Straight Edge AH, Aerial Evaluation Points SINR.



(f) Straight Edge AH, Ground Evaluation Point SINR.

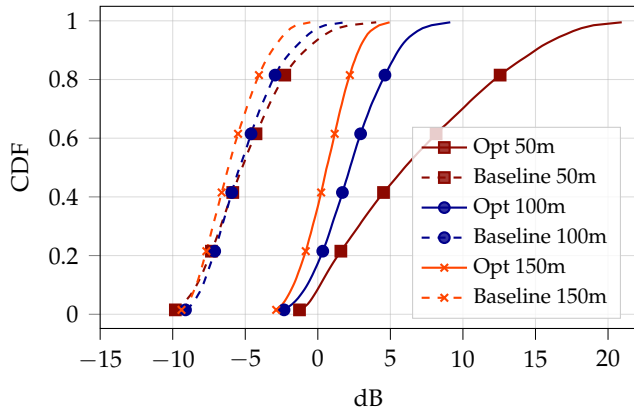
FIGURE 3.8: LTE Vertical tilt coverage SINR CDFs on aerial highway's evaluation points (left column) and on ground evaluation points (right column), considering different configurations for a 500 m aerial highway at different altitudes in a UMi scenario.

TABLE 3.5: Summary of LTE vertical tilt coverage SINR statistics, considering different configurations for a 500 m aerial highway at different altitudes in a UMi scenario.

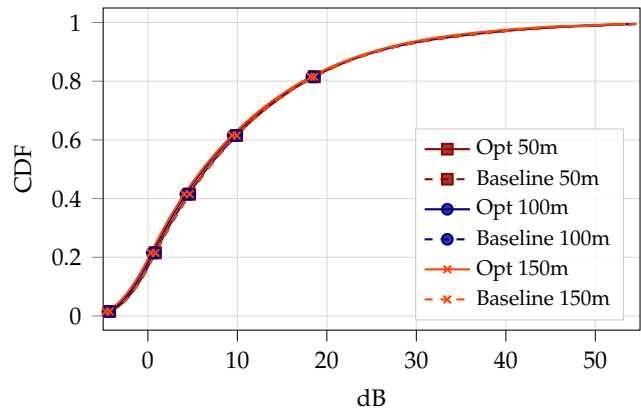
		UMi Cov. SINR Statistics					
		Aerial			Ground		
		Baseline	Opt	Gain	Baseline	Opt	Gain
		[dB]	[dB]	[dB]	[dB]	[dB]	[dB]
		Curved					
50m	5%-tile	-7.65	-3.27	4.38	-1.40	-1.58	-0.18
	Mean	-3.80	1.28	5.08	10.91	10.28	-0.63
100m	5%-tile	-9.09	-3.27	5.82	-1.40	-1.84	-0.44
	Mean	-6.43	0.90	7.33	10.91	9.97	-0.94
150m	5%-tile	-10.40	-9.18	1.22	-1.40	-2.00	-0.60
	Mean	-8.20	-1.73	6.47	10.91	9.61	-1.30
		Straight Centre					
50m	5%-tile	-8.39	-2.63	5.76	-1.40	-1.67	-0.27
	Mean	-4.48	1.29	5.77	10.91	10.36	-0.55
100m	5%-tile	-9.28	-7.31	1.97	-1.40	-1.86	-0.46
	Mean	-6.95	-0.28	6.67	10.91	10.00	-0.91
150m	5%-tile	-10.53	-4.11	6.42	-1.40	-1.98	-0.58
	Mean	-8.56	-0.88	7.68	10.91	9.66	-1.25
		Straight Edge					
50m	5%-tile	-9.20	-2.23	6.97	-1.40	-1.65	-0.25
	Mean	-5.94	1.81	7.75	10.91	10.39	-0.52
100m	5%-tile	-9.54	-4.09	5.45	-1.40	-1.88	-0.48
	Mean	-7.25	0.11	7.36	10.91	9.95	-0.96
150m	5%-tile	-10.63	-10.00	0.63	-1.40	-2.00	-0.60
	Mean	-8.47	-3.69	4.78	10.91	9.74	-1.17

TABLE 3.6: LTE vertical tilt aerial highway out of coverage rate, considering different configurations for a 500 m aerial highway at different altitudes in a UMi scenario.

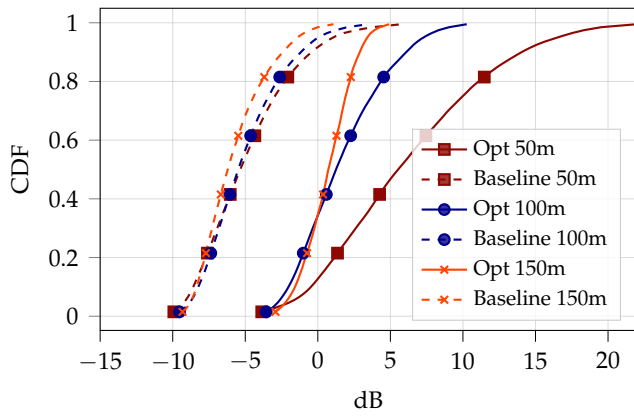
UMi - Aerial Highway Cov. Outage Rate						
	Curved		Straight Centre		Straight Edge	
	Baseline	Opt	Baseline	Opt	Baseline	Opt
50m	20.55%	0.12%	29.55%	0.26%	51.76%	0.00%
100m	61.44%	0.00%	75.23%	7.74%	80.06%	1.30%
150m	92.49%	26.04%	95.47%	1.23%	95.17%	43.27%



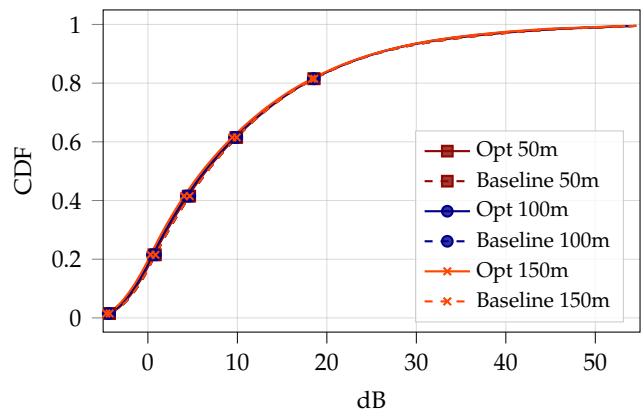
(a) Curved AH, Aerial Evaluation Points SINR.



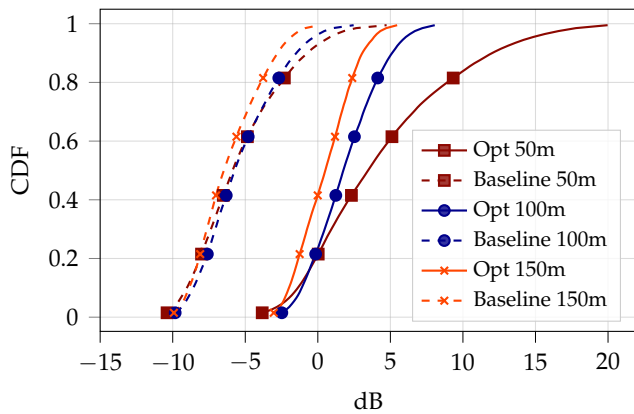
(b) Curved AH, Ground Evaluation Point SINR.



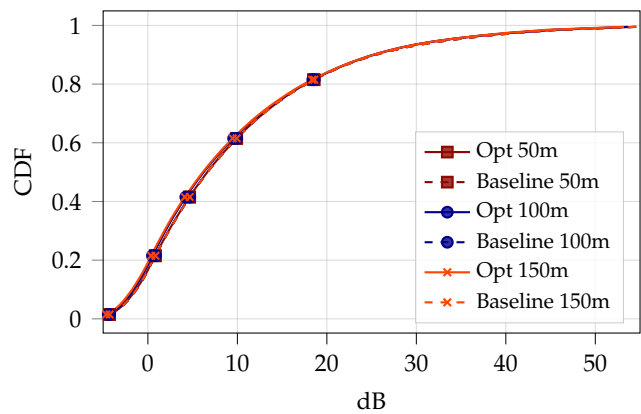
(c) Straight Centre AH, Aerial Evaluation Points SINR.



(d) Straight Centre AH, Ground Evaluation Point SINR.



(e) Straight Edge AH, Aerial Evaluation Points SINR.



(f) Straight Edge AH, Ground Evaluation Point SINR.

FIGURE 3.9: LTE vertical tilt coverage SINR CDFs on aerial highway's evaluation points (left column) and on ground evaluation points (right column), considering different configurations for a 1250 m aerial highway at different altitudes in a URD scenario.

TABLE 3.7: Summary of LTE vertical tilt coverage SINR statistics, considering different configurations for a 1250 m aerial highway at different altitudes in a URD scenario.

		URD Cov. SINR Statistics					
		Aerial			Ground		
		Baseline	Opt	Gain	Baseline	Opt	Gain
		[dB]	[dB]	[dB]	[dB]	[dB]	[dB]
		Curved					
50m	5%-tile	-9.03	-0.46	8.57	-2.63	-2.63	0.00
	Mean	-4.88	6.85	11.73	9.86	9.81	-0.05
100m	5%-tile	-8.45	-1.45	7.00	-2.63	-2.88	-0.25
	Mean	-5.10	2.35	7.45	9.86	9.49	-0.37
150m	5%-tile	-8.80	-2.21	6.59	-2.63	-3.13	-0.50
	Mean	-5.95	0.61	6.56	9.86	9.29	-0.57
		Straight Centre					
50m	5%-tile	-9.17	-1.82	7.35	-2.63	-2.73	-0.10
	Mean	-4.87	6.20	11.07	9.86	9.72	-0.14
100m	5%-tile	-8.77	-2.70	6.07	-2.63	-2.89	-0.26
	Mean	-5.06	1.65	6.71	9.86	9.55	-0.31
150m	5%-tile	-8.77	-2.18	6.59	-2.63	-3.10	-0.47
	Mean	-5.79	0.70	6.49	9.86	9.33	-0.53
		Straight Edge					
50m	5%-tile	-9.65	-2.34	7.31	-2.63	-2.67	-0.04
	Mean	-5.31	4.43	9.74	9.86	9.77	-0.09
100m	5%-tile	-9.14	-1.71	7.43	-2.63	-2.88	-0.25
	Mean	-5.32	1.90	7.22	9.86	9.50	-0.36
150m	5%-tile	-9.32	-2.42	6.90	-2.63	-3.08	-0.45
	Mean	-6.10	0.53	6.63	9.86	9.38	-0.48

TABLE 3.8: LTE vertical tilt aerial highway out of coverage rate, considering different configurations for a 1250 m aerial highway at different altitudes in a URD scenario.

URD - Aerial Highway Cov. Outage Rate						
	Curved		Straight Centre		Straight Edge	
	Baseline	Opt	Baseline	Opt	Baseline	Opt
50m	39.69%	0.00%	41.95%	0.20%	48.29%	0.00%
100m	40.32%	0.00%	42.38%	0.00%	46.13%	0.00%
150m	52.97%	0.00%	53.60%	0.00%	56.53%	0.00%

3.5.2 Coverage Serving Power and Interference

Although discussing the advantages of our methodology is essential, comprehending the origins of these benefits is even more important; for this reason, in the following, we report reports and discuss results obtained in terms of serving RSRP and interference power distribution concerning the AH evaluation points.

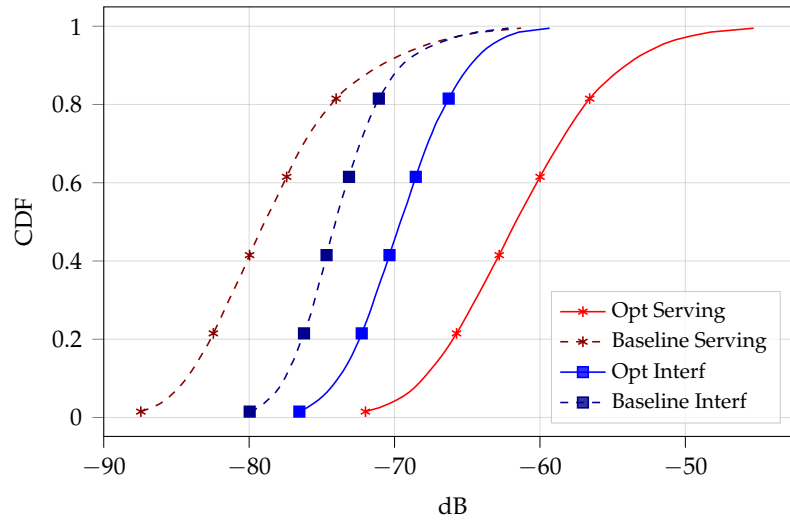
Here, we specifically address the *UMa Curved* scenario, with results illustrated in Figure 3.7a, although these considerations can be fully extended to all other network and AH setups. Figure 3.10 show the obtained CDF for both serving RSRP and interference power and Table 3.9 summarize those.

Analyzing these curves, we can derive that the coverage SINR gain achieved through our methodology is primarily driven by the more optimal and evenly distributed serving RSRP on the AH. However, as previously anticipated, these gains are somewhat diminished by the increased interference perceived along the AH, as some of the main lobes are pointed towards the sky, and the typically full LoS condition does not mitigate interference coming from those. In more detail, we can see in Figure 3.10 how the curves regarding the serving RSRP distribution result in a higher right shift with respect to the interference one, therefore suggesting higher overall gain in the serving power with respect to the interference. It should be noted that this trend is consistent with all the considered altitudes. Specifically, as reported in Table 3.9, the gain introduced in the serving RSRPs result in a value approximately within the range [10, 17] dB, while the interference reaches gains up to approximately 6 dB.

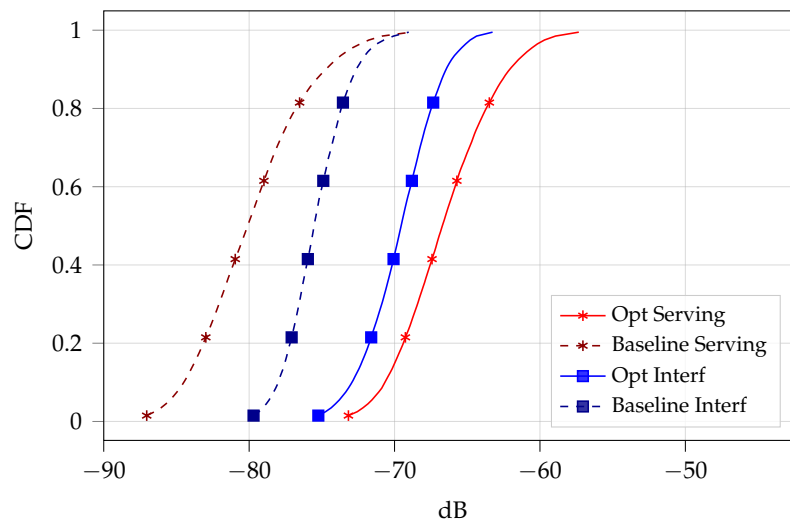
The gains introduced in the interference point out the main limitation of the vertical tilt optimization approach within LTE terrestrial networks: the adjustment of the tilt direction alone is insufficient to completely suppress or mitigate the interference from adjacent cells or sectors, and thereby limiting potential higher improvements.

TABLE 3.9: LTE vertical tilt aerial highway serving RSRP and interference CDF statistics, considering a 1250 m Curved aerial highway at different altitudes in a UMa scenario.

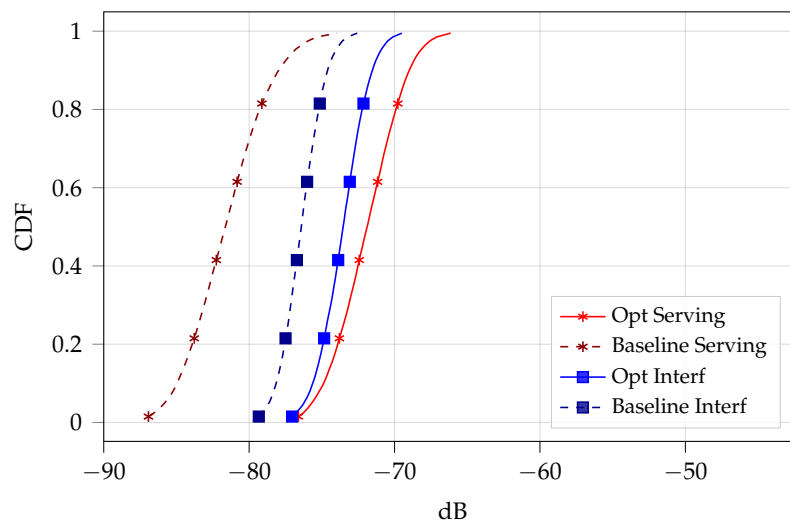
	Serving RSRP			Interference		
	Baseline [dB]	Opt [dB]	Gain [dB]	Baseline [dB]	Opt [dB]	Gain [dB]
	5%-tile					
50m	-85.58	-69.59	15.99	-78.56	-75.07	3.49
100m	-85.57	-71.68	13.89	-78.72	-73.92	4.80
150m	-85.80	-75.68	10.12	-78.63	-76.23	2.40
	Mean					
50m	-78.25	-61.32	16.93	-73.69	-69.45	4.24
100m	-79.87	-66.53	13.34	-75.40	-69.61	5.79
150m	-81.55	-71.90	9.65	-76.39	-73.56	2.83



(a) 50 m Altitude.



(b) 100 m Altitude.



(c) 150 m Altitude.

FIGURE 3.10: LTE vertical tilt aerial highway serving RSRP and interference CDF, considering a 1250 m Curved aerial highway at different altitudes in a UMA scenario.

3.6 LTE Achievable Data Rate

Moving beyond coverage aspects, this section presents results obtained for gUEs and UAVs achievable data rates. It should be noted that, as previously presented in Section 2.6.1, to transmit data to each of the connected UEs each cell adopts as transmitted beams employed during the coverage phase. For this reason, here we focus only on the resulting achievable data rate, as the data SINR will result, in the long term, as the one presented in previous Section 3.5 and depicted in Figures 3.7, 3.8 and 3.9.

Specifically, following what presented in Chapter 2, Section 2.1 regarding gUEs and UAVs distribution within the network, in the following we consider a total number of 228 gUEs (four in each cell on average) evenly distributed within the network and 12 UAVs located along the previously described AHs with a minimum IUD of 100 m [77, 78]. To provide a robust characterization of the obtained results, a total number of 1000 network realization N_{real} are considered; in each new realization a new random position for gUEs is computed while the UAVs one is updated such that it is resulting a collective movement of the UAVs along the AH with a fix equal IUD distance. In addition, it should be noted that, in order to maintain a continuous traffic condition, when a UAV exist the AH a new one enters. Finally, the resulting achievable data rate for each UE is computed according to eq. (2.33).

Figures 3.12, 3.13 and 3.14 show the achievable data rate CDF obtained for the three different network layout configurations and the three different aerial highway configurations at different altitudes. In each figure, the left column shows the distribution of the UAVs achievable data rates, while the right those of gUEs. Results obtained within the network configured according to our optimization process are denoted with “Opt” while those obtained considering the network configured solely for ground, i.e., all network cells downtilted at 105° , are denoted as “Baseline”. Finally, for each considered network layout scenario results on the obtained statistics are summarized, respectively, in Tables 3.10, 3.12, and 3.14.

Analyzing the obtained results, we observe substantial and consistent gains in UAVs rates across all considered scenarios and AHs configurations, with almost no impact on the gUEs achievable data rates. Specifically, our solution significantly enhances performance, with gains of up to 6 in the 5%-tile of the UAVs rate distribution and up to 10 in the mean values. For the sake of clarity, it should be noted here the gain is computed as $gain = Opt / Baseline$. Importantly, considering UMa and URD cases, with results respectively depicted and summarized in Figure 3.12, Table 3.10 and Figure 3.14, Table 3.14, the obtained results for the UAVs achievable data rate at 50 m and 100 m, for the 5%-tile reach those of gUEs. However, these considerations may not apply to the 150 m case or to scenarios within a UMi environment.

At 150 m, it should be noted that the significantly higher loss is somehow inconsistent with the losses observed within the SINR (see as example Figure 3.7a). The gaps in data rates between 150 m and other altitudes are more pronounced than

the variations in SINRs, therefore suggesting the influence of additional factors contributing to the increased loss in the data rates. The reasons stands in the typical number of cells uptoilted to serve the AH. As shown in Figures 3.3, 3.5 for the UMA and URD scenarios, the 150 m altitude results in fewer uptoilted cells for the AH coverage compared to other altitudes. For example, in Figure 3.3b, only two cells are fully uptoilted to serve the AH. Although this configuration minimizes the number of cells deviating significantly from their baseline tilt, it has a strong impact on the overall multiplexing capability along the AH. With only one or very few cells serving multiple UAVs, as discussed in Chapter 2 Section 3.6, the available bandwidth is evenly distributed among the connected UEs. This leads to a linear reduction in data rates as the number of devices increases, with a significant impact on the final rate performance.

Considering the UMi scenario instead, we can observe how gains and rate performances drastically drop. The reason can be attributed to the low associated SINR, along with the related issues discussed in the previous Section 3.5.

Therefore, remarking on the consideration drawn in the previous section regarding the coverage, a similar conclusion can be derived for the achievable data rate. Our results suggest that network operators should push for low altitude AHs operation within UMA layouts if their goal is to provide UAVs with data rates comparable to those of gUEs. As well as recommending further actions if the target are UMi scenarios.

3.6.1 Minimum PRBs required for C&C

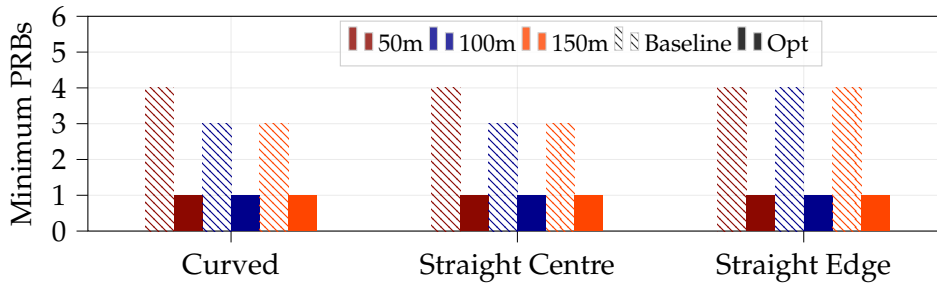
Although our results demonstrate that our proposed solution is capable of providing more reliable and higher UAVs rates, it should be kept in mind that one of the main targets of this work is fulfilling the minimum requirements for the C&C channels. Here, we propose an analysis on the minimum PRBs for achieving the minimum required rate $T_{c\&c}$ of 100 Kbps, as outlined by 3GPP [67]. In particular, for the following analysis, we consider as reference SINRs those values obtained at the 5%-tile of the previous curves, therefore characterizing the need for those UAVs in the worst conditions.

So, given for each scenario the 5%-tile SINR $\gamma_{5\%}^{lte}$, the minimum number of PRBs $N_{min,PRB}^{c\&c,lte}$ needed, is computed as follows,

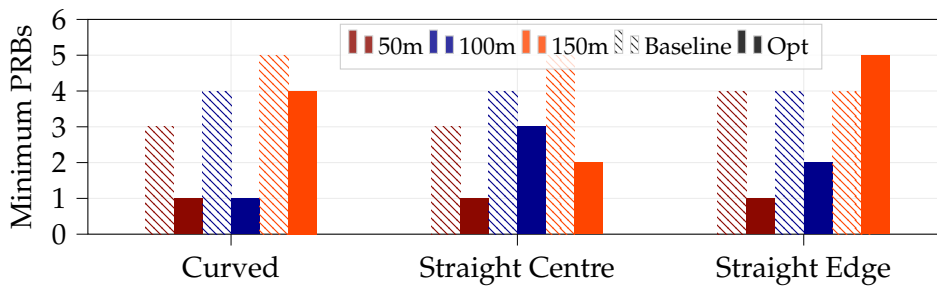
$$N_{min,PRB}^{c\&c,lte} = \left\lceil \frac{T_{c\&c}}{B_{PRB} \log_2 (1 + \gamma_{5\%}^{lte})} \right\rceil. \quad (3.9)$$

Figures 3.11 illustrates the obtained results, and Tables 3.11, 3.13 and 3.15 summarizes those. Our results, especially in the UMA and URD scenarios, as depicted in Figure 3.11, demonstrate that our solution significantly reduces the minimum number of required PRBs to just one, the bare minimum. This highlights the effectiveness of our methodology in minimizing resource usage while maintaining the same level

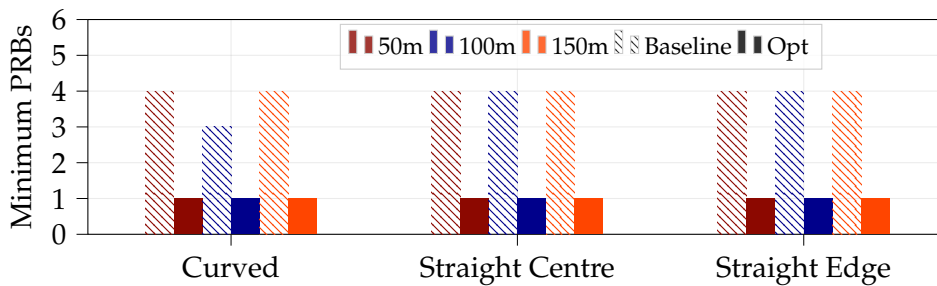
of UAVs traffic. Alternatively, it underscores how our solution increases the overall UAVs traffic capacity of the AH, as it can now accommodate 3 to 4 times more traffic with the same number of PRBs.



(a) UMa network layout considering 1250 m aerial highways.

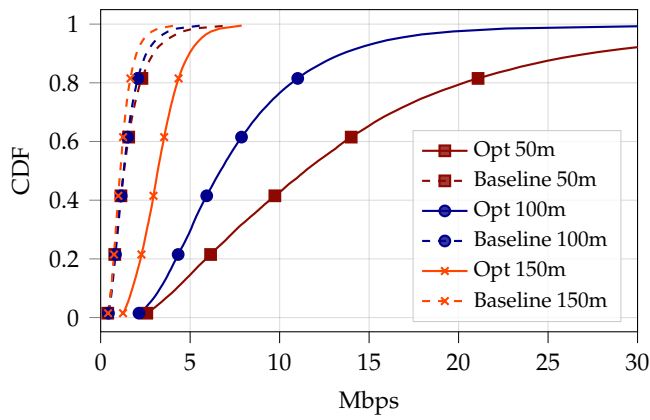


(b) UMi network layout considering 500 m aerial highways.

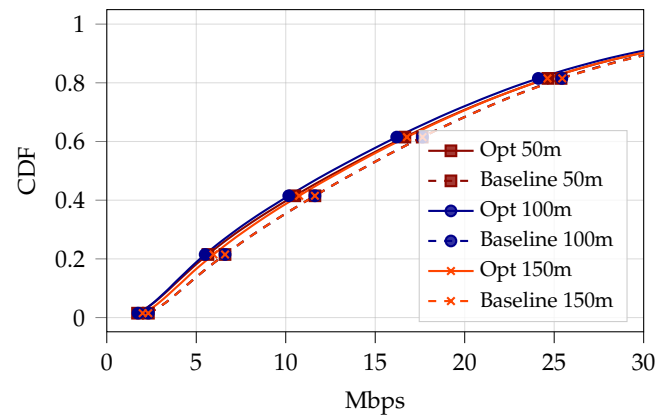


(c) URD network layout considering 1250 m aerial highways.

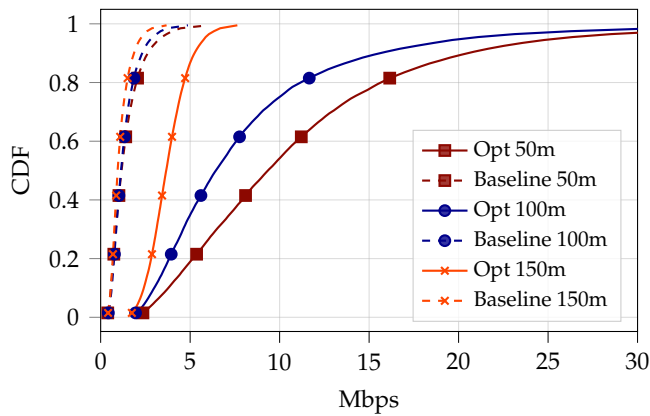
FIGURE 3.11: LTE vertical tilt minimum number of PRBs needed for achieving the 100 Kbps requirement for the C&C channel at the 5%-tile SINR, considering different configurations for AHs at different altitudes in different network layouts.



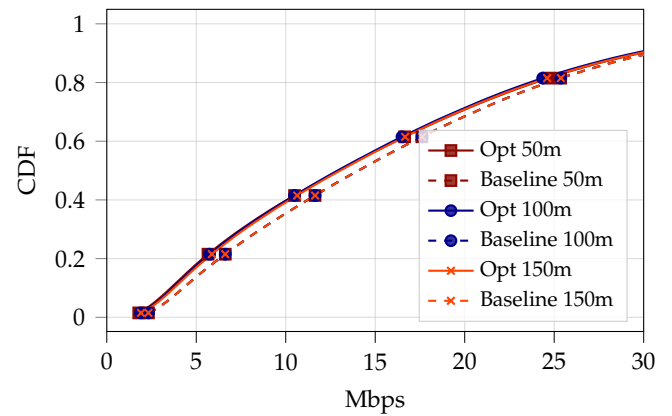
(a) Curved AH, UAVs.



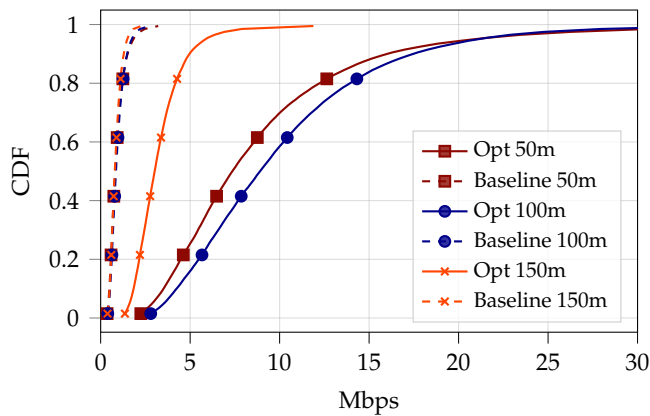
(b) Curved AH, gUEs.



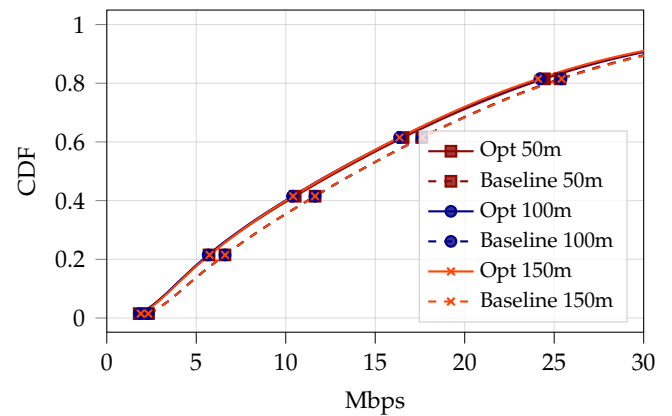
(c) Straight Centre AH, UAVs.



(d) Straight Centre AH, gUEs.



(e) Straight Edge AH, UAVs.



(f) Straight Edge AH, gUEs.

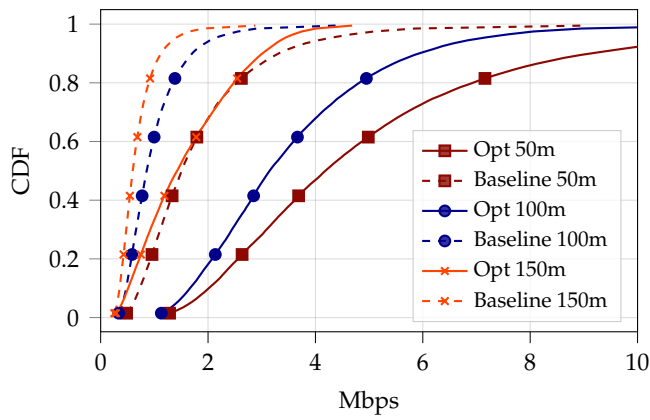
FIGURE 3.12: LTE vertical tilt resulting UAVs and gUEs data rate CDF, considering different configurations for a 1250 m aerial highway at different altitudes in a UMA scenario.

TABLE 3.10: Summary of LTE vertical tilt resulting UAVs and gUEs data rate statistics, considering different configuration for a 1250 m aerial highway at different altitudes in a UMa scenario.

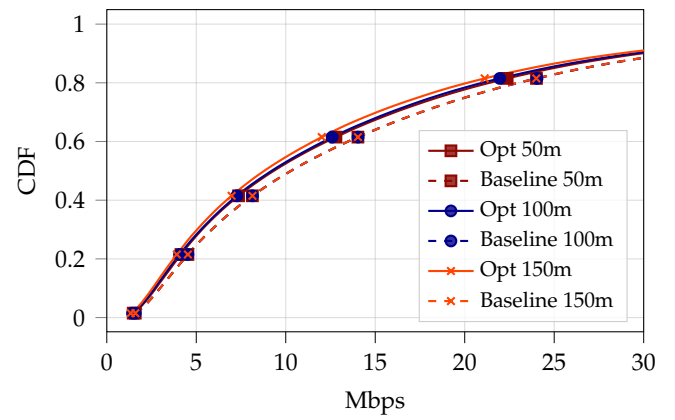
UMa Data Rate Statistics							
		UAVs			gUEs		
		Baseline	Opt	Gain	Baseline	Opt	Gain
		[Mbps]	[Mbps]		[Mbps]	[Mbps]	
Curved							
50m	5%-tile	0.49	3.34	6.82	3.27	2.62	0.80
	Mean	1.60	14.46	9.04	16.03	15.15	0.95
100m	5%-tile	0.54	2.74	5.07	3.27	2.60	0.80
	Mean	1.49	7.83	5.25	16.03	14.79	0.92
150m	5%-tile	0.51	1.51	2.96	3.27	2.91	0.89
	Mean	1.23	3.32	2.70	16.03	15.32	0.96
Straight Centre							
50m	5%-tile	0.48	3.01	6.27	3.27	2.65	0.81
	Mean	1.44	11.26	7.82	16.03	15.16	0.95
100m	5%-tile	0.53	2.49	4.70	3.27	2.76	0.84
	Mean	1.34	8.27	6.17	16.03	15.05	0.94
150m	5%-tile	0.50	2.10	4.20	3.27	2.83	0.87
	Mean	1.11	3.77	3.40	16.03	15.25	0.95
Straight Edge							
50m	5%-tile	0.42	2.90	6.90	3.27	2.69	0.82
	Mean	0.93	9.01	9.69	16.03	15.10	0.94
100m	5%-tile	0.47	3.54	7.53	3.27	2.70	0.83
	Mean	0.95	10.13	10.66	16.03	14.94	0.93
150m	5%-tile	0.45	1.62	3.60	3.27	2.76	0.84
	Mean	0.86	3.30	3.84	16.03	14.94	0.93

TABLE 3.11: LTE vertical tilt minimum number of PRBs needed for achieving the 100 Kbps requirement for the UAVs C&C channel, considering different configuration for a 1250 m aerial highway at different altitudes in a UMa scenario.

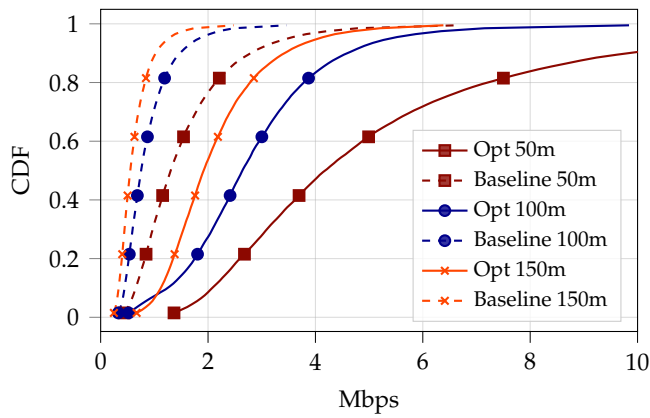
UMa - Aerial Highway Minimum PRBs at 5%-tile SINR						
	Curved		Straight Centre		Straight Edge	
	Baseline	Opt	Baseline	Opt	Baseline	Opt
50m	4	1	4	1	4	1
100m	3	1	3	1	4	1
150m	3	1	3	1	4	1



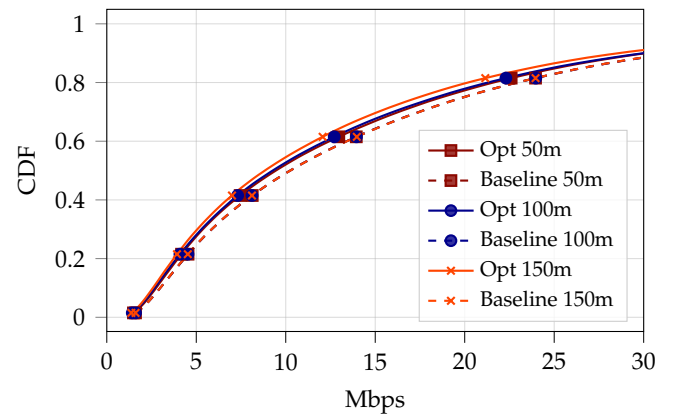
(a) Curved AH, UAVs.



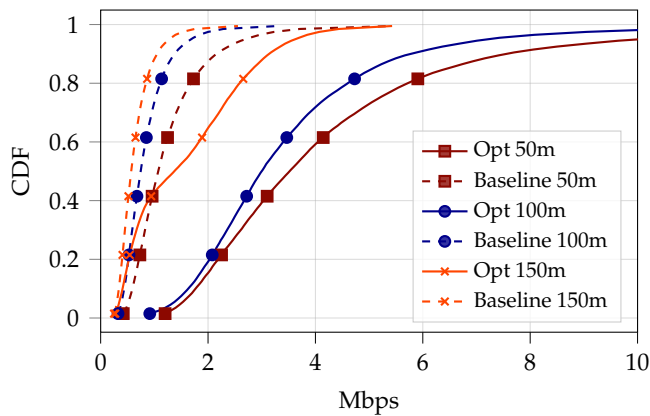
(b) Curved AH, gUEs.



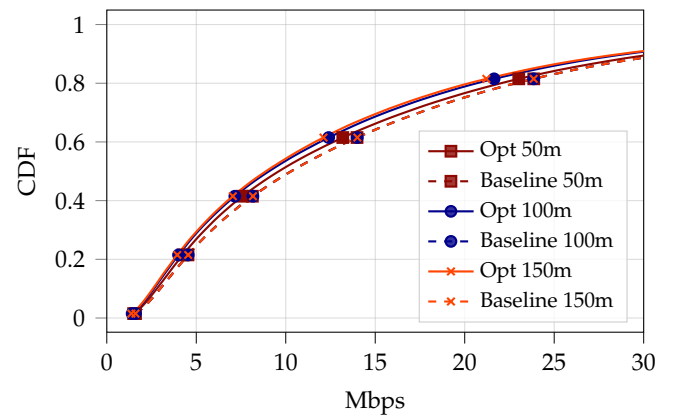
(c) Straight Centre AH, UAVs.



(d) Straight Centre AH, gUEs.



(e) Straight Edge AH, UAVs.



(f) Straight Edge AH, gUEs.

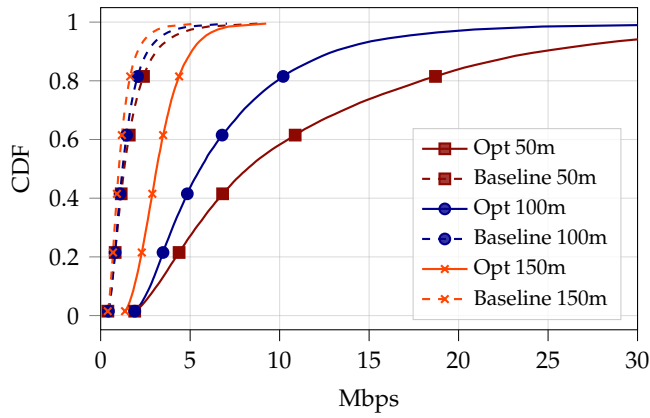
FIGURE 3.13: LTE vertical tilt resulting UAVs and gUEs data rate CDF, considering different configurations for a 1250 m aerial highway at different altitudes in a UMi scenario.

TABLE 3.12: Summary of LTE vertical tilt resulting UAVs and gUEs data rate statistics, considering different configuration for a 500 m aerial highway at different altitudes in a UMi scenario.

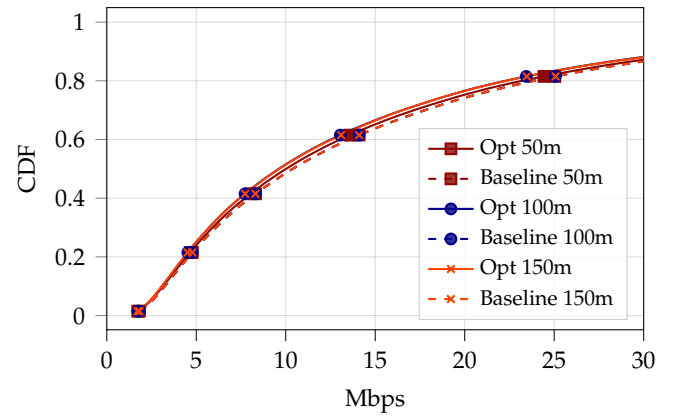
		UMi Data Rate Statistics					
		UAVs			gUEs		
		Baseline	Opt	Gain	Baseline	Opt	Gain
		[Mbps]	[Mbps]		[Mbps]	[Mbps]	
		Curved					
50m	5%-tile	0.61	1.67	2.74	2.27	2.10	0.93
	Mean	1.85	5.14	2.78	14.74	13.70	0.93
100m	5%-tile	0.41	1.42	3.46	2.27	2.04	0.90
	Mean	1.01	3.56	3.52	14.74	13.53	0.92
150m	5%-tile	0.31	0.40	1.29	2.27	1.94	0.85
	Mean	0.69	1.62	2.35	14.74	13.08	0.89
		Straight Centre					
50m	5%-tile	0.55	1.75	3.18	2.27	2.11	0.93
	Mean	1.57	5.33	3.39	14.74	13.83	0.94
100m	5%-tile	0.39	0.80	2.05	2.27	2.03	0.89
	Mean	0.89	2.85	3.20	14.74	13.71	0.93
150m	5%-tile	0.30	0.94	3.13	2.27	1.96	0.86
	Mean	0.64	2.13	3.33	14.74	13.07	0.89
		Straight Edge					
50m	5%-tile	0.51	1.50	2.94	2.27	2.13	0.94
	Mean	1.27	4.45	3.50	14.74	14.08	0.96
100m	5%-tile	0.38	1.34	3.53	2.27	2.01	0.89
	Mean	0.85	3.50	4.12	14.74	13.34	0.90
150m	5%-tile	0.30	0.34	1.13	2.27	1.96	0.86
	Mean	0.65	1.60	2.46	14.74	13.16	0.89

TABLE 3.13: LTE vertical tilt minimum number of PRBs needed for achieving the 100 Kbps requirement for the UAVs C&C channel, considering different configuration for a 500 m aerial highway at different altitudes in a UMi scenario.

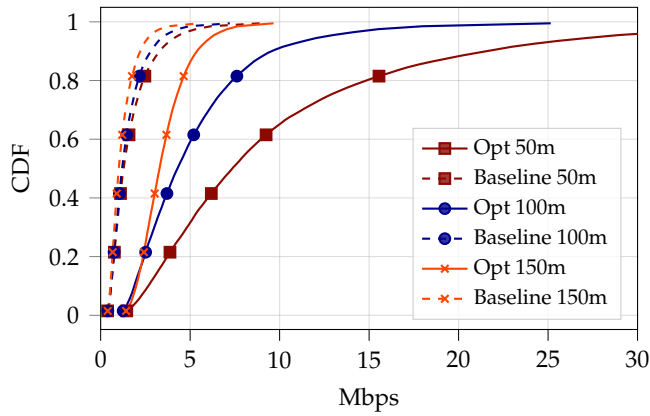
UMi - Aerial Highway Minimum PRBs at 5%-tile SINR						
	Curved		Straight Centre		Straight Edge	
	Baseline	Opt	Baseline	Opt	Baseline	Opt
50m	3	1	3	1	4	1
100m	4	1	4	3	4	2
150m	5	4	5	2	5	5



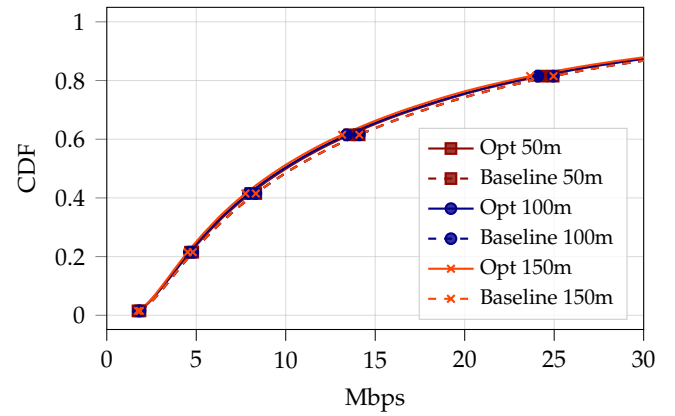
(a) Curved AH, UAVs.



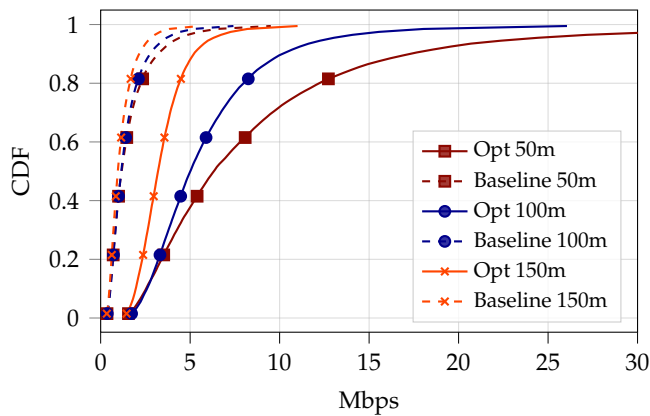
(b) Curved AH, gUEs.



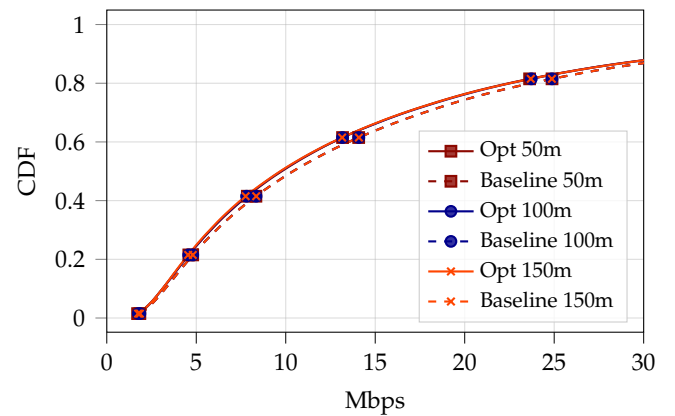
(c) Straight Centre AH, UAVs.



(d) Straight Centre AH, gUEs.



(e) Straight Edge AH, UAVs.



(f) Straight Edge AH, gUEs.

FIGURE 3.14: LTE vertical tilt resulting UAVs and gUEs data rate CDF, considering different configurations for a 1250 m aerial highway at different altitudes in a URD scenario.

TABLE 3.14: Summary of LTE vertical tilt resulting UAVs and gUEs data rate statistics, considering different configuration for a 1250 m aerial highway at different altitudes in a URD scenario.

		URD Data Rate Statistics					
		UAVs			gUEs		
		Baseline	Opt	Gain	Baseline	Opt	Gain
		[Mbps]	[Mbps]		[Mbps]	[Mbps]	
		Curved					
50m	5%-tile	0.51	2.51	4.92	2.53	2.44	0.96
	Mean	1.68	11.76	7.00	15.76	15.37	0.98
100m	5%-tile	0.54	2.35	4.35	2.53	2.41	0.95
	Mean	1.49	7.11	4.77	15.76	13.83	0.88
150m	5%-tile	0.48	1.64	3.42	2.53	2.40	0.95
	Mean	1.21	3.35	2.77	15.76	14.91	0.95
		Straight Centre					
50m	5%-tile	0.49	2.07	4.22	2.53	2.45	0.97
	Mean	1.70	10.12	5.95	15.76	15.32	0.97
100m	5%-tile	0.50	1.58	3.16	2.53	2.45	0.97
	Mean	1.51	5.28	3.50	15.76	15.19	0.96
150m	5%-tile	0.47	1.73	3.68	2.53	2.41	0.95
	Mean	1.24	3.54	2.85	15.76	14.95	0.95
		Straight Edge					
50m	5%-tile	0.44	2.06	4.68	2.53	2.42	0.96
	Mean	1.61	8.90	5.53	15.76	14.98	0.95
100m	5%-tile	0.46	2.18	4.74	2.53	2.44	0.96
	Mean	1.47	5.94	4.04	15.76	15.01	0.95
150m	5%-tile	0.42	1.72	4.10	2.53	2.43	0.96
	Mean	1.19	3.48	2.92	15.76	14.99	0.95

TABLE 3.15: LTE vertical tilt minimum number of PRBs needed for achieving the 100 Kbps requirement for the UAVs C&C channel, considering different configuration for a 1250 m aerial highway at different altitudes in a URD scenario.

URD - Aerial Highway Minimum PRBs at 5%-tile SINR						
	Curved		Straight Centre		Straight Edge	
	Baseline	Opt	Baseline	Opt	Baseline	Opt
50m	4	1	4	1	4	1
100m	3	1	4	1	4	1
150m	4	1	4	1	4	1

3.7 Conclusion

In this chapter, we introduced an optimization framework which leverages the AH information to optimise the vertical tilt of the terrestrial LTE cellular network to provide minimum coverage along the considered AH and thereby enhancing the UAVs cellular connectivity. Our results confirmed our hypothesis, showcasing how integrating AH and thereby fixing the trajectory of UAVs allows optimal control of the vertical tilt to strategically re-distributed power in the sky to cover and boost the UAVs rates along the AH with an almost null impact on gUEs.

Specifically, our simulation results showcase how our proposed solution introduces SINRs gains up to 9 dB at the 5%-tile and 12 dB at the mean value and drastically reduces out of coverage conditions for UAVs and enables reliable communication along the AH. On top of that, our proposed solution allows UAVs to achieve up to almost seven-fold values for the data rates, thereby allowing existing LTE terrestrial networks to support high-rate applications or facilitate a more efficient resource utilization to either sustain more UAVs traffic conditions or reduce the overall resource usage. Finally, it should be noted that those gains introduced for UAVs come at a minimal cost for gUEs, thus highlighting the efficacy of our proposed solution in re-using the terrestrial network to ensure reliable communication along the AH while maintaining continuous service on the ground.

However, our findings also reveal the main limitations of the considered LTE vertical tilt optimization frameworks. As shown in Section 3.5 and 3.6, within UMi the gains introduced by our proposed solution are significantly mitigated, as the lower heights sectors, characterizing this scenario, are more difficult to be uptilted for serving AH at increasing altitudes while continuously serving the ground. Therefore, this suggests the need for further methods for targeting joint AH and ground connectivity. Moreover, as previously discussed, the significant improvements are constrained by the additional interference introduced when uptilting cells to serve the AH. Controlling only the vertical direction, without shaping the uptilted beam, results in strong power being into the sky also in unnecessary directions, which results in additional strong interference.

To tackle those limitations, in the next chapter, we aim to introduce methods to exploit multi-antenna systems to further enhance coverage SINR performance by steering power in different directions while simultaneously suppressing the introduced interference.

Chapter 4

Aerial Highways NR Coverage SSB Beams Optimization

4.1 Introduction

In this chapter, we move a step forward toward cellular network generations and tackle the previously discussed limitation of LTE. Specifically, we investigate how the multi-antenna transmission capability inherited with 5G NR systems and the prior knowledge of the AH can be jointly leveraged to provide enhanced coverage along the AH.

As previously described in Chapter 2 Section 2.5.3, one of the key distinctions between 4G LTE and 5G NR networks lies in the capability of transmitting signals controlling network initial access, i.e., SSB signals made of PSS, SSS and PBCH, across multiple direction within the same cells, thereby improving received RSRPs, interference management and overall the coverage SINR of each cell. Therefore, unlike 4G LTE in which these coverage signals are transmitted within a unique larger beam, in 5G NR they are transmitted within a total of distinct N_{ssb} SSB beams following a sweeping mechanism.

Accounting for the conclusion and limitation of the LTE vertical tilt optimization drawn in the previous Chapter 3, in the following, we aim to design a set of optimal SSB beams to be transmitted all across the network to maximize the final coverage SINR along the AH. We envision that moving in the direction of multi-antenna systems and introducing much higher degrees of freedom in systems is the key to further enhancing coverage performance. Specifically, the capability of controlling the phase and amplitude of each transceiver permits us to control not only the direction of the transmitted beams but also its shape, allowing us to realize coverage beams which not only provide high directed serving RSRP but also minimize the interference introduced in the sky. Moreover, differently from the previous LTE network case, here we focus only on optimization of the performance over the set of AH evaluation points, as we are assuming that the remaining $N_{\text{ssb}} - 1$ transmitted at each cell would be rearranged in a next stage to address the coverage gaps caused by the sky-directed beams. It should be noted that this poses different advantages, such as fewer points and, notably, the enabled capability of completely

uptilt coverage beam and provide high coverage also in UMi environments, thereby overcoming the limitation of the previous LTE vertical tilt optimization.

Parts of the results presented in this chapter have been published in the following journal:

- M. Bernabè, D. López-Pérez, N. Piovesan, and D. Gesbert, “Gradient-Based Optimization of Terrestrial Cellular Networks for Aerial Highways” (under submission in IEEE Transaction on Vehicular Technology).

Moreover, it should be noticed that to the best of the author’s knowledge, there are no existing works in literature that target the coverage SSB beams shaping in the context of AH and/or UAVs systems.

4.2 Problem Formulation

Following a methodology similar to the one presented for the vertical tilt optimization within LTE networks in Chapter 3, here we formulate a maximization problem for the stochastic network spectral efficiency for the set of AH’ evaluation points by searching for the optimal set of complex codewords (each representing a specific beam) employed at each cell within the NR network.

In more detail, we aim to determine the optimal matrix $\hat{\mathbf{W}}^{\text{nr}} \in \mathbb{C}^{M \times N_{\text{BS}}}$ in which each column results being the optimal complex codeword $\hat{\mathbf{w}}_b^{\text{nr}} \in \mathbb{C}^M$ of cell b . Specifically, for each cell b , $\hat{\mathbf{w}}_b^{\text{nr}}$ represented its transmitted coverage SSB beam. Then, at each cell b the set of transmitted SSB beams $\mathbf{W}_b^{\text{ssb}}$ is defined as follows,

$$\mathbf{W}_b^{\text{ssb}} = [\mathbf{w}_0, \mathbf{w}_1, \mathbf{w}_3, \hat{\mathbf{w}}_b^{\text{nr}}, \mathbf{w}_5, \dots, \mathbf{w}_{N_{\text{ssb}}}] \quad (4.1)$$

Moreover, it should be noted that within all network cells, the obtained optimal codewords in $\hat{\mathbf{W}}^{\text{nr}}$ are associated with the same beam sweep index i_s^{ssb} .

Overall, the maximization problem can be formulated as follows,

Problem 2. NR Coverage SSB Beam Optimization

$$\max_{\hat{\mathbf{W}}^{\text{nr}}} \mathbb{E}_{\tau, \mathbf{h}^{\text{dl}}} \left\{ \sum_{a \in \mathcal{E}_a} \log \left(\log_2 \left(1 + \gamma_a^{\text{nr-cov}}(\hat{\mathbf{W}}^{\text{nr}}) \right) \right) \right\}$$

$$\text{s.t.} \quad \sum_{m=0}^{M-1} |\hat{w}_{m,b}^{\text{nr}}|^2 \leq 1, \quad \forall b \in \mathcal{B} \quad (\text{C2.1}),$$

$$\hat{w}_{m,b}^{\text{nr}} \in \mathbb{C}, \quad \forall w_{m,b}^{\text{nr}} \in \hat{\mathbf{W}}^{\text{nr}} \quad (\text{C2.2})$$

where $\gamma_a^{\text{nr-cov}}$ is the NR coverage SINR computed accordingly to eq. (2.30). Then, constraints C2.1 accounts for the normalization of the codeword.

Similar to the problem presented in Chapter 3 for cells vertical tilt optimization, Problem (2) is a no-concave problem characterized by non-linearities, inherent stochasticity and a strong interplay of the optimization variables. Therefore, to tackle

this problem, we leverage the gradient solution proposed in the previous Chapter 3 to formulate a new gradient-based optimization framework to solve the problem and determine the optimal set of SSB beams to be employed within the considered 5G NR network.

The no-concavity of the problem is discussed in Appendix C Section C.2.

4.3 NR Coverage SSB Beams Gradient Based Solution

Here, we observe that Problem 2 shares a similar structure with Problem 1; however, the main distinction lies in the solution space, which now is within the continuous space of complex numbers.

Consequently, in this section, akin to the methodology outlined in the previous Chapter 3 we reformulate Problem 2 and develop a robust gradient-based method to find the optimal solution for the employed set codewords $\hat{\mathbf{W}}^{\text{nr}}$ employed for covering the AH. Specifically, our first objective is to re-model Problem 2 and define a scalar function z^{nr} that encompasses both the objective function and the constraints. Then, leveraging ADAM as a gradient-based optimizer, we design an optimization framework to determine the optimal set of SSB beams, i.e., its set of codewords.

4.3.1 Optimization Variables and Objective Scalar Function

The main difference with respect to the LTE vertical tilt case is the mathematical domain of the variables to be optimized. To handle gradient computations of complex variables, for each antenna m at each cell b , we split the complex number $\hat{w}_{m,b}^{\text{nr}} \in \hat{\mathbf{w}}_b^{\text{nr}}$, representing the associated amplitude and phase shift at the considered antenna, into three components as follows,

$$\begin{aligned} \hat{w}_{m,b}^{\text{nr}} &= \frac{1}{\sqrt{M}} \hat{\alpha}_{m,b}^{\text{nr}} e^{j\hat{\psi}_{m,b}^{\text{nr}}} = \frac{1}{\sqrt{M}} \hat{\alpha}_{m,b}^{\text{nr}} (\cos(\hat{\psi}_{m,b}^{\text{nr}}) + j \sin(\hat{\psi}_{m,b}^{\text{nr}})) = \\ &= \frac{1}{\sqrt{M}} \hat{\alpha}_{m,b}^{\text{nr}} (\hat{p}_{m,b}^{\text{nr}} + j \hat{q}_{m,b}^{\text{nr}}), \end{aligned} \quad (4.2)$$

where

- $\hat{\alpha}_{m,b}^{\text{nr}}$ is what we denoted with “activation” variable of the considered antenna. With values constrained on the continuous interval $[0,1]$ to adhere to constraints C1.1.
- $e^{j\hat{\psi}_{m,b}^{\text{nr}}}$ is the complex number representing the phase shift component of the considered antenna. As illustrated in eq 4.2, the phase component is divided into two independent variables $\hat{p}_{m,b}^{\text{nr}}$ and $\hat{q}_{m,b}^{\text{nr}}$, where:
 - $\hat{p}_{m,b}^{\text{nr}} = \cos(\hat{\psi}_{m,b}^{\text{nr}})$ is the “phase” component, with values constrained in $[-1,1]$.

- $\hat{q}_{m,b}^{\text{nr}} = \sin(\hat{\psi}_{m,b})$ is the ‘‘quadrature’’ component, with values constrained in $[-1, 1]$.

Following this, the matrix $\hat{\mathbf{W}}^{\text{nr}}$ can be represented as,

$$\hat{\mathbf{W}}^{\text{nr}} = \frac{1}{\sqrt{M}} \hat{\mathbf{A}}^{\text{nr}} \odot (\hat{\mathbf{P}}^{\text{nr}} + j \hat{\mathbf{Q}}^{\text{nr}}), \quad (4.3)$$

where \odot is the Hadamard product, $\hat{\mathbf{A}}^{\text{nr}}$ is the beamforming activation matrix, and, in order, $\hat{\mathbf{P}}^{\text{nr}}$ and $\hat{\mathbf{Q}}^{\text{nr}}$ are the phase and quadrature phase matrices. Finally, the factor $1/\sqrt{M}$ embraces constraint C2.1, allowing for the normalization of the codewords.

Objective Scalar Function

In the following, we introduce a newly designed utility function along with a gradient-based algorithm to optimize the three variables $\hat{\mathbf{A}}^{\text{nr}}$, $\hat{\mathbf{P}}^{\text{nr}}$, and $\hat{\mathbf{Q}}^{\text{nr}}$ that characterize the matrix $\hat{\mathbf{W}}^{\text{nr}}$. Similar to the LTE vertical tilt case, we design the NR utility function \bar{z}^{nr} to embrace objective function of Problem 2 and the constraints inherited from the definition of the new optimization variables.

Specifically, we define the utility function \bar{z}^{nr} to maximize as follows,

$$\begin{aligned} \bar{z}^{\text{nr}}(\hat{\mathbf{W}}^{\text{nr}}) &= \mathbb{E}_{\tau, \text{h}^{\text{dl}}} \left\{ z^{\text{nr}}(\hat{\mathbf{A}}^{\text{nr}}, \hat{\mathbf{P}}^{\text{nr}}, \hat{\mathbf{Q}}^{\text{nr}}) \right\} = \\ &= \frac{1}{N_{\text{real}}} \sum_i^{N_{\text{real}}} \sum_{a \in \mathcal{E}_a} i f_a^{\text{nr}}(\hat{\mathbf{A}}^{\text{nr}}, \hat{\mathbf{P}}^{\text{nr}}, \hat{\mathbf{Q}}^{\text{nr}}) - \lambda^{\text{nr}} g^{\text{nr}}(\hat{\mathbf{A}}^{\text{nr}}, \hat{\mathbf{P}}^{\text{nr}}, \hat{\mathbf{Q}}^{\text{nr}}), \end{aligned} \quad (4.4)$$

where $N_{\text{real}}^{\text{nr}}$ is the total number of stochastic realizations of the network random variables, and $i f_a^{\text{nr}}$, computed for each network realization i , is designed to reflect objective function of Problem 2 and its defined as follows,

$$\begin{aligned} i f_a^{\text{nr}}(\hat{\mathbf{A}}^{\text{nr}}, \hat{\mathbf{P}}^{\text{nr}}, \hat{\mathbf{Q}}^{\text{nr}}) &= \\ &= \log \left(\log_2 \left(1 + i \gamma_a^{\text{nr-ADAM}}(\hat{\mathbf{A}}^{\text{nr}}, \hat{\mathbf{P}}^{\text{nr}}, \hat{\mathbf{Q}}^{\text{nr}}) \right) \right), \end{aligned} \quad (4.5)$$

with

$$\begin{aligned} i \gamma_a^{\text{nr-ADAM}}(\hat{\mathbf{A}}^{\text{nr}}, \hat{\mathbf{P}}^{\text{nr}}, \hat{\mathbf{Q}}^{\text{nr}}) &= \\ &= \frac{i \beta_{a, \hat{b}_a} \left| \frac{1}{\sqrt{M}} \sum_m i h_{a, \hat{b}_a, m}^{\text{dl}} \hat{\alpha}_{m, \hat{b}_a}^{\text{nr}} (\hat{p}_{m, \hat{b}_a}^{\text{nr}} + j \hat{q}_{m, \hat{b}_a}^{\text{nr}}) \right|^2}{\sum_{b \in \mathcal{B} \setminus \hat{b}_a} i \beta_{a, b} \left| \frac{1}{\sqrt{M}} \sum_m i h_{a, b, m}^{\text{dl}} \hat{\alpha}_{m, b}^{\text{nr}} (\hat{p}_{m, b}^{\text{nr}} + j \hat{q}_{m, b}^{\text{nr}}) \right|^2 + B_0 N_0}. \end{aligned} \quad (4.6)$$

It should be noted that the SINR equation defined above in eq (4.6) originates from the definition of the NR coverage SINR presented in eq. (2.30); however, the formulation in eq. (4.6) solely focuses on the AH evaluation points coverage SINR generated by the newly employed beams considered within the optimization.

Then, to embrace the domain constraints inherited from the definition of the new optimization set of variables $\hat{\mathbf{A}}^{\text{nr}}$, $\hat{\mathbf{P}}^{\text{nr}}$, and $\hat{\mathbf{Q}}^{\text{nr}}$, we introduce g^{nr} as a penalty function as follows,

$$g^{\text{nr}}(\hat{\mathbf{A}}^{\text{nr}}, \hat{\mathbf{P}}^{\text{nr}}, \hat{\mathbf{Q}}^{\text{nr}}) = \quad (4.7)$$

$$\begin{aligned} &= \sum_m \sum_b \text{ReLu}(0 - \hat{\alpha}_{m,b}^{\text{nr}}) + \text{ReLu}(\hat{\alpha}_{m,b}^{\text{nr}} - 1) \\ &+ \sum_m \sum_b \text{ReLu}(-1 - \hat{\rho}_{m,b}^{\text{nr}}) + \text{ReLu}(\hat{\rho}_{m,b}^{\text{nr}} - 1) \\ &+ \sum_m \sum_b \text{ReLu}(-1 - \hat{q}_{m,b}^{\text{nr}}) + \text{ReLu}(\hat{q}_{m,b}^{\text{nr}} - 1), \end{aligned} \quad (4.8)$$

where we recall the ReLu being defined as

$$\text{ReLu}(x) = \begin{cases} x, & \text{If } x \geq 0 \\ 0, & \text{Otherwise} \end{cases}. \quad (4.9)$$

Here, akin to the scenario outlined in Section 3.2, the introduced penalty function g^{nr} employs the ReLu function to reshape the surface, allowing the gradient-based optimizer to guide variables out from the infeasible area and converge to a solution that lies within the valid mathematical domain.

4.3.2 ADAM Optimizer

Mirroring the structure presented in the previous Chapter, here we present the ADAM optimizer-based structure tailored for the computation of the SSBs codewords $\hat{\mathbf{W}}^{\text{nr}}$ to maximize the proposed utility function \bar{z}^{lte} .

As depicted in the block diagram in Figure 4.1, the optimization process based on ADAM proceed iteratively. Given each configuration for the input matrices¹

$$\hat{\mathbf{A}}^{\text{nr}} = [\hat{\alpha}_0^{\text{nr}}, \dots, \hat{\alpha}_b^{\text{nr}}, \dots, \hat{\alpha}_{N_{\text{BS}}-1}^{\text{nr}}], \quad (4.10)$$

$$\hat{\mathbf{P}}^{\text{nr}} = [\hat{\rho}_0^{\text{nr}}, \dots, \hat{\rho}_b^{\text{nr}}, \dots, \hat{\rho}_{N_{\text{BS}}-1}^{\text{nr}}], \quad (4.11)$$

$$\hat{\mathbf{Q}}^{\text{nr}} = [\hat{q}_0^{\text{nr}}, \dots, \hat{q}_b^{\text{nr}}, \dots, \hat{q}_{N_{\text{BS}}-1}^{\text{nr}}], \quad (4.12)$$

where each column vector $\hat{\alpha}_b^{\text{nr}}$, $\hat{\rho}_b^{\text{nr}}$ and \hat{q}_b^{nr} have dimension equal to M , those matrices are flattened and concatenated to create a 1-D input vector as follows,

$$[\hat{\alpha}_0^{\text{nr}T}, \dots, \hat{\alpha}_{N_{\text{BS}}-1}^{\text{nr}T}, \dots, \hat{\rho}_0^{\text{nr}T}, \dots, \hat{\rho}_{N_{\text{BS}}-1}^{\text{nr}T}, \dots, \hat{q}_0^{\text{nr}T}, \dots, \hat{q}_{N_{\text{BS}}-1}^{\text{nr}T}]. \quad (4.13)$$

Then, similar to what was described in the previous Chapter, for each of the N_a the aerial evaluation points, channel models and resulting RSRPs are computed as described in Chapters 2 with the final goal of computing the coverage SINR defined in eq. (4.6). The resulting values, one for each aerial evaluation point a , in addition

¹Here, the iteration dependency (n) is removed for the sake of readability.

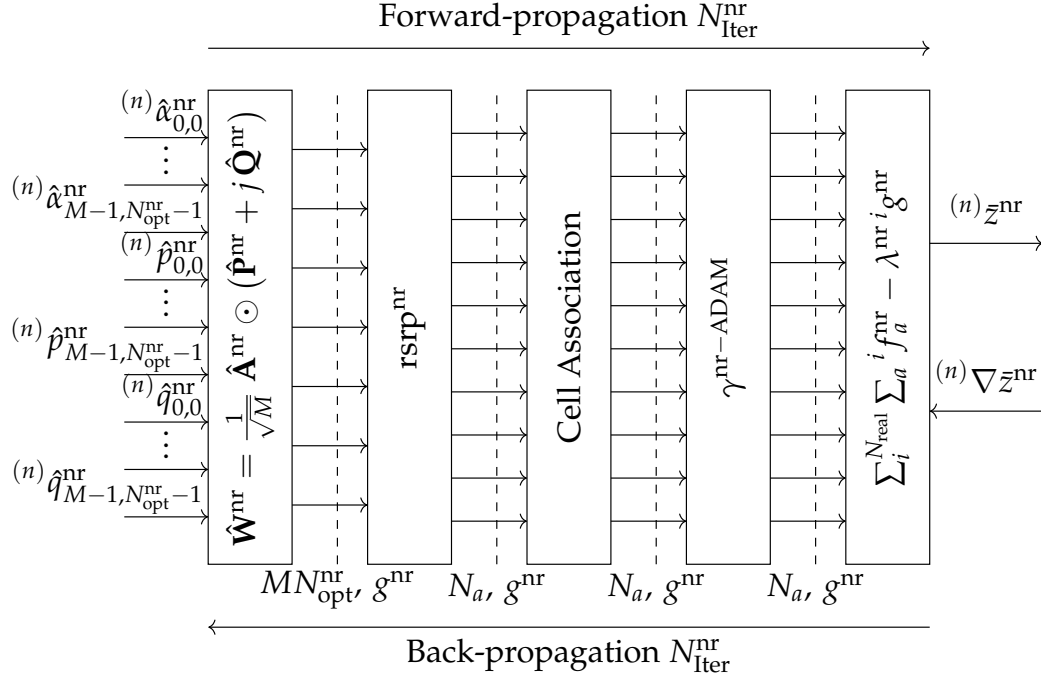


FIGURE 4.1: Block diagram for the ADAM NR SSB beam codeword optimizer.

to the penalty function g^{nr} initially computed as a function of the inputs, are jointly used to compute the final utility function \bar{z}^{nr} . All of these aforementioned steps are represented as consecutive and concatenate blocks in Figure 4.1, and the process of passing sequentially across all those blocks with the final step of computing the final output is denoted as “Forward Propagation”.

Then, we rely on ADAM to compute the gradients of the final utility function \bar{z}^{nr} , and at each iteration (n) of the total $N_{\text{iter}}^{\text{nr}}$, we “back propagate” gradients to the input, and, each variable $\hat{a}_{m,b}^{\text{nr}}$, $\hat{p}_{m,b}^{\text{nr}}$, $\hat{q}_{m,b}^{\text{nr}}$ is updated as follows,

$$\begin{aligned}
 {}^{(n+1)}\hat{a}_{m,b}^{\text{nr}} &\leftarrow {}^{(n)}\hat{a}_{m,b}^{\text{nr}} - {}^{(n)}\mu^{\text{nr}} \frac{\partial}{\partial \hat{a}_{m,b}^{\text{nr}}} \bar{z}^{\text{nr}} \left({}^{(n)}\hat{\mathbf{A}}^{\text{nr}}, {}^{(n)}\hat{\mathbf{P}}^{\text{nr}}, {}^{(n)}\hat{\mathbf{Q}}^{\text{nr}} \right), & (4.14) \\
 {}^{(n+1)}\hat{p}_{m,b}^{\text{nr}} &\leftarrow {}^{(n)}\hat{p}_{m,b}^{\text{nr}} - {}^{(n)}\mu^{\text{nr}} \frac{\partial}{\partial \hat{p}_{m,b}^{\text{nr}}} \bar{z}^{\text{nr}} \left({}^{(n)}\hat{\mathbf{A}}^{\text{nr}}, {}^{(n)}\hat{\mathbf{P}}^{\text{nr}}, {}^{(n)}\hat{\mathbf{Q}}^{\text{nr}} \right), \\
 {}^{(n+1)}\hat{q}_{m,b}^{\text{nr}} &\leftarrow {}^{(n)}\hat{q}_{m,b}^{\text{nr}} - {}^{(n)}\mu^{\text{nr}} \frac{\partial}{\partial \hat{q}_{m,b}^{\text{nr}}} \bar{z}^{\text{nr}} \left({}^{(n)}\hat{\mathbf{A}}^{\text{nr}}, {}^{(n)}\hat{\mathbf{P}}^{\text{nr}}, {}^{(n)}\hat{\mathbf{Q}}^{\text{nr}} \right),
 \end{aligned}$$

where ${}^{(n)}\mu^{\text{nr}}$ represent the value of the learning rate at iteration (n). Here, since we expect various values to converge towards zero (as further elaborated in the following paragraph) and thus approach the lower bounds of the variables’ domain, we introduce a learning rate scheduler mechanism to facilitate convergence. This mechanism reduces the learning rate of $\mu_{\%}^{\text{nr}}$ after every $N_{\mu^{\text{nr}}}$ iterations to ensure that the variables reach their optimal values.

4.3.3 Optimization Framework

In the following, we introduce an optimization framework incorporating the ADAM optimizer and its utility function described above. This framework does not only compute the optimal set of transmitted SSB beams using the aforementioned optimizer, but it further configures the NR network to embrace the most effective beams to be transmitted for optimal AH coverage while configuring the network to minimal deviate from the baseline configuration, i.e., those intended to serve gUEs only, as only few beams are expected to be transmitted in the sky. For the sake of clarity, let us consider the following scenario: an AH of 500 m length positioned within a network comprising 57 cells. Given the physical nature of the problem and the strong correlation among the AH's channels, inherited from strong LoS conditions, it seems unlikely that all beams from all 57 cells would positively contribute to the AH's coverage. Instead, it is more plausible that only a few beams would act as primary servers, While the majority of beams either point in directions for which the interference is minimized or need to be totally deactivated. Our proposed framework effectively detects these scenarios and takes consequent actions.

The proposed optimization framework is depicted in Figure 4.2 in a block diagram form. The overall solution is composed of five different blocks:



FIGURE 4.2: Block diagram for the NR SSB beam codeword optimization framework.

1. Network Init NR: it initializes the NR network by deploying all network cells as well as the set of AH evaluation points.

Then, it configures the transmitted SSB beams to be aligned with conventional setups designed primarily for gUEs. Specifically, in this configuration, each cell broadcasts 8 SSB beams covering its designated area. All beams are tilted at 105° and span the azimuth plane. We refer to this configuration as “Baseline-NR”.

2. Cell Selection: it implements a cell selection method to identify the set of cells to be in the optimization process; we denote this set as $\mathcal{B}_{\text{inOpt}}^{\text{nr}}$ and its cardinality as $N_{\text{opt}}^{\text{nr}}$. We compute this set as follows,

$$\mathcal{B}_{\text{inOpt}}^{\text{nr}} = \left\{ b \mid \exists a \in \mathcal{E}_a : \left(\phi_a - \phi_b^{\text{bst}} \right) \in [-90, 90] \right\}. \quad (4.15)$$

The defined set is based on the geometries of both the input AH and the surrounding network cells. Recalling that ϕ_b^{bst} represents the boresight direction of cell b , the set of cells included in the optimization process is determined by those oriented towards the AH. This approach not only reduces the number of

optimization variables and relaxes the optimization process complexity; additionally, pre-selecting these cells permits focusing solely on those expected to positively contribute to the AH, thereby limiting the deviation for the baseline-NR configuration.

3. Values Init: it random initializes optimization variables. Specifically, for all $\hat{\alpha}_{m,b}^{\text{nr}}, \hat{\rho}_{m,b}^{\text{nr}}, \hat{q}_{m,b}^{\text{nr}}$ values in, $\hat{\mathbf{A}}^{\text{nr}}, \hat{\mathbf{P}}^{\text{nr}}, \hat{\mathbf{Q}}^{\text{nr}}$ we have that:

$$\hat{\alpha}_{m,b}^{\text{nr}} \sim U(0, 1), \text{ and } \hat{\rho}_{m,b}^{\text{nr}}, \hat{q}_{m,b}^{\text{nr}} \sim U(-1, 1). \quad (4.16)$$

Then, it should be noted that for all cell $b \notin \mathcal{B}_{\text{inOpt}}^{\text{nr}}$, respective values in matrices $\hat{\mathbf{P}}^{\text{nr}}, \hat{\mathbf{Q}}^{\text{nr}}$ have been set as in baseline-NR and values $\hat{\mathbf{A}}^{\text{nr}}$ have been set to one.

4. ADAM Optimizer: starting from the matrices $\hat{\mathbf{A}}^{\text{nr}}, \hat{\mathbf{P}}^{\text{nr}}$, and $\hat{\mathbf{Q}}^{\text{nr}}$, it selects sub-matrices based on whether values belong to a cell within the $\mathcal{B}_{\text{inOpt}}^{\text{nr}}$ set and it flatten and concatenate those sub-matrices in a 1D vector to feed the input of the iterative ADAM optimizer, as depicted in Figure 4.1; this allows computations only for variables within the subset $\mathcal{B}_{\text{inOpt}}^{\text{nr}}$.
5. K-Means Beam Selection: As discussed in the introduction of this section, upon the convergence of the ADAM-based method, we expect that just a few beams will be steered up for the AH coverage, while the majority will be deactivated to reduce the amount of interference introduced. Therefore, in the following, we integrate a K-means clustering solution based on Lloyd's algorithm introduced in [93] to select, among the optimized beams, those effectively activated. To tackle this aspect and identify the activated beams, considering activation matrix $\hat{\mathbf{A}}^{\text{nr}}$, we select the sub-matrix referring to those values within the optimization process, i.e., belonging to cells in the set $\mathcal{B}_{\text{inOpt}}^{\text{nr}}$, and we introduce the beam-activation vector denoted as \mathbf{v}^{nr} and defined as follows,

$$\mathbf{v}^{\text{nr}} \in [0, 1]^{N_{\text{opt}}^{\text{nr}}} : \forall b \in \mathcal{B}_{\text{inOpt}}^{\text{nr}}, v_b = \frac{1}{M} \sum_{m=0}^{M-1} |\alpha_{m,b}|. \quad (4.17)$$

In eq. (4.17) for each cell within the optimization set, we compute the L1-norm normalized by the total number of antennas M of the vector of activation values $\hat{\alpha}_b$. This metric, together with a threshold later defined, helps determine whether the beam produced by a cell is effectively activated or deactivated. Specifically, considering coverage SINR eq. 4.6 which governs the final utility function computation, when a cell's beam acts as an interferer, the optimizer is expected to drive all the activation values $\hat{\alpha}_{m,b}$ of all M antennas within cell b towards zero; conversely, in scenarios where the beam is acting as a serving coverage beam, higher activation values are expected. As a result, the beam-activation vector \mathbf{v}^{nr} will exhibit corresponding variations, showing values that tend to zero in the first case and to one in the second one.

Then, using the obtained values in ν^{nr} as input for the K-means algorithm, we employ it fixing $K = 2$, and we compute the scalar value $\text{th}_{k-\text{mean}}$ representing the boundaries between the two clusters: the activated beams and the not activated beams, i.e., those to be selected and those not. Then, the algorithm selects as transmitted codeword those for which:

$$\nu_b^{\text{nr}} \geq \text{th}_{k-\text{mean}} . \quad (4.18)$$

Finally, if a beam is not selected from the optimized solution, it will be configured in $\hat{\mathbf{W}}^{\text{nr}}$ according to the ‘‘Baseline-NR’’ configuration described above. This approach helps to limit the overall deviation from the baseline configuration, thereby mitigating any negative impact on the ground. Additionally, it should be noted that this final action, aimed at nullifying the negative impact of ground coverage, does not influence the quality of the optimizer solution. The optimizer will determine the optimal beam configuration for the actually AH’s serving cells, with or without the inclusion of the detached ground-steered beams, as those, which do not influence gradient computation, act as a constant penalty within the SINR in eq. (4.6). From a mathematical perspective, this can be interpreted as a shift of the surface considered by the gradient-based optimizer when seeking maxima points.

4.3.4 Time Complexity

In the following, we analyze the time complexity of the NR coverage SSB beam optimization framework, and we compare it with the time complexity discussed in Section 3.3.4 for LTE vertical tilt optimization. It is important to note that in both scenarios, the key component is the ADAM optimizer, whose time complexity scales with the inputs and the complexity of the utility function. Given that the inputs and functions differ between the two cases, we will discuss how these differences impact the overall time complexity.

Mirroring the computation discussed in Section 3.3.4, even within this NR setup, the final time complexity, here denoted as C^{nr} , can be computed as the sum of each single block depicted in Figure 4.2 representing the optimization framework.

However, here four are the main differences with respect to the previous aLTE vertical tilt algorithm proposed in Chapter 3:

1. **Number of variables:** within the LTE setup, a single scalar value to be optimized was considered per cell. In contrast, the current approach for NR networks considers three scalar values for each antenna for each cell. This change significantly increases the input dimension of the variables to optimize, from $N_{\text{opt}}^{\text{nr}}$ to $3MN_{\text{opt}}^{\text{nr}}$.

2. **Number of evaluation points:** given the greater degree of freedom introduced by NR in the flexibility of beamforming coverage signals across multiple directions using different SSB beams permits us to concentrate solely on AH coverage beam optimization while assuming continuous coverage on the ground from the remaining beams. Therefore, this condition allows us to drastically reduce the number of considered evaluation points, passing now from $N_e = N_g + N_a$ to N_a .
3. **Penalty Function:** within the LTE vertical tilt algorithm, the penalty function was computed over the resulting coverage SINR across multiple random realizations of the network for each optimizer iteration. However, within our proposed NR SSB beam optimization, the penalty function is computed only once over the set of variables for each iteration of the optimizer.
4. **K-Means Algorithm:** The introduced K-mean algorithm for the selection of the activated beams.

Following this, the overall complexity C^{nr} scales as,

$$C^{\text{nr}} \equiv O\left(N_{\text{BS}} + N_{\text{BS}} + N_{\text{iter}}^{\text{nr}} (C_{\text{Forward}}^{\text{nr}} + C_{\text{Back}}^{\text{nr}}) + 2N_{\text{opt}}^{\text{nr}} N_{\text{iter}}^{\text{kmean}}\right), \quad (4.19)$$

with

$$C_{\text{Forward}}^{\text{nr}} \equiv O\left(N_{\text{real}}\left(MN_{\text{BS}}N_a + N_a\right) + 3MN_{\text{opt}}^{\text{nr}}\right), \quad (4.20)$$

where term and term $MN_{\text{BS}}N_a + N_a$ refer to the computation of utility function eq. (4.5) across multiple network realizations, and term $3MN_{\text{opt}}^{\text{nr}}$ to the computation of the penalty function in eq. (4.7). Then, the complexity for the backpropagation scales as the number of inputs:

$$C_{\text{Back}}^{\text{nr}} \equiv O\left(3MN_{\text{opt}}^{\text{nr}}\right). \quad (4.21)$$

Thus, we obtain for C^{nr} ,

$$\begin{aligned} C^{\text{nr}} &\equiv O\left(2N_{\text{BS}} + N_{\text{iter}}^{\text{nr}} \left(N_{\text{real}}\left(N_{\text{BS}}MN_a + N_a\right) + 6MN_{\text{opt}}^{\text{nr}}\right) + 2N_{\text{opt}}^{\text{nr}} N_{\text{iter}}^{\text{kmean}}\right) \\ &\leq O\left(2N_{\text{BS}} + N_{\text{iter}}^{\text{nr}} \left(N_{\text{real}}\left(N_{\text{BS}}MN_a + N_a\right) + 6MN_{\text{BS}}\right) + 2N_{\text{BS}} N_{\text{iter}}^{\text{kmean}}\right) \equiv \\ &\equiv O\left(N_{\text{BS}} + N_{\text{iter}}^{\text{nr}} \left(N_{\text{real}}\left(N_{\text{BS}}MN_a + N_a\right) + MN_{\text{BS}}\right) + N_{\text{BS}} N_{\text{iter}}^{\text{kmean}}\right). \end{aligned} \quad (4.22)$$

Similar to the LTE vertical tilt optimization presented in the previous Chapter 3, it is important to note the linear dependency of the overall time complexity with respect to all variables characterizing the problem. Remarking how increasing the number of network realizations and thereby providing robustness in the solution against random channel effect linearly affect the problem, as well as the dependencies on the number of aerial evaluation points, demonstrated how increasing accuracy in assessing coverage results in linear impact complexity.

4.4 Optimization Setup and Solution

In this section, we adopt models outlined in Chapter 2, and we present and discuss the adopted setup for the AH's enabled NR SSBs beams optimization design and we discuss the obtained results. Here, we illustrate the obtained evolution curve for the introduced utility function here adopted and the resulting activation vector ν^{nr} , thereby showing from which cells the final coverage SSBs beams have been transmitted.

To ensure a fair comparison and to underline how relying on NR networks overpass the limitation of previous LTE generation, here we consider the same network layouts and AH configuration previously explored in Section 3.4. Specifically, we analyze the three urban scenarios discussed in Section 2.1 and represented in Figure 2.2, namely UMa, UMi and URD, as well as the three different AH configuration presented and represented in Section 2.1 and in Figure 2.3, respectively. Finally, for all of these scenarios, we considered three different altitudes for the AHs: 50 m, 100 m, and 150 m. Similarly, considering the set of evaluation points previously remarked, in the following, we focus only on those building AHs. Thus, to accurately analyze those, the set of aerial evaluation points \mathcal{E}_a is defined by a sequence of consecutive located aerial evaluation points with IHD of 1 m; then, it should be noted that with both UMa and URD scenarios, we deploy AHs of total lengths 1250 m, while, within the UMi one, those are scaled down (to maintain proportion within the surrounding environment) and AHs of total length 500 m are considered.

Then, after an extensive search for the optimal hyper-parameters, we set the total number of iterations $N_{\text{iter}}^{\text{nr}}$ to 10000 and the initial value of the ADAM learning rate μ^{nr} to 0.001, with a decay of the 75% every 3000 iterations. Then, we set the total number of iterations $N_{\text{iter}}^{\text{kmean}}$ to 300 and the penalty factor λ^{nr} to 10^6 . To achieve a reliable and consistent solution across different environmental channel conditions, we adopt, at each iteration, $N_{\text{real}}=100$ realizations for the random variables characterizing the network. Finally, Table 4.1 and Table 4.2 summarize the network layout and the optimization parameters, respectively.

By analyzing the obtained curves, illustrated in Figure 4.3, 4.4 and 4.5, for the evolution of the utility function during the optimization process, we can note that

within all the considered scenarios, all the optimization processes effectively converge in [3000, 4000] iterations. Specifically, considering an UMa scenario characterized by N_a equal to 1250, and other values specified in Table 4.1, each iteration takes an average of 2.6 sec on a PC with an 11th Gen Intel(R) Core(TM) i7-1165G7 @ 2.80GHz, 2803 MHz, 4 cores, 8 logical processor; therefore resulting, considering 4k iterations, in a total converge time of approximately 2 h 53 min.

Considering Figures 4.3 and 4.5a and observing the final values for the utility function, we can note that in all the considered macro scenarios (i.e., UMa and URD), there is a clear trend between the final utility function value and the operating altitude. This trend suggests that the higher the altitude, the better it is in terms of final AH coverage. The main reason for this trend stands in the channel condition perceived at different altitudes. Within UMa and URD scenarios, according to the adopted 3GPP models (see Appendix B), above 100 m the LoS probability results equal to one and the channel reaches more static characteristics; in more detail, this channel condition permits to have better propagation, and most importantly, the standard deviation characterizing the network random variables decrease as the altitude increase, and consequently the less dynamicity in the channels allows the optimizer to achieve more precise solutions for coverage beams configuration, ultimately resulting in improved performance across the AH. On the other hand, in the UMi scenario, the dynamicity does not diminish with higher altitudes, as in macro scenarios. This leads to comparable performance across the considered altitudes.

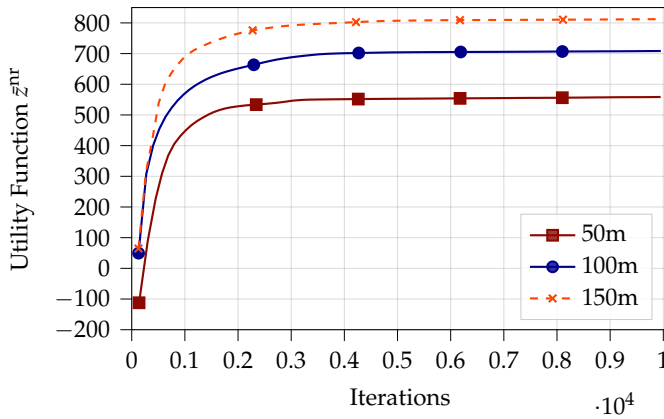
Finally, analyzing the obtained values for the activation vector \mathbf{v}^{nr} in each scenario, and represented in Figure 4.3, 4.4 and 4.5, we observe that, as expected, the majority of the values tend toward very low magnitudes. This highlights, as previously discussed that the final solution requires only a few active beams displaced along the AH to achieve optimal coverage.

TABLE 4.1: NR coverage SSB beams optimization network layout and evaluation point configuration summary.

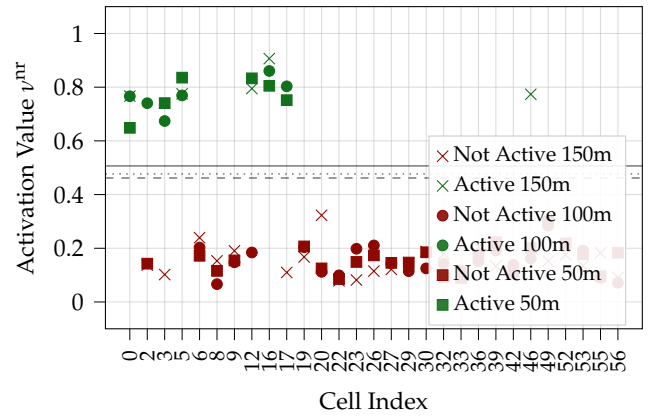
Network Layout	AH Altitude	AH Configuration	IHD	N_a	N_{BS}	$M_h \times M_v$
UMa	50m, 100m, 150m	Curved, Straight Centre, Straight Edge	1	1250	57	8×4
URD	50m, 100m, 150m	Curved, Straight Centre, Straight Edge	1	1250	57	8×4
UMi	50m, 100m, 150m	Curved, Straight Centre, Straight Edge	1	500	57	8×4

TABLE 4.2: NR coverage SSB beams optimization hyperparameters summary.

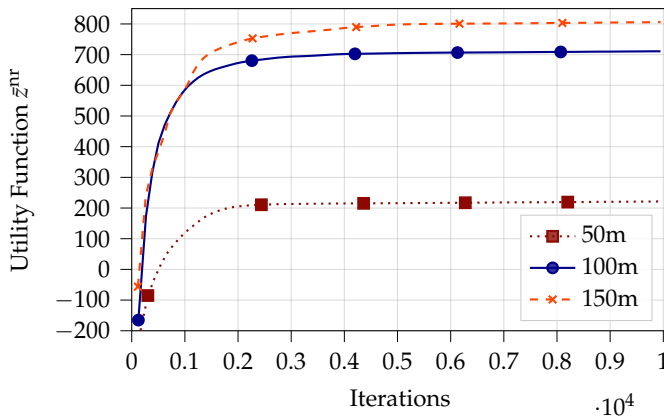
λ^{nr}	$^{(0)}\mu^{nr}$	N_{iter}^{nr}	N_{real}	$\mu_{\%}^{nr}$	N_{μ}^{nr}	N_{iter}^{kmean}
10^6	0.001	10000	100	75%	3000	300



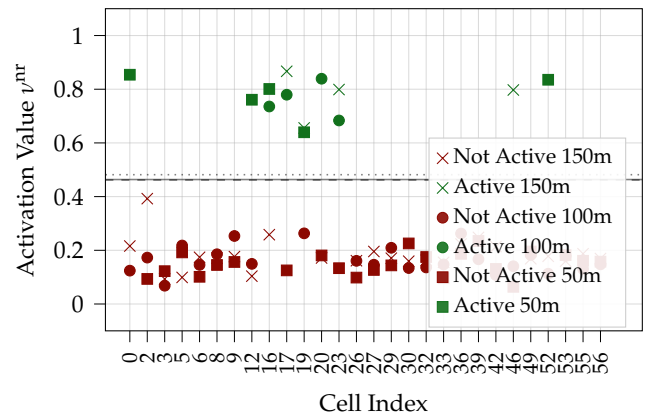
(a) Utility Function evolution for a Curved aerial highway.



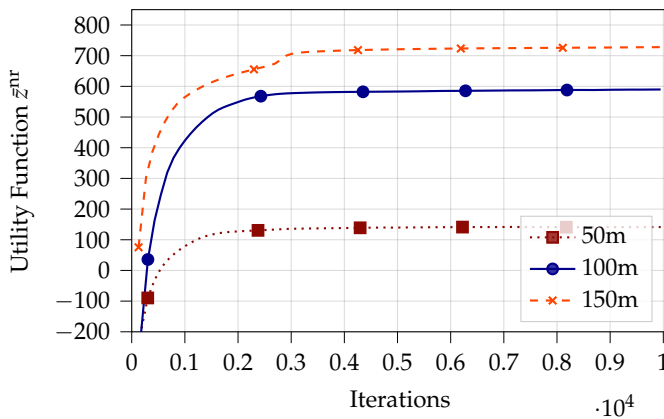
(b) Obtained Vertical Tilt Network Configuration for a Curved aerial highway.



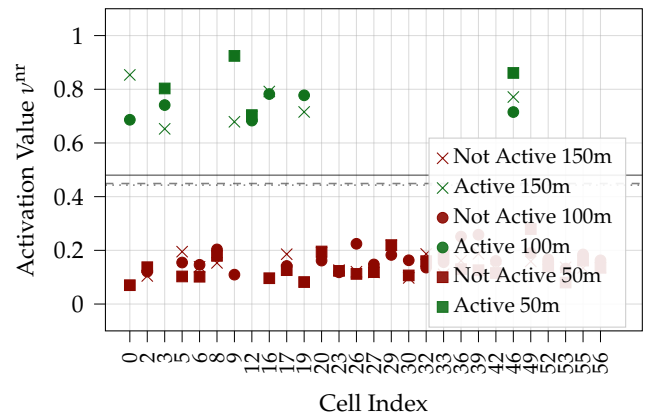
(c) Utility Function evolution for a Straight Centre aerial highway.



(d) Obtained Vertical Tilt Network Configuration for a Straight Centre aerial highway.

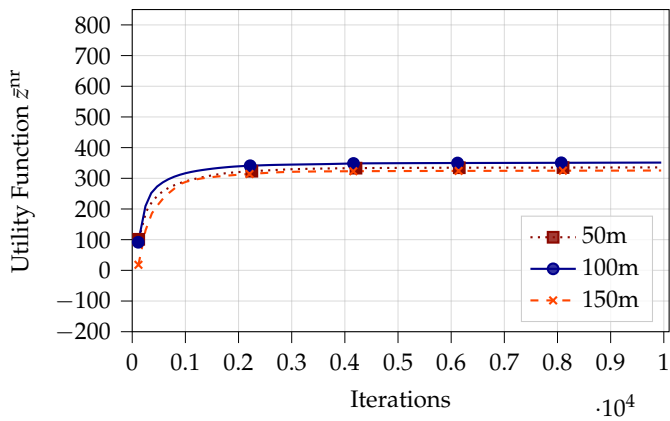


(e) Utility Function evolution for a Straight Edge aerial highway.

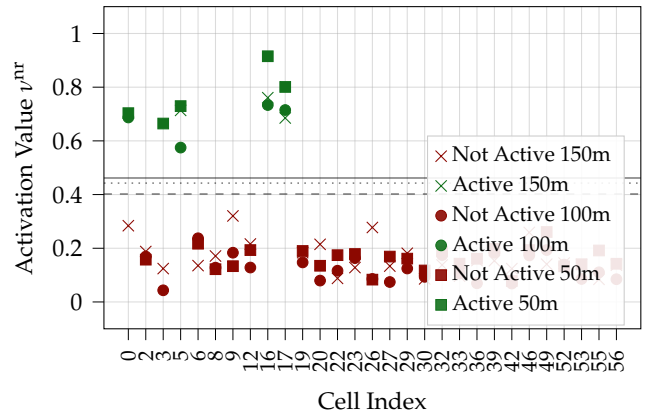


(f) Obtained Vertical Tilt Network Configuration for a Straight Edge aerial highway.

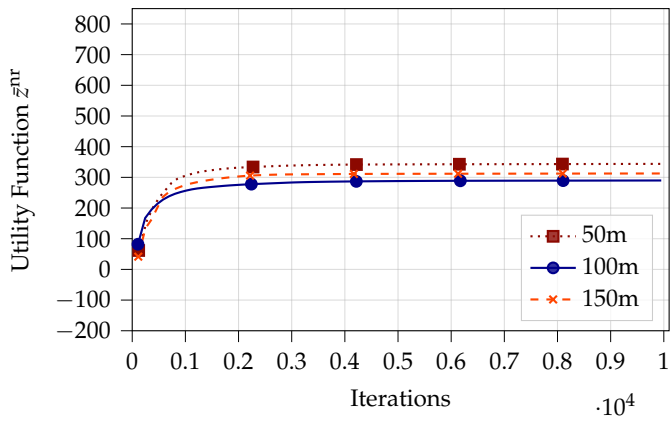
FIGURE 4.3: NR coverage SSB beam optimization ADAM utility function evolution (left column) and obtained activation values μ^{nr} for optimized network cells (right column), considering different configurations for a 1250 m aerial highway at different altitudes in a UMA scenario.



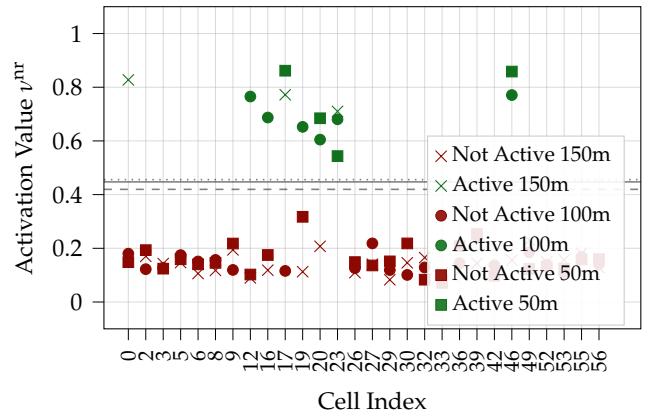
(a) Utility Function evolution for a Curved aerial highway.



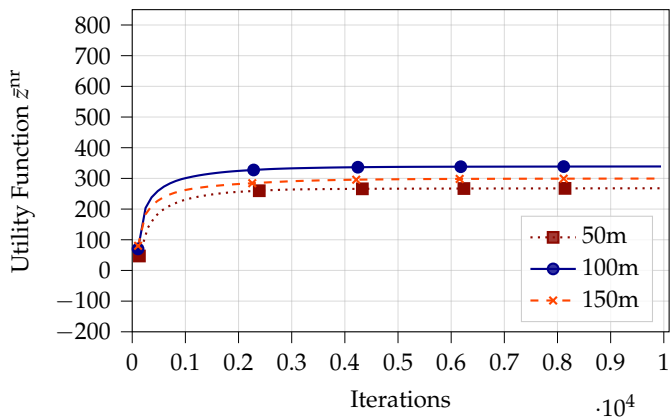
(b) Obtained Vertical Tilt Network Configuration for a Curved aerial highway.



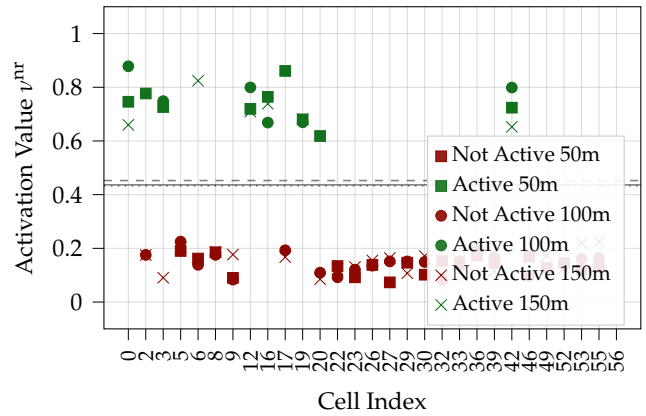
(c) Utility Function evolution for a Straight Centre aerial highway.



(d) Obtained Vertical Tilt Network Configuration for a Straight Centre aerial highway.

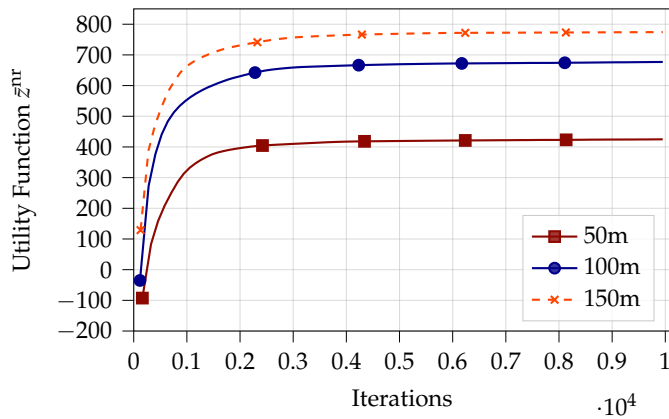


(e) Utility Function evolution for a Straight Edge aerial highway.

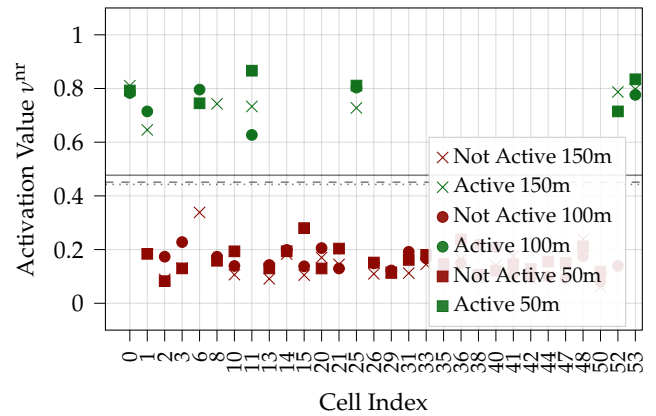


(f) Obtained Vertical Tilt Network Configuration for a Straight Edge aerial highway.

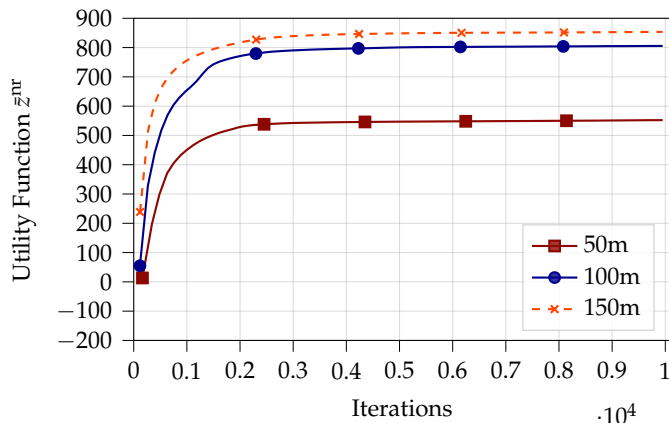
FIGURE 4.4: NR coverage SSB beam optimization ADAM utility function evolution (left column) and obtained activation values μ^{nr} for optimized network cells (right column), considering different configurations for a 500m aerial highway at different altitudes in a UMi scenario.



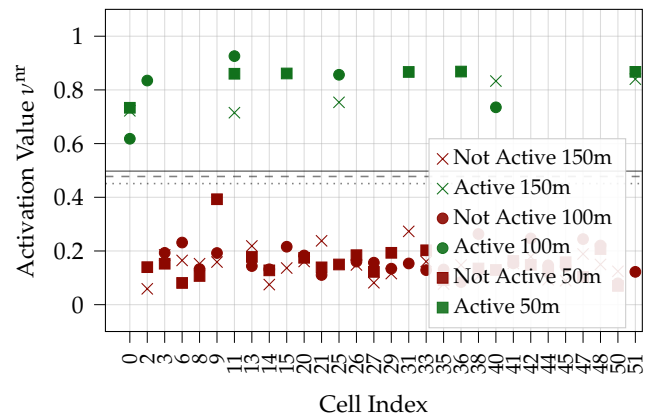
(a) Utility Function evolution for a Curved aerial highway.



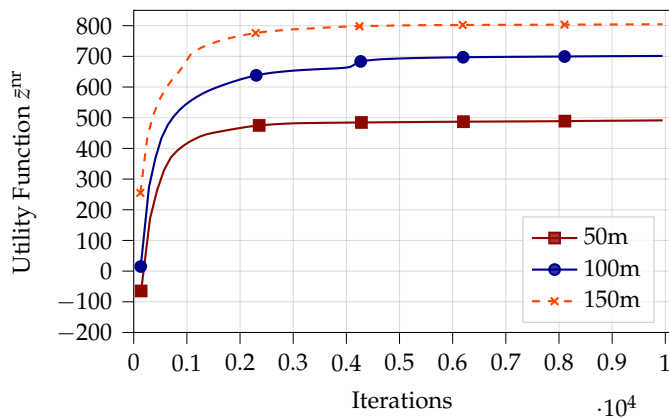
(b) Obtained Vertical Tilt Network Configuration for a Curved aerial highway.



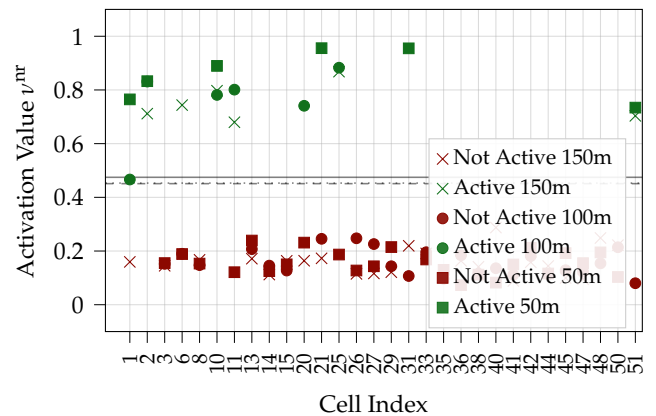
(c) Utility Function evolution for a Straight Centre aerial highway.



(d) Obtained Vertical Tilt Network Configuration for a Straight Centre aerial highway.



(e) Utility Function evolution for a Straight Edge aerial highway.



(f) Obtained Vertical Tilt Network Configuration for a Straight Edge aerial highway.

FIGURE 4.5: NR coverage SSB beam optimization ADAM utility function evolution (left column) and obtained activation values μ^{nr} for optimized network cells (right column), considering different configurations for a 1250 m aerial highway at different altitudes in a URD scenario.

4.5 NR Coverage SINR

Analyzing only the utility function evolution curves during the optimization process is insufficient to fully understand the coverage benefits introduced by our NR SSB beam optimization algorithm. Therefore, in the following sections, to provide a clearer understanding of the algorithm's impact, we further investigate and discuss the results obtained, specifically focusing on CDF of the coverage SINR obtained over the considered AHs. Figures 4.6, 4.7 and 4.8 illustrate the CDFs obtained for the UMa, UMi, and URD scenarios, with each showing results for different aerial highway configurations at various altitudes.

Within each scenario, we report results considering two different configurations for the NR network setup:

1. "Baseline NR": within each network cell $N_{\text{ssb}}=8$ SSB beams are transmitted. Those beams, generated via 2D-DFT precoding, as discussed in Chapter 2, are all downtilted at 105° and evenly spaced in the azimuth plane to cover the cell's designated area, as depicted in Figure 2.8.
2. "Opt NR": following the methodology presented for our proposed NR SSB beam optimization algorithm, each cell transmits $N_{\text{ssb}}=8$ SSB beams as in the previous baseline. However, if one of the cells is identified as one of the designed cells aimed to serve the AH, the SSB with index 4 (most lateral beam in Figure 2.8) is substituted with the one resulting from our optimization process.

Additionally, to further emphasize the improvements compared to the LTE solution discussed in Chapter 3, we include, as a reference, results obtained from the vertical tilt optimization within LTE networks. We refer to those as "Opt LTE".

Figures 4.6, 4.7, and 4.8 present the CDF curves for the SSB coverage SINR in the UMa, UMi, and URD scenarios, respectively. Similarly, Tables 4.3, 4.3, and 4.3 summarize these results and the corresponding gains. Finally, Figure 4.9 provides an overview of the gains achieved across all scenarios. Our obtained resulting CDF for the NR coverage SINR demonstrate significant improvements over the baseline, with average gains of approximately 5 dB at the 5%-tile of the resulting CDF curves, and even higher gains at the mean, reaching up to 10 dB in the UMa and URD network layouts, and up to 14 dB in the UMi scenario. Additionally, our SSB beam optimization solution consistently outperforms the previous-generation LTE optimization at higher altitudes, yielding gains of up to 10 dB. For the sake of clarity, two types of gains are reported in these tables and figures:

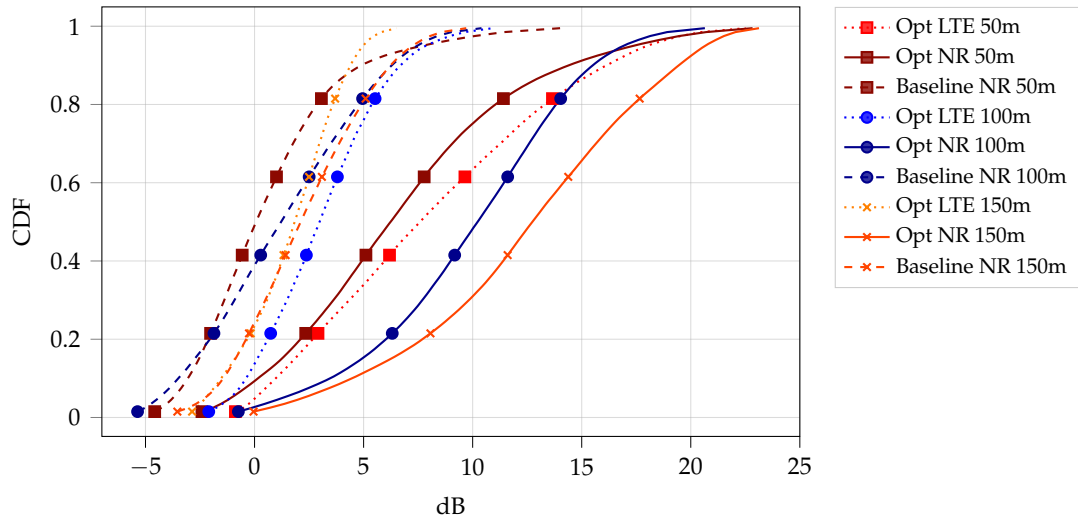
- "Gain NR", which compares "Opt NR" to "Baseline NR".
- "Gain NR-LTE", quantifying the improvements of "Opt NR" over "Opt LTE".

Similarly to the obtained result presented in the previous Chapter 3, the obtained coverage NR SINR CDF curves in Figures 4.6, 4.7, and 4.8 exhibit distinct trends between altitudes and performance; precisely, considering "Baseline NR", as it was

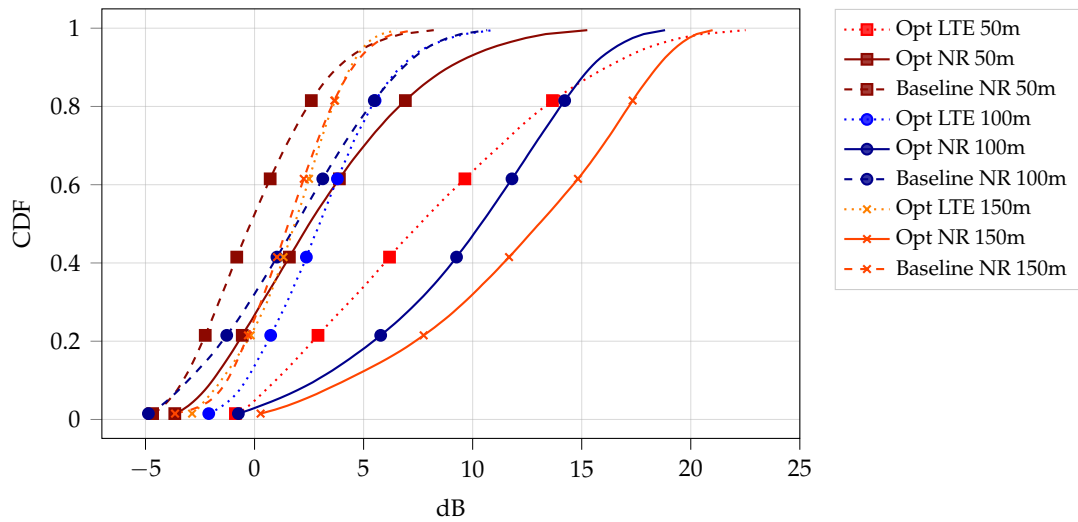
within LTE networks, the higher the altitude, the lower the performance. However, in the NR optimized scenario, for both UMa and URD layouts, the trend reverses; specifically, here, the higher the altitude, the better it is. This trend inversion is mainly caused by a combination of different factors, such as the only focus on aerial points, the higher achieved directivity, the reduced interference perceived by the surrounding ground-directed coverage beams, and most importantly, the joint design of the beams directed towards the AH permits to minimize the interference that they may generate. It should be emphasized that the capability of serving high power while controlling the introduced interference is the key to overcoming the limitation discussed within previous Chapter 3.

In the UMi network layout, with results depicted in Figure 4.7, we observe consistent gains across various altitudes, with no significant disparities or trends between altitude and performance. This is not the result of a single factor but rather a combination of multiple elements, including lower sectors' height, increased network densification, and different channel characteristics. As early anticipated, channels within UMi do not behave as in macro scenarios; precisely in UMi LoS conditions are not predominant, thereby resulting in more channel dynamicity regardless of the actual altitude; as a consequence there are no notable gaps in the results obtained at different heights.

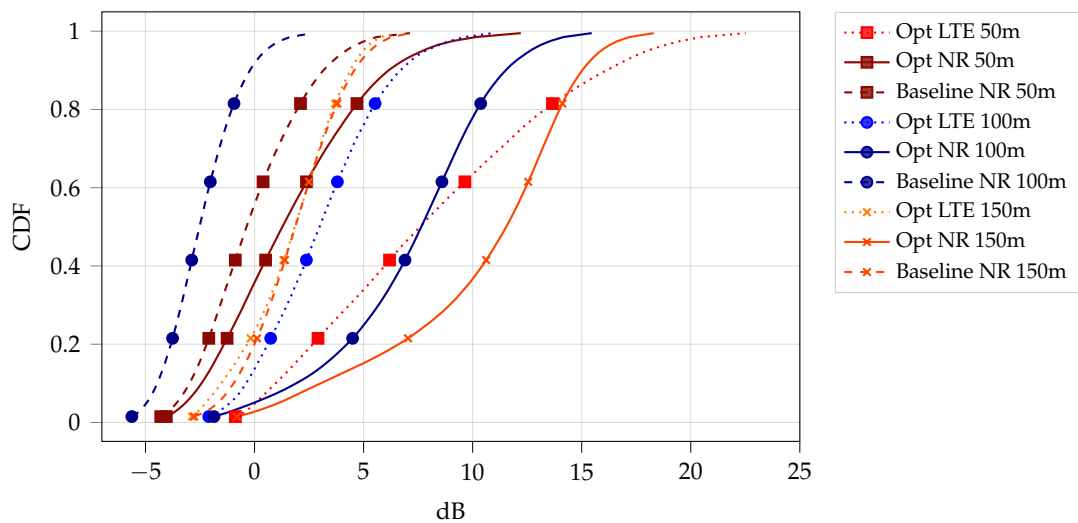
In the above consideration, it is important to emphasize a key aspect achieved by our proposed solution. By grouping all the obtained results by different altitudes, we can note how our proposed solution, regardless of the network layout and the AHs, brings NR coverage SINR performance working within the same range of values. As illustrated in Figure 4.10, all the obtained 5%-tile and mean values are concentrated over specific intervals, with those intervals reducing with increased altitudes. Therefore, these results suggest that network operators which aim to integrate and support AHs using our proposed NR coverage solution can achieve consistent and predictable SINR performance across various network layouts and AH configurations, particularly at high altitudes.



(a) Curved AH.



(b) Straight Centre AH.

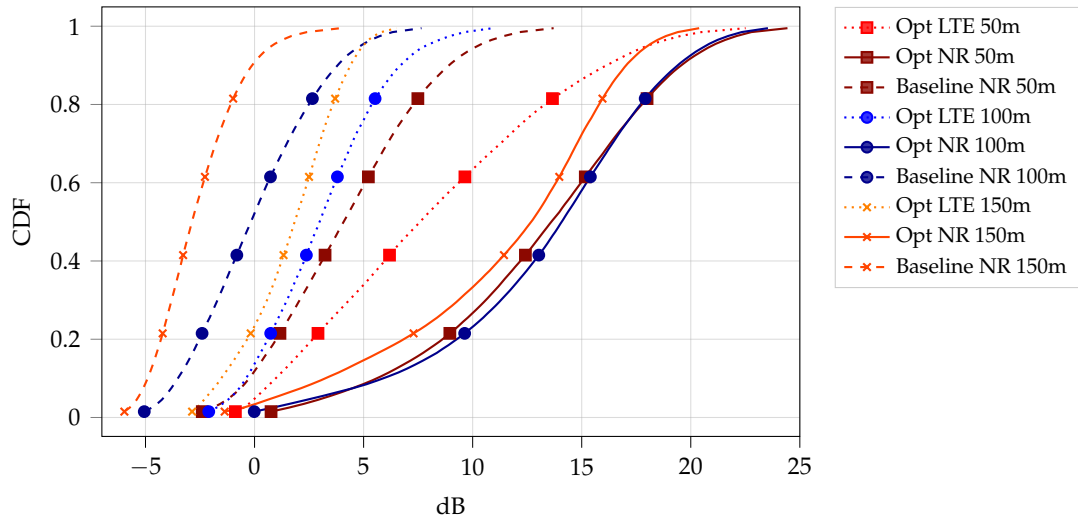


(c) Straight Edge AH.

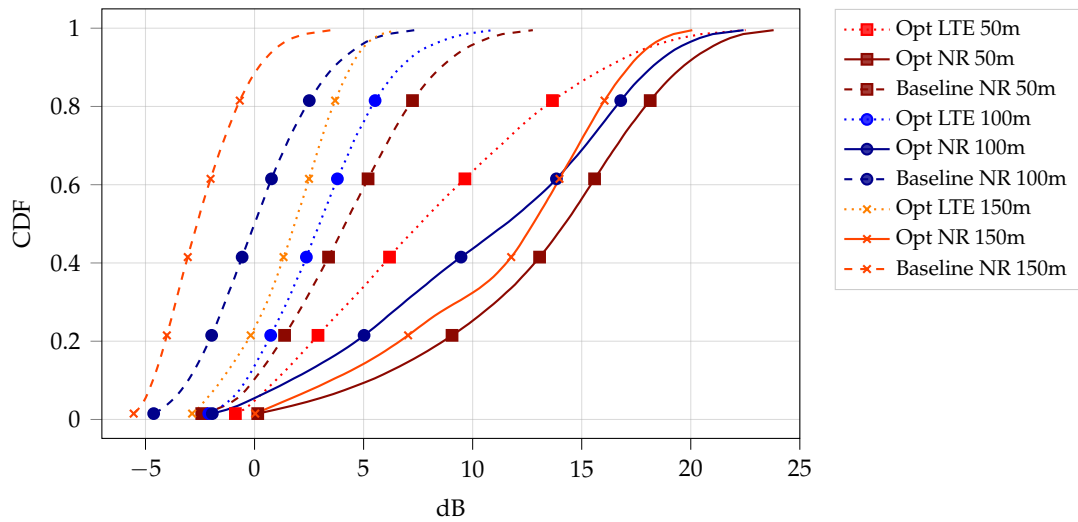
FIGURE 4.6: NR coverage SSB beams optimization SINR CDFs of aerial highway evaluation points, considering different configurations for a 1250 m aerial highway at different altitudes in a Uma scenario.

TABLE 4.3: Summary of NR coverage SINR statistics, considering different configurations for a 1250 m aerial highway at different altitudes in a UMa scenario.

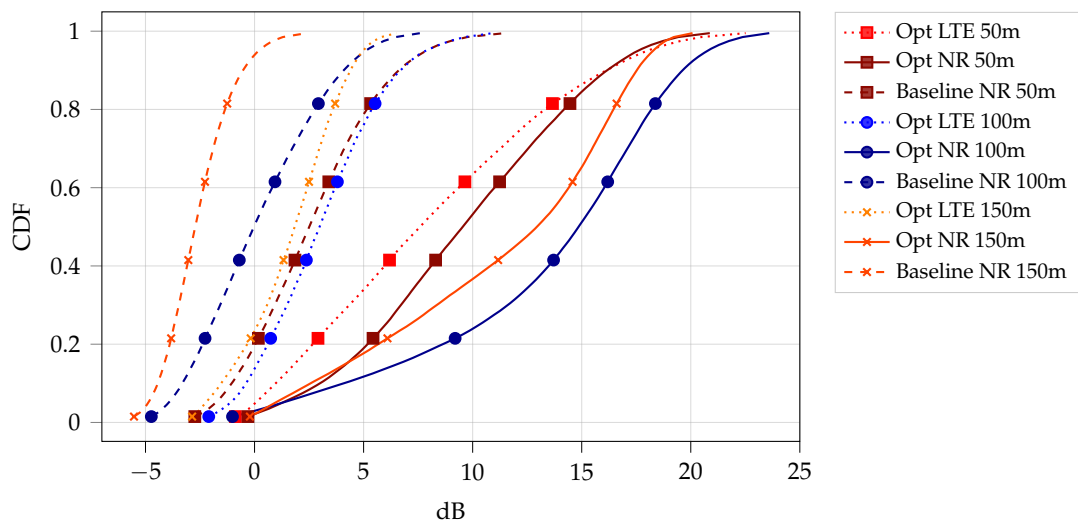
		UMa SSB Cov. SINR Statistics				
				Aerial		
		Opt LTE	Baseline NR	Opt NR	Gain NR	Gain NR-LTE
		[dB]	[dB]	[dB]	[dB]	[dB]
		Curved				
50m	5%-tile	0.04	-3.74	-1.08	2.66	-1.12
	Mean	8.13	0.66	6.82	6.16	-1.31
100m	5%-tile	-1.12	-4.40	1.28	5.68	2.40
	Mean	3.09	1.35	9.88	8.53	6.79
150m	5%-tile	-2.24	-2.27	2.22	4.49	4.46
	Mean	1.66	2.26	12.38	10.12	10.72
		Straight Centre				
50m	5%-tile	0.15	-3.92	-2.71	1.21	-2.86
	Mean	7.29	0.09	3.07	2.98	-4.22
100m	5%-tile	-1.55	-3.96	0.97	4.93	2.52
	Mean	2.72	1.94	9.76	7.82	7.04
150m	5%-tile	0.02	-1.99	2.19	4.18	2.17
	Mean	3.03	1.56	12.21	10.65	9.18
		Straight Edge				
50m	5%-tile	-0.54	-3.57	-3.17	0.40	-2.63
	Mean	4.21	-0.10	1.64	1.74	-2.57
100m	5%-tile	0.07	-4.95	-0.04	4.91	-0.11
	Mean	5.46	-2.41	7.18	9.59	1.72
150m	5%-tile	-2.65	-1.69	1.11	2.80	3.76
	Mean	0.08	1.84	10.34	8.50	10.26



(a) Curved AH.



(b) Straight Centre AH.

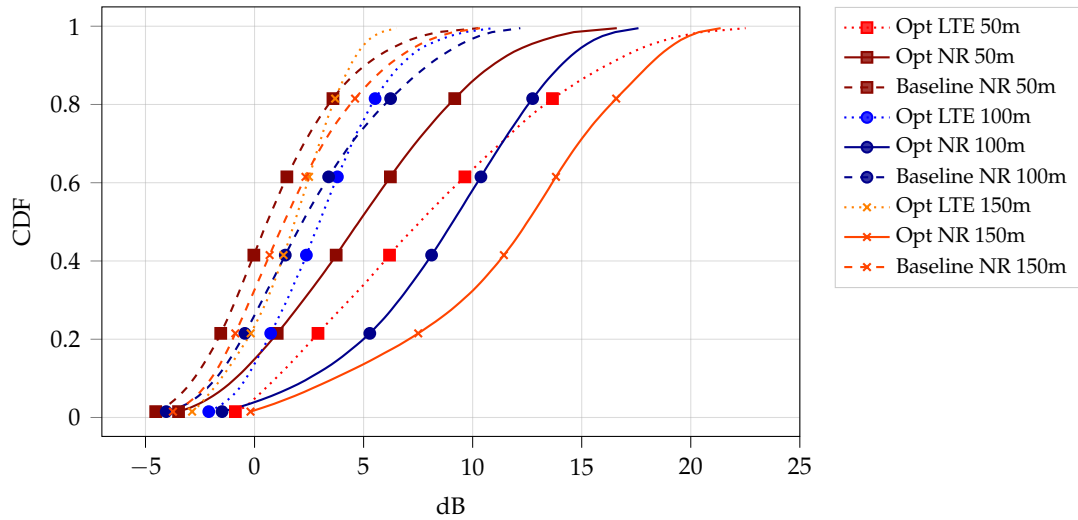


(c) Straight Edge AH.

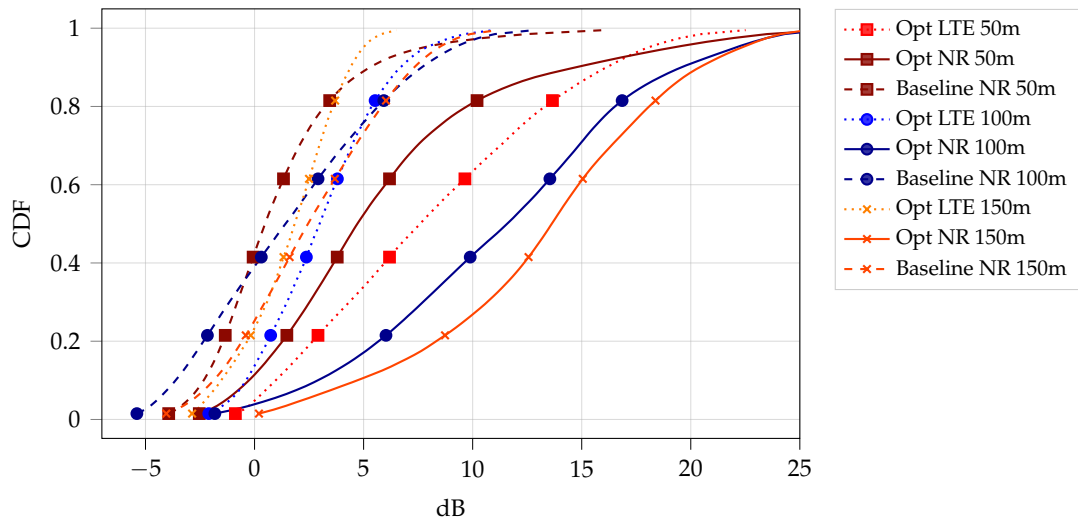
FIGURE 4.7: NR coverage SSB beams optimization SINR CDFs of aerial highway evaluation points, considering different configurations for a 500 m aerial highway at different altitudes in a UMi scenario.

TABLE 4.4: Summary of NR coverage SINR statistics, considering different configurations for a 500 m aerial highway at different altitudes in a UMi scenario.

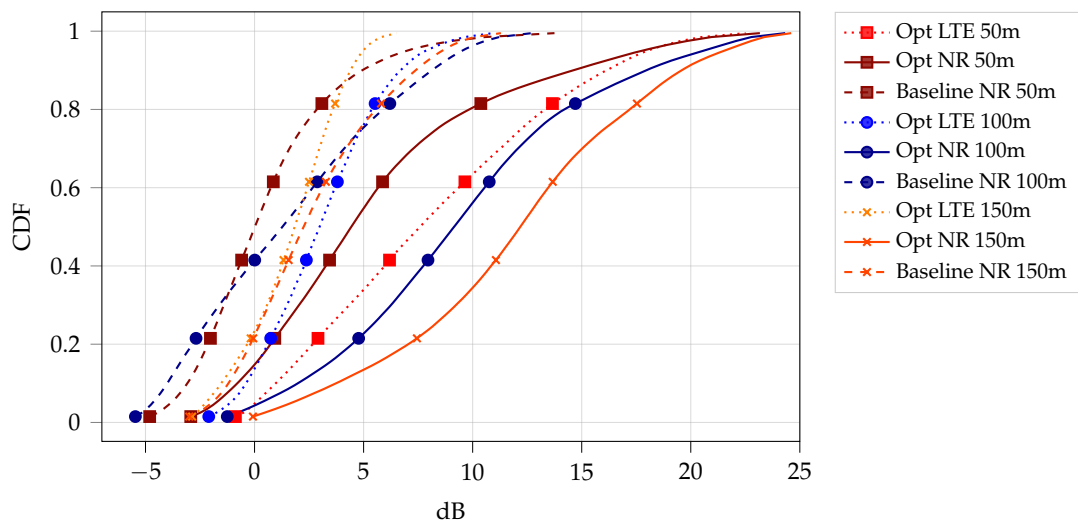
		UMi SSB Cov. SINR Statistics				
				Aerial		
		Opt LTE	Baseline NR	Opt NR	Gain NR	Gain NR-LTE
		[dB]	[dB]	[dB]	[dB]	[dB]
		Curved				
50m	5%-tile	-3.27	-1.16	3.22	4.38	6.49
	Mean	1.28	4.22	13.10	8.88	11.82
100m	5%-tile	-3.27	-4.17	2.74	6.91	6.01
	Mean	0.90	0.02	13.32	13.30	12.42
150m	5%-tile	-9.18	-5.35	0.86	6.21	10.04
	Mean	-1.73	-2.64	11.36	14.00	13.09
		Straight Centre				
50m	5%-tile	-2.63	-0.89	2.73	3.62	5.36
	Mean	1.29	4.21	13.29	9.08	12.00
100m	5%-tile	-7.31	-3.75	-0.18	3.57	7.13
	Mean	-0.28	0.17	13.42	13.25	13.70
150m	5%-tile	-4.11	-5.04	1.51	6.55	5.62
	Mean	-0.88	-2.40	11.51	13.91	12.39
		Straight Edge				
50m	5%-tile	-2.23	-1.80	1.25	3.05	3.48
	Mean	1.81	2.68	9.59	6.91	7.78
100m	5%-tile	-4.09	-3.94	1.24	5.18	5.33
	Mean	0.11	-3.75	13.42	17.17	13.31
150m	5%-tile	-10	-4.88	0.92	5.80	10.92
	Mean	-3.69	-2.59	11.37	13.96	15.06



(a) Curved AH.



(b) Straight Centre AH.

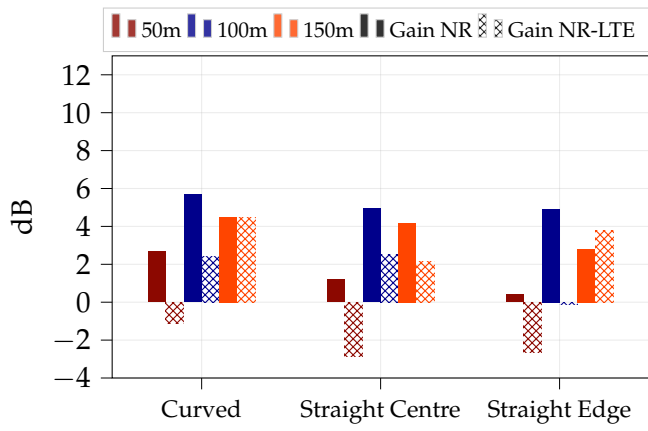


(c) Straight Edge AH.

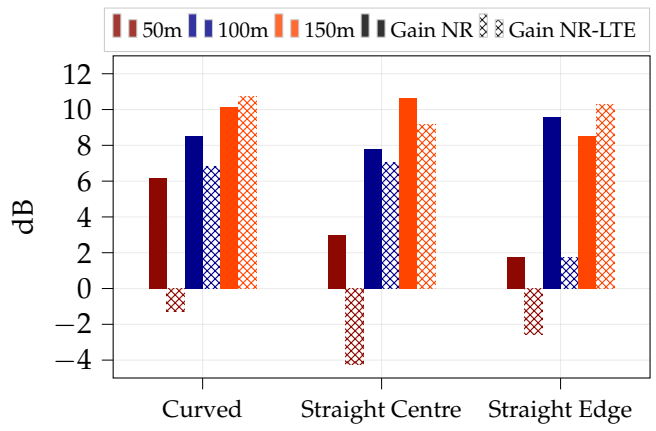
FIGURE 4.8: NR coverage SSB beams optimization SINR CDFs of aerial highway evaluation points, considering different configurations for a 1250 m aerial highway at different altitudes in a URD scenario.

TABLE 4.5: Summary of NR coverage SINR statistics, considering different configurations for a 1250 m aerial highway at different altitudes in a URD scenario.

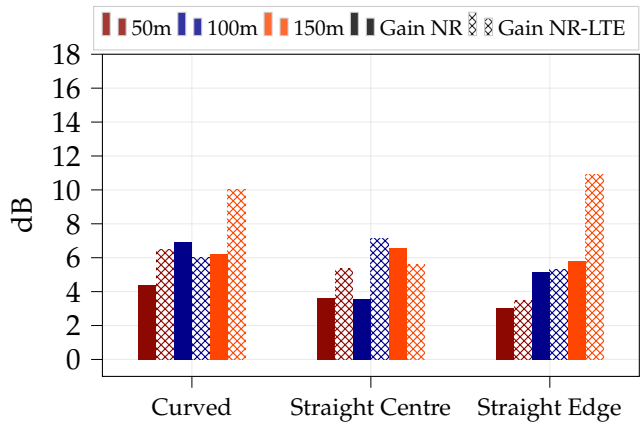
		URD SSB Cov. SINR Statistics				
				Aerial		
		Opt LTE	Baseline NR	Opt NR	Gain NR	Gain NR-LTE
		[dB]	[dB]	[dB]	[dB]	[dB]
		Curved				
50m	5%-tile	-0.46	-3.57	-2.05	1.52	-1.59
	Mean	6.85	0.91	4.93	4.02	-1.92
100m	5%-tile	-1.45	-2.69	0.55	3.24	2.00
	Mean	2.35	2.65	8.68	6.03	6.33
150m	5%-tile	-2.21	-2.77	1.60	4.37	3.81
	Mean	0.61	1.72	11.70	9.98	11.09
		Straight Centre				
50m	5%-tile	-1.82	-3.05	-1.31	1.74	0.51
	Mean	6.20	1.14	6.01	4.87	-0.19
100m	5%-tile	-2.70	-4.46	0.66	5.12	3.36
	Mean	1.65	1.74	11.31	9.57	9.66
150m	5%-tile	-2.18	-2.85	2.24	5.09	4.42
	Mean	0.70	2.62	13.16	10.54	12.46
		Straight Edge				
50m	5%-tile	-2.34	-3.84	0.55	4.39	2.89
	Mean	4.43	-1.78	5.60	7.38	1.17
100m	5%-tile	-1.71	-4.67	0.27	4.94	1.98
	Mean	1.90	1.62	9.52	7.90	7.62
150m	5%-tile	-2.42	-1.97	1.69	3.66	4.11
	Mean	0.53	2.67	12.00	9.33	11.47



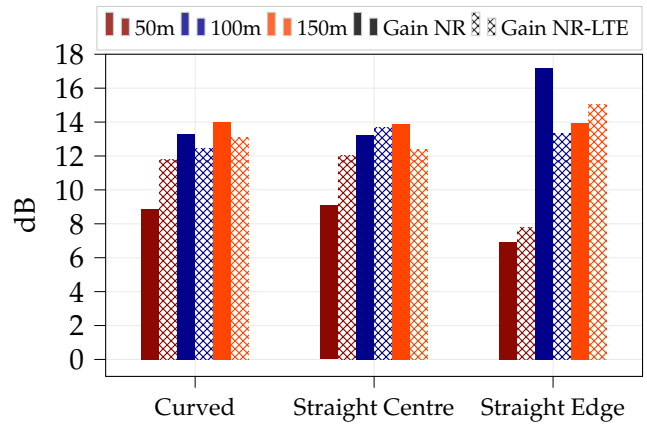
(a) UMa, gains at 5%-tile.



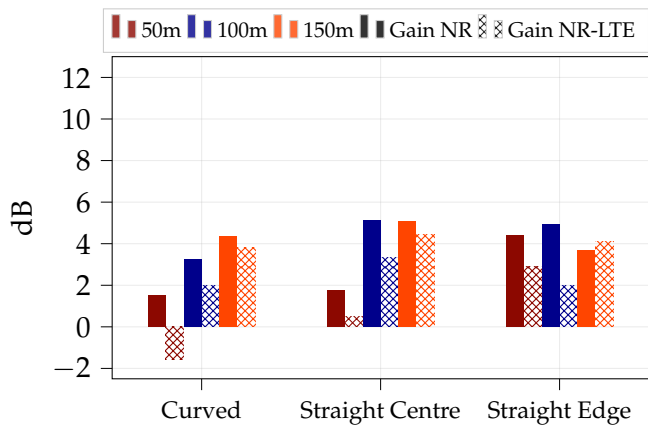
(b) UMa, gains at mean.



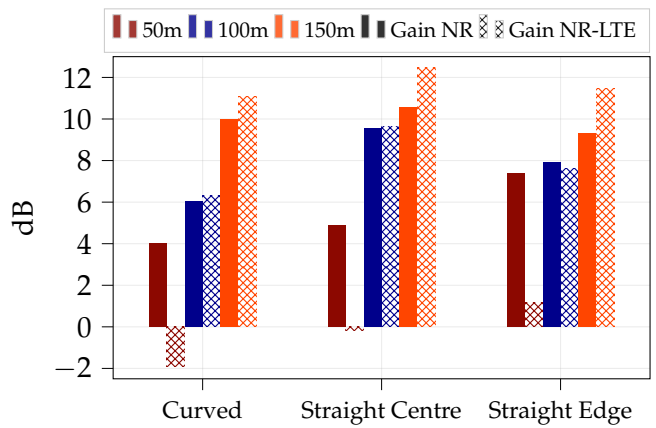
(c) UMi, gains at 5%-tile.



(d) UMi, gains at mean.

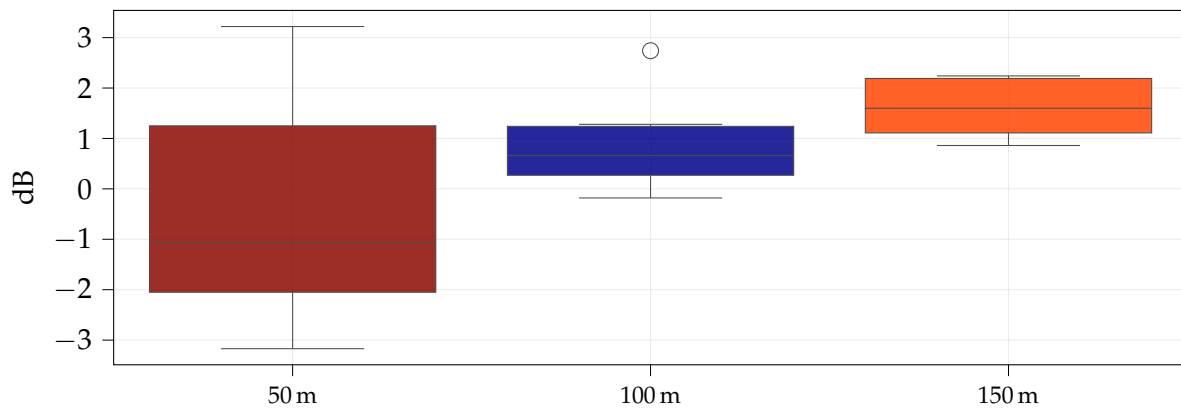


(e) URD, gains at 5%-tile.

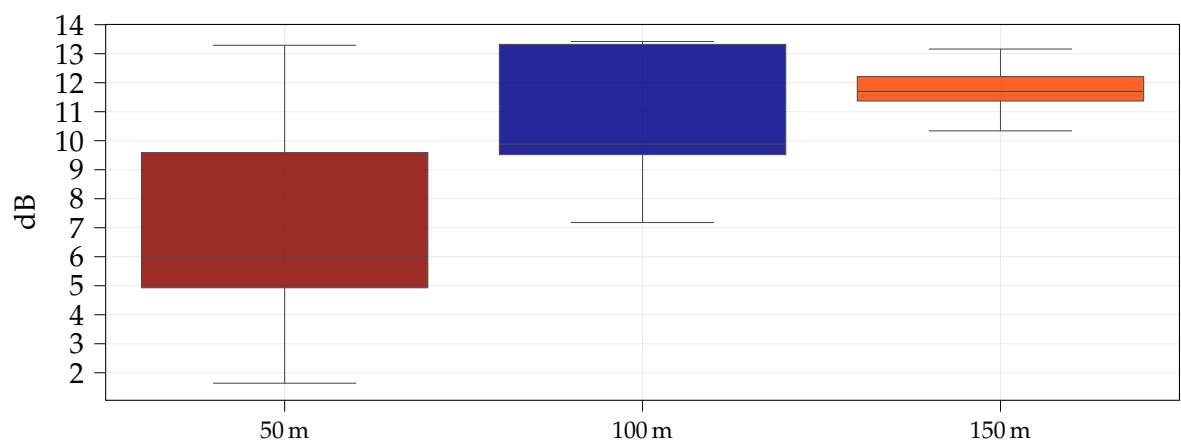


(f) URD, gains at mean.

FIGURE 4.9: NR coverage SSB beams optimization summary of gains for the 5%-tile (left column) and mean value (right column) of NR coverage SINR, considering different configurations for aerial highways at different altitudes in different network layouts.



(a) 5%-tile NR Coverage SINR.



(b) Mean NR Coverage SINR.

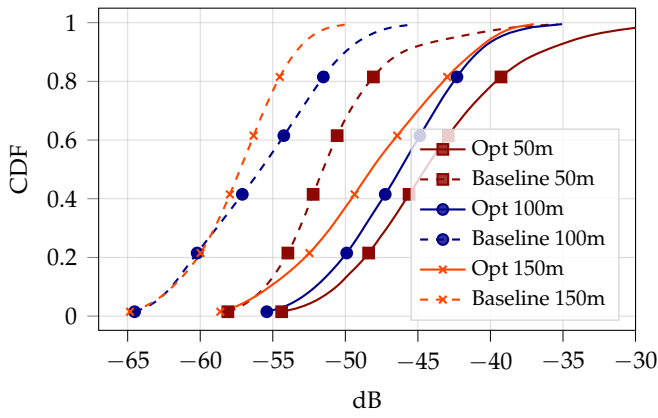
FIGURE 4.10: Distribution of the obtained NR SSB beams coverage SINR 5%-tile and mean values at different altitudes considering all network layouts and all aerial highways configurations.

4.5.1 Coverage Serving Power and Interference

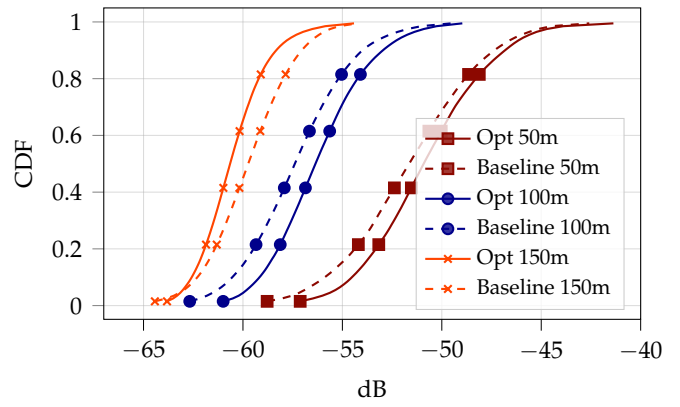
In the following, to clarify the origin of the SINR gains introduced by our proposed solution, we present and discuss the distribution of the resulting serving power and interference perceived along the AH. Specifically, Figure 4.11, 4.12 and 4.13 shows, respectively for UMa, UMi and URD networks layout, the obtained CDF for the serving power (left column) for different AH configurations at different altitudes as well as the resulting interference (right column)

Analyzing the obtained curves in Figure 4.11, 4.12 and 4.13, we observe that the significant improvements in the final SINRs across all scenarios are mainly driven by the substantial enhancements in the serving power distribution across the AH, with gains up to 10 dB in both 5%-tile and mean value. Crucially, those gains come with almost null cost in terms of additional introduced interference. Furthermore, in a few scenarios, especially those at in 150 m and those in UMi network layout, our solution, while enhancing serving power, even reduces the total overall interference, resulting so in higher gains within the final SINRs.

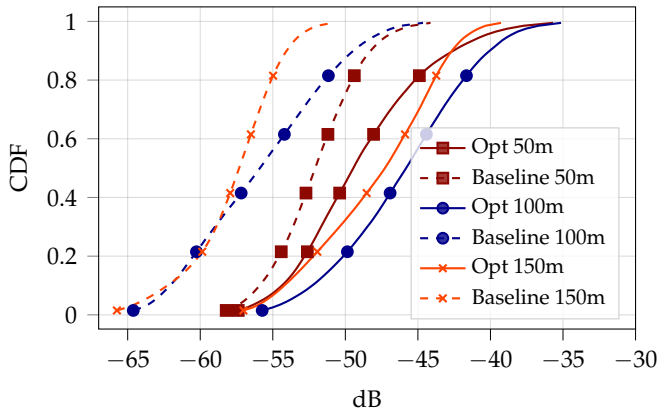
The obtained interference outcomes are crucial to demonstrate the advantages of our proposed solution. By effectively directing high power toward the sky without introducing interference, we show how jointly optimizing the design of NR coverage SSB beams is the key to overcoming the limitations discussed for LTE networks.



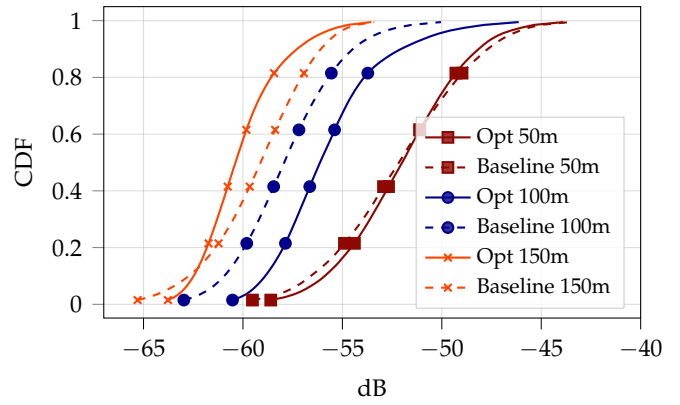
(a) Curved AH, Serving RSRP.



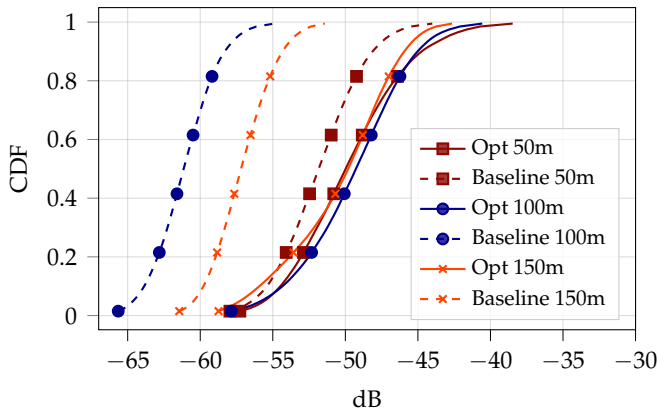
(b) Curved AH, Interference.



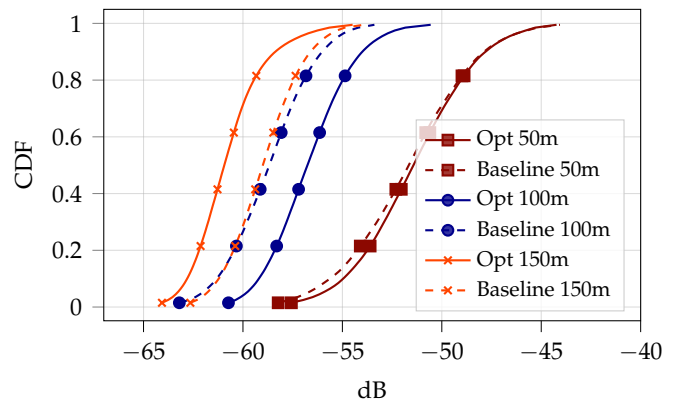
(c) Straight Centre AH, Serving RSRP.



(d) Straight Centre AH, Interference.

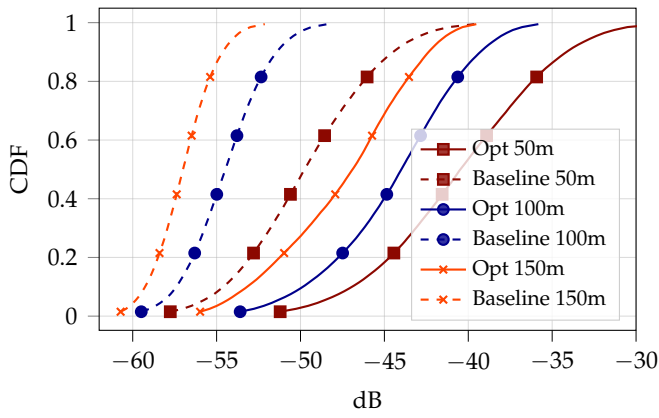


(e) Straight Edge AH, Serving RSRP.

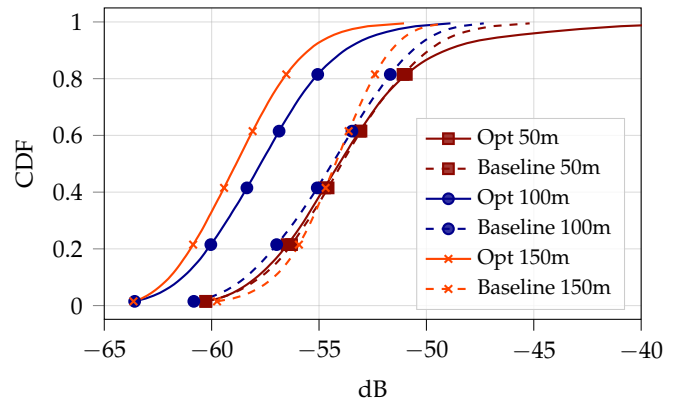


(f) Straight Edge AH, Interference.

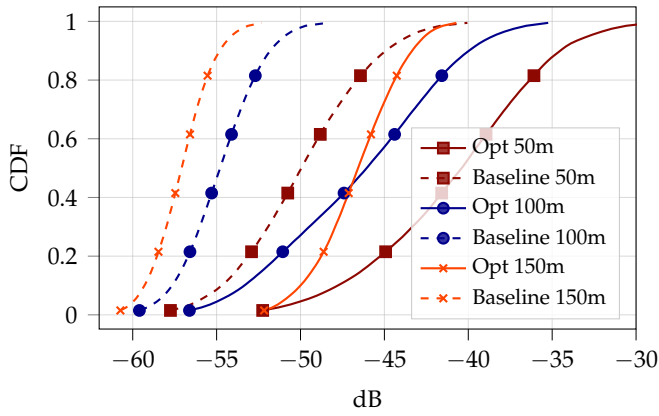
FIGURE 4.11: NR coverage SSB beam optimization serving RSRP and interference CDFs on aerial highway's evaluation points, considering different configurations for a 1250 m aerial highway at different altitudes in a UMa scenario.



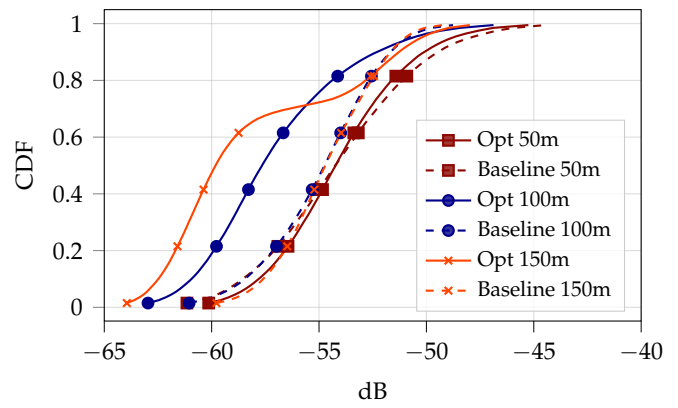
(a) Curved AH, Serving RSRP.



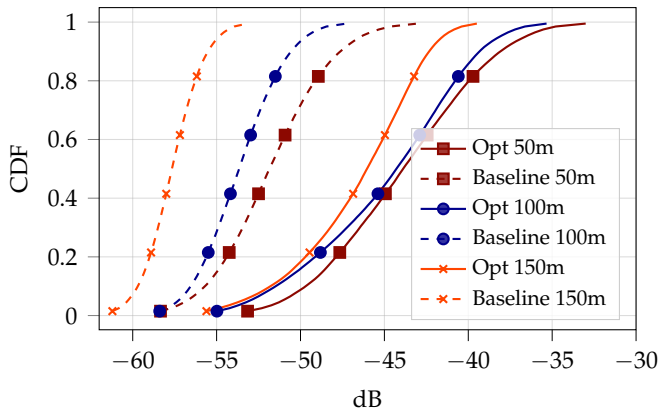
(b) Curved AH, Interference.



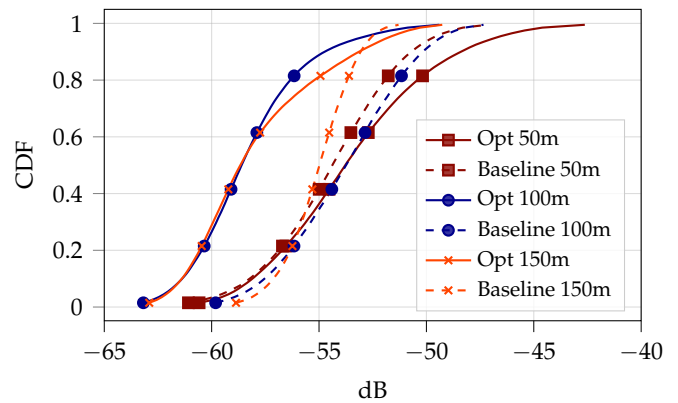
(c) Straight Centre AH, Serving RSRP.



(d) Straight Centre AH, Interference.

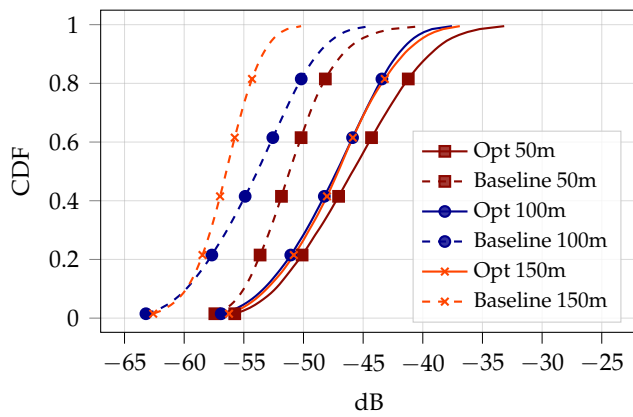


(e) Straight Edge AH, Serving RSRP.

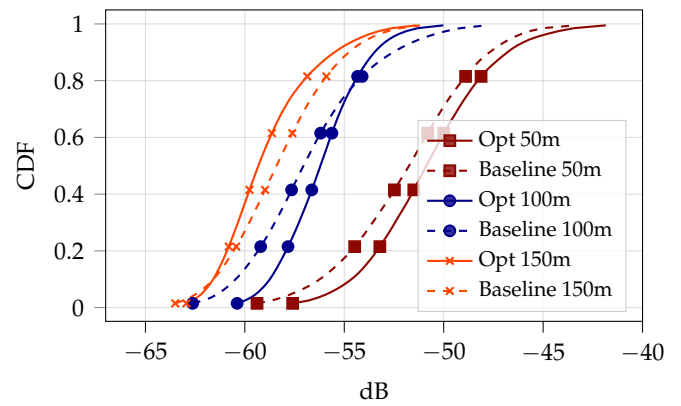


(f) Straight Edge AH, Interference.

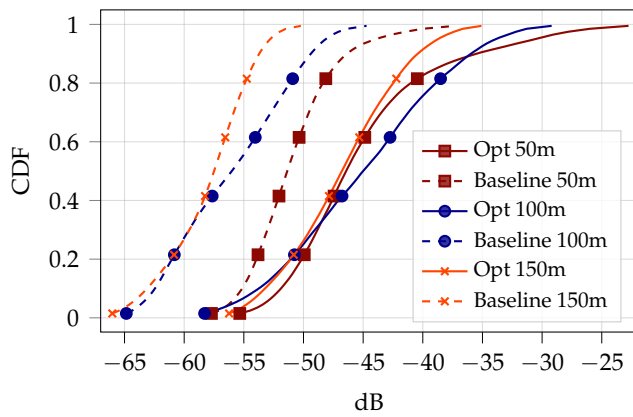
FIGURE 4.12: NR coverage SSB beam optimization serving RSRP and interference CDFs on aerial highway's evaluation points, considering different configurations for a 500 m aerial highway at different altitudes in a UMi scenario.



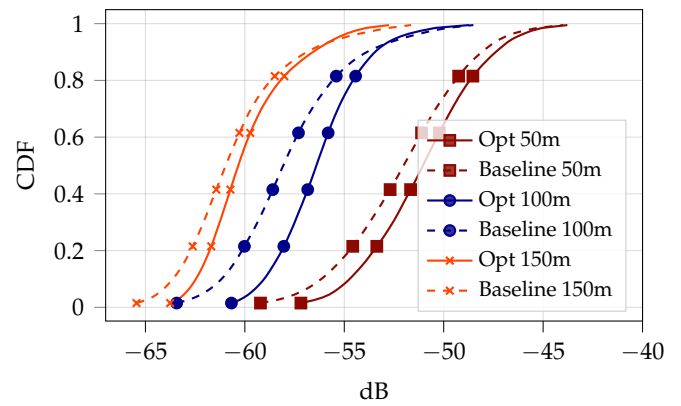
(a) Curved AH, Serving RSRP.



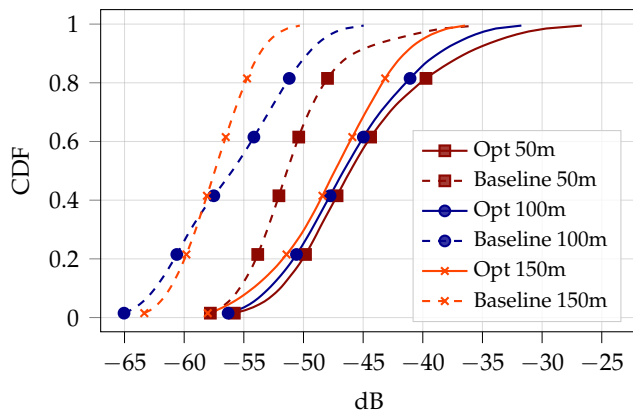
(b) Curved AH, Interference.



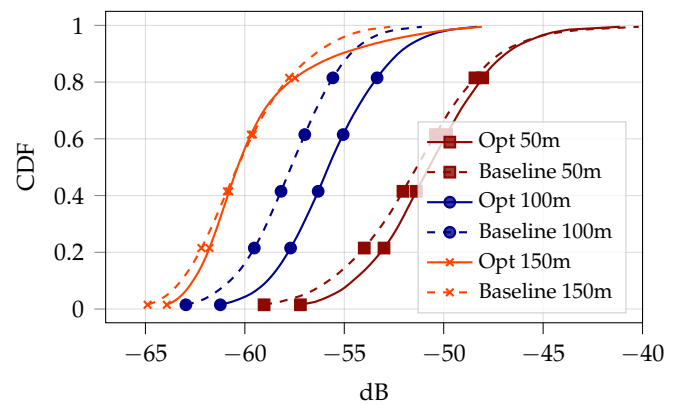
(c) Straight Centre AH, Serving RSRP.



(d) Straight Centre AH, Interference.



(e) Straight Edge AH, Serving RSRP.



(f) Straight Edge AH, Interference.

FIGURE 4.13: NR coverage SSB beam optimization serving RSRP and interference CDFs on aerial highway's evaluation points, considering different configurations for a 1250 m aerial highway at different altitudes in a URD scenario.

4.6 NR Data SINR and Achievable Data Rate

Extending our analysis beyond the coverage aspect, in the following, we discuss obtained performance in terms of final UAVs data SINR and achievable data rate.

However, before delving into these aspects, it is essential to recall from Chapter 2 how data are precoded within the considered networks. 5G NR fully leverages multiple antenna systems' beamforming and multiplexing capabilities also during the UEs data phase transmission; precisely, as outlined in Section 2.6.2, this work focuses on a *Type-I CSI* based precoding scheme.

In this configuration, after the cell association process, each cell illuminates its connected UEs using a different set of beams/codewords, known as CSI-RS beams, different from those used for SSB coverage; specifically, these CSI-RS beams are generated via 2D-DFT precoding [75]. Then, each UE measures the received power from each of those and reports back to its serving cell an index representing the strongest received beam. Finally, each cell will use this reported beam as precoder for the UE data transmission.

This distinction between the beams used for coverage and those used for data transmission, according to our system-level analysis, allows for a clear decoupling between the coverage phase and the data transmission phase. This condition poses an important limitation to the work conducted in this chapter, highlighting how focusing solely on coverage aspects may not automatically imply benefits regarding final data communication performances.

To support those considerations, we present in the following as an example the result obtained by considering a *Curved* AH located at 150 m within the URD network layout (see Figures 2.2 and 2.3).

Then, according to what is described in Chapter 2, Section 2.1, a total of 228 gUEs, averaging four per cell, are evenly distributed across the network. Additionally, 12 flying UAVs are positioned along the previously mentioned AHs, maintaining a minimum inter-UAV distance of 100 meters [77, 78]; then, a total of 1000 network realizations N_{real} are considered. Within each iteration, all the random variables characterizing the network are updated, as well as the position of the gUEs randomly changes and the UAVs all together move along the AH while maintaining the same inter-distance. Moreover, we recall that, to maintain consistent UAVs traffic conditions when one exits the AH, a new one starts his flight.

Figure 4.14 show the obtained UAVs data SINR (left column) and achievable data rate (right column) obtained when considering the NR network configured as in "NR Baseline" (i.e., all the SSB beams downtilted at 105°) and as result of our coverage SSB beam optimization process, labelled here as "NR Cov Opt" to emphasize the optimization's focused on coverage enhancement. Here, we remark that the optimized coverage SSB beams solely control coverage and, thereby, cell association, while the beams adopted for the data transmission are used those identified by the *Type-I CSI* reporting discussed above.

Although the proposed example scenario exhibits a high level in terms of coverage and previous gains, it results in no improvements, or even degradation, in final data SINR and achievable rate. As depicted in Figure 4.14a, the optimized configuration shows a 6.92 dB loss at the 5%-tile of the data SINR curve, with no improvement at both mean and head of the resulting CDF. Results are summarized in Table 4.6.

Thus, our results confirm the main limitation of the work pursued in this chapter, highlighting how focusing only on coverage optimization for AHs does not automatically yield improvements within the final downlink data transmission. Therefore, this suggests the need for further mechanisms within the optimization process to jointly bridge AH coverage optimization and final data rate performances.

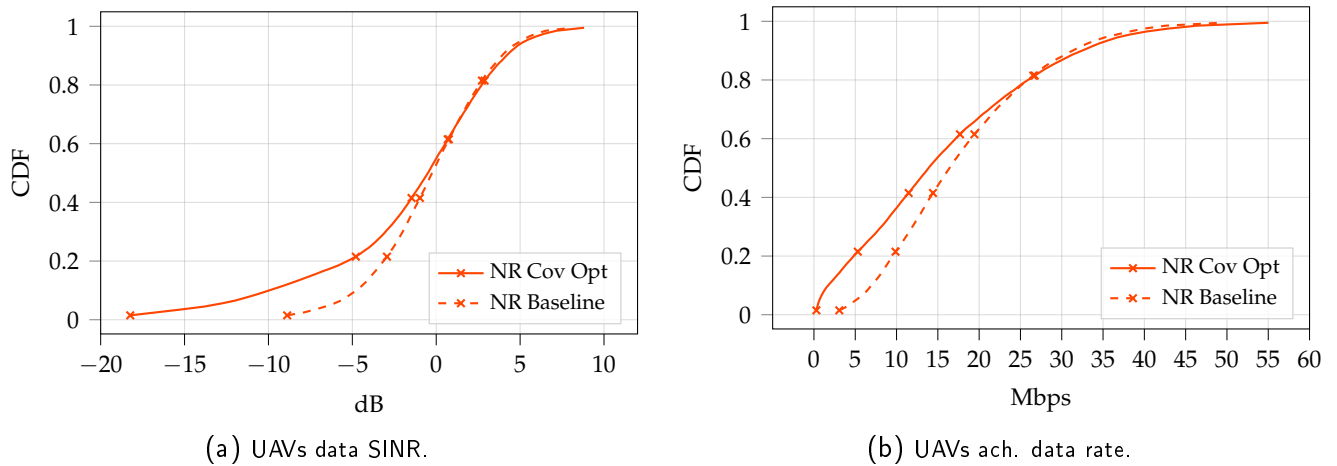


FIGURE 4.14: UAVs NR data SINR (left column) and achievable rate (right column) CDFs considering coverage SSBs beam optimization with a Curved AH in URD network layout at 150 m.

TABLE 4.6: Summary of NR UAVs data SINR and achievable rate statistics resulting from coverage SSBs beam optimization.

UAVs Data Statistics - URD Curved at 150 m				
		NR Baseline	NR Cov Opt	Gain
Data SINR [dB]	5% Tile	-6.34	-13.26	-6.92
	Mean	0.36	-1.67	-2.03
Ach. Data Rate [Mbps]	5% Tile	5.07	0.65	0.13
	Mean	17.99	15.91	0.88

4.7 Conclusion

In this chapter, we introduced an optimization framework for the design of the coverage SSB beams within NR networks; here, we demonstrated how the prior knowledge of the AH can be leveraged to design optimal beams for provisioning high coverage of it. Specifically, we propose a problem for the optimal design of those transmitted beams, and we propose a gradient-based solution to find the optimal configuration for the phase shift of each antenna as well as the activation of those. Then, to solve it, we proposed a gradient-based solution which, leveraging ADAM, efficiently address the non-concave stochastic nature of the problem and finds the optimal solution. Additionally, we propose a mechanism to select only the beams that effectively contribute to coverage while restoring the remaining beams to the configuration designed to serve solely the ground, thereby reducing the ground negative impact of our proposed solution.

In more detail, our findings show that relying on our proposed solution for AHs SSB coverage allow to reach improvements up to 6 dB at the 5%-tile and gains exceeding 10 dB in mean SSB beam coverage SINR, with respect to those obtained when relying on the NR network optimally configured for ground coverage.

When comparing the results of our proposed solution with those achieved by the previously discussed LTE vertical tilt optimization, our approach outperforms the previous LTE generation, delivering gains exceeding 10 dB in the SINR, when considering relatively high altitudes. Those higher gains are achieved by the higher complexity and flexibility of multi-antenna systems, allowing our NR proposed solution to completely overcome the limitations of the previous generation LTE networks; the inherited full flexibility permits optimal control of not only the steering direction but also the shape of those transmitted beams, thereby allowing to radiate strong serving power along the AH without introducing additional interference.

Despite the significant improvements in coverage introduced by our solution, the results for UAVs data SINR and achievable rate reveal a key limitation. The disconnection between the beams used for coverage and those used for data transmission suggests that focusing solely on optimizing coverage beams does not necessarily improve final data communication performance, as completely different beams may be employed during transmission, therefore negating the previously introduced gains.

Hence, this underscores the necessity for further research that not only addresses coverage considerations but also accounts for other critical aspects of UAV communication. These include the reduced spatial complexity influenced by the predominant LoS components in the channels, the close proximity of UAVs, as well as challenges related to channel quality and interference. Accordingly, the subsequent chapter will focus on these issues, presenting practical and efficient solutions that can be integrated during the network planning stages to maximise final UAVs data transmission rates and avoid complex real-time algorithms that require specific assumptions.

Chapter 5

Aerial Highway Segmentation and SSB Beam Planning for UAVs Rate Maximization

5.1 Introduction

Within 5G NR networks, mMIMO offers a paradigm shift and is capable of enhancing UAVs communications too [61–63]. Notably, beamforming has proven to be especially valuable in managing interference to and from UAVs, while spatial multiplexing capabilities have played a pivotal role in enhancing UAVs data rates. However, these studies have largely focused on scenarios involving sparsely located, hovering UAVs, overlooking the complexities of closely located UAVs operating in dense networks, such as AH systems.

Thus, in this chapter, we introduce a novel approach for enhancing cellular connectivity for UAVs on aerial highways via terrestrial 5G NR networks. Moving forward from the results obtained in the previous chapter for aerial highways 5G NR coverage optimization, we now focus on formulating a problem aimed at improving the data rates for UAVs. Therefore, we propose a solution that leverages prior information of the planned aerial highways to optimally plan and configure terrestrial 5G NR networks and maximise achievable UAVs data rates. Specifically, we propose a solution capable of maximizing UAVs rates by focusing on coverage optimization.

In more detail, we envision that by optimally selecting UAVs serving cell within mMIMO network is the most efficient method to maximize data performances from terrestrial network. Owing to their ability to navigate 3D space, UAVs may experience favourable channel gains across multiple network cells; thus, from a network operator's perspective, selecting serving cells that maximize UAV capacity is not straightforward. Merely considering conventional metrics like RSRP may lead to selecting cells that offer high power but are inefficient in multiplexing UAVs, leading to possible reduced data rate performance. To tackle this problem, we propose a novel 5G SSB beams planning solution to strategically control the UAVs cell association and maximize UAVs capacity without affecting terrestrial users. Specifically, we propose a new metric to optimally define the set of cells aimed to serve UAVs

over multiple segments of the AH, by jointly considering multiplexing capability, average channel gain, and interference of each cell.

Previous studies showed significant advantages of optimizing serving cells in mMIMO ultra dense networks (UDNs) [94, 95], suggesting that similar principles may also benefit UAV in UMa scenarios. Indeed, the typical LoS for UAVs creates similar cell association dynamics as in UDNs, therefore controlling cell association along the AH become crucial for improving UAVs connectivity. Existing solutions in the literature generally rely on centralized control mechanisms that optimize whether or not to serve UEs, often adding complexity through real-time algorithms. Our approach, however, avoids such additional complexity by addressing the problem during the network planning phase. Specifically, we devise a new metric and develop a method for identifying the optimal set of serving cells in the terrestrial network aimed to provide stable coverage from and, in turn, enhance UAVs data rate performance. Thus bridging together coverage maximization methods and UAVs data rate maximization.

The remainder of this chapter is organized as follows: Section 5.2 presents the constrained optimization problem for the codebook selected SSB beam planning aimed at maximizing UAV achievable rates while minimizing impact on the terrestrial network. Section 5.3 motivates and introduces a novel metric for selecting serving cells for AHs, Section 5.4, leveraging the designed metric, details the two-stage algorithm solution to solve the optimization problem efficiently. Section 5.7 motivates and introduce a gradient-based solution to optimally designed coverage SSB beams and, finally, Section 5.8 presents and compares different schemes as well as discusses simulation results that demonstrate the efficacy of our approach.

Finally, it should be noted that parts of the results presented in this chapter have been published in the following conferences and journal:

- M. Bernabè, D. López-Pérez, N. Piovesan, G. Geraci and D. Gesbert, “A Novel Metric for mMIMO Base Station Association for Aerial Highway Systems,” 2023 IEEE International Conference on Communications Workshops (ICC Workshops), Rome, Italy, 2023, pp. 1063-1068 [70].
- M. Bernabè, D. López-Pérez, N. Piovesan, G. Geraci and D. Gesbert, “Massive MIMO for Aerial Highways: Enhancing Cell Selection via SSB Beams Optimization,” in IEEE Open Journal of the Communications Society, vol. 5, pp. 3975-3996, 2024 [71].
- M. Bernabè, D. López-Pérez, N. Piovesan, G. Geraci and D. Gesbert, “Optimal SSB Beam Planning and UAV Cell Selection for 5G Connectivity on Aerial Highways,” GLOBECOM 2024 - 2024 IEEE Global Communications Conference, Cape Town, South Africa, 2024 [72].

5.2 Problem Formulation

Optimizing large-scale sub-6 GHz mMIMO networks for AHs presents significant complexity. Our hypothesis suggests that the UAVs achievable data rate operating within AHs can be significantly enhanced by optimally managing UAVs cell associations alone. The foremost benefit of this strategy lies in its feasibility, as focusing exclusively on optimising the SSB beams transmission at the network planning stage, permits the enhancement of the overall UAV performance without requiring specific and unrealistic assumptions.

In this section, we formulate an optimization problem to strategically plan SSB beams, therefore managing UAV cell associations along AHs. This involves optimizing the selection and transmit power of SSBs beams that dictate network UE cell associations, aiming to enhance UAV data rates while ensuring no negative impact on gUEs. Moreover, following the realistic constraints of network operators—who often resist extensive network changes due to the potential deviation from well-performing configurations, management cost concerns, or general risk aversion—we account for the number of changes applied to the network, specifically focusing on the number of varied SSB coverage beams.

The overall problem is formulated in what follows.

Problem 3. Constrained NR SSB Beams Planning for UAVs Rate Maximization

$$\max_{\mathbf{X}, \mathbf{P}} a_0 f_{\text{uav}}(\mathbf{X}, \mathbf{P}) - a_1 g_{\text{gUE}}(\mathbf{X}, \mathbf{P}, \mathbf{X}^{\text{bl}}, \mathbf{P}^{\text{bl}}) - a_2 k(\mathbf{X}, \mathbf{X}^{\text{bl}})$$

$$\text{s.t.} \quad \sum_s^{N_{\text{CB}}} x_{s,b} = N_{\text{ssb}}, \quad \forall b \in \mathcal{B} \quad (\text{C5.1}),$$

$$\frac{1}{2} \sum_s^{N_{\text{CB}}} (1 - x_{s,b} x_{s,b}^{\text{bl}}) \leq N'_{\text{ssb}}, \quad \forall b \in \mathcal{B} \quad (\text{C5.2}),$$

$$0 \leq p_{s,b}^{\text{ssb}} \leq p_{\text{max}}^{\text{ssb}}, \quad \forall p_{s,b}^{\text{ssb}} \in \mathbf{P} \quad (\text{C5.3}),$$

$$\mathbf{X} \in \{0, 1\}^{N_{\text{CB}} \times N_{\text{BS}}} \quad (\text{C5.4}),$$

$$\mathbf{P} \in \mathbb{R}^{N_{\text{CB}} \times N_{\text{BS}}} \quad (\text{C5.5}),$$

with

$$f_{\text{uav}}(\mathbf{X}, \mathbf{P}) = \mathbb{E}_{\tau, \text{hdI}} \left\{ \log \left(\sum_a^{N_a} R_a^{\text{nr}}(\mathbf{X}, \mathbf{P}) \right) \right\}, \quad (5.1)$$

$$\begin{aligned} g_{\text{gUE}}(\mathbf{X}, \mathbf{P}, \mathbf{X}^{\text{bl}}, \mathbf{P}^{\text{bl}}) &= \\ &= \mathbb{E}_{\tau, \text{hdI}} \left\{ \sum_g^{N_g} \left| R_g^{\text{nr}}(\mathbf{X}, \mathbf{P}) - R_g^{\text{nr}}(\mathbf{X}^{\text{bl}}, \mathbf{P}^{\text{bl}}) \right| \right\}, \end{aligned} \quad (5.2)$$

and

$$\begin{aligned}
 k(\mathbf{X}, \mathbf{X}^{\text{bl}}) &= \frac{1}{2} \mathbf{e}^T \left(\mathbf{1} - (\mathbf{X} \odot \mathbf{X}^{\text{bl}}) \right) \mathbf{e} \\
 &= \frac{1}{2} \sum_b^{N_{\text{BS}}} \sum_s^{N_{\text{CB}}} 1 - x_{s,b} x_{s,b}^{\text{bl}},
 \end{aligned} \tag{5.3}$$

where the binary matrices \mathbf{X} , \mathbf{P} , introduced in Chapter 2 Section 2.5.4, control the transmitted SSB beam, thereby directly affecting UEs cell associations as detailed in eq. (2.28). Specifically, an element $x_{s,b}$ within matrix \mathbf{X} equaling one indicates the selection of the s -th SSB beam at cell b . Correspondingly, an element $p_{b,s}^{\text{ssb}}$ within matrix \mathbf{P} indicates the transmit power allocated by cell b to the s -th SSB beam. Additionally, matrices \mathbf{X}^{bl} and \mathbf{P}^{bl} represent the SSB configuration before the optimization process begins, i.e. in an scenario with no UAVs. We refer to this scenario as the baseline one.

The objective function in Problem (3) comprises the following terms:

- $f_{\text{uav}}(\cdot)$, defined in eq. (5.1) and leveraging the $\log(\cdot)$ function to calculate a fair sum rate across all UAVs, ensuring equitable UAV service.
- $g_{\text{gUE}}(\cdot, \cdot)$, defined in eq. (5.2) and evaluating the impact of UAV integration on gUE data rates through the optimization decisions made and represented in matrices \mathbf{X} and \mathbf{P} , aiming to minimize disruption to existing services.
- $k(\cdot, \cdot)$, defined in eq. (5.3) and measuring optimization-induced changes to SSBs beams via the Hadamard product of \mathbf{X} and \mathbf{X}^{bl} , with all element summation, adjusted by a factor of $1/2$, to reflect the change count. Note that in eq. (5.3) \mathbf{e} is a vector of all ones.

where coefficients a_0, a_1, a_2 are introduced to ensure consistency across different units of measurement.

Data rates in eqs. (5.1) and (5.2) are calculated according to eq. (2.36).

Feasible solutions to Problem (3) must meet the following constraints:

- C5.1, mandating each cell b to deploy N_{ssb} SSB beams.
- C5.2, limiting cell modifications to of N'_{ssb} SSB beams for adaptability without compromising stability.
- C5.3, controlling the transmit power per SSB beam.
- C5.4 and C5.5, defining \mathbf{X} and \mathbf{P} matrices space.

Problem (3), characterized by high dimensionality, inherent stochasticity, non-linearity, and the combinatorial nature of the mixed binary integer variables, represents an NP-hard problem. To tackle this problem, in Section 5.3 we introduce a novel metric to optimally select aerial highway serving cells. Then, leveraging the proposed metric, in Section 5.4 we propose a heuristic solution which divides Problem (3) into two substantially less complex sub-problems and solves them.

5.3 MAMA - An Aerial Highway Serving Cell Metric

Utilizing mMIMO to serve closely located UAVs in an AH poses challenges, primarily due to the inherent high channel correlation. Channel correlation is intensified in the AH environment as UAVs fly in close proximity to each other, often with direct LoS, as highlighted by models outlined by 3GPP. This diminishes spatial diversity, crucial for effective mMIMO operation, limiting the system's capacity for simultaneous transmission/reception of multiple data streams to/from different UAVs. The independent design of the AH with respect to the network can further exacerbate this challenge. For instance, consider a scenario where the AH is perpendicular to the mMIMO planar array of the sector providing the highest power. In such a case, the sector may be unable to resolve the highly-correlated spatial signatures of the UAVs flying along the AH, as they appear at approximately the same angle of arrival (AoA) and angle of departure (AoD). To address these challenges, it may prove advantageous to associate with a sector offering superior multiplexing capabilities at the expense of a slightly weaker signal.

To address this issue, we introduce a novel metric that aims to optimize the selection of the set of cells aimed to serve UAVs along the AH. The proposed metric leverages AH a-priori information, i.e., define trajectory, and channel state information measurements, and it accounts for received signal strength, spatial diversity, and potential interference.

5.3.1 MAMA Metric

In order to define our proposed metric, we discretize the AH into N_r points \mathbf{r}_{AH} with equal inter-point distance d_r to simplify the problem. Leveraging existing simulations and/or measurements collected during exploratory UAV flights in the planning phase, we derive the expected complex channel vector $\tilde{\mathbf{h}}_{r,b}$ between each of these N_r points and each cell b , as expressed by:

$$\tilde{\mathbf{h}}_{r,b} = \mathbb{E}_{\tau, \mathbf{h}^{\text{dl}}} \left[\beta_{r,b} \mathbf{h}_{r,b}^{\text{dl}} \right] = \mathbb{E}_{\tau, \mathbf{h}^{\text{dl}}} \left[\rho_{r,b} \tau_{r,b} g_{r,b} \mathbf{h}_{r,b}^{\text{dl}} \right]. \quad (5.4)$$

Subsequently, we utilize these vectors to construct the expected complex channel matrix $\tilde{\mathbf{H}}_{r,b} \in \mathbb{C}^{N_r \times M}$.

Furthermore, we define the segment \mathbf{z} within the AH \mathbf{r}_{AH} as the set of consecutive discrete N_z points such that

$$\mathbf{z} \subset \mathbf{r}_{\text{AH}} \quad \text{and,} \quad M < N_z < N_r. \quad (5.5)$$

Then, from matrix $\tilde{\mathbf{H}}_{r,b}$, we define two sub-matrices $\tilde{\mathbf{H}}_{\mathbf{z},b}$ and $\tilde{\mathbf{H}}_{\mathbf{r}-\mathbf{z},b}$, respectively denoting the complex channel vectors of segment \mathbf{z} and of the remaining AH discrete points, such that,

$$\tilde{\mathbf{H}}_{r,b} = \begin{bmatrix} \tilde{\mathbf{H}}_{\mathbf{z},b} \\ \tilde{\mathbf{H}}_{\mathbf{r}-\mathbf{z},b} \end{bmatrix}. \quad (5.6)$$

According to the above-defined channel matrices, we introduce our proposed metric, referred to as MAMA aimed at addressing the limitations of the widely adopted best-RSRP association policy when dealing with AHs:

$$\begin{aligned} \chi_{z,b}(\tilde{\mathbf{H}}_{z,b}, \tilde{\mathbf{H}}_{r-z,b}) &= \\ &= c_{z,b}(\tilde{\mathbf{H}}_{z,b}) \log_2 \left(1 + \frac{P_{z,b}(\tilde{\mathbf{H}}_{z,b})}{F_{z,b}(\tilde{\mathbf{H}}_{z,b}, \tilde{\mathbf{H}}_{r-z,b}) + N_0} \right). \end{aligned} \quad (5.7)$$

The proposed MAMA metric is defined as a scalar function designed to mirror the Hartley-Shannon spectral efficiency. It is comprised of three components, each designed to address distinct channel properties. In the following, we present each component along with its physical significance.

Average Channel Gain

The first component of the proposed metric in eq. (5.7) is the average channel gain $P_{z,b}$ provided by cell b along segment \mathbf{z} , and it is computed as follows,

$$P_{z,b}(\tilde{\mathbf{H}}_{z,b}) = \frac{1}{N_z} \sum_z^{N_z} \frac{1}{M} \sum_m^M |\tilde{h}_{m,z,b}|^2, \quad (5.8)$$

This term offers insight into the average channel gain that a UAV can expect from a cell in a given segment, similarly to traditional RSRP-based association.

Channel Diversity Assessment

The second element of our metric is the inverse of the condition number of matrix $\tilde{\mathbf{H}}_{z,b}$ [96], referred to as $c_{z,b}$, and defined as follows,

$$c_{z,b}(\tilde{\mathbf{H}}_{z,b}) = \frac{\lambda_{z,b}^{(M-1)}(\tilde{\mathbf{H}}_{z,b})}{\lambda_{z,b}^{(0)}(\tilde{\mathbf{H}}_{z,b})}, \quad (5.9)$$

This component offers insights into the expected spatial multiplexing capabilities of cell b with respect to the considered segment \mathbf{z} .

To compute this scalar component for segment \mathbf{z} , we consider the expected complex channel matrix $\tilde{\mathbf{H}}_{z,b}$ and we compute its set of singular values using single value decomposition (SVD). Those are then organized into vector $\lambda_{z,b}$ in decreasing order, as follows:

$$\lambda_{z,b}(\tilde{\mathbf{H}}_{z,b}) = \left[\lambda_{z,b}^{(0)}, \lambda_{z,b}^{(1)}, \dots, \lambda_{z,b}^{(M-1)} \right]^T. \quad (5.10)$$

It should be noted that, maintaining a minimum segment length (number of points within the segment greater than the number of antennas ensures that the cardinality of the singular values vector is equal to M). We then derive $c_{z,b}$ as the ratio between the lowest and highest singular value of vector $\lambda_{z,b}$, as defined in eq. (5.9). This ratio serves as a crucial component of our metric, offering insights into the spread

of singular values and the variation of AoAs/AoDs across the segment concerning each cell, thereby assessing the diversity of the complex channels to enable higher and fairer UE data rates. Note that this metric, defined as the inverse of the condition number, decreases with the increasing singular values spread and, therefore, increases with AoAs/AoDs diversity. Moreover, it bounds its values in the range $[0, 1]$, preventing undefined operations when the lowest singular value is zero.

Inter Cell Interference Assessment

The last component is the squared Frobenius norm, $F_{\mathbf{z},b}$, of the cross-correlation matrix between the two matrices $\tilde{\mathbf{H}}_{\mathbf{z},b}$, $\tilde{\mathbf{H}}_{\mathbf{r}-\mathbf{z},b}$, and it is defined as follows,

$$\begin{aligned} F_{\mathbf{z},b}(\tilde{\mathbf{H}}_{\mathbf{z},b}, \tilde{\mathbf{H}}_{\mathbf{r}-\mathbf{z},b}) &= \|\tilde{\mathbf{H}}_{\mathbf{r}-\mathbf{z},b} \tilde{\mathbf{H}}_{\mathbf{z},b}^H\|_F^2 = \\ &= \sum_i^{N_r-N_z} \sum_z^{N_z} \left| \sum_m^M \tilde{h}_{m,i,b} \tilde{h}_{m,z,b}^* \right|^2. \end{aligned} \quad (5.11)$$

This component allows us to gain insight into the inter-cell interference generated from cell b , which is using different precoders to serve UAVs in segment \mathbf{z} , to UAVs located over the remaining part of the AH. Then, considering UAVs in each discrete point, the expected inter-cell interference introduced on the remaining segments can be computed as:¹

$$\tilde{\mathbf{i}}_{\mathbf{r}-\mathbf{z},b}^{\text{inter}} = \left| \tilde{\mathbf{H}}_{\mathbf{r}-\mathbf{z},b} \mathbf{W}_{\mathbf{r}-\mathbf{z},b}^{\text{dl}} \right|^2 \mathbf{e}, \quad (5.12)$$

where we recall that \mathbf{e} is defined as a vector of all ones. As described in Section 2.6.2, during the UE's data precoding phase, the network selects the codewords that maximizes UEs' received power. This can be interpreted as a maximum ratio transmission (MRT) approach, in which the precoders are selected as those which better approximate the Hermitian of the channels, i.e.,

$$\begin{aligned} \mathbf{W}_{\mathbf{r}-\mathbf{z},b}^{\text{dl}} &= \underset{\mathbf{W}_{\mathbf{r}-\mathbf{z},b}^{\text{dl}}}{\text{argmin}} \left\{ \left\| \tilde{\mathbf{H}}_{\mathbf{z},b} \tilde{\mathbf{H}}_{\mathbf{z},b}^H - \tilde{\mathbf{H}}_{\mathbf{z},b} \mathbf{W}_{\mathbf{r}-\mathbf{z},b}^{\text{dl}} \right\| \right\} \\ &= \underset{\mathbf{W}_{\mathbf{r}-\mathbf{z},b}^{\text{dl}}}{\text{argmin}} \left\{ \left\| \tilde{\mathbf{H}}_{\mathbf{z},b} \left(\tilde{\mathbf{H}}_{\mathbf{z},b}^H - \mathbf{W}_{\mathbf{r}-\mathbf{z},b}^{\text{dl}} \right) \right\| \right\}. \end{aligned} \quad (5.13)$$

Thus, eq. (5.12) can be approximated as follows:

$$\tilde{\mathbf{i}}_{\mathbf{r}-\mathbf{z},b}^{\text{inter}} \approx \tilde{\mathbf{i}}_{\mathbf{r}-\mathbf{z},b}^{\text{inter}'} = \left| \tilde{\mathbf{H}}_{\mathbf{r}-\mathbf{z},b} \tilde{\mathbf{H}}_{\mathbf{z},b}^H \right|^2 \mathbf{e}. \quad (5.14)$$

Finally, we calculate $F_{\mathbf{z},b}$ as the squared Frobenius norm of the obtained cross-correlation channel matrix, as described in eq (5.11).

¹Note that, in eqs.(5.12) and (5.14), the term $|\cdot|^2$ represents the element-wise squared absolute operation

This last component offers insights into the potential introduced interference, particularly crucial in typical LoS scenarios where lower channel gains from neighbouring cells do not mitigate inter-cell interference.

Aerial Segment Serving Cell Selection

Mirroring the Hartley-Shannon spectral efficiency, the three aforementioned components $F_{z,b}(\cdot, \cdot)$, $c_{z,b}(\cdot)$ and $P_{z,b}(\cdot)$, are melted together to compute the MAMA metric $\chi_{z,b}$, as defined in eq. (5.7). Then, leveraging MAMA, the designed serving cell \hat{b}_z for each segment \mathbf{z} is computed as follows,

$$\hat{b}_z = \operatorname{argmax}_{b \in \mathcal{B}} \{ \chi_{z,b}(\tilde{\mathbf{H}}_{z,b}, \tilde{\mathbf{H}}_{r-z,b}) \}. \quad (5.15)$$

This scalar metric exploits the prior information of the AH to blend together important and different network physical aspects, such as the expected average gain that UAVs will perceive while flying along it, the cell capability of multiplexing different UAVs on the same PRBs and the introduced interference to other segments. Therefore, this metric allows us to select the serving cell that offers the most effective trade-off among them.

5.3.2 Illustrative Example

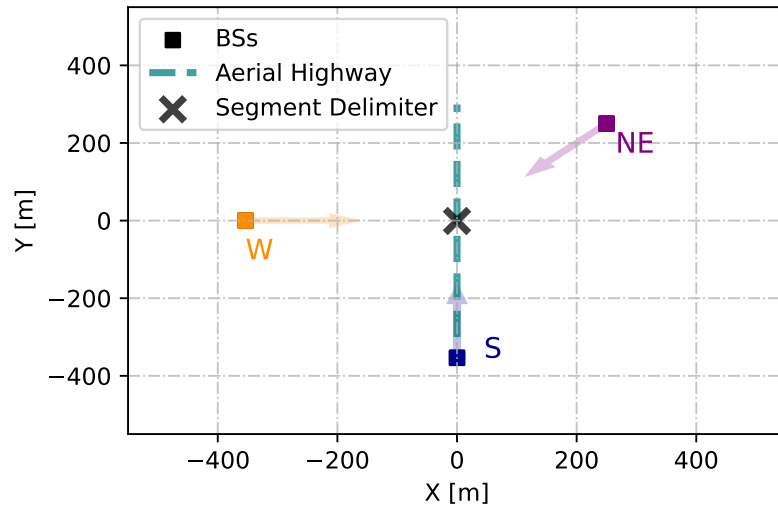


FIGURE 5.1: Simplified 2D Network Layout with a AH directed from South to North in the network centre.

To illustrate the advantages of the proposed metric in selecting the serving cell for UAVs within AHs, we present results in a simplified scenario based on the system model described in Chapter 2. More complex scenarios will be studied later in the Chapter. Consider the scenario depicted in Figure 5.3.2, where three single-sector base stations are positioned at the Southern (S), Western (W), and Northeastern (NE) edges, at a height of 25 m. An AH passes from south to north over the centre of the

scenario. For illustration purposes, we divide the AH into two segments: Northern and Southern. In this configuration, each sector broadcasts 8 SSB beams covering its designated area. All beams are tilted at 105° and span the azimuth plane. In the reference setup, referred to as “Baseline”, when UAVs traverse the AH and measure the received power from different cells, they tend to associate with the S cell due to higher measured RSRP. However, UAVs appear almost collinear (i.e., one behind the other) from S cell viewpoint, and this cell cannot efficiently exploit its spatial multiplexing capabilities. Furthermore, this association introduces high interference on the AH to UAVs not connected to the S cell. In contrast, when selecting the serving cell according to the proposed MAMA metric, we find that UAVs on the Southern segment are served by the E cell, while UAVs in the Northern segment are served by the NE one. We refer to this scenario as “Opt”.

TABLE 5.1: Summary of NR UAVs data SINR and rate statistics in the simplified scenario (Figure 5.2), considering serving cell selection according to belonging segment and MAMA metric.

	KPI			
	$\text{SINR}_{5\%-\text{tile}}$ [dB]	$\text{SINR}_{\text{mean}}$ [dB]	$\text{Rate}_{5\%-\text{tile}}$ [Mbps]	$\text{Rate}_{\text{mean}}$ [Mbps]
Baseline	-6.73	1.88	1.60	6
Opt	-3.47	2.40	4	15
Gain	3.26	0.52	250%	250%

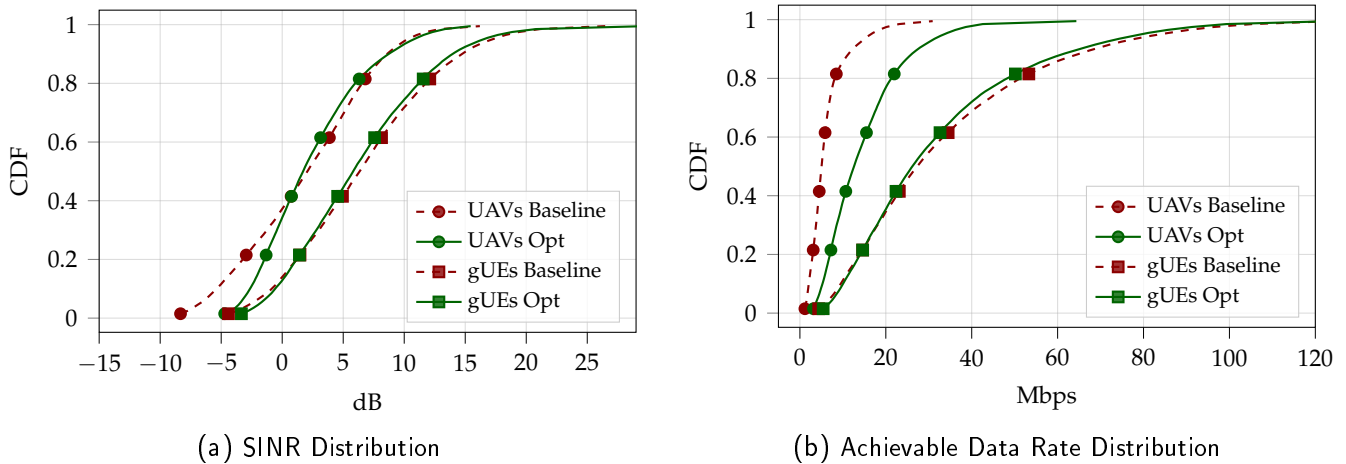


FIGURE 5.2: UAVs NR SINR distribution (left) and achievable data rate distribution (right) in the illustrative network example (Figure 5.3.2), considering serving cell selection according to belonging segment and MAMA metric.

Then, Figure 5.2 shows results in terms of SINR and achievable data rate distributions. It should be noted that a gain of 3.26 dB and a percentage gain of 250% are achieved for the 5%-tile of UAVs’ SINR and achievable data rate, respectively. And Table 5.1, summarize results in terms of 5%-tile and mean value.

This scenario demonstrates the clear benefits of the proposed metric in optimizing cell association for UAVs within AHs, leading to improved performance.

5.4 Two Stage solution: Aerial Highway Split and SSB Beam Selection

In this section, we introduce a heuristic approach designed to efficiently tackle Problem (3) and finding the optimal SSB planning solution. This approach divides the overall problem into two sub-problems: I) the AH split into multiple segments, segment-to-cell association and ii) the SSBs beam design.

The initial sub-problem focuses on segmenting the AH and identifying the most suitable serving cell for each segment. This process aims to maximize our proposed metric MAMA. Building on this, the resolution of the first sub-problem guides the approach for the second sub-problem, which narrows down the search to identify the most efficient combination of SSB beams to be deployed at each cell to ensure an optimal association between UAVs and cells, in alignment with the findings from the first sub-problem.

5.4.1 Split and Segment-to-cell Association Problem

By leveraging a priori planning information of the AH, and the proposed metric in Section 5.3, in the following, we formulate the first sub-problem as follows:

Problem 1 *Aerial Highway Split and Segment-To-Cell Association*

$$\begin{aligned} \max_{\mathcal{Z}_{\text{AH}}^{\text{split}}, \hat{\mathcal{B}}^{\text{split}}} \quad & \sum_{\mathbf{z} \in \mathcal{Z}_{\text{AH}}^{\text{split}}} \chi_{\mathbf{z}, b_{\mathbf{z}}} (\tilde{\mathbf{H}}_{\mathbf{z}, b_{\mathbf{z}}}, \tilde{\mathbf{H}}_{\mathbf{r}-\mathbf{z}, b_{\mathbf{z}}}) \\ \text{s.t.} \quad & \cup_{\mathbf{z} \in \mathcal{Z}_{\text{AH}}^{\text{split}}} \mathbf{z} = \mathcal{Z}_{\text{AH}}^{\text{split}} \quad (\text{C4.1}), \\ & \mathbf{z}_i \cap \mathbf{z}_j = \emptyset, \forall \mathbf{z}_i, \mathbf{z}_j \in \mathcal{Z}_{\text{AH}}^{\text{split}} \quad (\text{C4.2}), \quad (\text{P2}) \\ & [\mathbf{z}_0^T, \dots, \mathbf{z}_i^T, \dots, \mathbf{z}_{n_{\text{seg}}}^T] = \mathbf{r}_{\text{AH}} \quad (\text{C4.3}), \\ & b_{\mathbf{z}_i} \neq b_{\mathbf{z}_j}, \forall b_{\mathbf{z}_i}, b_{\mathbf{z}_j} \in \hat{\mathcal{B}}^{\text{split}} \quad (\text{C4.4}), \\ & \text{Card} \{ \mathcal{Z}_{\text{AH}}^{\text{split}} \} = \text{Card} \{ \hat{\mathcal{B}}^{\text{split}} \} \quad (\text{C4.5}), \end{aligned}$$

where $n_{\text{seg}} = \text{Card} \{ \mathcal{Z}_{\text{AH}}^{\text{split}} \}$ is the total number of segments.

Our goal is to identify the set of segments $\mathcal{Z}_{\text{AH}}^{\text{split}}$ and the corresponding set of serving cells $\hat{\mathcal{B}}^{\text{split}}$ that maximizes the sum of our proposed MAMA metric for each segment. In the problem formulation outlined, solutions must satisfy the following constraints:

- C4.1, guaranteeing the representation of the set \mathcal{Z}_{AH} through the union of all obtained segment.

- C4.2, mandating mutual disjoint condition for each pair of segments. Here, notation \cap is used to define that no element of \mathbf{z}_i is in \mathbf{z}_j .
- C4.3, ensuring the representation of the all overall AH \mathbf{r}_{AH} by consecutive concatenation of segments.
- C4.4, requiring a unique serving cell for each segment.
- C4.5, imposing the number of total segments equals the number of serving cells.

Collectively, constraints C4.2, C4.4 and C4.5 define a bijective relationship between the set of segments and the set of serving cells, guaranteeing a unique pairing between each segment and its corresponding serving cell.

5.4.2 Aerial Highway Split Algorithm

In the following sections, we introduce an algorithm based on PSO [97–99], aimed at addressing Problem (P2). This algorithm is structured into two main components: i) an outer loop, as detailed in Algorithm 1, which aims to determine the optimal number of segments; ii) an inner loop, outlined in Algorithm 2 and referred to as Particle Aerial Highway Swarm Segmentation (PAHSS), specifically designed to ascertain the most efficient dimension of each segment, while establishing for each segment the optimal serving cell via MAMA metric.

Outer Split Algorithm

Algorithm 1 systematically iterates over the number of segments n_s , starting from a minimum value N_{seg}^{\min} and incrementing up to a maximum threshold N_{seg}^{\max} . During each iteration, the current number of segments and \mathbf{r}_{AH} serve as inputs to the PAHSS algorithm.

The iteration process continues until one of two conditions is met: either the process exhausts the range of segment numbers, reaching N_{seg}^{\max} , or it encounters a specific intermediate stopping condition. This condition evaluates whether any pair of neighbouring segments are assigned to the same serving cell; if they are, these segments can be represented by a unique one, thereby falling under the previous case, i.e., n_s-1 . Thus, if such a scenario is detected, the algorithm halts, adopting the configuration from the preceding iteration as its final output.

PAHSS Algorithm

To find the optimal configuration for the indicated number of segments, we propose an evolutionary algorithm based on PSO [97–99], as it is a robust and fast method to solve non-convex non-linear, non-differentiable multidimensional problems.

Algorithm 1: Outer Loop Split Algorithm

Data: $\mathbf{r} \leftarrow \mathbf{r}_{\text{AH}}$
Result: $\mathcal{Z}_{\text{AH}}^{\text{split}}, \hat{\mathcal{B}}^{\text{split}}$

- 1 $\mathcal{Z}_{\text{AH}}^{(\text{opt})}, \hat{\mathcal{B}}^{(\text{opt})} \leftarrow \text{PAHSS}(\mathbf{r}, 1)$;
- 2 **for** $n_s \in [N_{\text{seg}}^{\text{min}}, N_{\text{seg}}^{\text{max}}]$ **do**
- 3 $\mathcal{Z}_{\text{AH}}^{(n_s)}, \hat{\mathcal{B}}^{(n_s)} \leftarrow \text{PAHSS}(\mathbf{r}, n_s)$;
- 4 **if** $\exists \mathbf{z}_i, \mathbf{z}_j \in \mathcal{Z}_{\text{AH}}^{(n_s)} : \hat{b}_{\mathbf{z}_i} = \hat{b}_{\mathbf{z}_j}$ **then**
- 5 $\mathcal{Z}_{\text{AH}}^{\text{split}} = \mathcal{Z}_{\text{AH}}^{(\text{opt})}$;
- 6 $\hat{\mathcal{B}}^{\text{split}} = \hat{\mathcal{B}}^{(\text{opt})}$;
- 7 **Terminate;**
- 8 **else**
- 9 $\mathcal{Z}_{\text{AH}}^{(\text{opt})} = \mathcal{Z}_{\text{AH}}^{(n_s)}$;
- 10 $\hat{\mathcal{B}}^{(\text{opt})} = \hat{\mathcal{B}}^{(n_s)}$;
- 11 **end**
- 12 **end**
- 13 $\mathcal{Z}_{\text{AH}}^{\text{split}} = \mathcal{Z}_{\text{AH}}^{(n_s)}$;
- 14 $\hat{\mathcal{B}}^{\text{split}} = \hat{\mathcal{B}}^{(n_s)}$;

In this work, each particle p represents an AH segmentation, represented by \mathbf{x}^p :

$$\mathbf{x}^p = [x_0^p, \dots, x_n^p, \dots, x_{n_s-2}^p]^T, \quad (5.16)$$

where n_s is the number of desired segments, and each element of this vector serves as a delimiter or boundary for the segments composing the aerial highway \mathbf{r}_{AH} , which we refer to as pivots.

Subsequently, for each AH segmentation p and its defined pivots \mathbf{x}^p , each segment $\mathbf{z}^p \in \mathcal{Z}_{\text{AH}}^{(n_s)}$ is delineated as the interval between two consecutive pivots. Specifically, this segmentation is represented as:

$$\mathbf{z}_0^p \doteq [r_0, x_0^p), \quad \mathbf{z}_{n_s}^p \doteq [x_{n_s-2}^p, r_{-1}] \quad (5.17)$$

and

$$\forall n \in [0, n_s - 2], \mathbf{z}_n^p \doteq [x_n^p, x_{n+1}^p), \quad (5.18)$$

where the first and last segments' bounds are defined by the limits of the AH, represented in eq. (5.17). Notably, r_0 and r_{-1} denote the initial and final elements of the AH, respectively.

Based on the derived segmentation, for each segment \mathbf{z} , the expected complex matrices $\hat{\mathbf{H}}_{\mathbf{z},b}$ and $\hat{\mathbf{H}}_{\mathbf{r}-\mathbf{z},b}$, representing channels between each segment \mathbf{z} and each cell b are calculated, and the objective function to maximize for our PSO algorithm is then computed as the summation of the maximum MAMA metric for every segment

with respect to each cell, as follows,

$$f^{\text{psO}}(\mathbf{x}_p) = \sum_{\mathbf{z} \in \mathcal{Z}_{\text{AH}}^p(\mathbf{x}_p)} \max_{b \in \mathcal{B}} \left(\chi_{\mathbf{z},b}(\tilde{\mathbf{H}}_{\mathbf{z},b}, \tilde{\mathbf{H}}_{\mathbf{r}-\mathbf{z},b}) \right), \quad (5.19)$$

where we denoted with $\mathcal{Z}_{\text{AH}}^p(\mathbf{x}_p)$ the set of segments obtained according to \mathbf{x}_p .

The position \mathbf{x}^p of each particle p , iteration after iteration, is adjusted according to its velocity \mathbf{v}^p , defined as follows,

$$\mathbf{v}^p \leftarrow \omega \mathbf{v}^p + \phi_c c_1 (\mathbf{x}_{\text{best}}^p - \mathbf{x}^p) + \phi_s c_2 (\mathbf{x}_{\text{best}} - \mathbf{x}^p) \quad (5.20)$$

$$\mathbf{x}^p \leftarrow \mathbf{x}^p + \mathbf{v}^p \quad (5.21)$$

Specifically, in velocity definition, ω represents the inertia weight, the term ϕ_c is the cognitive coefficient, and ϕ_s is the social coefficient. The constants c_1 and c_2 are random numbers within the range $[0, 1]$, introducing stochasticity into the velocity update. The cognitive component ϕ_c accounts for the particle's personal best position it has encountered $\mathbf{x}_{\text{best}}^p$, promoting the exploration of promising regions based on individual experience. Conversely, the social component ϕ_s considers the global best position found by any particle in the swarm \mathbf{x}_{best} , encouraging convergence towards optimal solutions discovered collectively. During each iteration i , the algorithm updates the personal best position $\mathbf{x}_{\text{best}}^p$ for each particle p if a better position is found. Similarly, the global best position \mathbf{x}_{best} is updated if a new optimal solution is discovered by the swarm. The algorithm proceeds until it either reaches a predefined number of iterations $N_{\text{psO}}^{\text{Iter}}$ or an early stopping criterion is met, based on the convergence of particles towards the global best position \mathbf{x}_{best} . Upon termination of the iterative process, the MAMA metric is adopted to compute the optimal serving cell for each obtained segment (see eq. (5.15)), thereby defining the set $\hat{\mathcal{B}}^{\text{split}}$. It should be noted that this operation retrieves the set of serving cells that maximized objective function (5.19). Detailed steps of the algorithm are outlined in Algorithm 2.

Algorithm 2: PAHSS Algorithm

```

1 Input:  $\mathbf{r}, n_s$ 
2 Output:  $\mathcal{Z}_{\text{AH}}^{(n_s)}, \hat{\mathcal{B}}^{(n_s)}$ 
3  $x_{\text{LB}}, x_{\text{UB}} \leftarrow r_0, r_{-1}$ ;
4  $\mathcal{Z}_{\text{AH}}^{(n_s)}, \hat{\mathcal{B}}^{(n_s)} = \emptyset, \emptyset$ ;
5  $\mathbf{x}^p \leftarrow \text{init\_random\_current\_position}(\mathbf{r}, N_{\text{swarm}}, n_s - 1)$ ;
6  $\mathbf{v}^p \leftarrow \text{init\_zeros\_velocity}(N_{\text{swarm}}, n_s - 1)$ ;
7 if  $n_s = 1$  then
8    $\mathcal{Z}_{\text{AH}}^{(n_s)} \leftarrow \mathcal{Z}_{\text{AH}}^{(n_s)} \cup \mathbf{r}$ ;
9    $\hat{b}_r \leftarrow \text{argmax}_{b \in \mathcal{B}} \{ \chi_r^b(\cdot) \}$ ;
10   $\hat{\mathcal{B}}^{(n_s)} \leftarrow \hat{\mathcal{B}}^{(n_s)} \cup \hat{b}_r$ ;
11  Terminate;
12 end
13 for  $i \in [0, N_{\text{psso}}^{\text{iter}} - 1]$  do
14   for  $p \in [0, N_{\text{swarm}} - 1]$  do
15     if  $f^{\text{psso}}(\mathbf{x}_{\text{best}}^p) < f^{\text{psso}}(\mathbf{x}^p)$  then
16        $\mathbf{x}_{\text{best}}^p \leftarrow \mathbf{x}^p$ ;
17     end
18     if  $f^{\text{psso}}(\mathbf{x}_{\text{best}}) < f^{\text{psso}}(\mathbf{x}_{\text{best}}^p)$  then
19        $\mathbf{x}_{\text{best}} \leftarrow \mathbf{x}_{\text{best}}[p]$ ;
20     end
21   end
22   for  $p \in [0, N_{\text{swarm}} - 1]$  do
23      $\mathbf{v}^p \leftarrow \omega \mathbf{v}^p + \phi_c c_1 (\mathbf{x}_{\text{best}}^p - \mathbf{x}^p) + \phi_s c_2 (\mathbf{x}_{\text{best}} - \mathbf{x}^p)$ ;
24      $\mathbf{x}^p \leftarrow \mathbf{x}^p + \mathbf{v}^p$ ;
25     if  $\forall x_i^p \in \mathbf{x}^p, \exists x_i^p < x_{\text{LB}}$  then
26        $x_i^p \leftarrow x_{\text{LB}}$ ;
27     end
28     if  $\forall x_i^p \in \mathbf{x}^p, \exists x_i^p > x_{\text{UB}}$  then
29        $x_i^p \leftarrow x_{\text{UB}}$ ;
30     end
31   end
32 end
33  $\mathbf{z}_0 \leftarrow [r_0, x_{\text{best},0}]$ ;
34  $\mathbf{z}_{n_s} \leftarrow [x_{\text{best},n_s-2}, r_{-1}]$ ;
35 for  $n \in [0, n_s - 2]$  do
36    $\mathbf{z}_n \leftarrow [x_{\text{best},n}, x_{\text{best},n+1}]$ ;
37 end
38  $\mathcal{Z}_{\text{AH}}^{(n_s)} \leftarrow \mathcal{Z}_{\text{AH}}^{(n_s)} \cup_n^{n_s} \mathbf{z}_n$ ;
39 for  $\mathbf{z} \in \mathcal{Z}_{\text{AH}}^{(n_s)}$  do
40    $\hat{\mathcal{B}}^{(n_s)} \leftarrow \hat{\mathcal{B}}^{(n_s)} \cup \text{argmax}_{b \in \mathcal{B}} \{ \chi_z^b(\cdot) \}$ ;
41 end

```

5.4.3 SSB Codebook Beams and Transmit Power Selection Problem

Building upon the split and serving cell resulting from Algorithm 1, we formulate a problem to select codewords from a fixed codebook \mathcal{W}^{ssb} and their transmit power for each identified serving cell. The goal is to determine the optimal value for \mathbf{X} and \mathbf{P} , respectively representing the SSBs codeword selection matrix and their transmit power levels, for maximizing the minimum expected SSB SINR over the AH across multiple channel realizations, therefore providing a reliable solution that is robust to different environmental conditions and ensures optimal network coverage from the set of serving cells $\hat{\mathcal{B}}^{\text{split}}$ determined by Algorithm 1.

The problem is formulated as follows:

Problem 4. SSB Codebook Beams and Transmit Power Selection

$$\begin{aligned} \max_{\mathbf{X}, \mathbf{P}} \quad & \min \left(\left\{ \mathbb{E}_{\tau, \mathbf{h}^{\text{ah}}} \left\{ \gamma_a^{\text{ssb}}(\mathbf{X}, \mathbf{P}) \right\} \mid \forall a \in \mathcal{E}_a \right\} \right) \\ \text{s.t.} \quad & \hat{b}_a = \hat{\mathbf{z}}^{\text{split}}, \forall \mathbf{z} \in \mathcal{Z}_{\text{AH}}^{\text{split}}, \forall a \in \mathcal{E}_a \end{aligned} \quad (\text{C5.1}),$$

$$\sum_s^{N_{\text{CB}}} x_{s,b} = N_{\text{ssb}}, \forall b \in \mathcal{B}, \quad (\text{C5.2}),$$

$$\frac{1}{2} \sum_s^{N_{\text{CB}}} (1 - x_{s,b} x_{s,b}^{\text{bl}}) \leq 1, \forall b \in \hat{\mathcal{B}}^{\text{split}} \quad (\text{C5.3}),$$

$$0 \leq p_{s,b}^{\text{ssb}} \leq p_{\text{max}}^{\text{ssb}}, \forall p_{s,b}^{\text{ssb}} \in \mathbf{P} \mid b \in \hat{\mathcal{B}}^{\text{split}} \quad (\text{C5.4}),$$

$$x_{s,b} = x_{s,b}^{\text{bl}}, \forall x_{s,b} \in \mathbf{X} \mid b \notin \hat{\mathcal{B}}^{\text{split}} \quad (\text{C5.5}),$$

$$p_{s,b}^{\text{ssb}} = p_{\text{max}}^{\text{ssb}}, \forall p_{s,b}^{\text{ssb}} \in \mathbf{P} \mid b \notin \hat{\mathcal{B}}^{\text{split}} \quad (\text{C5.6}),$$

$$\mathbf{X} \in \{0, 1\}^{N_{\text{CB}} \times N_{\text{BS}}} \quad (\text{C5.7}),$$

$$\mathbf{P} \in \mathbb{R}^{N_{\text{CB}} \times N_{\text{BS}}} \quad (\text{C5.8}).$$

Feasible solution to Problem (4) must satisfy the following constraints:

- C5.1, imposing the serving cell for each point of segment \mathbf{z} , as specified by Algorithm 1 outcome.
- C5.2, specifying, for each cell b , the maximum number of deployed SSB beams to N_{ssb} .
- C5.3, restricting the permissible modifications of each cell within the set $\hat{\mathcal{B}}^{\text{split}}$ to 1.
- C5.4, limiting the SSB beams transmitting power for cell withing the set $\hat{\mathcal{B}}^{\text{split}}$.
- C5.5 and C5.6, mandating no modification with respect to baseline configuration $\mathbf{X}^{\text{bl}}, \mathbf{P}^{\text{bl}}$, for cells not in the set $\hat{\mathcal{B}}^{\text{split}}$; thereby preserving the network's baseline performance and stability.
- C5.7 and C5.8, defining \mathbf{X} and \mathbf{Y} matrices space.

Relative to Problem (3), the complexity of Problem (4) is significantly reduced. This simplification arises from the pre-determined set of serving cells $\hat{\mathcal{B}}^{\text{split}}$, which narrows the search space to these cells exclusively. Furthermore, by limiting the number of beam changes to a maximum of one (as specified in C5.3), the spectrum of potential configurations is significantly condensed.

5.4.4 Extended SSB Codebook

Mirroring real-world scenarios within our modeling, to accommodate beams with varied beamwidths and beamforming gains in the total set of \mathcal{W}^{ssb} , we adopt a switching pattern that begins deactivating antenna columns from the rightmost to the leftmost column. Here, we define the SSB codebook as a complex matrix $\mathbf{W}^{\text{ssb}} \in \mathbb{C}^{M \times N_{\text{CB}}}$, where each column is a M size complex vector representing a defined beam.

In each j -th panel configuration, $M_h^{(j)}$ antenna columns are active, with i denoting the number of deactivated antenna columns. Consequently, the total count of active antennas $M^{(j)}$ is determined by $M_h^{(j)} \times M_v$. Utilizing this configuration, the 2D-DFT codebook $\mathbf{W}^{(j)} \in \mathbb{C}^{M^{(j)} \times M^{(j)}}$ is computed to embody the beamforming characteristics of the active antenna framework. The final codebook $\mathbf{W}^{\text{ssb}} \in \mathbb{C}^{M \times N_{\text{CB}}}$ is defined as follows:

$$\mathbf{W}^{\text{ssb}} = [\bar{\mathbf{W}}^{(0)}, \bar{\mathbf{W}}^{(1)}, \dots, \bar{\mathbf{W}}^{(M_h-1)}], \quad (5.22)$$

with

$$\bar{\mathbf{W}}^{(j)} = \mathbf{F}_{M, M^{(j)}} \mathbf{W}^{(j)}, \quad (5.23)$$

where $\mathbf{F}_{M, M^{(j)}}$ facilitates the mapping of codewords from active to full antenna configurations by inserting zeros for deactivated antennas. Recall that M is the total number of antennas in the antenna panel, and N_{CB} is the total number of codewords. Specifically, $\mathbf{F}_{M, M^{(j)}}$ is defined as follows,

$$\mathbf{F}_{M, M^{(j)}} \in \{0, 1\}^{M \times M^{(j)}}, \quad (5.24)$$

$$\mathbf{F}_{M, M^{(j)}} = \left[\overbrace{\begin{array}{ccc} \mathbf{I}_{M_h, M_h^{(j)}} & \mathcal{O}_{M_h, M_h^{(j)}} & \mathcal{O}_{M_h, M_h^{(j)}} \\ \mathcal{O}_{M_h, M_h^{(j)}} & \mathbf{I}_{M_h, M_h^{(j)}} & \mathcal{O}_{M_h, M_h^{(j)}} \\ \mathcal{O}_{M_h, M_h^{(j)}} & \mathcal{O}_{M_h, M_h^{(j)}} & \mathbf{I}_{M_h, M_h^{(j)}} \end{array}}^{M_v} \right]_{M_v}. \quad (5.25)$$

Matrix $\mathbf{F}_{M, M^{(j)}}$ is composed, both vertically and horizontally, of M_v sub-matrix blocks. $\mathbf{I}_{M_h, M_h^{(j)}}$ denotes an identity matrix reflecting the active antennas, while $\mathcal{O}_{M_h, M_h^{(j)}}$ represents a zeros matrix corresponding to the deactivated ones.

$$f^{\text{eGA}}(\mathbf{y}^q) = f^{\text{eGA}}\left(\begin{bmatrix} \mathbf{s}^q \\ \mathbf{p}^{\text{ssb},q} \end{bmatrix}^T\right) = \min\left(\left\{\mathbb{E}_{\tau, \mathbf{h}^{\text{dl}}}\left\{\gamma_a^{\text{ssb}}\right\} \mid \forall a \in \mathbf{z} \in \mathcal{Z}_{\text{AH}}^{\text{split}}, \hat{b}_a = \hat{b}_z^{\text{split}}, \right. \right. \\ \left. \left. \hat{s}_z = s_{b_z}^q, p_{\hat{s}_z, \hat{b}_z}^{\text{ssb},q} = p_{b_z}^{\text{ssb}}, \mathbf{X} = \mathbf{X}^q(\mathbf{y}^q), \mathbf{P} = \mathbf{P}^q(\mathbf{y}^q)\right\}\right) \quad (5.29)$$

5.4.5 Beam And Power Selection Genetic algorithm

In this section, we present an evolutionary algorithm tailored to address Problem (4), employing a GA framework recognized for its efficacy in solving non-convex mixed-integer optimization problems [99–101]. To enhance the standard GA procedure, we incorporate an elite selection mechanism [102], henceforth referred to as elite genetic algorithm (eGA).

Echoing the approach used in PSO, our eGA initiates its search with a randomly generated population. This population iteratively evolves, guided by a fitness function, towards an optimal solution across successive generations. Within this framework, each individual, denoted as q , symbolizes a feasible solution to the posed problem. The representation of each individual is a multi-dimensional vector, elaborated as follows:

$$\mathbf{y}^q = \begin{bmatrix} \mathbf{s}^q \\ \mathbf{p}^{\text{ssb},q} \end{bmatrix}^T = [s_{b_0}^q, \dots, s_{b_{n_s}}^q, p_{b_0}^{\text{ssb},q}, \dots, p_{b_{n_s}}^{\text{ssb},q}], \quad (5.26)$$

with

$$\forall s_{b_z}^q \in \mathbf{s}^q, s_{b_z}^q \in [0, N_{\text{CB}}], \quad (5.27)$$

$$\forall p_{b_z}^{\text{ssb},q} \in \mathbf{p}^{\text{ssb},q}, 0 \leq p_{b_z}^{\text{ssb},q} \leq p_{\text{max}}^{\text{ssb}}, \quad (5.28)$$

where s_{b_z} indicates the index of the selected beam from a codebook containing N_{CB} entries for cell b_z within set $\hat{\mathcal{B}}^{\text{split}}$, and $p_{b_z}^{\text{ssb}}$ represents its transmitting power. Matrices \mathbf{X}^q and \mathbf{P}^q are subsequently determined based on \mathbf{y}^q .

The evolutionary progress across generations is governed by a fitness/objective function defined as in eq. (5.29), where for each point z in a segment the expected SINR is computed, with γ_a^{ssb} calculated in accordance with eq. (2.30). By considering the expected SINR across multiple shadowing and fast-fading realizations, it is possible to account for different channel conditions, therefore providing robust solutions that can adapt to varying environmental conditions. Moreover, for each point, the assigned serving cell is determined as per the outcomes of the segmentation and selection process detailed in Algorithm 1, with the designated serving SSB beam and its transmit power being set in accordance with \mathbf{y}^q . To accommodate this network variation, \mathbf{X} and \mathbf{P} are updated, accordingly to \mathbf{y}^q , to reflect these selections

and their implications on the network configuration. In this work we consider all the modified SSB beams at cells $\hat{\mathbf{b}}_z^{\text{split}}$ associated with the same i^{ssb} sweep index.

In the eGA, three key operations permit the transmission of information from one generation of the population to the next. These operations are crucial for the evolutionary process: *i*) Selection: individuals/solutions of the population are ranked by their objective function, with the top N_p of them chosen as parents for the next generation. The highest-ranking individual is noted as the generation's optimal solution. *ii*) Crossover: with a chance P_{cross} , elements of \mathbf{y}^q for a random pair of parents are exchanged, thereby creating offspring that blend traits from both. This operation is crucial for diversity and exploration of the searching space. *iii*) Mutation: elements of the new created individuals \mathbf{y}^q (i.e., offsprings) are randomly changed with probability P_{mut} . This step is crucial for diversity and overcoming saddle points. In addition, the algorithm incorporates an "elistic parent selection" mechanism, for which the best N_{el} parents are directly passed to the next generation without undergoing crossover or mutation. This strategy helps to preserve excellent solutions from one generation to the next.

The algorithm iterates through these operations until it reaches a predefined number of generations, $N_{\text{eGA}}^{\text{Iter}}$, or the best solution does not change for a certain number of generations. In Algorithm 3, we present the details of the implementation of our eGA-based algorithm.

Algorithm 3: elite Genetic Algorithm Beam and Power Selection

Data: $\mathcal{Z}_{\text{AH}}^{\text{split}}, \mathcal{B}^{\text{split}}$

Result: \mathbf{y}_{best}

- 1 $\mathbf{y}^{(p)} \leftarrow \text{init_random_population}(N_{\text{pop}}, N_{\text{CB}}, p_{\text{max}}^{\text{ssb}});$
- 2 $\mathbf{f} \leftarrow \text{init_zeros}(N_{\text{pop}});$
- 3 **for** $i \in [0, N_{\text{eGA}}^{\text{Iter}} - 1]$ **do**
- 4 **for** $q \in [0, N_{\text{pop}} - 1]$ **do**
- 5 $\mathbf{f}[q] \leftarrow f^{\text{eGA}}(\mathbf{y}^q);$
- 6 **end**
- 7 $\text{sort_population}(\mathbf{f});$
- 8 $\mathbf{y}_{\text{best}} \leftarrow \mathbf{y}^{(0)};$
- 9 $\text{par}_e \leftarrow [\mathbf{y}^{(0)}, \mathbf{y}^{(N_{\text{el}})}];$
- 10 $\text{par}_q \leftarrow [\mathbf{y}^{(0)}, \mathbf{y}^{(N_p)}];$
- 11 **for** $q \in N_{\text{cross}}$ **do**
- 12 $\mathbf{y}^{(i)}, \mathbf{y}^{(j)} \leftarrow \text{randomUniform_selPair}(\text{par}_q);$
- 13 **for** $k \in 0, [2n_s - 1]$ **do**
- 14 **if** $\text{random}() \leq P_{\text{cross}}$ **then**
- 15 $\mathbf{y}^{(i)}[k], \mathbf{y}^{(j)}[k] \leftarrow \mathbf{y}^{(j)}[k], \mathbf{y}^{(i)}[k];$
- 16 **end**
- 17 **end**
- 18 **end**
- 19 **for** $q \in 0, [N_{\text{pop}} - 1]$ **do**
- 20 **for** $k \in [0, n_s - 1]$ **do**
- 21 **if** $\text{random}() \leq P_{\text{mut}}$ **then**
- 22 $\mathbf{y}^q[k] \leftarrow \text{randInt}(0, N_{\text{CB}} - 1);$
- 23 **end**
- 24 **end**
- 25 **for** $k \in [n_s, 2n_s - 1]$ **do**
- 26 **if** $\text{random}() \leq P_{\text{mut}}$ **then**
- 27 $\mathbf{y}^q[k] \leftarrow \text{rand}(0, p_{\text{max}}^{\text{ssb}});$
- 28 **end**
- 29 **end**
- 30 **end**
- 31 $e \leftarrow 0;$
- 32 **for** $q \in [N_{\text{pop}} - N_{\text{el}}, N_{\text{pop}} - 1]$ **do**
- 33 $\mathbf{y}^q \leftarrow \text{par}_e[e];$
- 34 $e \leftarrow e + 1;$
- 35 **end**
- 36 **end**

5.4.6 Time Complexity

In the following, we discuss convergence and the complexity of the proposed two-stage solution. Specifically, as previously discussed, we rely on two stages, in which the first, based on PSO, aims to optimally segment the AH, while the second, based on eGA, leverage the obtained segmentation and aim to find the optimal cell SSB beams and power configuration for desired cell coverage.

The total complexity of our proposed solution can be computed as the sum of the complexities of each stage, as they are connected in a cascading sequence. Therefore, the overall complexity C^{tot} is expressed as follows,

$$C^{\text{tot}} \equiv C^{\text{split}} + C^{\text{eGA}} \quad (5.30)$$

where C^{split} and C^{eGA} are, respectively, the complexity of the AH split algorithm and the beam power eGA-based algorithm. Note that complexities depend on the number of segments of each iteration, Therefore, in the rest of the section, we upper-bound complexities by always considering the maximum admissible number.

Complexity C^{split} is driven by the number of iterations of the outer loop and the complexity of PAHSS algorithm C^{PAHSS} . So, complexity C^{split} scales as follows,

$$C^{\text{split}} \equiv O\left(N_{\text{seg}}^{\text{max}} C^{\text{PAHSS}}(N_{\text{seg}}^{\text{max}})\right), \quad (5.31)$$

where C^{PAHSS} follow the complexity of PSO algorithm [97,103], and can be expressed as

$$C^{\text{PAHSS}} = O\left(N_{\text{psO}}^{\text{Iter}} N_{\text{swarm}} N_{\text{seg}}^{\text{max}} N_r N_{\text{BS}} M^2\right), \quad (5.32)$$

where term $(N_r M^2)$ refer to SVD complexity, which drives the MAMA metric computation for all the N_{BS} cells, and term $N_{\text{seg}}^{\text{max}}$ is the maximum number of admissible segments and refers to the maximum dimension of each particle within the swarm.

Considering the beam and power selection algorithm, its complexity C^{eGA} follows the one of eGA [99–101], and scales as,

$$C^{\text{eGA}} \equiv O\left(N_{\text{eGA}}^{\text{Iter}} N_{\text{pop}} \left(\log_2(N_{\text{pop}}) + N_{\text{seg}}^{\text{max}} + N_r\right)\right), \quad (5.33)$$

where term $\log_2(N_{\text{pop}})$ refer to crossover and mutation complexity, $N_{\text{seg}}^{\text{max}}$ to each individual dimension and N_r to the objective function complexity computation.

Finally, combining the above equations, the complexity C^{tot} of the overall solution scales as:

$$C^{\text{tot}} \equiv O\left(N_{\text{psO}}^{\text{Iter}} N_{\text{swarm}} N_{\text{seg}}^{\text{max}^2} N_r N_{\text{BS}} M^2 + N_{\text{eGA}}^{\text{Iter}} N_{\text{pop}} \left(\log_2 N_{\text{pop}} + N_{\text{seg}}^{\text{max}} + N_r\right)\right). \quad (5.34)$$

It should be noted that the overall complexity depends linearly on the number of points of the AH N_r and grows quadratically with the maximum number of admissible segments $N_{\text{seg}}^{\text{max}}$, thus showing how the complexity scales with the dimension of the AH. Additionally, similar behaviour is observed for the number of cells in the network N_{BS} and the total number of antennas per sector M , which describes how the complexity evolves with the network deployment dimensions. Finally, the overall complexity scales linearly with almost all hyperparameters of PAHSS and the beam power eGA algorithm, with the exception of the population size in eGA, which suggests that it is preferable to increase the number of iterations instead of the population size for the optimal tuning of this algorithm.

5.5 Optimization Setup

In this section, we adopt models outlined in Chapter 2, and we present and discuss the adopted optimization setup and the converges curves for both algorithms. Specifically, as previously discussed, we rely on two stages, in which the first, based on PSO, aims to optimally segment the AH, while the second, based on eGA, leverage the obtained segmentation and aim to find the optimal cell SSB beams and power configuration for desired cell coverage.

It should be noted that throughout all the analyzed scenarios, the curves show very similar behaviour without exhibiting any consistent trend or relationship with the final UAVs data rate performance. Therefore, in the following, we consider as a reference scenario the URD *Curved* scenario at 150 m altitude, discussed in Section 4.6.

After an extensive search for the optimal hyper-parameters, we set those as reported in Tables 5.2. Within the PAHSS PSO based algorithm, we set the total number of iterations $N_{\text{psO}}^{\text{Iter}}$ to 50, with a total swarm size N_{swarm} set to 100 particles. of particles in the swarm enhances the exploration capabilities of the algorithm, enabling it to cover a broader search area and thereby increasing the probability of escaping local optima and identifying diverse solutions. While increasing iterations allow for more extensive exploitation of the search space, as particles have more opportunities to fine-tune their trajectories towards the most promising areas identified during exploration. Despite the fact they both impact the complexity of PSO based algorithm linearly, as shown in eq. (5.32), it should be noted that typically larger swarms require more iterations to converge, as all the particles need to converge to the same solution. Therefore, the choice between increasing swarm size and iterations depends on the specific nature of the problem, balancing between exploration and exploitation. We recognize in $N_{\text{psO}}^{\text{Iter}}=50$ and $N_{\text{swarm}}=100$ the optimal values for our problem. Then, we set the inertial w , cognitive ϕ_c and social coefficients ϕ_s to respective, 0.75, 0.75, and 0.90; balancing these coefficients further ensures an effective mix of exploration and exploitation, crucial for optimal performance. However,

as for the number of iterations and number of particles in the swarm, precise values depend on the actual problem to solve [104].

Considering the proposed eGA employed to solve the mixed-integer codeword and transmit power selection problem, we set the total number of iterations N_{eGA}^{Iter} to 15k and the population N_{pop} size to 100; despite the decision for the population size follows the same logic for the previous swarm size, here a much higher of iterations are needed due to the random nature of the generation within eGA. Then, to control the evolution among multiple generations, the crossover probability P_{cross} is set to 0.20 to avoid high randomness across multiple generations, the P_{cross} is set to 0.75 to allow to high explore the solution space, and finally the number of parents N_p is 75 with $N_{el}=20$ of them selected as elites. Here, it should be noted that as for the previous PSO-based algorithm, those values highly depend on the nature of the problem and the solution space.

TABLE 5.2: Summary of PAHSS and eGA hyperparameters.

PAHSS (PSO)					
N_{psO}^{Iter}	N_{swarm}	ω	ϕ_c	ϕ_s	$(N_{seg}^{min}, N_{seg}^{max})$
50	100	0.75	0.75	0.90	(2, 12)
Beam and Power Selection (eGA)					
N_{eGA}^{Iter}	N_{pop}	P_{cross}	P_{mut}	N_p	N_{el}
15k	100	0.20	0.75	75	20

Figure 5.3 shows the evolution of the objective function for both PSO-based PAHSS algorithm and eGA-based beam and power selection algorithm. Figure 5.3a specifically reports the evolution of the mean value and the standard deviation of the objective function computed across all the particles.

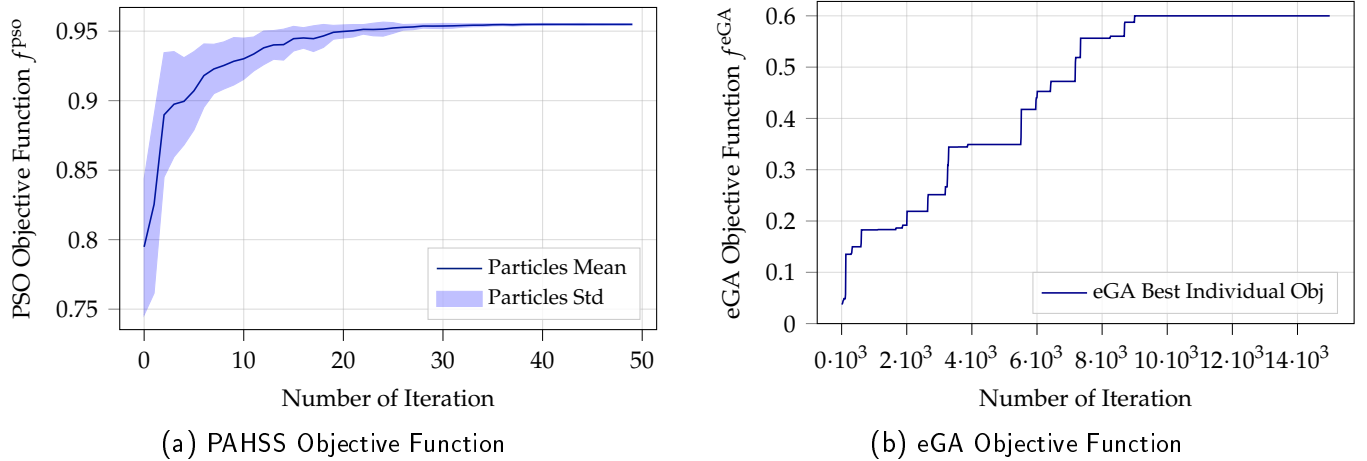


FIGURE 5.3: Objective function evolution for PAHSS PSO-based algorithm (left), and beam and power selection eGA-based algorithm (right).

As depicted in Figure 5.3a, the particles in the swarm tend to converge to the same position and objective function value, thereby converging to the optimal point;

in line with the proof of converges outlined in [103,105,106]. Specifically, it converges in around 40 iterations.

Similarly, Figure 5.3b depict the objective function evolution of the fittest individual in the population for the considered eGA. Authors in [102,107,108] discussed the convergence of GA, showing how optimality is reached if the best solution for each population is maintained and the mutation probability is greater than zero, therefore describing the eGA algorithm here implemented. Specifically, our eGA converge in approximately 12k iterations.

5.6 Two Stage Solution Resulting UAV Data Results

In this section, we examine UAVs data SINR and data rate resulting from our proposed solution aimed at maximizing rates through the optimal deployment of the NR SSB beams within the network.

To demonstrate the benefit of the introduced MAMA metric and the consecutive AH segmentation and SSB beam planning, in the following we present the results obtained by considering a *Curved* AH located within the URD network layout at 150 m of altitude (see Figures 2.2 and 2.3). It should be noted that this scenario is the same scenario discussed in Section 4.6 while discussing the limitation of the work conducted in Chapter 4.

Following the details provided in Chapter 2 Section 2.1, the network consists of 228 gUEs—approximately four per cell—distributed evenly. Additionally, 12 UAVs are positioned along the AHs, with each UAV separated by at least 100 meters [77, 78]. Then, a total of $N_{\text{real}}=1000$ network realization are considered. In each realization, the network random variables are updated, with gUEs positions being randomly re-located and the UAVs advancing along the AH while preserving their relative distances. Moreover, to ensure a continuous flow of UAVs traffic, a new UAV takes off as soon as another completes its journey through the AH.

Figure 5.4 shows the obtained UAVs data SINR (left) and achievable data rate (right) CDFs. In more detail, here we compare three different NR network setups:

- **Baseline**, in which the network is configured with all the SSB beams down-tilted at 105° . Thereby representing the network solely configured to serve gUEs.
- **Cov Opt** in which the network, and in particular the transmitted SSB beams controlling coverage, are configured as a result of the proposed NR coverage SSB beams gradient-based algorithm and framework proposed in the previous Chapter 4.
- **MAMA Codebook**, for which the network is configured as a result of our proposed two-stage algorithm. We refer to this scenario as “MAMA Codebook”

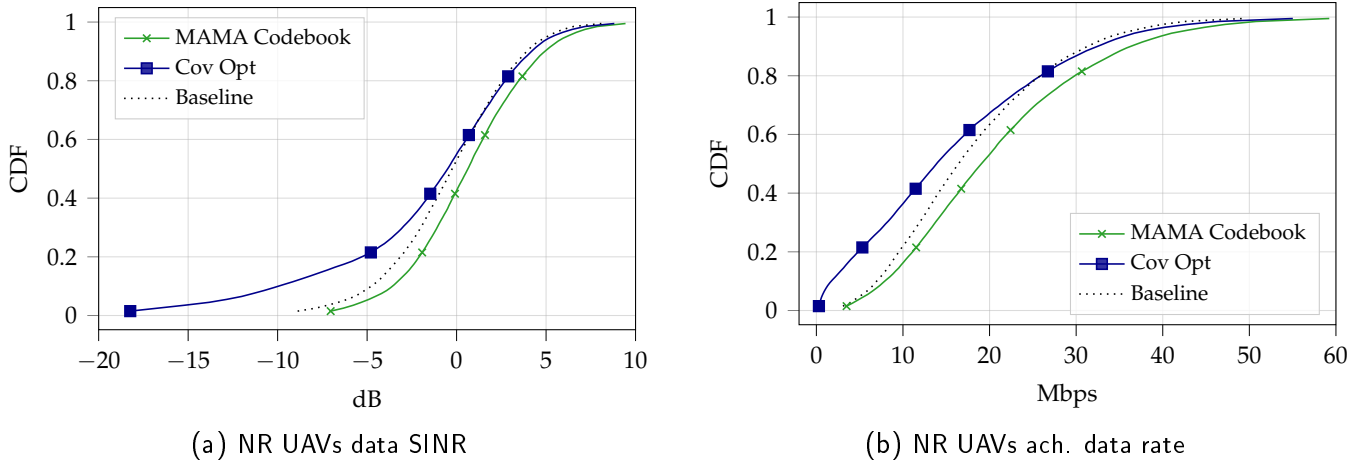


FIGURE 5.4: UAVs NR data SINR (left) and achievable data rate (right) in a curved AH at 150 m in URD, considering AH split and coverage SSB beam codebook selection.

to highlight the use of the MAMA metric for the segmentation and segment-to-cell association and the selection for the SSB beams made over a discrete codebook.

Table 5.3 summarize the obtained results.

Finally, it is important to recall that during the data transmission phase, each cell utilizes a *Type-I CSI* reporting and precoding scheme characterized by its transmission beams.

TABLE 5.3: UAVs NR UAVs data SINR and achievable rate statistics obtained for the aerial highway split algorithm and NR coverage SSB beam codebook selection.

		UAVs Data Statistics		
		Aerial		
		Baseline	Cov Opt	MAMA Codebook
		URD Curved at 150 m		
Data SINR [dB]	5%-tile	-6.34	-13.26	-5.09
	Mean	-0.36	-1.67	0.63
Ach. Data Rate [Mbps]	5%-tile	5.07	0.65	5.67
	Mean	17.99	15.91	20.85

Our obtained results demonstrate the efficacy of our proposed solution, showing how selecting the serving cell and then maximizing coverage from those over specified area, can bridge together coverage and final UAVs data rate performance.

The gain introduced within the final UAVs is resulting from *i)* an overall better SINR condition along the AH during the data transmission, and *ii)* by serving cell choice (i.e., driven by the MAMA metric) for which the better spatial resolution allows multiple beams transmission, thereby allowing increased spatial multiplex gain at the cost of potentially increased of intra-cell interference.

5.6.1 SSB Codeword Beam Selection Limitation

While we have demonstrated how selecting the optimal AH serving cell set can significantly improve the achievable data rates for UAVs, we now turn to discuss the main limitation of the proposed approach. Despite the advantages of the proposed metric (as confirmed by the results presented later), a key challenge remains in the design of the SSB beam codebook. Specifically, the AH might be positioned in locations where the discrete set of beams lacks an optimal configuration, limiting their ability to effectively guide and re-direct UAVs to the serving cell identified by MAMA.

Building upon the previous example, where a *Curved* AH is located at an altitude of 150 m within the considered URD network layout, Figure 5.5 shows the percentage accuracy rate of UAVs associating to the optimal indicated serving cell when passing over specific points of the AHs. From Figure 5.5, we can clearly observe that our solution effectively selects beams capable of letting UAVs associate with the desired serving cell identified by MAMA, with decreasing values observed near the segment edge, where transitions between segments occur as identified by our segmentation Algorithm 2. It should be recognized that within the baseline configuration, MAMA shows a significant rate of association with the designated serving cell. However, it has to be highlighted that this is completely unpredictable, as it is a consequence of an uncontrolled realization of the transmitted coverage SSB beams and the sourcing network layout.

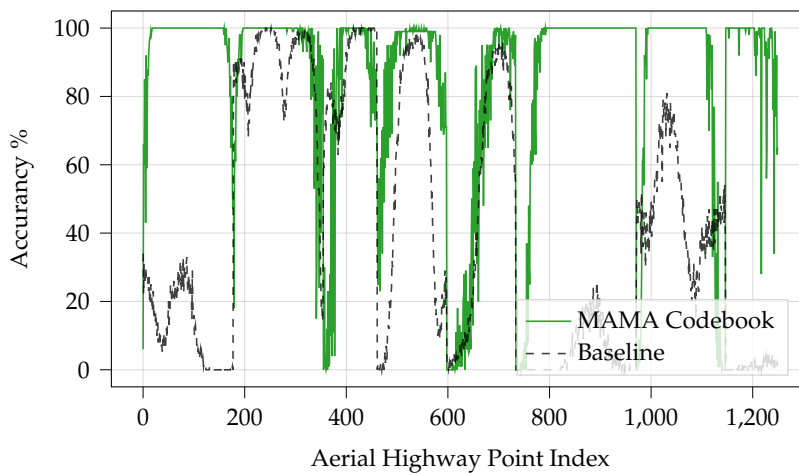


FIGURE 5.5: UAVs association accuracy with MAMA serving cells in each point of the AH and its segments, considering a Curved AH located in URD at 150 m and coverage SSB beam codebook selection.

However, it is sufficient to slightly pull down the AH of 50 m, thereby passing from 150 m to 100 m, to reach a completely different conclusion. Indeed, we step into the scenario where there are cells lacking adequate beams to accommodate the desired coverage. Figure 5.6 illustrate the UAVs desired association accuracy within this scenario.

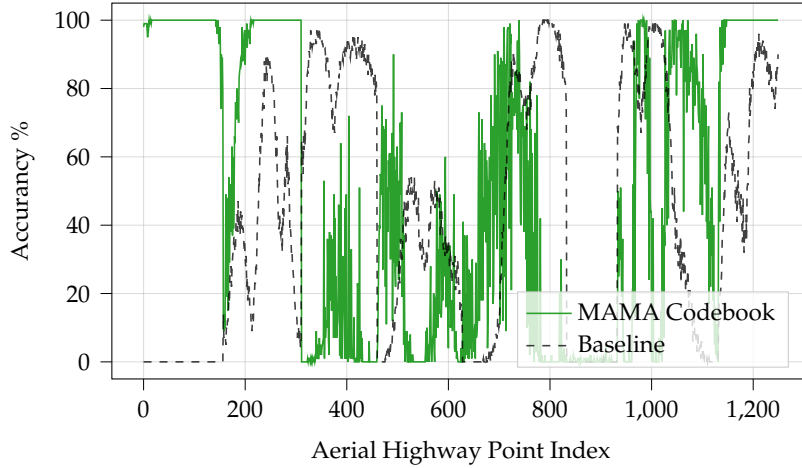


FIGURE 5.6: UAVs association accuracy with MAMA serving cells in each point of the AH and its segments, considering a Curved AH located in URD at 100 m and coverage SSB beam codebook selection.

5.7 MAMA Coverage SSB Beam Continuous Solution

In the following, we tackle the limitation of the previously discussed codebook SSB beam selection. Precisely, we propose a solution that leverages the proposed optimization coverage SSB beam framework proposed in Chapter 4 to find the optimal of SSB beam to transmit within the NR to jointly maximize coverage and let the UAVs associating to the identified serving cell for the belonging AH segment. Thereby searching for the optimal beam solution in the continuous domain and overcoming the limitations of the discrete codebook.

Recalling the problem presented and formulated in Section 4.2, we aim to determine the optimal matrix $\hat{\mathbf{W}}^{\text{MAMA}} \in \mathbb{C}^{M \times N_{\text{BS}}^{\text{MAMA}}}$, where each column is the optimal complex codeword $\hat{\mathbf{w}}_b^{\text{nr}} \in \mathbb{C}^M$ representing the optimal transmitted beam at each cell $b \in \hat{\mathbf{b}}_z^{\text{split}}$, i.e., the set of cells identified by our split algorithm 2 and MAMA metric. Following the methodology present in Section 4.2, we consider the input AH consisting of N_a consecutive evaluation points, which together form set \mathcal{E}_a . Then, following the same objective as the codebook SSB beam selection Problem (4), we aim to maximize the AH coverage SINR $\gamma^{\text{nr-cov}}$ (see eq. (2.30)) by assigning the serving cell for each point according to its segment and the MAMA metric. We recall that all the considered beams within the optimization process in $\hat{\mathbf{W}}^{\text{MAMA}}$ are associated with the same beam sweep index i_s^{ssb} .

The optimization problem is formulated as follows,

Problem 5. NR MAMA Coverage SSB Beam Optimization

$$\begin{aligned} & \max_{\hat{\mathbf{W}}^{\text{MAMA}}} \mathbb{E}_{\tau, \text{hd}} \left\{ \sum_{a \in \mathcal{E}_a} \log \left(\log_2 \left(1 + \gamma_a^{\text{nr-cov}} \left(\hat{\mathbf{W}}^{\text{MAMA}} \right) \right) \right) \right\} \\ \text{s.t.} \quad & \sum_{m=0}^{M-1} |\hat{w}_{m,b}^{\text{nr}}|^2 \leq 1, \quad \forall b \in \hat{\mathcal{B}}^{\text{split}} \quad (\text{C4.1}), \\ & \hat{w}_{m,b}^{\text{MAMA}} \in \mathbb{C}, \quad \forall w_{m,b}^{\text{nr}} \in \hat{\mathbf{W}}^{\text{MAMA}} \quad (\text{C4.2}), \\ & \hat{b}_a = \hat{b}_{\mathbf{z}}^{\text{split}}, \quad \forall \mathbf{z} \in \mathcal{Z}_{\text{AH}}^{\text{split}}, \quad \forall a \in \mathbf{z} \quad (\text{C4.3}). \end{aligned}$$

The problem outlined above exactly mirrors the formulation presented in Chapter 4; however, here two are the main differences with respect to Problem (2), precisely:

1. instead of blindly searching the solution among all the considered network cells, here we only focus on searching for solution within the set of cells identified by our split algorithm 2 and MAMA metric; in other words, we aim to find a solution within the set of cells $\hat{\mathcal{B}}^{\text{split}} \subseteq \mathcal{B}$.
2. We consider an additional constraint to the problem, C4.3. This constraint imposes the serving cell of each point AH evaluation point a according to the belonging AH segment \mathbf{z} and its defined serving cell by MAMA.

The proposed Problem (5) present the same characteristics and challenges as the previously discussed Problem (2). Therefore, to efficiently solve the problem, we adopt the gradient-based optimization framework presented in Section 4.3. We use the same objective function defined in eq. (4.4) to derive the optimal matrices $\hat{\mathbf{A}}^{\text{MAMA}}$, $\hat{\mathbf{P}}^{\text{MAMA}}$, and $\hat{\mathbf{Q}}^{\text{MAMA}}$, thereby realizing optimal matrix $\hat{\mathbf{W}}^{\text{MAMA}}$ as follows,

$$\hat{\mathbf{W}}^{\text{MAMA}} = \frac{1}{\sqrt{M}} \hat{\mathbf{A}}^{\text{MAMA}} \odot \left(\hat{\mathbf{P}}^{\text{MAMA}} + j \hat{\mathbf{Q}}^{\text{MAMA}} \right), \quad (5.35)$$

as discussed in Section 4.3.

However, it should be noted that to handle the search over the limited set of serving cells $\hat{\mathcal{B}}^{\text{split}} \subseteq \mathcal{B}$ and enforce the serving cell, the gradient-based optimization framework presented in Section 4.3.3 must be adjusted to account for variation introduced by Problem (5). Specifically, considering the iterative process based on ADAM depicted in Figure 4.1, to accommodate the MAMA serving cell imposition, we substitute the ‘‘Cell Association’’ block. Figure 5.7 shows the modified structure.

Additionally, it should be noted that modifications have to be also made within the overall optimization framework structure depicted in Figure 4.2. Precisely, given the prior knowledge of the cell from which the solution is sought, i.e., $\hat{\mathcal{B}}^{\text{split}}$, both the ‘‘Cell Selection’’ block and the final ‘‘K-Means Beam Selection’’ blocks can be omitted. Consequently, the updated optimization framework is illustrated as a block diagram in Figure 5.8.

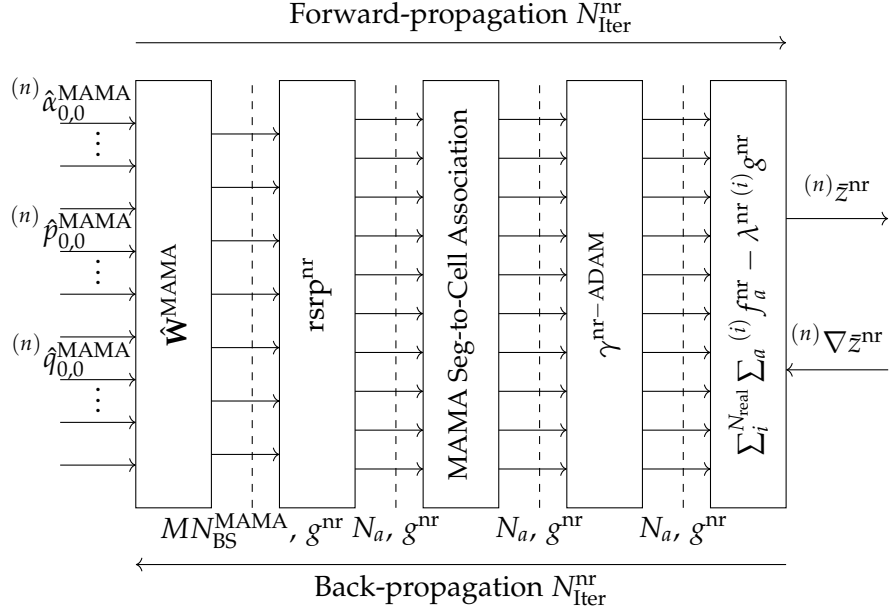


FIGURE 5.7: Block diagram for the MAMA ADAM NR SSB beams optimizer.

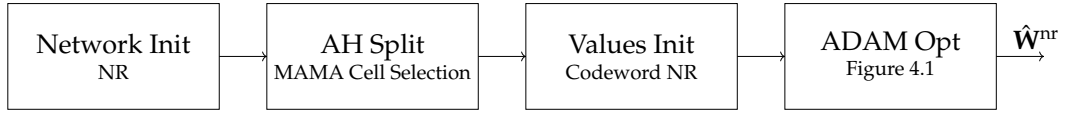


FIGURE 5.8: Block diagram for the NR MAMA SSB beams optimization framework.

Finally, it is important to highlight that these two differences, i.e., the reduced set of cells and the imposed association, simplify the problem. First, the solution now only needs to be sought among a limited number of cells. Second, the imposition of the serving cells eliminates the need for cell selection based on instantaneous SSB beam RSRP measurements, thereby preventing potential ping-pong effects during the solution search.

5.7.1 Two Stage with Beam Coverage Optimization Data Results

In the following, we aim to discuss the optimization result obtained for the AH segmentation and the proposed gradient-based SSB beam optimization.

As no changes in the design of the utility function and input variables occurred, in the following, we rely on the same set of hyperparameters adopted in Chapter 5. Specifically, we set the total number of iterations $N_{\text{iter}}^{\text{nr}}$ to 10k, we initialize the ADAM learning rate μ^{nr} at $5 \cdot 10^{-4}$ applying a 75% decay after every 3000 iterations, and finally, to achieve a consistent solution across multiple channel condition we set the total number of network realization N_{real} to 100.

Then, to underline the benefit of the proposed solution, here we present the results obtained for the URD scenario with a *Curved* URD located at 100 m. Thereby considering the challenging scenario described in Section 5.6.1.

Specifically, Figure 5.9 show on the left the utility function evolution curve obtained for the MAMA coverage SSB beam gradient-based optimization; here referred as “MAMA Cov Opt” to highlight the coverage optimization from the set of cells identified by our MAMA metric and segmentation algorithm. Then, on the right, Figure 5.9 reports the accuracy rate in terms of correct association to the indicated cell by MAMA along the considered AH.

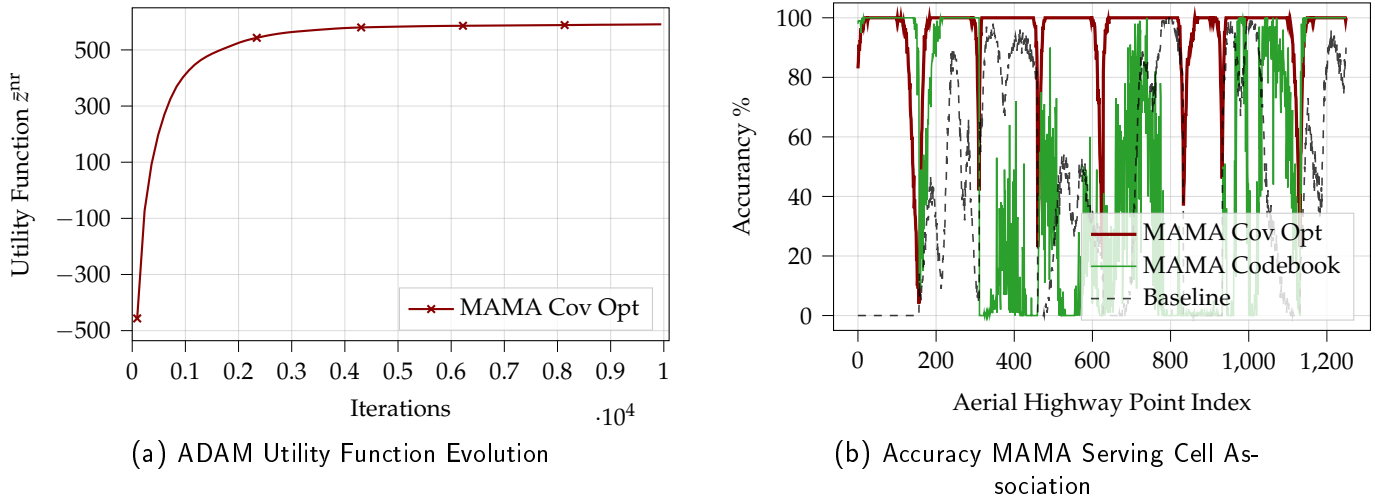


FIGURE 5.9: NR MAMA SSB beam optimization ADAM utility function evolution (left) and UAVs association accuracy with MAMA serving cells (right), considering a Curved AH in URD layout at 100 m.

Figure 5.9b illustrates how our proposed approach, which searches for the optimal SSB beam configuration in the continuous space of complex number, enables the precise design of beams aimed to cover the AH, allowing UAVs to associate with the serving cells identified by the MAMA metric with a major accuracy all along the AH. Thereby overcoming the limitation of the discrete codebook.

To further highlight the benefit of the proposed solution, Figure 5.10 illustrates the obtained final UAVs data SINR and achievable data rate. Precisely, Figure 5.10 show the obtained result within three setups:

- **Baseline:** In this configuration, all SSB beams are downtilted at 105° , representing a network setup exclusively designed to serve gUEs.
- **Cov Opt:** In this scenario, the network is configured based on the proposed gradient-based algorithm for optimizing only NR coverage SINR by “blindly” searching among all the network cells. This configuration is the result of the optimization framework devised in Chapter 4.
- **MAMA Codebook:** This setup is the result of our proposed two-stage algorithm with coverage SSB beams selected from a discrete codebook at each of the cells identified by our MAMA metric.

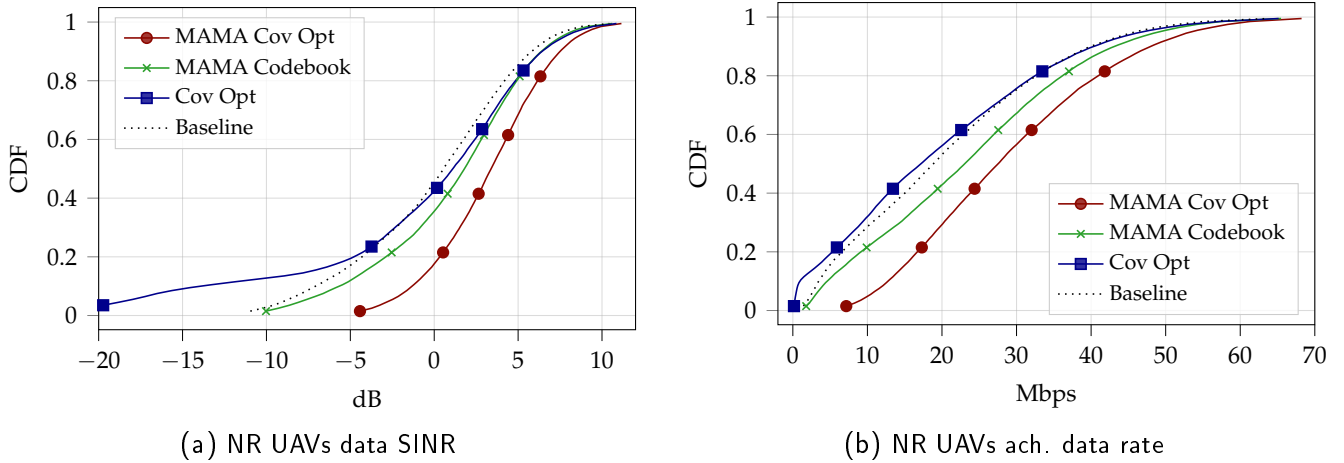


FIGURE 5.10: UAVs NR data SINR (left) and achievable data rate (right) in a Curved AH at 100 m in URD, considering AH split, codebook beam selection and MAMA continuous beam optimization solution.

- MAMA Cov Opt:** This configuration is derived from our two-stage algorithm, where the coverage SSB beams are computed as the optimal solution to Problem (5), using the gradient-based approach outlined in this section.

It is important to note that, within all the proposed schemes, what is modified in the network it is just the set of transmitted NR SSB beams controlling coverage and, most importantly, UAVs cell association. While, during the data transmission phase, each cell within the network relies on the *Type-I CSI* reporting and transmission scheme described in Section 2.6.2.

Analyzing the obtained CDFs in Figure 5.10, we can note how relying on our proposed AH split and selection of coverage beam from a discrete codebook may not be sufficient to increase significantly the overall final data SINR and rate within some scenarios. Whereas the design of precise beams through our proposed gradient-based method allows us to further increase performance and thereby overcome the limitation of a discrete codebook selection.

Results obtained in Figure 5.10 show that splitting the AH according to our proposed solution and optimally design coverage beams from the identified cells permits to accurate control their cell association and, consequently, sensibly increase gains in both data SINR and rates especially at the tails of the distribution; with values up to -2.67 dB and 10.13 Mbps for the 5%-tile of data SINR and achievable rate. Table 5.4 summarize the obtained results.

5.8 Type-A Data Precoder and Simulation Results

Although our MAMA metric and the strategy of transmitting SSB beams to guide UAVs toward optimal serving cells introduce significant enhancements, it is important to note that these adjustments do not lead to dramatic improvements in the final

TABLE 5.4: Summary of final NR UAVs downlink data SINR and achievable rate considering aerial highway split, codebook beam selection and MAMA continuous beam optimization solution.

UAVs Data Statistics - URD Curved at 100 m				
Data SINR [dB]				
	Baseline	Cov Opt	MAMA Codebook	MAMA Cov Opt
	Values [dB]			
5% Tile	-8.90	-18.34	-7.83	-2.67
Mean	-0.02	0.88	1.05	3.23
	MAMA Cov Opt Gain [dB]			
5% Tile	6.23	15.67	5.16	-
Mean	3.25	2.35	2.18	-
Data Achievable Data Rate [Mbps]				
	Baseline	Cov Opt	MAMA Codebook	MAMA Cov Opt
	Values			
5% Tile	2.37	0.36	2.93	10.13
Mean	20.53	19.54	23.68	29.12
	MAMA Cov Opt Gain			
5% Tile	4.27	28.14	3.46	-
Mean	1.42	1.49	1.23	-

SINR or achievable data rates for the UAVs. The reasons stand in the target of the optimization. In this chapter, we have investigated how solely controlling serving cell association for UAVs within segments of the AH can increase their final data performance without the need to introduce real-time schedulers or relying on ad-hoc transmission schemes; thereby realizing a solution capable of being integrated within the planning stage of the network and remaining unchanged regardless of the instantaneous network conditions.

Therefore, in the following, leveraging the results obtained for coverage in Chapter 4, we aim to extend our finding and define an alternative data transmission scheme for UAVs within AH, and finally, conclude this chapter with a comprehensive analysis of the all proposed schemes.

Before introducing this scheme, let's first clarify the reasoning behind its necessity and its formulation. As discussed in Section 5.6.1, relying solely on a discrete codebook can result in a scenario where cells lack beams. Although this concept was previously applied to NR SSB beams, it can easily be extended to the data transmission phase, where beams are selected from a discrete 2D-DFT codebook, as described in Chapter 2 Section 2.6.2 for a *Type-I CSI* precoding scheme. Consequently, it may lead to a scenario where, despite UAVs being connected to the optimal serving cell, the available beams lack sufficient diversity to ensure high data SINRs and rate. Additionally, it should be noted that for each UAV, the selected transmitting beam is chosen based on maximizing the received power at the UAV; therefore, it may not

be fully directed at the intended UAV, as well as it may introduce interference to other UAVs in different segments.

Observing the results obtained for the NR coverage in Chapter 5 Section 4.5, we can note that larger values are achieved for SINR values. As discussed in Chapter 5 these values are achieved through the knowledge of the AH and the joint design of the coverage beams across all the network cells to admit strong serving RSRP while limiting interference; all factors that, if applied also during the data transmission phase, may further enhance UAVs achievable data rate.

Therefore, in the following, we propose two transmission schemes:

- **NR Type-A Cov Opt:** within this setup, upon the optimization of the coverage SSB beams obtained by the optimization framework presented in Section 4.3.3, each cell will use the same beams as serving data beams for its set of connected UAVs.
- **NR Type-A MAMA:** Within this configuration, leveraging the optimal AH split algorithm and the selection of the segments serving cells according to MAMA, the optimal coverage SSB beams are computed as for the gradient-based proposed solution outlined in Section 5.7. Then, each cell will adopt these coverage beams also for transmitting data to all its connected UAVs.

Here, it is important to highlight that both of these proposed solutions are fully compatible with 5G NR multi-antenna transmission configurations. As discussed in Appendix A for multi-antenna systems, although signals and the reported information are standardized, each cell has the capability to selectively disregard certain information and proceed with its own precoder preferences. In this context, a cell may ignore the reported PMI, and if higher-layer signalling identifies the UE as a UAV, the cell can opt to use as data precoder/beam configuration those beams previously employed for coverage.

5.8.1 UAV Data SINR and Achievable Data Rate

In this section, we extend the previously discussed results on UAVs data SINR and achievable rate by incorporating the two proposed schemes outlined above.

We analyse performances obtained for different transmission schemes within URD network layout and different AH configurations such as *Curved*, *Straight Centre* and *Straight Edge* as illustrated in Figure 2.3. Then, for each, we consider three different altitudes, precisely 50, 100 and 150 m. Here, we focus on the performance within URD since, due to the random deployment of network cells within the area network, it is the most generic network layout.

Following models outlined in Chapter 2 Section 2.1, here we consider a total number of 228 gUEs, 4 per each cell on average, uniformly random distributed within the network and 12 UAVs evenly positioned along the AH separated by at least 100 meters [77, 78]. We consider multiple realizations for the network, precisely, we consider a total number of N_{real} realizations equal to 1000 realizations. At

each realization, the network random variables are re-computed, the gUEs are randomly relocated, and the position of the UAVs is advanced along the AH. It should be noted that to have a continuous UAVs traffic condition over the AH when a UAV reaches the AH end, a new one enters.

Then, we compare the obtained performance according to the following transmission scheme:

- **NR Baseline:** the network is configured within all SSB beams downtilted at 105° , and it rely on a *Type-I CSI* reporting and data precoding scheme. This configuration reflects a 5G NR network optimized for gUEs only.
- **NR Type-I Cov Opt:** the network is configured with optimized coverage SSBs beams resulted from the optimization framework presented Chapter 4. We recall that, within this setup, the obtained coverage beams are optimized for maximizing only AH coverage SINR; during the data transmission phase, the network adopts a *Type-I CSI* reporting and data precoding scheme.
- **NR Type-A Cov Opt:** similar to the previous setup, the network is configured as a result of the optimization process presented in Chapter 4. However, here, the network also employs the obtained coverage SSB beams as data beams for its set of connected UAVs.
- **NR Type-I MAMA Codebook:** the network is configured as a result of our proposed MAMA two-stage algorithm with SSB beams selected from a discrete codebook. Here the network uses a *Type-I CSI* reporting and precoding.
- **NR Type-I MAMA Cov Opt:** similar to the previous setup, according to our proposed algorithm, the AH is divided into multiple segments and each serving cell is identified by MAMA metric; indeed, here, the coverage SSB beams are computed as the solution of Problem 5, using the gradient-based proposed approach. Then, for the data transmission, the network relies on a *Type-I CSI* reporting and data precoding scheme.
- **NR Type-A MAMA:** this configuration follows the configuration outlined for “NR Type-I MAMA Cov Opt”, but here, the network employs the obtained coverage SSB beams also as data beams for its set of connected UAVs.

Figure 5.11, 5.12 and 5.13 reports, respectively the obtained CDFs for the UAVs data SINR and achievable data rate within the three analyzed AH configurations, wherein each of them, the results for different altitudes as reported. Table 5.5 reports statistics of the obtained results; precisely, it summarises values for the 5%-tile and mean values.

By analyzing the obtained results, particularly the worst- and best-performing cases, we can draw the following conclusion: referring to “NR Type-I Cov Opt”, we can note that this scheme results in the worst, even worse than “NR Baseline”, which consider the network solely configured for gUEs without UAVs; these results further

highlights that focusing on solely optimizing AH coverage while ignoring any action over the data transmission phase not only fails to enhance performances but actually reduces them. Instead, moving towards the two curves achieving the best results, “NR Type-A Cov Opt” and “NR Type-I MAMA Cov Opt”, we can see that both of them rely on a “Type-A” scheme, and so both using the optimized coverage beams also for the transmission of data along the AH. These results highlight one of the main limitations for UAVs communication on AH: due to the strong LoS component of the channel if the overall distribution of the beamformed power along the AH from terrestrial cells is not controlled, UAVs can perceive low serving power and disruptive interference, thereby resulting in poor SINR condition; thus, relying on the “Type-A” proposed scheme allows to overcome those limitations, allowing to optimal distribute power and maximize communication performances.

Nevertheless, it should be noted that the proposed “NR Type-A MAMA” outperforms all the proposed schemes, especially at the 5%-tile of the obtained curves. Thereby showing how this proposed scheme can provide overall fair and higher results. This gain at the tail of the curves is the result of our introduced AH split and proposed MAMA metric, which prior defines the set of serving cells from which coverage has to be provided for overall enhancing performance in a fairer manner; this is in contraposition to the “NR Type-A Cov Opt” which indeed consider only maximization of mean values (see eq.(4.4)).

It should be noted that solely analyzing the rate, within some scenarios, such as the Single Centre at 100 m depicted in Figure 5.12d, the gain provided by the “NR Type-A MAMA” is limited. However, by analyzing the obtained UAVs data SINR in the same scenario, we can see our solution performs the other in terms of SINR. Therefore, the “NR Type-A MAMA” either outperforms the other scheme in terms of data rate or offers marginally better rates while maintaining a higher SINR. This consideration can be extended to all other scenarios.

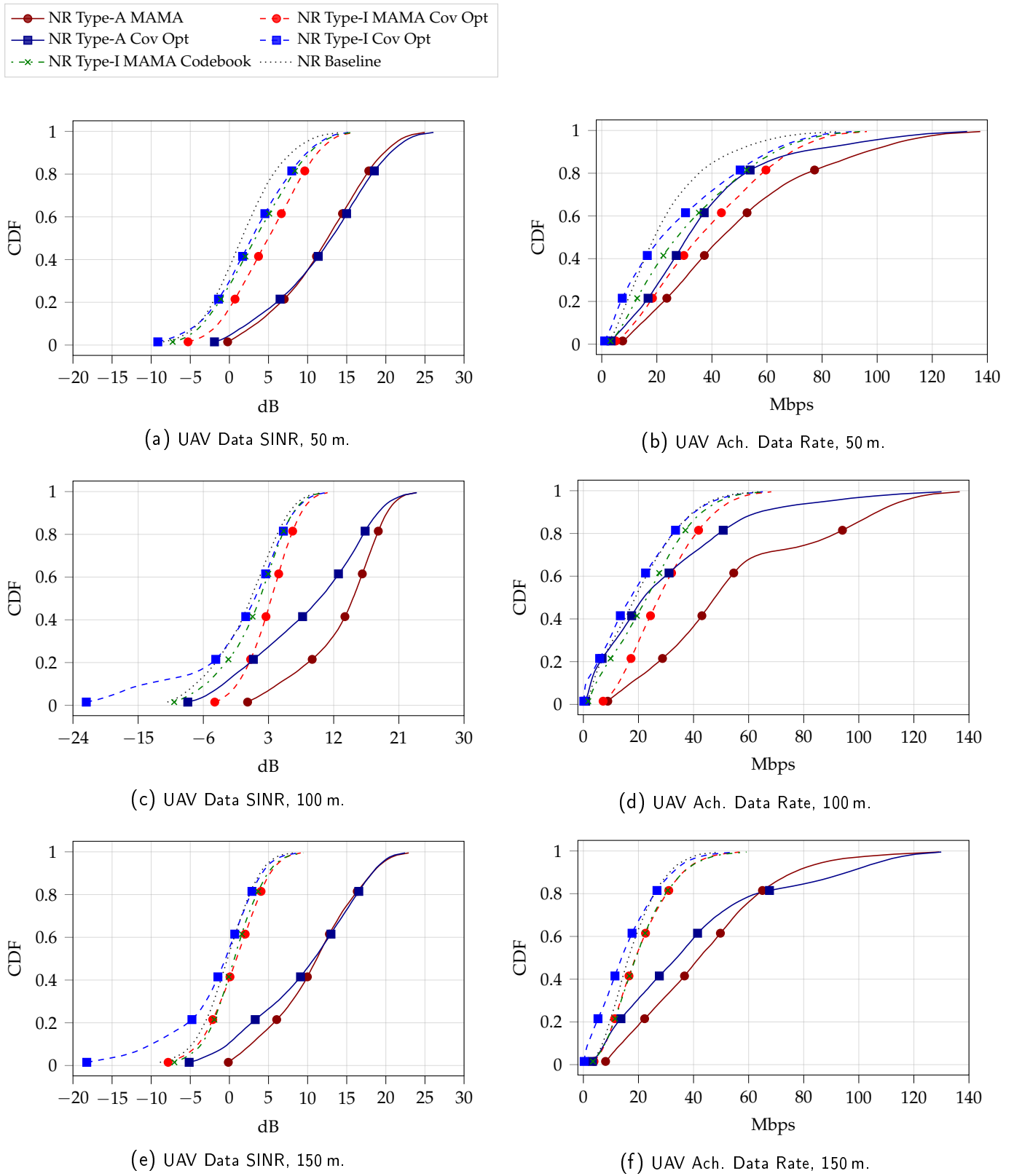
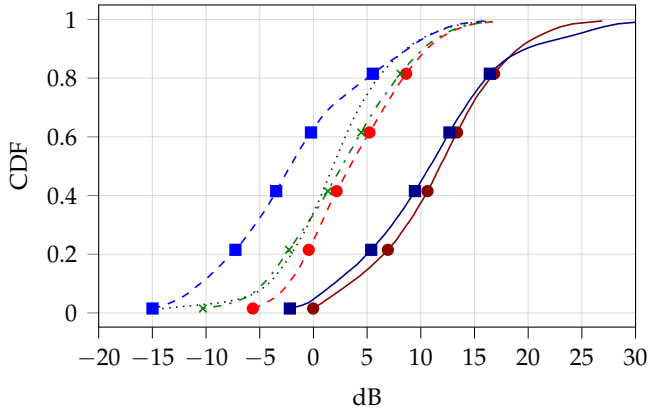
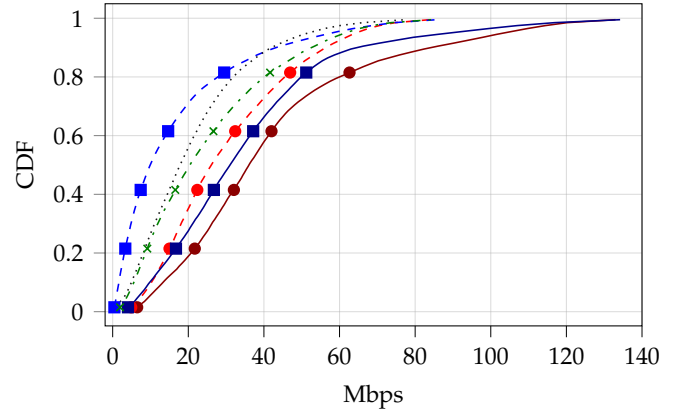


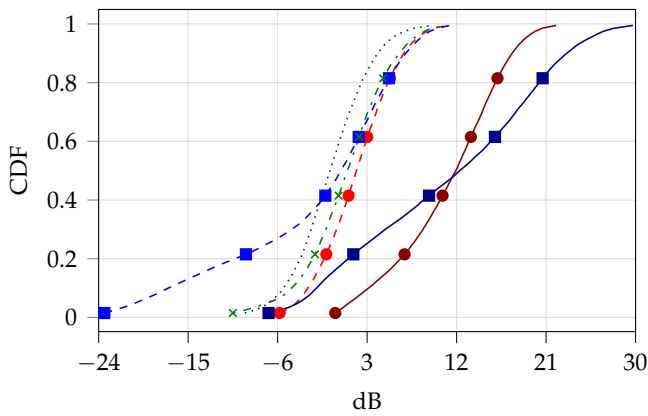
FIGURE 5.11: UAVs data SINR and achievable rate for different scheme considering a Curved AH in URD at different altitudes.



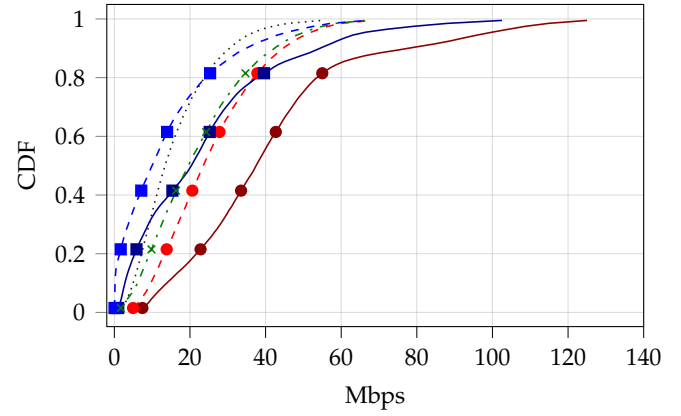
(a) UAV Data SINR, 50 m.



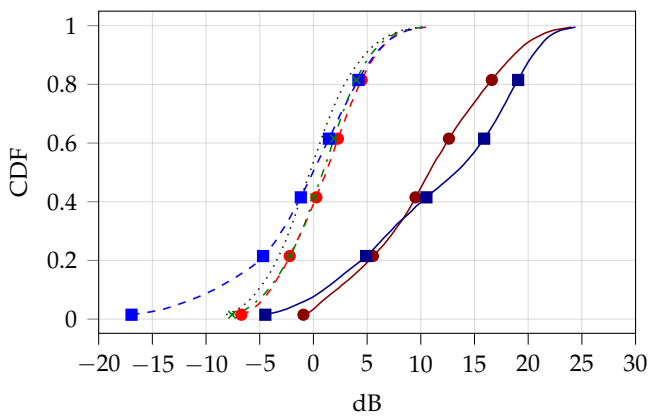
(b) UAV Data Rate, 50 m.



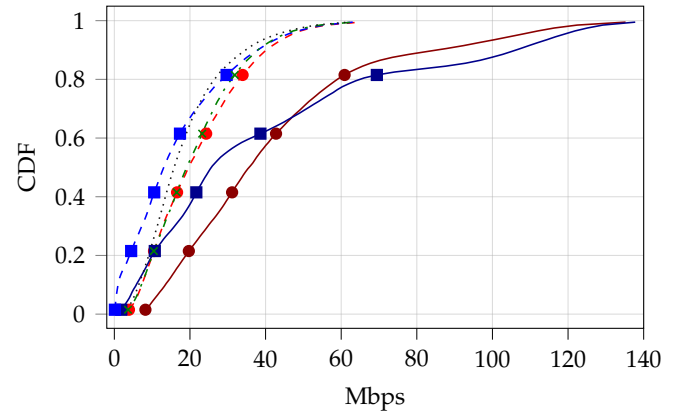
(c) UAV Data SINR, 100 m.



(d) UAV Data Rate, 100 m.

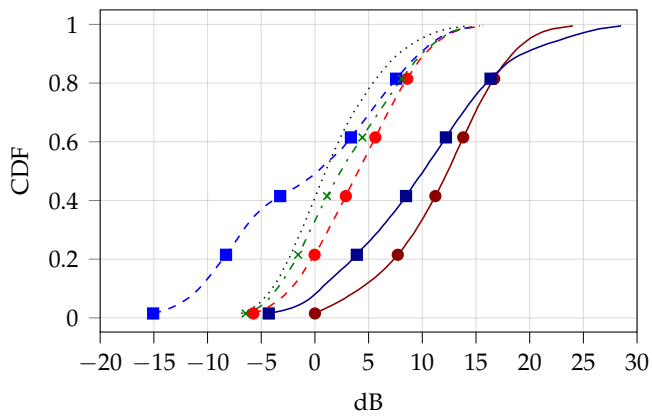
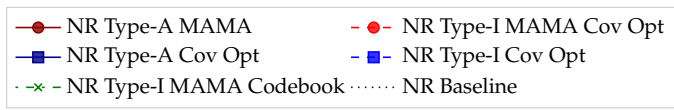


(e) UAV Data SINR, 150 m.

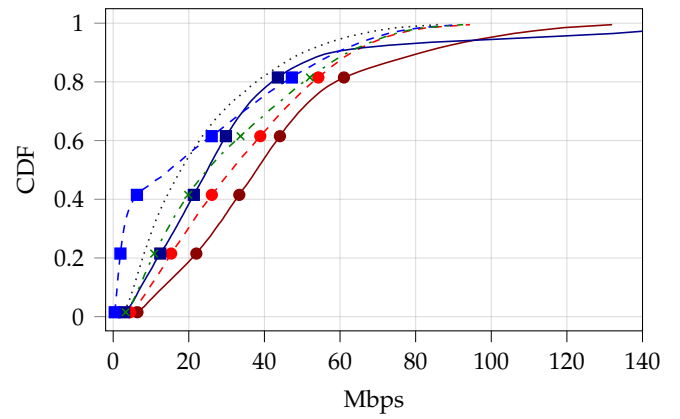


(f) UAV Data Rate, 150 m.

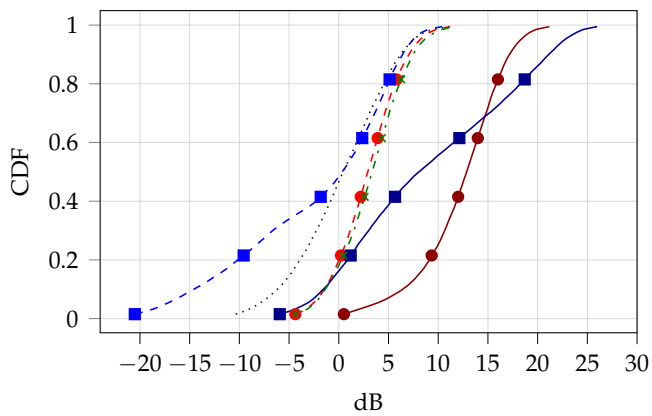
FIGURE 5.12: UAVs data SINR and achievable rate for different scheme considering a Straight Centre AH in URD at different altitudes.



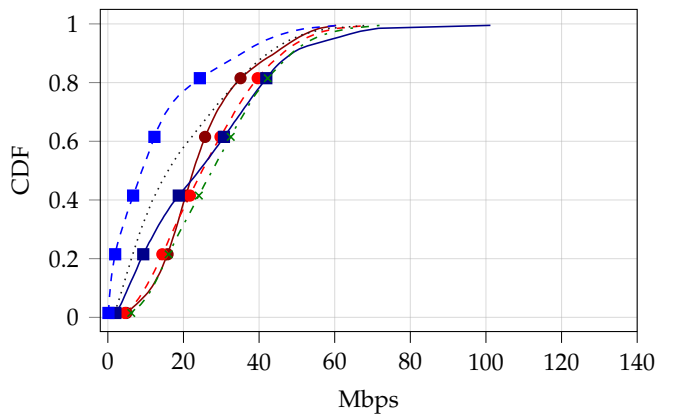
(a) UAV Data SINR, 50 m.



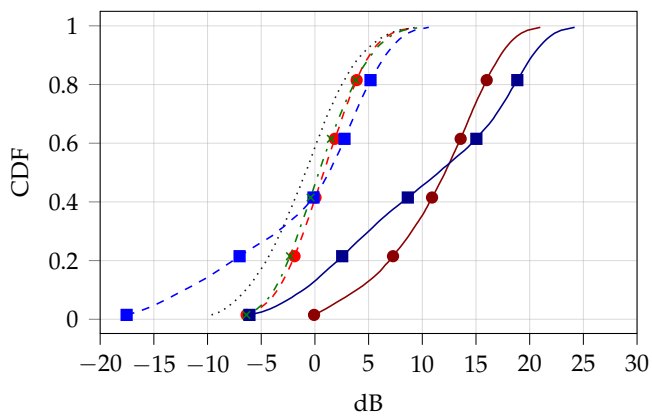
(b) UAV Data Rate, 50 m.



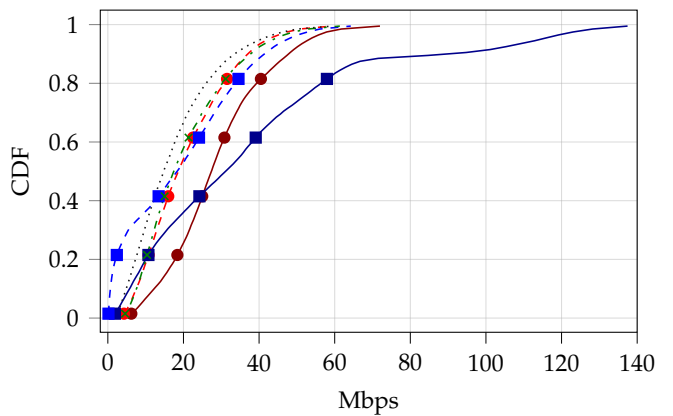
(c) UAV Data SINR, 100 m.



(d) UAV Data Rate, 100 m.



(e) UAV Data SINR, 150 m.



(f) UAV Data Rate, 150 m.

FIGURE 5.13: UAVs data SINR and achievable rate for different scheme considering a Straight Edge AH in URD at different altitudes.

TABLE 5.5: UAVs data SINR and achievable rate for different schemes considering different AH in URD at different altitudes.

	UAVs Data SINR Statistics [dB]					
	50m		100m		150m	
	5%-tile	Mean	5%-tile	Mean	5%-tile	Mean
	Curved					
NR Baseline	-5.67	1.74	-8.90	-0.02	-6.34	-0.36
NR Type-I Cov Opt	-6.32	2.86	-18.34	-0.88	-13.26	-1.67
NR Type-A Cov Opt	0.25	12.24	-5.39	8.61	-2.52	9.79
NR Type-I MAMA Codebook	-4.95	3.38	-7.83	1.05	-5.09	0.63
NR Type-I MAMA Cov Opt	-2.97	4.91	-2.67	3.23	-5.60	0.73
NR Type-A MAMA Cov Opt	1.39	12.13	2.03	13.33	1.14	10.89
	Straight Centre					
NR Baseline	-6.62	1.85	-6.87	-0.71	-6.42	-0.24
NR Type-I Cov Opt	-12.41	-1.52	-20.23	-2.25	-12.55	-0.91
NR Type-A Cov Opt	0.12	11.01	-3.89	11.21	-1.51	11.74
NR Type-I MAMA Codebook	-6.44	2.64	-6.93	0.81	-5.63	0.72
NR Type-I MAMA Cov Opt	-3.67	3.83	-4.11	1.91	-5.14	1.02
NR Type-A MAMA Cov Opt	1.44	11.62	1.23	11.27	0.46	10.71
	Straight Edge					
NR Baseline	-5.16	1.49	-8.08	0.25	-7.83	-0.97
NR Type-I Cov Opt	-12.53	-0.52	-17.40	-2.19	-14.82	-0.86
NR Type-A Cov Opt	-1.16	10.06	-3.30	9.11	-3.32	10.43
NR Type-I MAMA Codebook	-4.70	2.91	-2.52	3.22	-4.93	0.55
NR Type-I MAMA Cov Opt	-3.80	4.02	-2.62	2.85	-4.70	0.81
NR Type-A MAMA Cov Opt	1.93	11.87	3.61	12.28	1.69	11.35
	UAVs Data Achievable Data Rate Statistics [Mbps]					
	50m		100m		150m	
	5%-tile	Mean	5%-tile	Mean	5%-tile	Mean
	Curved					
NR Baseline	4.27	23.41	2.37	20.53	5.07	17.99
NR Type-I Cov Opt	2.34	27.72	0.36	19.54	0.65	15.91
NR Type-A Cov Opt	5.80	36.88	1.67	29.83	5.49	41.12
NR Type-I MAMA Codebook	5.64	31.93	2.93	23.68	5.67	20.85
NR Type-I MAMA Cov Opt	8.55	38.24	10.13	29.12	5.93	20.83
NR Type-A MAMA Cov Opt	10.61	49.53	12.17	55.53	10.39	44.34
	Straight Centre					
NR Baseline	3.03	21.09	3.50	15.91	4.88	18.56
NR Type-I Cov Opt	0.95	16.79	0.10	14.02	0.41	16.75
NR Type-A Cov Opt	6.70	35.76	1.90	24.00	3.72	40.44
NR Type-I MAMA Codebook	3.77	25.04	3.70	22.07	5.50	21.20
NR Type-I MAMA Cov Opt	7.50	30.18	7.34	25.60	5.70	22.04
NR Type-A MAMA Cov Opt	9.52	42.42	10.09	41.39	10.49	42.31
	Straight Edge					
NR Baseline	4.07	23.38	2.68	20.17	3.55	17.32
NR Type-I Cov Opt	0.68	22.99	0.33	13.29	0.34	19.36
NR Type-A Cov Opt	5.21	32.41	3.67	26.30	3.56	37.75
NR Type-I MAMA Codebook	5.08	30.43	9.06	29.05	6.07	20.41
NR Type-I MAMA Cov Opt	6.97	34.31	7.27	26.73	5.83	20.81
NR Type-A MAMA Cov Opt	9.28	42.67	8.03	25.01	8.86	28.88

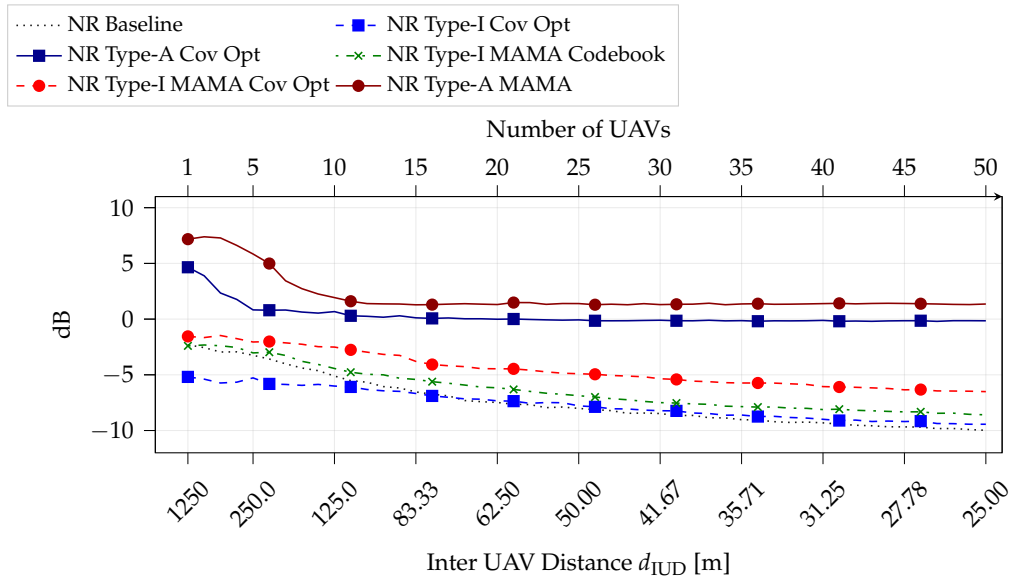
UAV Traffic Analysis

To delve deeper into the advantages of our proposed solution, we explore the impact of different traffic conditions on the AH in terms of UAVs data SINR and achievable rates. Precisely we focus on how the 5%-tile SINR and rates evolve. Building on the URD scenario outlined earlier, we extend the analysis by increasing the number of UAVs on the AH from 1 to a total of 50. These UAVs, maintain a fixed uniform separation distance from one another, denoted as d_{IUD} . Specifically, considering the three AH configurations, Figure 5.14 and 5.15 show how the UAVs data SINR and achievable data rates evolve considering a Curved AH, Figure 5.16 and 5.17 illustrate results obtained for a Straight Centre AH and, finally, Figure 5.16 and 5.17 those obtained for a Straight Edge one.

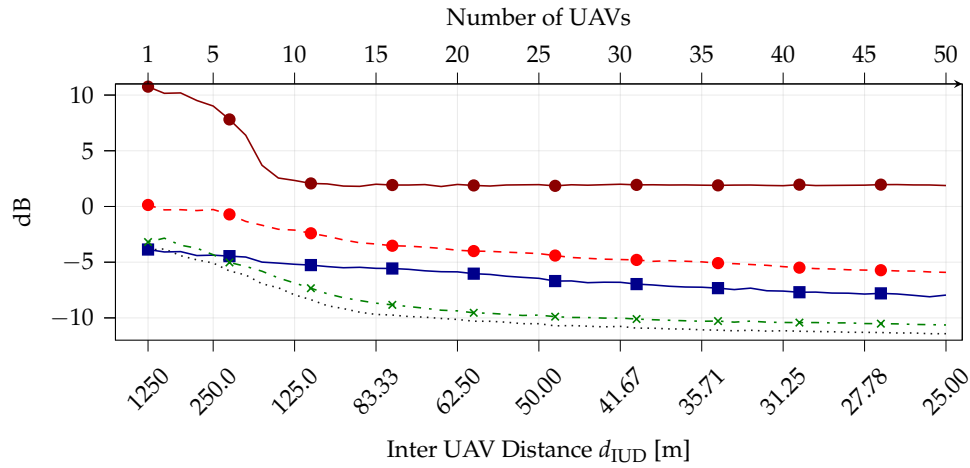
As expected, for most schemes, the data SINR values across all transmission schemes decrease as traffic increases. This is due to the higher number of UAV on the AH, which likely require distinct data beams and, in turn, enhance both intra- and intercell interference. Despite that, it should be noted that our proposed “NR Type-I MAMA Cov Opt” consistently surpass other transmission schemes, therefore highlighting the benefits of our MAMA based AH split and coverage approach.

Considering the obtained data SINR values, when considering the “Type-A” based approaches (solid lines), we observe very high initial values, which drastically drop to a floor condition. The explanation lies in the typical total number of beams fully transmitted over the AH. In the “Type-A” scheme, only a limited number of beams are generally employed to cover the AH and then utilized for data transmission. Due to the fact that these beams are typically well-spaced to cover a specific area (either defined by our AH partitioning or naturally resulting from coverage maximization), the likelihood of all beams being activated increases as the number of UAVs rises. Moreover, once the number of UAVs reaches a certain threshold and all the beams are utilized, no additional beams will be activated. As a result, the SINR will remain constant, regardless of the increasing number of UAVs. A similar consideration can be applied to the achievable data rate performance. However, in the case of “Type-A” schemes, once the number of UAVs surpasses a certain threshold, the performance decreases linearly, as now UAVs must be served across multiple different PRBs.

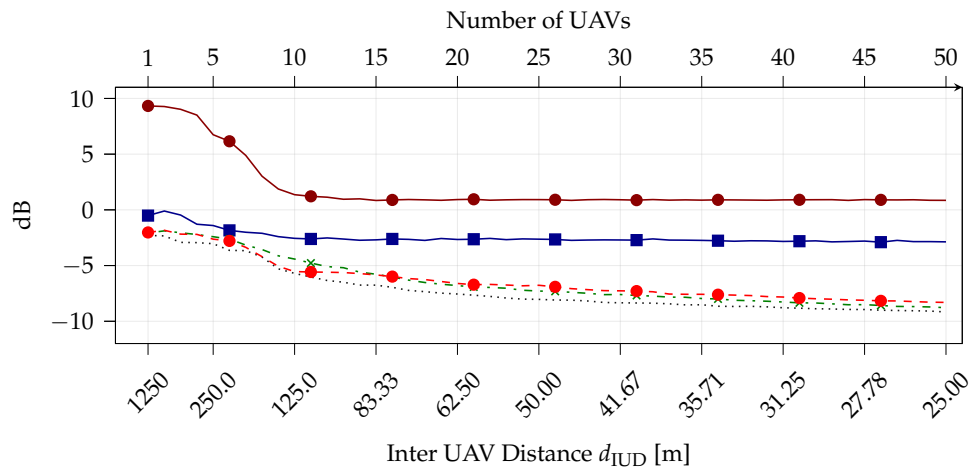
Despite maintaining higher signal quality, our results indicate a significant deterioration in achievable data rate when UAVs are spaced more than one-tenth of the total length (i.e., the threshold number discussed above). This suggests that network operators aiming to integrate AH into their NR cellular networks should carefully manage flight traffic according to the AH if higher data rates are required.



(a) UAVs 5%-tile Data SINR, 50 m.

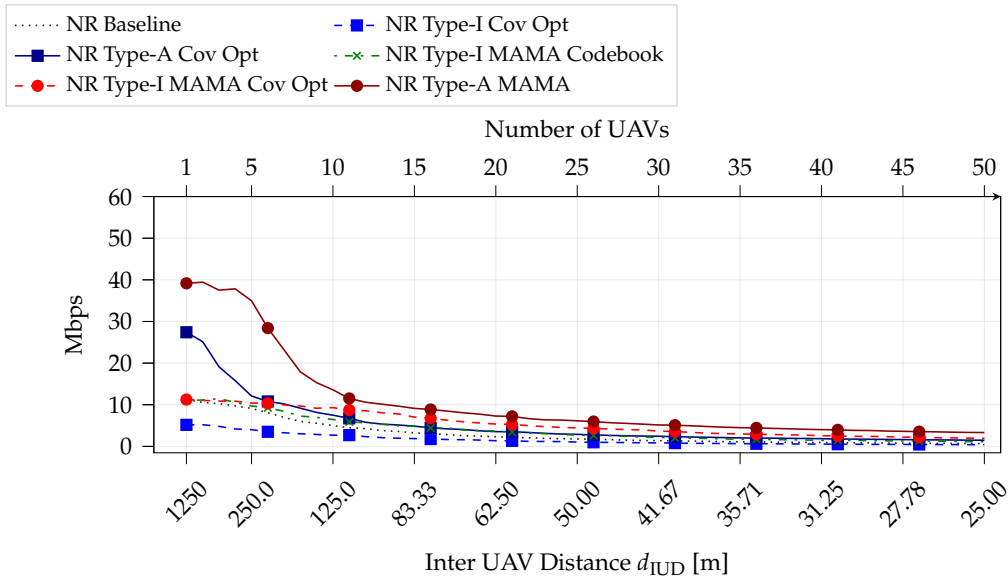


(b) UAVs 5%-tile Data SINR, 100 m.

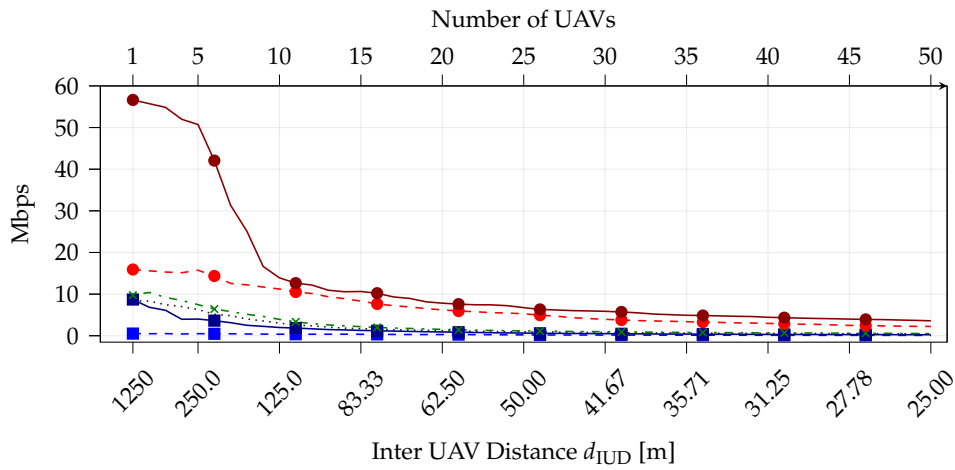


(c) UAVs 5%-tile Data SINR, 150 m.

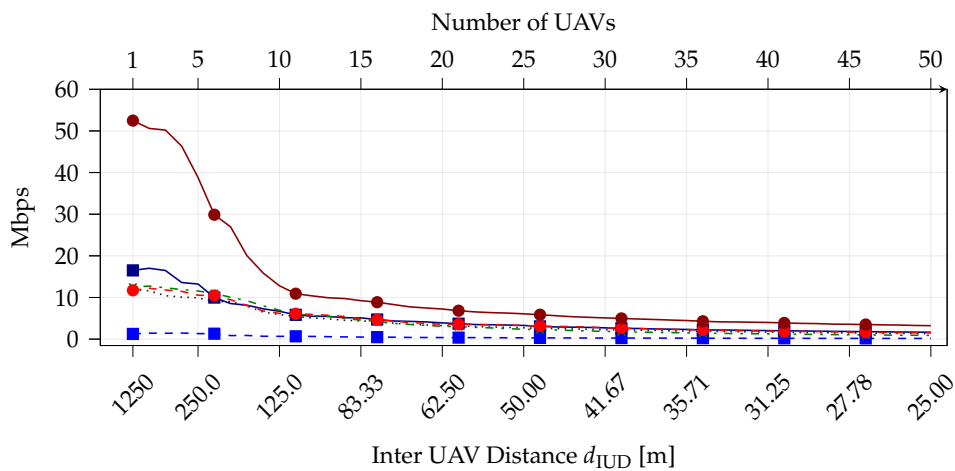
FIGURE 5.14: UAVs 5%-tile data SINR with different traffic aerial highway traffic condition and different schemes considering a Curved AH at different altitude within URD.



(a) UAVs 5%-tile Ach. Data Rate, 50 m.

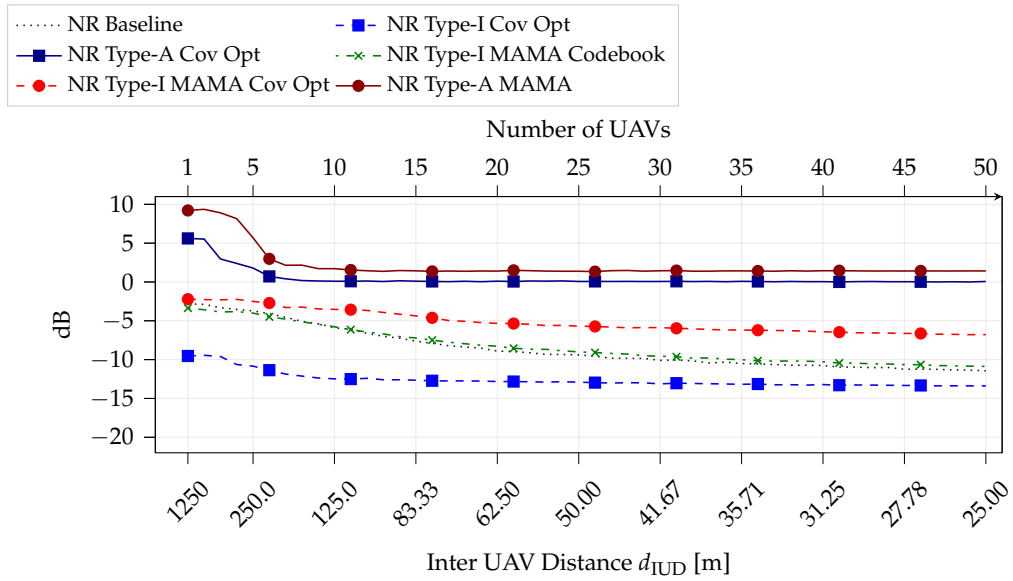


(b) UAVs 5%-tile Ach. Data Rate, 100 m.

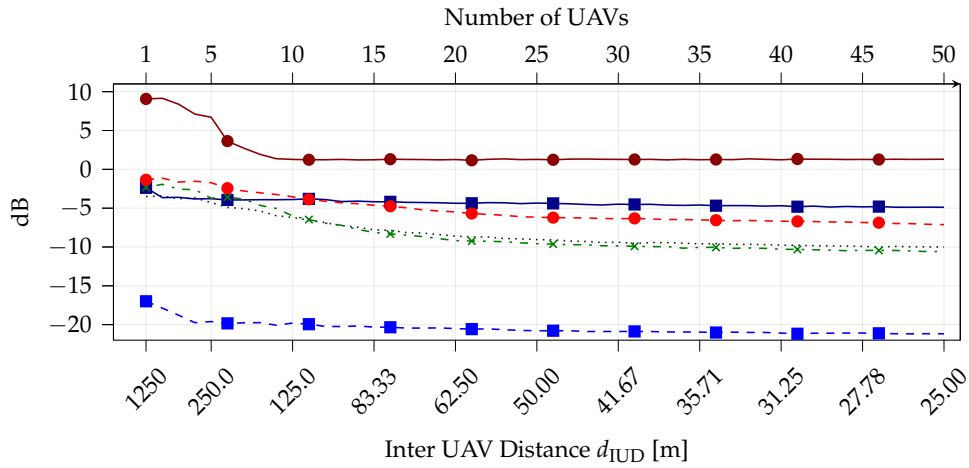


(c) UAVs 5%-tile Ach. Data Rate, 150 m.

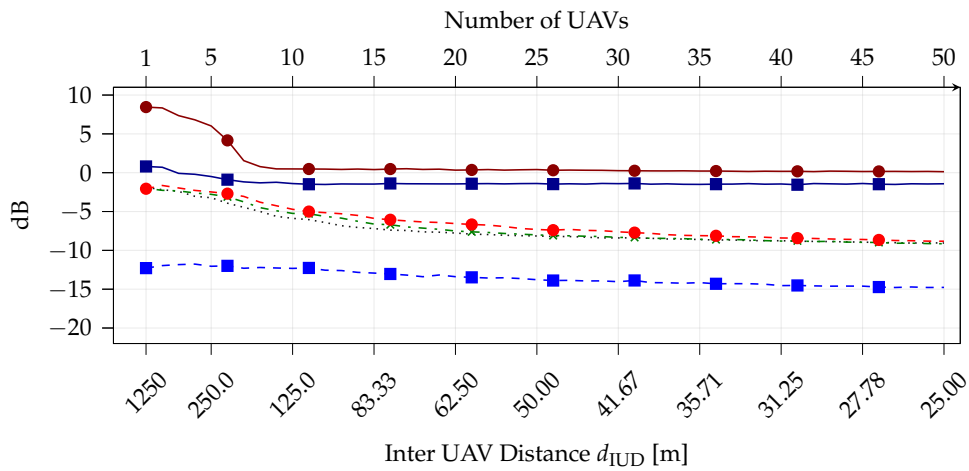
FIGURE 5.15: UAVs 5%-tile achievable data rate with different traffic AH's traffic condition and different schemes considering a Curved AH at different altitude within URD.



(a) UAVs 5%-tile Data SINR, 50 m.

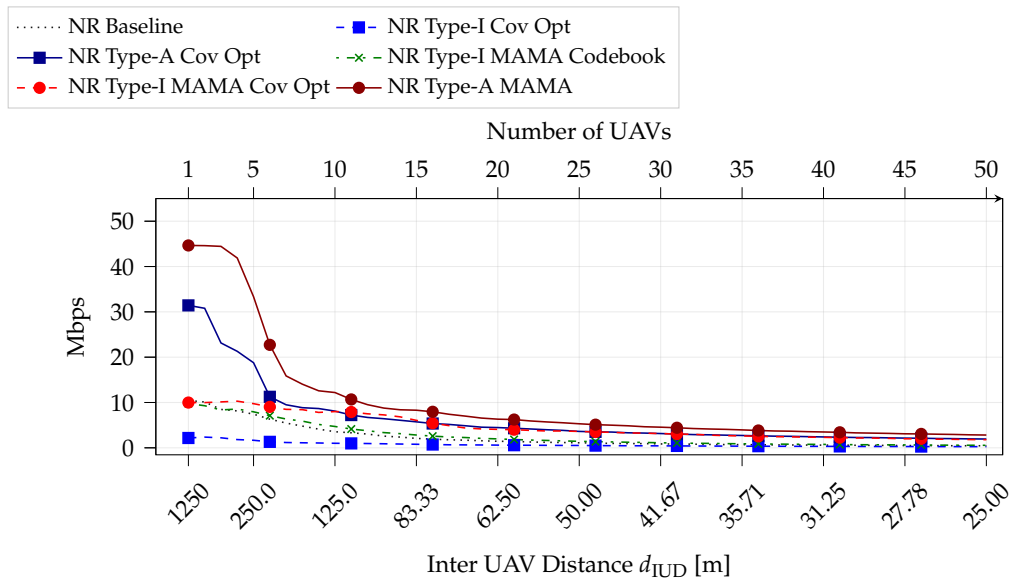


(b) UAVs 5%-tile Data SINR, 100 m.

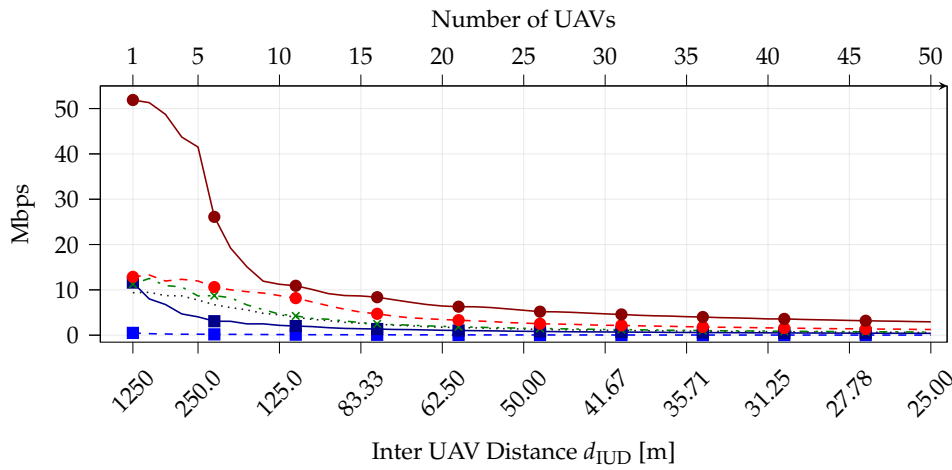


(c) UAVs 5%-tile Data SINR, 150 m.

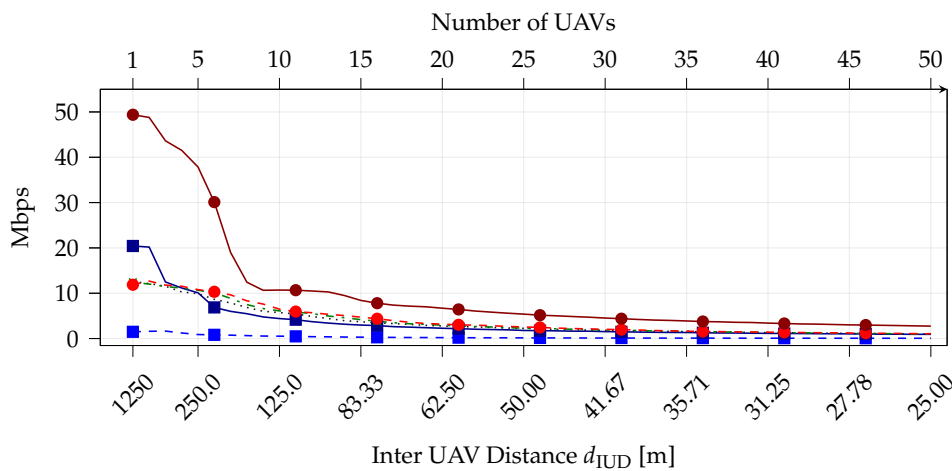
FIGURE 5.16: UAVs 5%-tile data SINR with different traffic aerial highway traffic condition and different schemes considering a Straight Centre AH at different altitude within URD.



(a) UAVs 5%-tile Ach. Data Rate, 50 m.

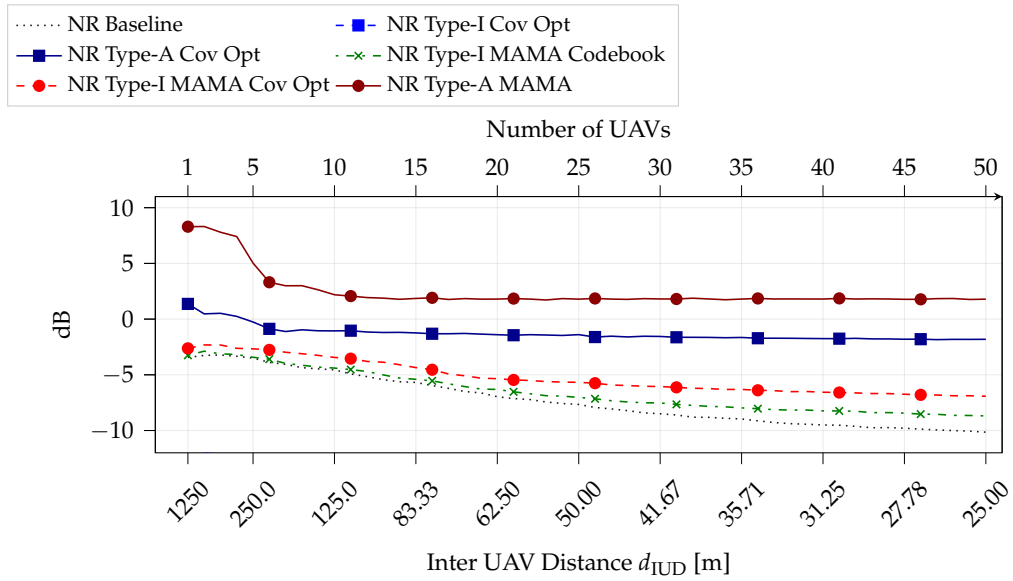


(b) UAVs 5%-tile Ach. Data Rate, 100 m.

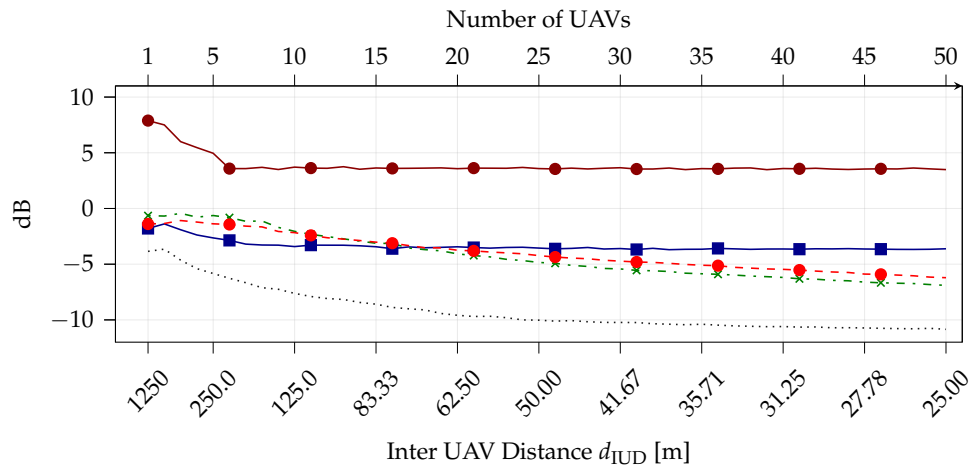


(c) UAVs 5%-tile Ach. Data Rate, 150 m.

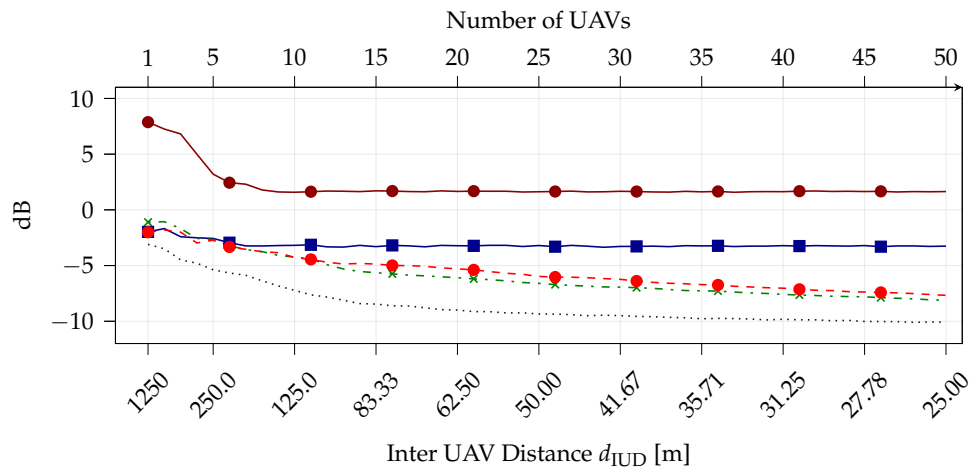
FIGURE 5.17: UAVs 5%-tile achievable data rate with different traffic aerial highway traffic condition and different schemes considering a Straight Centre AH at different altitude within URD.



(a) UAVs 5%-tile Data SINR, 50 m.

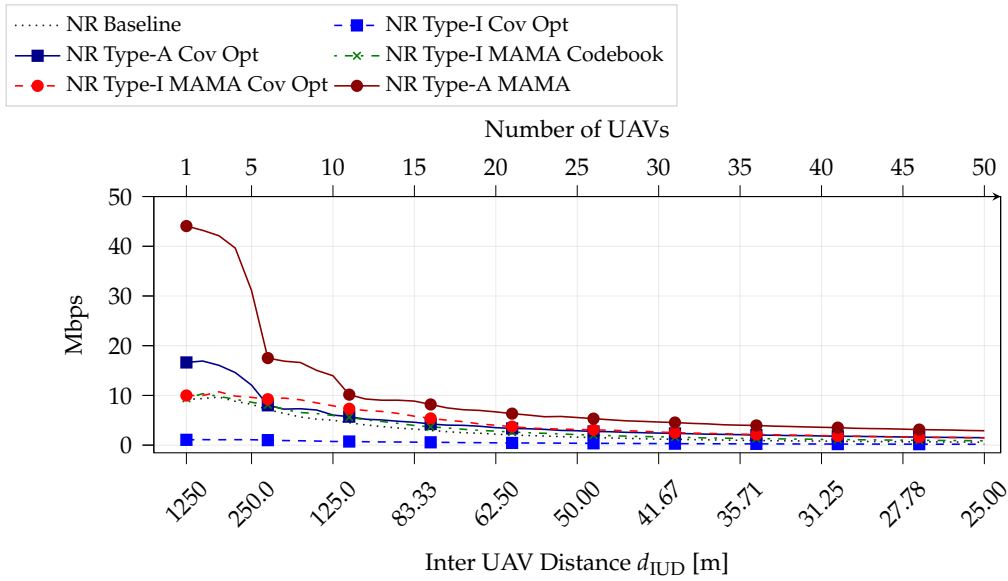


(b) UAVs 5%-tile Data SINR, 100 m.

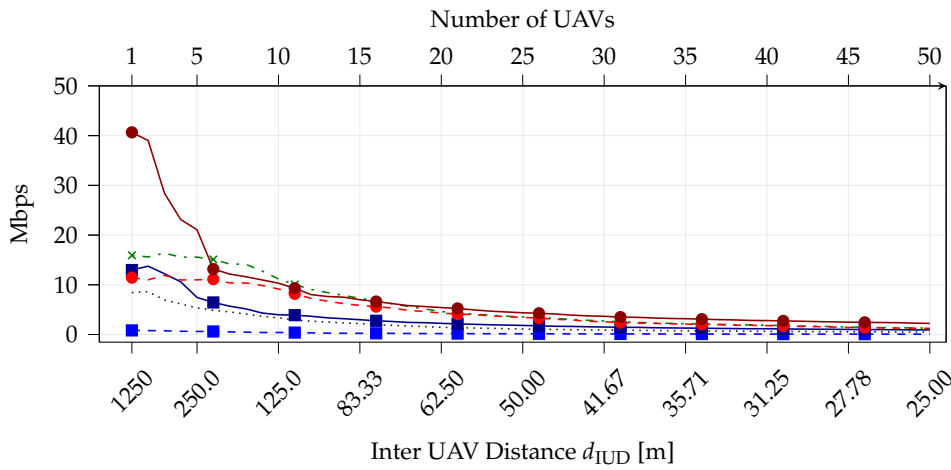


(c) UAVs 5%-tile Data SINR, 150 m.

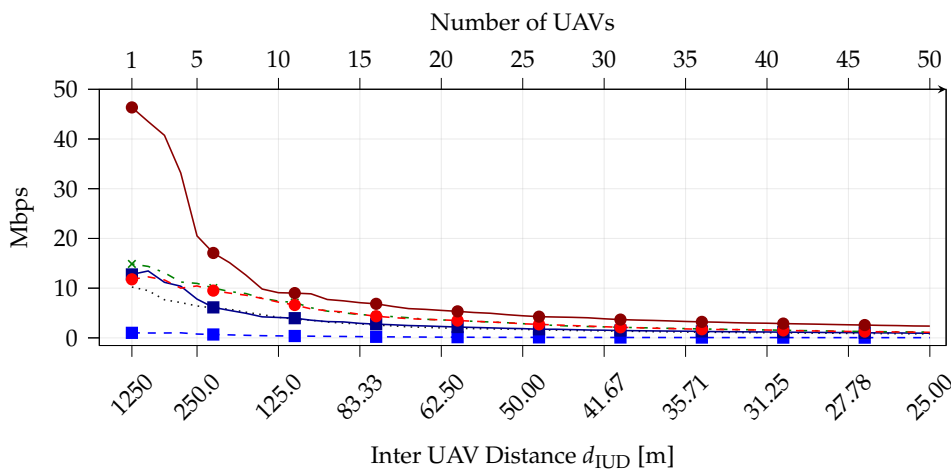
FIGURE 5.18: UAVs 5%-tile data SINR with different traffic aerial highway traffic condition and different schemes considering a Straight Edge AH at different altitude within URD.



(a) UAVs 5%-tile Ach. Data Rate, 50 m.



(b) UAVs 5%-tile Ach. Data Rate, 100 m.



(c) UAVs 5%-tile Ach. Data Rate, 150 m.

FIGURE 5.19: UAVs 5%-tile achievable data rate with different traffic aerial highway traffic condition and different schemes considering a Straight Edge AH at different altitude within URD.

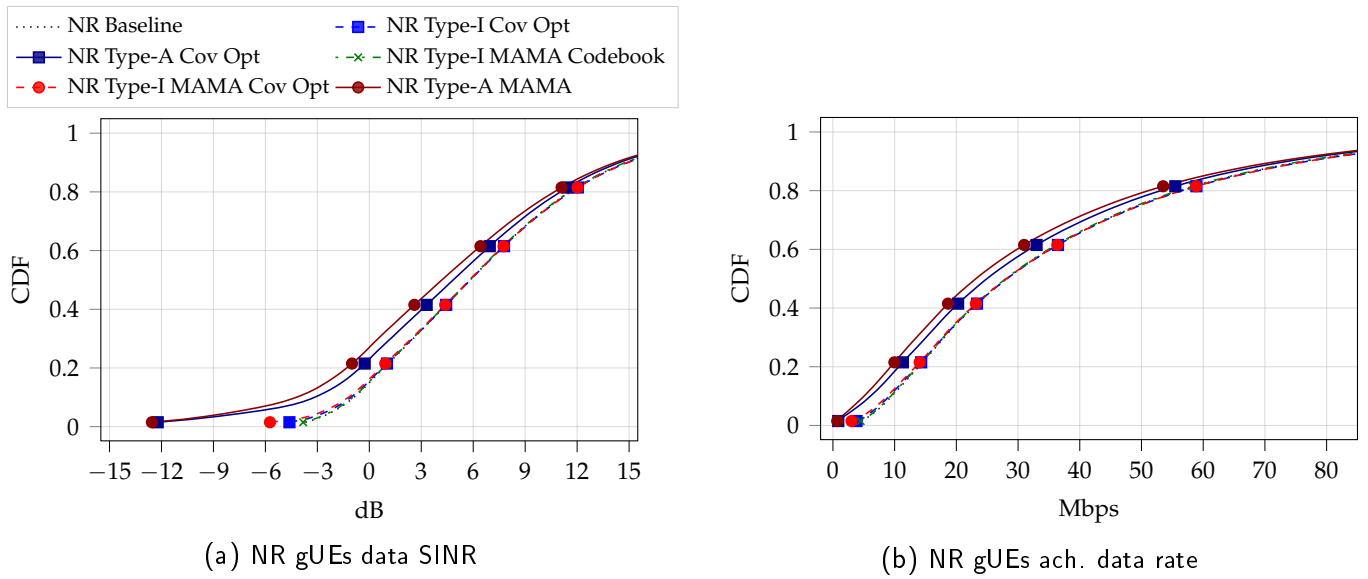


FIGURE 5.20: gUEs NR data SINR (left) and achievable data rate (right) in a Curved AH at 100 m in URD, considering different schemes.

Ground UEs Analysis

In the following, we discuss the impact of our proposed solution on gUEs data SINR and achievable data rate. In particular, we focus on the reference scenario involving a Curved AH positioned at 100 m in URD discussed in Section 5.7.1. It should be noted that similar conclusion can be drawn for all configurations.

Then, models outlined in Chapter 2 are adopted, with a total of 228 gUEs randomly distributed within the ground network, 12 UAVs evenly spaced along the AH and a total of 1000 considered network iterations. Within each iterations, the position of gUEs is randomly updated while the UAVs are together moved along the AH.

Figure 5.20 illustrate the obtained gUEs data SINR and achievable rate CDFs when considering different UAVs optimization schemes.

By analyzing the obtained curves for both gUEs data SINR and rate, two key observations can be made. When utilizing “Type-I”-based schemes, our proposed solutions introduce no sensible degradation in gUEs SINR and rate. This is primarily because the optimization target is only the optimal selection of the serving cell aimed to serve UAVs on the AH; therefore, by keeping the data transmission phase unchanged whether UAVs are present or not, we maintain a similar interference level on gUEs. However, the situation changes when adopting a solution based on “Type-A” transmission schemes. The main reason for this discrepancy is that the beams used for UAVs data transmission can differ considerably from the mutually orthogonal beams generated by 2D-DFT and used in the “Type-I” schemes. As a result, when considering “Type-A” schemes, performances shows a 5 dB and 0.13 negative gain at the 5%-tile of gUEs data SINR and achievable rate, respectively.

These results showcase an interesting trade-off between the achievable improvements for UAV on AH and the cost to pay for gUEs. As such, it is recommended that network operators carefully assess the specific requirements of UAV applications and select the most appropriate optimization and precoding scheme. If high data rate demands are critical, operators must be prepared to accept potential degradation in ground performance.

Chapter 6

Conclusion

Following the growing market of UAVs operations in civil urban areas, we envision that regulatory bodies and government agencies will move towards the implementation of AHs to ensure secure and safe operations. AHs are planned trajectories tailored to comply with different constraints that UAVs have to follow while pursuing their task. Within this new paradigm, we foresee that AHs design will be driven only by safety and business criteria, with cellular connectivity being treated as a commodity. However, relying on current legacy cellular networks for UAVs connectivity is not a reliable solution so far, as networks are optimised to serve solely gUEs. Therefore, to provide reliable connectivity in the sky, further solutions must be investigated to tackle the inherited challenges of UAVs communications.

In this thesis, we mainly focused on investigating, from a system-level network perspective, how sub-6 GHz cellular network can be re-optimized and re-used to provision reliable and robust connectivity to UAVs along AHs. Precisely, we focus on providing solutions to address our research question **“How to use the information regarding the planned AH to optimize deployed terrestrial cellular network at their planning stage, such that optimal service can be provisioned to UAVs without affecting ground performance?”**

In the first part of this thesis, in Chapter 3, we concentrated on optimizing terrestrial 4G LTEs networks to ensure connectivity along the AHs. We introduced an optimization framework based on gradient computations, utilizing AH data to adjust the vertical tilt of the terrestrial LTE network, enabling optimal power distribution and enhancing coverage across the AH. Our simulation results demonstrated the efficacy of our approach. Specifically, when comparing to traditional network configurations, i.e., cellular networks optimized solely for gUEs, our solution introduced SINRs gains up to 9 dB at the 5%-tile and 12 dB at the mean value of the distributions, drastically reducing out of coverage conditions for UAVs with an almost null loss on gUEs performances. In terms of achievable data rate, our solution achieved up to almost seven-fold values, providing gains at each altitude and network layout configuration. Thereby allowing to support high demand rates and/or facilitate a more efficient resource utilization for 4G LTEs AHs connectivity. Finally, large gains

obtained for UAVs data rates came at a minimal cost for gUEs, thereby further highlighting the benefits of our approach. Despite the improvements achieved, our results also reveal key limitations of the LTE vertical tilt optimization frameworks we examined. Within the UMi scenario, or in general relative high altitudes, the benefits of our proposed solution are considerably less. This reduction occurs because of the limited height of the sectors, especially in UMi, which are more challenging to uptilt to serve AHs at higher altitudes while still maintaining ground coverage. Therefore, our results suggested that network operators who aim to integrate AHs and serve them with 4G LTE networks should push for low altitude operation if, in addition to minimum performance, they also target high data rate peaks. In addition, we recommend network operators carefully study the surrounding environment within UMi scenarios, as well as consider additional techniques to enhance UAVs performance along AHs.

Then, we moved a step forward in the cellular network generation and, to tackle the limitation discussed for 4G LTE, in Chapter 4, we investigated how the multi-antenna transmission capability inherited with 5G NR systems and the information regarding the planned AH can be jointly leveraged to provide enhanced coverage along the AH. Specifically, unlike 4G LTE in which coverage signals are transmitted within a unique larger beam, 5G NR has the capability of transmitting those signals within multiple specific directions using multiple distinct coverage beams. Therefore, we developed a gradient-based optimization framework that utilizes AHs information to design optimal coverage beams from surrounding network cells. Additionally, this framework identifies the most crucial beams for providing coverage over the AH while retaining the remaining beams as per the legacy network configuration, i.e., those designed to serve gUEs only, thereby minimizing deviations from the original setup. Our findings demonstrated the efficacy of our approach, highlighting how the higher complexity and flexibility of multi-antenna systems can significantly enhance coverage with all scenarios, thereby overcoming the limitations of previous network generations. In particular, when comparing obtained performance against those resulting from the network configured only for gUEs, our solution introduced gains up to 6 dB at the 5%-tile and gains exceeding 10 dB at the mean of the distribution of coverage SINR along the AH. Moreover, when comparing performance against 4G LTE network setups, our solution significantly outperformed the previous LTE generation, especially at higher altitudes where gains exceeding 10 dB are achieved. Therefore, our results proved the effectiveness of our approach, offering network operators an effective method for designing and planning their 5G NR networks to achieve enhanced AH coverage. Additionally, we recommend to operators to consider higher operating altitudes when utilizing multi-antenna systems; since the downtilted narrow beams help reduce interference from neighbouring cells, and the flexibility of fully digital beamforming allows for delivering strong serving power.

Nevertheless, the separation between the beams allocated for coverage and those

utilized for data transmission limits the advantages of the method proposed above in improving UAVs data transmission. Therefore, in the rest of the manuscript, we focused on devising a solution capable of merging coverage and capacity optimization. Thus, in Chapter 5, to increase the final UAVs data rate along the AH, we investigated a solution that can be adopted during the planning stage of the network and remain unchanged regardless of the instantaneous network conditions. To account for that, we devised a solution capable of optimizing the final UAVs achievable data by solely controlling the serving cell selection along the AH; first, by identifying the set of optimal AH serving cells and then by defining the set of their transmitted beams to maximize coverage. Specifically, we introduced a novel metric called MAMA to optimally select the serving cell for each AH segment. This metric jointly accounts for multiplexing capability, average gains, and interference information across each segment and cell within the network. Then, leveraging the proposed metric, we devised a two-stage solution to define the optimal set of segments composing the AH, their respective optimal serving cells and define the optimal set of beams to maximize coverage from those. To define the set of coverage beams, we proposed two solutions in which: *i*) by exploring realistic conditions, the set coverage beams are limited to a discrete set and *ii*) it is possible to design precise beams by optimally adjusting the antenna phase shifters within the continuous space to maximize coverage. Our results demonstrated the efficacy of our proposed approach. Nevertheless, when considering beams selected from a discrete set, our result showed the main limitation of this method; as, for certain network and AHs configurations, the discrete set lacks of beams pointing towards the AH segment to serve, consequently preventing the desired association. Instead, when considering coverage beams designed from continuous spaces, this problem is overcome. Therefore, suggesting to network operators which aim to integrate AHs, divide and illuminate them according to our proposed scheme, to study the available set of beams carefully and, if needed, integrate our proposed solution to facilitate the design of precise beams and in turn maximize UAVs data rate.

Finally, to further enhance UAV data rates, we proposed adopting a dedicated data transmission scheme along the AH, utilizing the designed coverage beams not only for optimal coverage but also for data transmission. Our results demonstrate the efficacy of this approach, with values up to 10 Mbps at the 5% tile and 44 Mbps at the mean of the obtained achievable data rate distributions. Where best results, particularly at the 5%-tile, have been achieved when considering beams transmitted according to segmentation and MAMAs serving cell definition. The main drawback of this proposed scheme is the larger loss introduced on gUEs data rate performance. This suggests that network operators should carefully select the appropriate precoder for UAVs communication based on the specific application requirements, as achieving higher fairer rate values for UAVs may result in a reduction in rates for gUEs.

6.1 Future Research Directions

Future work will extend our analysis by addressing additional challenges inherent by UAVs cellular communications, as well as exploring diverse communication technologies and transmission schemes. Specifically, future studies will examine and assess solutions for handover issues, which are critical for maintaining seamless connectivity in cellular networks. Similarly, uplink aspects will be investigated, including solutions to optimize onboard equipment and transmission schemes; thereby enhancing integration within urban environments.

Moreover, future research will address how the information derived from planned AHs can be utilized to design linear and non-linear precoders for UAVs; as well as studying how AHs information can be used to enhance cooperation among multiple cells to improve connectivity, as in cell free mMIMOs (CF-mMIMOs) systems. Additionally, future work will also study and analyze solutions and optimization problems employing different technologies and spectrum bands, such as mmWaves.

Importantly, understanding how to employ and optimally integrate NTN, such as satellites and high-altitude platform stations (HAPSs), will also be a focus of future works. As, in a broader context, we may consider generalizing AHs to only “highways” –thereby embracing aerial, terrestrial and even railways– and investigate how to utilize this planning information to optimize key parameters of NTN and HAPS systems.

Appendix A

NR Multi Antenna Transmission

Multi-antenna transmission is a key component of NR and provides substantial benefits in mobile communication systems. By adjusting the phase and amplitude of each antenna element, multiple antennas at the transmitter can direct and focus transmitted power in specific spatial directions. Thereby increasing achievable data rates by optimally directing power and possibly reducing overall interference within the system.

Moreover, the capability of transmitting beamformed signals allows multi-antenna systems to enable simultaneous downlink transmission to multiple devices using the same physical resources. This facilitates the implementation of multi-user multiple-input multiple-output (MU-MIMO) and further improves overall network spectral efficiency.

Additionally, the capability of transmitting beamformed signals allows multi-antenna systems to enable simultaneous downlink transmission to multiple devices using the same physical resources, thus enabling the implementation of MU-MIMO and boosting overall network spectral efficiency. The basic principle of MU-MIMO based on multi-antenna precoding involves selecting optimal beam configurations, referred to as precoders, that not only focus energy toward the target but also consider interference to other scheduled devices. MU-MIMO enables data transmission to multiple devices simultaneously by utilizing the spatial domain, offering an ideally orthogonal communication path to each device. This is known as spatial-multiplexing capability.

Thus, the main advantages of multi-antenna systems can be summarized into two essential aspects: *beamforming* and *multiplexing*. Although both terms introduce gains in final sum rate performance and may seem synonymous, they are not; as beamforming gains do not automatically imply multiplexing gains. The first, beamforming, refers to the capability of directing/steering to a specific target, while the second, multiplexing, refers to the capability of distributing the power to orthogonally serve multiple UE on the same physical resources. [29–31,84].

The 5G NR [75,76] specifications are mainly related to the measurement that each UEs must pursue and report to its serving cell to enable multi-antenna transmission schemes for the downlink physical data shared channel (PDSCH). Specifically, each cell transmits a set of precoded reference signals, referred to as CSI-RS in 5G NR

networks terminology, within specific resource elements (REs), and instructs each UEs to conduct measurement over them and then report back different standardized values, such as: RI, PMI, and CQI.

In this thesis, we do not delve into the details of those measurements. Instead, we concentrate on the PMI and the multi-antenna precoding techniques enabled. Within more details, the PMI reports information regarding the measured CSI-RSs, indicating which, among them, the device believes is the most suitable precoder to be used for its downlink data transmission. It is important to note that this reporting does not impose any restrictions on which precoder the network eventually adopts for the data downlink transmission; however, in many cases, if not the majority, the network uses the precoder indicated by the UEs.

The set of measurement information, along with additional extensions introduced in Release 16, can be reported using two different configurations. Specifically, NR defines two types of CSI, which differ in structure and size: *Type-I CSI* and *Type-II CSI*.

- *Type-I CSI*, is characterized by a relatively simple structure, primarily designed to focus power at the receiver. In this context, the reported PMI, represented by a few bits, indicates the index of the beam selected from a discrete codebook for transmission. Therefore, the cell will adopt the indicated CSI-RS precoder as the data transmitting one.

The leanness of this configuration makes this kind of reporting suitable for high mobility scenarios, as the low overhead allows for increased reporting frequency.

- *Type-II CSI*, is characterized by significantly more information, and it allows to provide channel information with much higher granularity.

The extended granularity within this PMI reporting allows for a better channel resolution, thereby enabling the network to rely on linear precoding techniques to create a precise precoding matrix for instantaneous channel realizations. Moreover, the better resolution of the feedback comes at the cost of significantly higher signalling overhead. A PMI report of *Type-II CSI* may consist of several hundred of bits, therefore is primarily applicable for low-mobility scenarios.

Enhancements for *Type-II CSI* reporting have been introduced in Release 16 and extended in Release 17 and 18. However, those extensions mainly concern the optimization and compression of the UE measurements, leaving unchanged the fundamental difference between *Type-I CSI* reporting (i.e., discrete beam selection) and *Type-II CSI* reporting (i.e., detailed CSI-RS measurements) [75,76,84,109].

On a high level, the set of precoders employed for the PDSCH at each cell can be represented as precoding matrix \mathbf{W} , which can be expressed as the product of two matrices,

$$\mathbf{W} = \mathbf{W}_1 \mathbf{B} , \quad (\text{A.1})$$

where matrix \mathbf{B} is a generic set of mutually orthogonal precoders representing each CSI-RS. These precoders have been utilized to realize beams to illuminate UEs and form the basis for their measurements. Then, matrix \mathbf{W}_1 is computed according to the reported information of each UE. Therefore, in case of *Type-I CSI*, \mathbf{W}_1 will be an assignment matrix, i.e., a binary matrix, representing the association between each UE and its selected precoder in \mathbf{B} . While, in case of *Type-II CSI*, matrix \mathbf{W}_1 will be a real matrix representing any linear combination of the set of precoders in \mathbf{B} , thereby enabling any linear precoding technique (e.g., MRT, zero forcing (ZF), etc.).

It should be noted that at the moment of writing this thesis, the total number of distinct CSI-RS is limited to 32 (Release 18), thereby constraining the total number of degree of freedom (DoF) of the system (i.e., number of parallel stream and/or multiplexed UEs). Given any matrix \mathbf{H} characterizing the channel between each cell and the all connected UEs, the discussed multi-antenna system can be described as,

$$\mathbf{y} = \mathbf{H} \mathbf{W}_1 \mathbf{B} \mathbf{x} \quad (\text{A.2})$$

where \mathbf{x} and \mathbf{y} represent the transmitted and received signals, respectively. Then, in the first turn, the total DoF can be seen as the rank characterizing $\mathbf{H} \mathbf{W}_1 \mathbf{B}$, for which it holds

$$\text{Rank}(\mathbf{H} \mathbf{W}_1 \mathbf{B}) \leq \min \{ \text{Rank}(\mathbf{H}), \text{Rank}(\mathbf{W}_1), \text{Rank}(\mathbf{B}) \}. \quad (\text{A.3})$$

Thus, although ideal channel condition and the optimal design of the precoders, the total DoF will always be upper bounded by the total number of CSI-RS precoders in \mathbf{B} .

Finally, it should be noted that in this thesis we focus on *Type-I CSI* precoding and multi-user massive multiple-input multiple-output (MU-mMIMO) application with a single-layer transmission per UE.

Appendix B

Line of Sight Probability and Path Loss

In the following, we report the adopted models outlined by 3GPP in [67,73] for LoS probability $P_{u,b}^{\text{LoS}}$ and path loss gain $\rho_{u,b}$ between each UEs u and each cell b ; both considering UMA, UMi scenarios as well as UEs located on the ground segment and UAVs on the aerial one. Here, distances and frequencies are expressed in meters and GHz.

B.1 UMA Ground Segment

Following models presented in [73], we consider a UMA scenario with outdoor gUE at a fixed altitude h_g of 1.5 m.

B.1.1 Line of Sight Probability

Between each gUE g and cell b the LoS probability $P_{g,b}^{\text{LoS}}$ is computed as follows,

$$P_{g,b}^{\text{LoS}} = \begin{cases} 1, & \text{If } d_{g,b}^{2D} \leq 18\text{m} \\ \left[\frac{18}{d_{g,b}^{2D}} + e^{-\frac{d_{g,b}^{2D}}{63}} \left(1 - \frac{18}{d_{g,b}^{2D}} \right) \right], & \text{Otherwise} \end{cases}, \quad (\text{B.1})$$

where $d_{g,b}^{2D}$ is the 2D distance between gUE g and cell b .

B.1.2 Path Loss Gain

Following this, we compute, for both LoS and NLoS scenario, the path loss gain in dB $\rho_{g,b}^{\text{UMa-LoS,dB}}$ and $\rho_{g,b}^{\text{UMa-NLoS,dB}}$ as follows,

$$\begin{aligned} \rho_{g,b}^{\text{UMa-LoS,dB}} &= & (\text{B.2}) \\ &= \begin{cases} -PL_1^{\text{UMa-LoS,dB}}, & \text{If } 10\text{m} \leq d_{g,b}^{2D} \leq d_{\text{BP}} \\ -PL_2^{\text{UMa-LoS,dB}}, & \text{If } d_{\text{BP}} \leq d_{g,b}^{2D} \leq 5\text{km} \end{cases} \end{aligned}$$

where

$$PL_1^{\text{UMa-LoS,dB}} = 28.0 + 22 \log_{10} \left(d_{g,b}^{3D} \right) + 20 \log_{10} (f_c) \quad (\text{B.3})$$

$$PL_2^{\text{UMa-LoS,dB}} = 28.0 + 40 \log_{10} \left(d_{g,b}^{3D} \right) + 20 \log_{10} (f_c) - 9 \log_{10} \left(d_{\text{BP}}^2 + (h_{\text{BS}} - h_g)^2 \right), \quad (\text{B.4})$$

and

$$\rho_{g,b}^{\text{UMa-NLoS,dB}} = \min \left(\rho_{g,b}^{\text{UMa-LoS,dB}}, -PL^{\text{UMa-NLoS,dB}} \right), \quad (\text{B.5})$$

$$PL^{\text{UMa-NLoS,dB}} = 13.54 + 39.08 \log_{10} \left(d_{g,b}^{3D} \right) + 20 \log_{10} (f_c) - 0.6 (h_g - 1, 5), \quad (\text{B.6})$$

where $d_{g,b}^{3D}$ is 3D distances between gUE g and cell b , and d_{BP} is the breakpoint distance computed as in [73],

$$d_{\text{BP}} = \frac{4(h_{\text{BS}} - 1)(h_g - 1)f_c}{c}, \quad (\text{B.7})$$

where c is the speed of light.

B.2 UMi Ground Segment

Here, we present the adopted model for outdoor gUEs in a UMi scenario.

B.2.1 Line of Sight Probability

Following models in [73], the LoS probability $P_{g,b}^{\text{LoS}}$ in this scenario is computed as in eq. (B.1).

B.2.2 Path Loss Gain

Differently, the path loss gains in dB $\rho_{g,b}^{\text{LoS,dB}}$, $\rho_{g,b}^{\text{NLoS,dB}}$ are computed according to the following models,

$$\rho_{g,b}^{\text{UMi-LoS,dB}} = \begin{cases} -PL_1^{\text{UMi-LoS,dB}}, & \text{If } 10\text{m} \leq d_{g,b}^{2D} \leq d_{\text{BP}} \\ -PL_2^{\text{UMi-LoS,dB}}, & \text{If } d_{\text{BP}} \leq d_{g,b}^{2D} \leq 5\text{km} \end{cases}, \quad (\text{B.8})$$

where

$$PL_1^{\text{UMi-LoS,dB}} = 32.4 + 21 \log_{10} \left(d_{g,b}^{3D} \right) + 20 \log_{10} (f_c), \quad (\text{B.9})$$

$$\begin{aligned}
PL_2^{\text{UMi-LoS,dB}} &= 32.4 + 40 \log_{10} \left(d_{g,b}^{3D} \right) + 20 \log_{10} (f_c) \\
&\quad - 9.5 \log_{10} \left(d_{\text{BP}}^2 + (h_{\text{BS}} - h_g)^2 \right), \tag{B.10}
\end{aligned}$$

with d_{BP} computed as in eq. (B.7).

B.3 UMa Aerial Segment

In the following, we introduce the adopted models for UAVs outlined in [67] for a UMa scenario.

B.3.1 Line of Sight Probability

Between each UAVs a and cell b , the LoS probability $P_{a,b}^{\text{UMa-LoS}}$ is computed as follows,

$$P_{a,b}^{\text{UMa-LoS}} = \begin{cases} 1, & \text{If } 100\text{m} < h_{\text{AH}} \leq 300\text{m} \\ p_1^{\text{UMa}}, & \text{Otherwise} \end{cases}, \tag{B.11}$$

with

$$p_1 = \begin{cases} 1, & \text{If } d_{a,b}^{2D} \leq d_1^{\text{UMa}} \\ \frac{d_1^{\text{UMa}}}{d_{a,b}^{2D}} + e^{-\frac{d_{a,b}^{2D}}{\bar{p}_1^{\text{UMa}}}} \left(1 - \frac{d_1^{\text{UMa}}}{d_{a,b}^{2D}} \right), & \text{Otherwise} \end{cases}, \tag{B.12}$$

and

$$\bar{p}_1^{\text{UMa}} = 4300 \log_{10} (h_{\text{AH}}) - 3800, \tag{B.13}$$

$$d_1^{\text{UMa}} = \max (460 \log_{10} (h_{\text{AH}}) - 700, 18). \tag{B.14}$$

B.3.2 Path loss Gain

Then, we compute the path loss gain in dB as follows,

$$\rho_{a,b}^{\text{UMa-LoS,dB}} = -28.0 - 22 \log_{10} \left(d_{a,b}^{3D} \right) - 20 \log_{10} (f_c) \tag{B.15}$$

$$\begin{aligned}
\rho_{a,b}^{\text{UMa-NLoS,dB}} &= +17.5 - 20 \log_{10} \left(\frac{40\pi f_c}{3} \right) \\
&\quad - (46 - 7 \log_{10} (h_{\text{AH}})) \log_{10} \left(d_{a,b}^{3D} \right). \tag{B.16}
\end{aligned}$$

B.4 UMi Aerial Segment

Here, we present the adopted model for outdoor UAVs in a UMi scenario.

B.4.1 Line of Sight Probability

Following models in [67], the LoS probability $P_{a,b}^{\text{UMi-LoS}}$ is computed as follows,

$$P_{a,b}^{\text{UMi-LoS}} = \begin{cases} 1, & \text{If } d_{a,b}^{2D} \leq d_1^{\text{UMi}} \\ \frac{d_1^{\text{UMi}}}{d_{a,b}^{2D}} + e^{-\frac{d_{a,b}^{2D}}{\bar{p}_1^{\text{UMi}}}} \left(1 - \frac{d_1^{\text{UMi}}}{d_{a,b}^{2D}}\right), & \text{Otherwise} \end{cases}, \quad (\text{B.17})$$

where

$$\bar{p}_1^{\text{UMi}} = 233.98 \log_{10}(h_{\text{AH}}) - 0.95, \quad (\text{B.18})$$

$$d_1^{\text{UMi}} = \max(294.05 \log_{10}(h_{\text{AH}}) - 432.94, 18). \quad (\text{B.19})$$

B.4.2 Path Loss Gain

Then, we compute the path loss gains in dB for the UMi scenario as follows,

$$\rho_{a,b}^{\text{UMi-LoS,dB}} = \min \begin{cases} -30.9 - (22.25 - 0.5 \log_{10}(h_{\text{AH}})) \log_{10}(d_{a,b}^{3D}) \\ -20 \log_{10}(f_c) \\ -\text{FS}_{a,b} \end{cases}, \quad (\text{B.20})$$

$$\rho_{a,b}^{\text{UMi-NLoS,dB}} = \min \begin{cases} -32.4 - (43.42 - 7.6 \log_{10}(h_{\text{AH}})) \log_{10}(d_{a,b}^{3D}) \\ -20 \log_{10}(f_c) \\ \rho_{a,b}^{\text{UMi-LoS,dB}} \end{cases}, \quad (\text{B.21})$$

where FS is the free space path loss computed as follows,

$$\text{FS}_{a,b} = 32.45 + 20 \log_{10}(d_{a,b}^{3D}) + 20 \log_{10}(f_c). \quad (\text{B.22})$$

In the rest of the paper, to simplify notation, we refer to the path loss gain in linear scale, between UE u and cell b , with $\rho_{u,b}$.

Appendix C

Optimization Problem Concavity

In this appendix, we present a numerical analysis to empirically demonstrate that the maximization problems considered in this work do not exhibit concavity. Precisely, here we consider the maximization problems defined in Chapter 3 Section 3.2 Problem 1 for the LTE vertical tilt optimization, and the maximization problem defined in Chapter 4 Section 2 Problem 4.2 for the NR coverage SSB beam maximization. In more detail, by examining their objective functions of the problems and employing the definition of concavity alongside numerical algorithms, we show that concavity does not manifest.

To accommodate our analysis, in the following, we rely on the analytical definition of concavity, for which a function $f(\mathbf{x})$ is said concave if, for any points $\mathbf{x}^0, \mathbf{x}^1$ in the defined domain, and for any $\lambda \in [0, 1]$, it holds:

$$f(\lambda \mathbf{x}^0 + (1 - \lambda) \mathbf{x}^1) \geq \lambda f(\mathbf{x}^0) + (1 - \lambda) f(\mathbf{x}^1). \quad (\text{C.1})$$

Then, for both the LTE vertical tilt and NR coverage SSB beam problems analyzed in the following, models and network parameters presented in Chapter 2, 3 and 4 are adopted. Precisely, the UMa *Curved* at 100 m is used as a reference scenario with a total of $N_{\text{real}}=100$ for the realization of the random variables characterizing the network.

For both the LTE vertical tilt and NR coverage SSB beam problems analyzed in the following sections, we adopt the models and network parameters outlined in Chapters 2, 3 and 4. Specifically, the UMa *Curved* scenario at 100,m is used as the reference, with $N_{\text{real}}=100$ realizations of the random variables that characterize the network.

C.1 LTE Vertical Tilt Concavity

In the following, we aim to discuss the concavity of the LTE tilt vertical optimization defined in Chapter 3 Problem 1. Due to the high complexity of the problem, proving analytically the concavity of the objective function may be challenging; therefore, we aim to devise a numerical algorithm that empirically verifies whether, for any two points \mathbf{x}^0 and \mathbf{x}^1 , the left hand side (lhs) is greater or equal to the right hand side

(rhs) of eq. (C.1). Here, each point \mathbf{x} is a vector with dimension N_{BS} representing the vertical tilt configuration for all the network cells \mathcal{B} .

Then, recalling the maximization Problem 1, in the following we aim to analyze the concavity of its utility function

$$f(\mathbf{x}) = \sum_i^{N_{\text{real}}} \sum_{e \in \mathcal{E}} \log \left(\log_2 \left(1 + \gamma_e^{\text{lte-cov}}(\mathbf{x}) \right) \right) \quad (\text{C.2})$$

$$= \sum_i^{N_{\text{real}}} \sum_{e \in \mathcal{E}} \log \left(\log_2 \left(1 + \frac{\rho_{e, \hat{b}_e} \tau_{e, \hat{b}_e} p_b g_{e, \hat{b}_e}^{\text{lte}}(x_{\hat{b}_e})}{\sum_{b \in \mathcal{B} \setminus \hat{b}_e} \rho_{e, b} \tau_{e, b} p_b g_{e, b}^{\text{lte}}(x_b) + B_0 N_0} \right) \right),$$

where γ_e^{lte} is the resulting coverage LTE SINR, with variables characterizing the channels defined in Chapter 2.

Then, for a total of N_{random} realizations we randomly generate each vector element $x_b^0 \in \mathbf{x}^0$ and $x_b^1 \in \mathbf{x}^1$ as follows,

$$\mathbf{x}^0 \sim U(-90^\circ, 90^\circ), \quad \mathbf{x}^1 \sim U(-90^\circ, 90^\circ), \quad (\text{C.3})$$

and, for each random generation, we consider different values for λ within the interval $[0, 1]$. Finally, we compute the lhs and rhs of eq. (C.1) computed according to the objective function in eq. (C.2). Finally, in each iteration, we compare the lhs with the rhs and count the instances where the lhs exceeds the rhs, thereby determining how often the function satisfies the concavity conditions.

Algorithm 4 presents the detailed procedure.

Figure C.1 presents the obtained results in terms of the percentage of instances in which the eq.(C.1) is verified, therefore representing the percentage in which the concavity condition is verified. The results indicate that the objective function for the LTE vertical tilt optimization problem, as defined in eq. (C.2), fails to satisfy the concavity condition in 40% of the analyzed instances. Consequently, this demonstrates the non-concavity of the objective function.

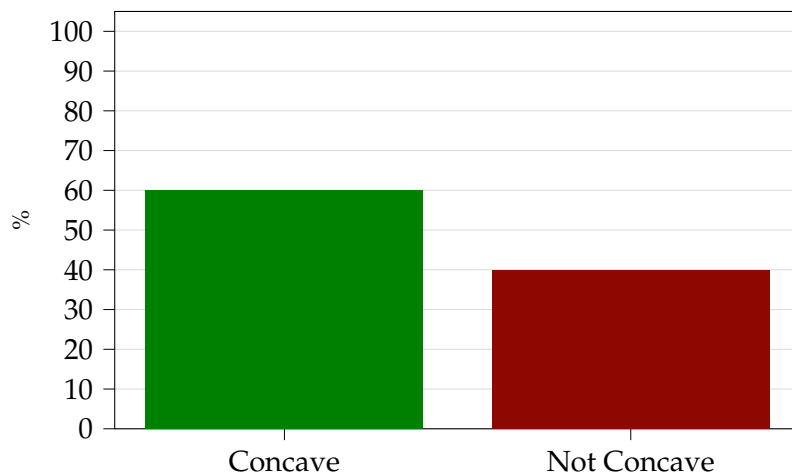


FIGURE C.1: Percentage of concavity instances resulting from Algorithm 4 considering LTE vertical tilt optimization objective function.

Algorithm 4: LTE vertical tilt empirical numerical concavity algorithm.

```

1  $f \leftarrow \sum_i^{N_{\text{real}}} \sum_{e \in \mathcal{E}} \log \left( \log_2 \left( 1 + \frac{\rho_{e,b_e} i \tau_{e,b_e} P_b g_{e,b_e}^{\text{lte}}(x_{b_e})}{\sum_{b \in \mathcal{B} \setminus \{b_e\}} \rho_{e,b} i \tau_{e,b} P_b g_{e,b}^{\text{lte}}(x_b) + B_0 N_0} \right) \right)$ ;

2 Function Concavity_LHS_RHS_Comp( $f, \mathbf{x}^0, \mathbf{x}^1, \lambda$ ):
3    $lhs \leftarrow f(\lambda \mathbf{x}^0 + (1 - \lambda) \mathbf{x}^1)$ ;
4    $rhs \leftarrow \lambda f(\mathbf{x}^0) + (1 - \lambda) f(\mathbf{x}^1)$ ;
5   return  $lhs, rhs$ ;

6  $count\_c \leftarrow 0$ ;
7  $count\_nc \leftarrow 0$ ;
8 for  $i = 0$  to  $N_{\text{random}} - 1$  do
9    $\mathbf{x}^0 \leftarrow \text{Random}(-90, 90, \text{dim} = N_{\text{BS}})$ ;
10   $\mathbf{x}^1 \leftarrow \text{Random}(-90, 90, \text{dim} = N_{\text{BS}})$ ;
11   $\lambda \leftarrow 0$ ;
12  while  $\lambda \leq 1$  do
13     $lhs, rhs \leftarrow \text{Concavity\_LHS\_RHS\_Comp}(f, \mathbf{x}^0, \mathbf{x}^1, \lambda)$ ;
14    if  $lhs \geq rhs$  then
15       $count\_c \leftarrow count\_c + 1$ ;
16    else
17       $count\_nc \leftarrow count\_nc + 1$ ;
18    end
19     $\lambda \leftarrow \lambda + 0.001$ ;
20  end
21 end
22  $\%concave \leftarrow ((count\_c / (count\_c + count\_nc)) \times 100)$ ;
23  $\%NotConcave \leftarrow ((count\_nc / (count\_c + count\_nc)) \times 100)$ ;

24 output  $P\%concave, P\%NotConcave$ ;

```

C.2 NR Coverage SSB Beam Concavity

In the following, we discuss the concavity of the objective function characterizing the NR coverage SSB beam maximization Problem 2 presented in Chapter 4. Akin to what was discussed in the previous Section C.1, here we present a numerical algorithm to empirically prove the no concavity of Problem 2 objective function. Specifically, as previously presented, we aim to verify if any couple of points \mathbf{Y}^0 and \mathbf{Y}^1 in the complex space $\mathbb{C}^{M \times N_{\text{BS}}}$ accomplish with the definition of concavity in eq. (C.1). Then, in the following we represent each complex number $y_{m,b} \in \mathbf{Y}$ as $y_{m,b} = 1/\sqrt{M} \alpha_{m,b} (p_{m,b} + jq_{m,b})$, and each matrix \mathbf{Y} as

$$\mathbf{Y} = \frac{1}{\sqrt{M}} \mathbf{A} \odot (\mathbf{P} + j\mathbf{Q}), \quad (\text{C.4})$$

where \odot represents the Hadamard product, and $\frac{1}{\sqrt{M}}$ account for normalization.

Then, recalling the maximization Problem 2, we analyze the concavity of its objective function:

$$\begin{aligned}
 f(\mathbf{Y}) &= \sum_i^{N_{\text{real}}} \sum_{a \in \mathcal{E}_a} \log \left(\log_2 \left(1 + \gamma_a^{\text{nr-cov}}(\hat{\mathbf{Y}}) \right) \right) \xrightarrow{y=\alpha(p+jq)} \\
 &= \sum_i^{N_{\text{real}}} \sum_{a \in \mathcal{E}_a} \log \left(\log_2 \left(1 + \frac{i \beta_{a, \hat{b}_a} \left| \frac{1}{\sqrt{M}} \sum_m^i h_{a, \hat{b}_a, m}^{\text{dl}} \hat{\alpha}_{m, \hat{b}_a}^{\text{nr}} \left(\hat{p}_{m, \hat{b}_a}^{\text{nr}} + j \hat{q}_{m, \hat{b}_a}^{\text{nr}} \right) \right|^2}{\sum_{b \in \mathcal{B} \setminus \hat{b}_a} i \beta_{a, b} \left| \frac{1}{\sqrt{M}} \sum_m^i h_{a, b, m}^{\text{dl}} \hat{\alpha}_{m, b}^{\text{nr}} \left(\hat{p}_{m, b}^{\text{nr}} + j \hat{q}_{m, b}^{\text{nr}} \right) \right|^2 + B_0 N_0} \right) \right)
 \end{aligned} \tag{C.5}$$

where $\gamma_a^{\text{nr-cov}}$ represent the NR SSB beam coverage, with channel parameters defined in Chapter 2.

Then, following the same steps presented in Section C.1, for a total of N_{random} iteration, we random generate points \mathbf{Y}^0 and \mathbf{Y}^1 . For both matrices, considering the representation through matrix \mathbf{A} , \mathbf{P} , and \mathbf{Q} , we have that:

$$\alpha_{m,b} \sim U(0,1), p_{m,b} \sim U(-1,1), q_{m,b} \sim U(-1,1). \tag{C.6}$$

Next, for each random generation, we employ several values of λ within the interval $[0,1]$ and assess whether the concavity condition specified in eq. (C.1) is satisfied. Finally, we count the instances where this condition is met and those where it is not. Algorithm 5 shows the detailed procedure.

Figure C.2 illustrates the results as the percentage of instances where eq. (C.1) is satisfied, reflecting the proportion of cases where the concavity condition holds. The results show that in 33.7% of the analyzed instances, the objective function for the NR coverage SSB beam optimization problem, as defined in eq. (C.5), does not meet the concavity condition; therefore highlighting the non-concave nature of the problem.

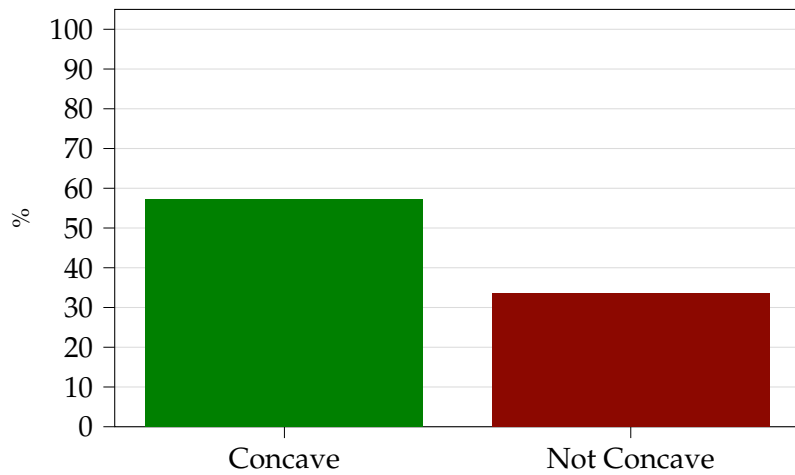


FIGURE C.2: Percentage of concavity instances from Algorithm 5 considering NR coverage SSB beam optimization objective function.

Algorithm 5: NR coverage SSB beam empirical numerical concavity algorithm.

```

1  $f \leftarrow \sum_i^{N_{\text{real}}} \sum_{a \in \mathcal{E}_a} \log \left( \log_2 \left( 1 + \frac{\beta_{a, \hat{b}_a} \left| \frac{1}{\sqrt{M}} \sum_m^i h_{a, \hat{b}_a, m}^{\text{dl}} \hat{a}_{m, \hat{b}_a}^{\text{nr}} (\hat{p}_{m, \hat{b}_a}^{\text{nr}} + j \hat{q}_{m, \hat{b}_a}^{\text{nr}}) \right|^2}{\sum_{b \in \mathcal{B} \setminus \hat{b}_a} \beta_{a, b} \left| \frac{1}{\sqrt{M}} \sum_m^i h_{a, b, m}^{\text{dl}} \hat{a}_{m, b}^{\text{nr}} (\hat{p}_{m, b}^{\text{nr}} + j \hat{q}_{m, b}^{\text{nr}}) \right|^2 + B_0 N_0} \right) \right)$ ;

2 Function Concavity_LHS_RHS_Comp( $f, \mathbf{Y}^0, \mathbf{Y}^1, \lambda$ ):
3    $lhs \leftarrow f(\lambda \mathbf{Y}^0 + (1 - \lambda) \mathbf{Y}^1)$ ;
4    $rhs \leftarrow \lambda f(\mathbf{Y}^0) + (1 - \lambda) f(\mathbf{Y}^1)$ ;
5   return  $lhs, rhs$ ;

6  $count\_c \leftarrow 0$ ;
7  $count\_nc \leftarrow 0$ ;
8 for  $i = 0$  to  $N_{\text{random}} - 1$  do
9    $\mathbf{A}^0 \leftarrow \text{Random}(0, 1, \text{dim} = (M, N_{\text{BS}}))$ ;
10   $\mathbf{P}^0 \leftarrow \text{Random}(-1, 1, \text{dim} = (M, N_{\text{BS}}))$ ;
11   $\mathbf{Q}^0 \leftarrow \text{Random}(-1, 1, \text{dim} = (M, N_{\text{BS}}))$ ;
12   $\mathbf{Y}^0 \leftarrow \frac{1}{\sqrt{M}} \mathbf{A}^0 \odot (\mathbf{P}^0 + j \mathbf{Q}^0)$ ;
13   $\mathbf{A}^1 \leftarrow \text{Random}(0, 1, \text{dim} = (M, N_{\text{BS}}))$ ;
14   $\mathbf{P}^1 \leftarrow \text{Random}(-1, 1, \text{dim} = (M, N_{\text{BS}}))$ ;
15   $\mathbf{Q}^1 \leftarrow \text{Random}(-1, 1, \text{dim} = (M, N_{\text{BS}}))$ ;
16   $\mathbf{Y}^1 \leftarrow \frac{1}{\sqrt{M}} \mathbf{A}^1 \odot (\mathbf{P}^1 + j \mathbf{Q}^1)$ ;
17   $\lambda \leftarrow 0$ ;
18  while  $\lambda \leq 1$  do
19     $lhs, rhs \leftarrow \text{Concavity\_LHS\_RHS\_Comp}(f, \mathbf{Y}^0, \mathbf{Y}^1, \lambda)$ ;
20    if  $lhs \geq rhs$  then
21       $count\_c \leftarrow count\_c + 1$ ;
22    else
23       $count\_nc \leftarrow count\_nc + 1$ ;
24    end
25     $\lambda \leftarrow \lambda + 0.001$ ;
26  end
27 end
28  $\%_{\text{concave}} \leftarrow ((count\_c / (count\_c + count\_nc)) \times 100)$ ;
29  $\%_{\text{NotConcave}} \leftarrow ((count\_nc / (count\_c + count\_nc)) \times 100)$ ;

30 output  $P\%_{\text{concave}}, P\%_{\text{NotConcave}}$ ;

```

Bibliography

- [1] D. Floreano and R. J. Wood, "Science, technology and the future of small autonomous drones," *Nature*, vol. 521, pp. 460–466, 2015.
- [2] A. Fotouhi, H. Qiang, M. Ding, M. Hassan, L. G. Giordano, A. Garcia-Rodriguez, and J. Yuan, "Survey on UAV cellular communications: Practical aspects, standardization advancements, regulation, and security challenges," *IEEE Commun. Surveys Tuts.*, vol. 21, no. 4, pp. 3417–3442, Mar. 2019.
- [3] M. Giordani, M. Polese, M. Mezzavilla, S. Rangan, and M. Zorzi, "Toward 6G networks: Use cases and technologies," *IEEE Commun. Mag.*, vol. 58, no. 3, pp. 55–61, Mar. 2020.
- [4] G. Geraci, D. López-Pérez, M. Benzaghta, and S. Chatzinotas, "Integrating terrestrial and non-terrestrial networks: 3D opportunities and challenges," *IEEE Commun. Mag.*, vol. 61, no. 4, pp. 42–48, Dec. 2023.
- [5] B. Li, Z. Fei, and Y. Zhang, "UAV communications for 5G and beyond: Recent advances and future trends," *IEEE Internet Things J.*, vol. 6, no. 2, pp. 2241–2263, 2019.
- [6] M. Giordani and M. Zorzi, "Non-terrestrial networks in the 6G era: Challenges and opportunities," *IEEE Netw.*, vol. 35, no. 2, pp. 244–251, 2021.
- [7] M. Mozaffari, W. Saad, M. Bennis, Y.-H. Nam, and M. Debbah, "A tutorial on UAVs for wireless networks: Applications, challenges, and open problems," *IEEE Commun. Surveys Tuts.*, vol. 21, no. 3, pp. 2334–2360, Mar. 2019.
- [8] G. Geraci, A. Garcia-Rodriguez, M. M. Azari, A. Lozano, M. Mezzavilla, S. Chatzinotas, Y. Chen, S. Rangan, and M. D. Renzo, "What will the future of UAV cellular communications be? A flight from 5G to 6G," *IEEE Commun. Surveys Tuts.*, vol. 24, no. 3, pp. 1304–1335, 2022.
- [9] E. Vinogradov, H. Sallouha, S. De Bast, M. M. Azari, and S. Pollin, "Tutorial on UAV: A blue sky view on wireless communication," *arXiv preprint arXiv:1901.02306*, Jan. 2019.
- [10] H. Kong, M. Lin, L. Han, W.-P. Zhu, Z. Ding, and M.-S. Alouini, "Uplink multiple access with semi-grant-free transmission in integrated satellite-aerial-terrestrial networks," *IEEE J. Sel. Areas Commun.*, vol. 41, no. 6, pp. 1723–1736, May 2023.

- [11] Y. Zeng, Q. Wu, and R. Zhang, "Accessing from the sky: A tutorial on UAV communications for 5G and beyond," *Proc. IEEE*, vol. 107, no. 12, pp. 2327–2375, Dec. 2019.
- [12] Market Growth Reports, "Global civil drone industry research report 2023, competitive landscape, market size, regional status and prospect," Jan. 2023.
- [13] The Business Research Company, "Commercial drones global market report 2023," Jan. 2023.
- [14] A. Saboor, S. Coene, E. Vinogradov, E. Tanghe, W. Joseph, and S. Pollin, "Elevating the future of mobility: UAV-enabled intelligent transportation systems," 2021.
- [15] The New York Times, "Drone delivery? amazon moves closer with F.A.A. approval," Aug. 2020.
- [16] Amazon, "Amazon is launching ultra-fast drone deliveries in Italy, the UK, and a third location in the U.S." Oct. 2023.
- [17] The Times, "Amazon prime delivery drones to take flight in the UK next year," Oct. 2023.
- [18] M. Doole, J. Ellerbroek, and J. Hoekstra, "Drone delivery: Urban airspace traffic density estimation," *8th SESAR Innovation Days*, 2018.
- [19] N. Cherif, W. Jaafar, H. Yanikomeroğlu, and A. Yongacoglu, "3D aerial highway: The key enabler of the retail industry transformation," *IEEE Commun. Mag.*, vol. 59, no. 9, pp. 65–71, Sep. 2021.
- [20] S. Singh, M. L. Sichitiu, I. Guvenc, and A. Bhuyan, "Minimizing ground risk in cellular-connected drone corridors with mmwave links," *IEEE Trans. Aerospace Elec. Systems*, vol. 59, no. 6, pp. 7923–7937, Aug. 2023.
- [21] F.A.A., *Pilot's Handbook of Aeronautical knowledge*. U.S. Department of Transportation, 2016.
- [22] V. Marojevic, I. Guvenc, R. Dutta, M. L. Sichitiu, and B. A. Floyd, "Advanced wireless for unmanned aerial systems: 5G standardization, research challenges, and AERPAW architecture," *IEEE Veh. Technol. Mag.*, vol. 15, no. 2, pp. 22–30, Apr. 2020.
- [23] D. López-Pérez, M. Ding, H. Li, L. G. Giordano, G. Geraci, A. Garcia-Rodriguez, Z. Lin, and M. Hassan, "On the downlink performance of UAV communications in dense cellular networks," in *Proc. IEEE Global Commun. Conf. (GLOBECOM)*, Feb. 2018, pp. 1–7.

- [24] M. M. Azari, F. Rosas, and S. Pollin, "Cellular connectivity for uavs: Network modeling, performance analysis, and design guidelines," *IEEE Trans. Wireless Commun.*, vol. 18, no. 7, pp. 3366–3381, Apr. 2019.
- [25] Z. Wang, M. Lin, J. Ouyang, J.-B. Wang, W.-P. Zhu, and N. Al-Dhahir, "Multi-objective robust beamforming for integrated satellite and aerial networks supporting heterogeneous services," *IEEE Trans. Wireless Commun.*, vol. 22, no. 10, pp. 6870–6882, Feb. 2023.
- [26] X. Lin, V. Yajnanarayana, S. D. Muruganathan, S. Gao, H. Asplund, H.-L. Maattanen, M. Bergstrom, S. Euler, and Y.-P. E. Wang, "The sky is not the limit: LTE for unmanned aerial vehicles," *IEEE Commun. Mag.*, vol. 56, no. 4, pp. 204–210, Apr. 2018.
- [27] R. Muzaffar, C. Raffelsberger, A. Fakhreddine, J. L. Luque, D. Emini, and C. Bettstetter, "First experiments with a 5G-connected drone," in *Proc. 5th Workshop Micro Aerial Vehicle Net., Syst, Appl.*, ser. DroNet'20, Jun. 2020, p. 1–5.
- [28] M. M. Azari, F. Rosas, A. Chiumento, and S. Pollin, "Coexistence of terrestrial and aerial users in cellular networks," in *Proc. IEEE Global Commun. Conf. Workshops (GLOBECOM Workshops)*, Dec. 2017, pp. 1–6.
- [29] D. Gesbert, M. Shafi, D. shan Shiu, P. Smith, and A. Naguib, "From theory to practice: an overview of MIMO space-time coded wireless systems," *IEEE J. Sel. Areas Commun.*, vol. 21, no. 3, pp. 281–302, Apr. 2003.
- [30] A. Goldsmith, S. Jafar, N. Jindal, and S. Vishwanath, "Capacity limits of MIMO channels," *IEEE J. Sel. Areas Commun.*, vol. 21, no. 5, pp. 684–702, Jun. 2003.
- [31] D. Gesbert, H. Bolcskei, D. Gore, and A. Paulraj, "Outdoor MIMO wireless channels: models and performance prediction," *IEEE Trans. Commun.*, vol. 50, no. 12, pp. 1926–1934, Dec. 2002.
- [32] M. Wu, K. Guo, Z. Lin, X. Li, K. An, and Y. Huang, "Joint optimization design of RIS-assisted hybrid FSO SAGINs using deep reinforcement learning," *IEEE Trans. Veh. Technol.*, vol. 73, no. 3, pp. 3025–3040, Oct. 2024.
- [33] M. Wu, K. Guo, X. Li, Z. Lin, Y. Wu, T. A. Tsiftsis, and H. Song, "Deep reinforcement learning-based energy efficiency optimization for RIS-aided integrated satellite-aerial-terrestrial relay networks," *IEEE Trans. Commun.*, pp. 1–1, 2024.
- [34] S. Karimi-Bidhendi, G. Geraci, and H. Jafarkhani, "Analysis of UAV corridors in cellular networks," in *Proc. IEEE Int. Conf. on Comm. (ICC)*, 2023, pp. 2662–2667.

- [35] D. Gesbert, O. Ebrahimi, J. Chen, R. Gangula, and U. Mitra, "UAV-aided RF mapping for sensing and connectivity in wireless networks," *IEEE Wireless Commun.*, vol. 30, no. 4, pp. 116–122, Aug. 2023.
- [36] M. Drago, A. Gürses, R. W. Heath, M. L. Sichitiu, and M. Zorzi, "End-to-end full-stack drone measurements: A case study using AERPAAW," in *Proc. IEEE Int. Conf. on Comm. Workshops (ICC Workshops)*, Oct. 2023, pp. 1422–1427.
- [37] A. H. F. Raouf, S. J. Maeng, I. Guvenc, O. Ozdemir, and M. Sichitiu, "Cellular spectrum occupancy probability in urban and rural scenarios at various UAS altitudes," in *Proc. IEEE Int. Symp. on Personal, Indoor and Mob. Radio Commun. (PIMRC)*, 2023, pp. 1–6.
- [38] Y. Zeng, R. Zhang, and T. J. Lim, "Wireless communications with unmanned aerial vehicles: opportunities and challenges," *IEEE Commun. Mag.*, vol. 54, no. 5, pp. 36–42, May 2016.
- [39] S. Hayat, E. Yanmaz, and R. Muzaffar, "Survey on unmanned aerial vehicle networks for civil applications: A communications viewpoint," *IEEE Commun. Surveys Tuts.*, vol. 18, no. 4, pp. 2624–2661, Apr. 2016.
- [40] M. Alzenad, A. El-Keyi, F. Lagum, and H. Yanikomeroglu, "3-D placement of an unmanned aerial vehicle base station (UAV-BS) for energy-efficient maximal coverage," *IEEE Commun. Letters*, vol. 6, no. 4, pp. 434–437, May 2017.
- [41] O. Ebrahimi, R. Gangula, and D. Gesbert, "UAV-aided wireless node localization using hybrid radio channel models," in *Proc. IEEE Int. Conf. on Comm. Workshops (ICC Workshops)*, Jul. 2022, pp. 1083–1088.
- [42] R. Gangula, O. Ebrahimi, D. Gesbert, C. Roux, F. Kaltenberger, and R. Knopp, "Flying rebots: First results on an autonomous UAV-based LTE relay using open airinterface," in *Proc. IEEE Workshop on Signal Process. Advances in Wireless Commun. (SPAWC)*, Aug. 2018, pp. 1–5.
- [43] S. J. Maeng, O. Ozdemir, I. Guvenc, M. L. Sichitiu, M. Mushi, and R. Dutta, "LTE I/Q data set for UAV propagation modeling, communication, and navigation research," *IEEE Commun. Letters*, vol. 61, no. 9, pp. 90–96, Oct. 2023.
- [44] Y. Zeng, R. Zhang, and T. J. Lim, "Throughput maximization for uav-enabled mobile relaying systems," *IEEE Trans. Commun.*, vol. 64, no. 12, pp. 4983–4996, Sep. 2016.
- [45] A. Merwaday and I. Guvenc, "Uav assisted heterogeneous networks for public safety communications," in *Proc. IEEE Wireless Commun. Networking Conference (WCNC)*, 2015, pp. 329–334.

- [46] N. Cherif, W. Jaafar, H. Yanikomeroğlu, and A. Yongacoglu, "Disconnectivity-aware energy-efficient cargo-UAV trajectory planning with minimum hand-offs," in *Proc. IEEE Int. Conf. on Comm. (ICC)*, Jun. 2021.
- [47] O. Esrafilian, R. Gangula, and D. Gesbert, "Three-dimensional-map-based trajectory design in UAV-aided wireless localization systems," *IEEE Internet Things J.*, vol. 8, no. 12, pp. 9894–9904, Sep. 2021.
- [48] U. Challita, W. Saad, and C. Bettstetter, "Deep reinforcement learning for interference-aware path planning of cellular-connected UAVs," in *Proc. IEEE Int. Conf. on Comm. (ICC)*, Jul. 2018, pp. 1–6.
- [49] S. De Bast, E. Vinogradov, and S. Pollin, "Cellular coverage-aware path planning for UAVs," in *Proc. IEEE Workshop on Signal Process. Advances in Wireless Commun. (SPAWC)*, Aug. 2019, pp. 1–5.
- [50] O. Esrafilian, R. Gangula, and D. Gesbert, "3D-map assisted UAV trajectory design under cellular connectivity constraints," in *Proc. IEEE Int. Conf. on Comm. (ICC)*, Jul. 2020, pp. 1–6.
- [51] A. Colpaert, M. Raes, E. Vinogradov, and S. Pollin, "Drone delivery: Reliable cellular UAV communication using multi-operator diversity," in *Proc. IEEE Int. Conf. on Comm. (ICC)*, Aug. 2022, pp. 1–6.
- [52] R. Amorim, I. Z. Kovacs, J. Wigard, G. Pocovi, T. B. Sorensen, and P. Mogensen, "Improving drone's command and control link reliability through dual-network connectivity," in *Proc. IEEE Veh. Tech. Conference (VTC)*, Jun. 2019, pp. 1–6.
- [53] J. Sæe, R. Wirén, J. Kauppi, J. Torsner, S. Andreev, and M. Valkama, "Reliability of UAV connectivity in dual-MNO networks: A performance measurement campaign," in *Proc. IEEE Int. Conf. on Comm. (ICC)*, Jul. 2020, pp. 1–5.
- [54] S. Singh, U. Bhattacharjee, E. Ozturk, I. Guvenc, H. Dai, M. Sichitiu, and A. Bhuyan, "Placement of mmwave base stations for serving urban drone corridors," in *Proc. IEEE Veh. Tech. Conference (VTC)*, Jun. 2021, pp. 1–6.
- [55] A. Bhuyan, I. Güvenç, H. Dai, M. L. Sichitiu, S. Singh, A. Rahmati, and S. J. Maeng, "Secure 5G network for a nationwide drone corridor," in *IEEE Aerospace Conf. (AeroConf)*, Jun. 2021, pp. 1–10.
- [56] S. J. Maeng, M. M. U. Chowdhury, I. Güvenç, A. Bhuyan, and H. Dai, "Base station antenna uptilt optimization for cellular-connected drone corridors," *IEEE Trans. Aerospace Elec. Systems*, vol. 59, no. 4, pp. 4729–4737, Jan. 2023.
- [57] S. J. Maeng and I. Güvenç, "UAV corridor coverage analysis with base station antenna uptilt and strongest signal association," *IEEE Trans. Aerospace Elec. Systems*, vol. 60, no. 4, pp. 5621–5630, Apr. 2024.

- [58] M. M. U. Chowdhury, I. Guvenc, W. Saad, and A. Bhuyan, "Ensuring reliable connectivity to cellular-connected UAVs with up-tilted antennas and interference coordination," *ITU J. Future and Evolving Technol.*, 2021.
- [59] S. Karimi-Bidhendi, G. Geraci, and H. Jafarkhani, "Optimizing cellular networks for UAV corridors via quantization theory," *IEEE Trans. Wireless Commun.*, pp. 1–1, Jul. 2024.
- [60] M. Benzaghta, G. Geraci, D. López-Pérez, and A. Valcarce, "Designing cellular networks for UAV corridors via bayesian optimization," in *Proc. IEEE Global Commun. Conf. (GLOBECOM)*, Feb. 2023, pp. 4552–4557.
- [61] Y. Huang, Q. Wu, R. Lu, X. Peng, and R. Zhang, "Massive MIMO for cellular-connected UAV: Challenges and promising solutions," *IEEE Commun. Mag.*, vol. 59, no. 2, pp. 84–90, Feb. 2021.
- [62] A. Garcia-Rodriguez, G. Geraci, D. Lopez-Perez, L. G. Giordano, M. Ding, and E. Bjornson, "The essential guide to realizing 5G-connected UAVs with massive MIMO," *IEEE Commun. Mag.*, vol. 57, no. 12, pp. 84–90, Oct. 2019.
- [63] G. Geraci, A. Garcia-Rodriguez, L. Galati Giordano, D. López-Pérez, and E. Björnson, "Understanding UAV cellular communications: From existing networks to massive MIMO," *IEEE Access*, vol. 6, Nov. 2018.
- [64] P. Chandhar and E. G. Larsson, "Massive MIMO for connectivity with drones: Case studies and future directions," *IEEE Access*, vol. 7, pp. 94 676–94 691, Jul. 2019.
- [65] P. Chandhar, D. Danev, and E. G. Larsson, "Massive MIMO for communications with drone swarms," *IEEE Trans. Wireless Commun.*, vol. 17, no. 3, pp. 1604–1629, Dec. 2018.
- [66] L. Yang and W. Zhang, "Beam tracking and optimization for uav communications," *IEEE Trans. Wireless Commun.*, vol. 18, no. 11, pp. 5367–5379, Aug. 2019.
- [67] Enhanced LTE support for aerial vehicles, 3GPP TR36.777, Jan. 2017, v.15.0.
- [68] Uncrewed Aerial System (UAS) support in 3GPP, 3GPP TS22.125, Jun. 2024, v.19.2.0.
- [69] M. Bernabè, D. Lopez-Perez, D. Gesbert, and H. Bao, "On the optimization of cellular networks for UAV aerial corridor support," in *Proc. IEEE Global Commun. Conf. (GLOBECOM)*, Dec. 2022, pp. 2969–2974.
- [70] M. Bernabè, D. López-Pérez, N. Piovesan, G. Geraci, and D. Gesbert, "A novel metric for mMIMO base station association for aerial highway systems," in *Proc. IEEE Int. Conf. on Comm. Workshops (ICC Workshops)*, Oct. 2023, pp. 1063–1068.

- [71] —, “Massive MIMO for aerial highways: Enhancing cell selection via SSB beams optimization,” *IEEE O.J. on Commun.*, pp. 1–1, Jun. 2024.
- [72] M. Bernabe, D. Lopez-Perez, N. Piovesan, G. Geraci, and D. Gesbert, “Optimal SSB beam planning and UAV cell selection for 5G connectivity on aerial highways,” 2024. [Online]. Available: <https://arxiv.org/abs/2409.01812>
- [73] Study on channel model for frequencies from 0.5 to 100 GHz, 3GPP TR38.901, Mar. 2017, v.14.0.
- [74] Evolved Universal Terrestrial Radio Access (E-UTRA), 3GPP TR36.814, Mar. 2017, v.9.2.
- [75] Physical layer procedure for data, 3GPP TR38.214, Sep. 2023, v.18.0.
- [76] Physical channels and modulation, 3GPP TS38.211, Sep. 2023, v.18.0.
- [77] E. Vinogradov and S. Pollin, “Reducing safe UAV separation distances with U2U communication and new remote ID formats,” in *Proc. IEEE Global Commun. Conf. Workshops (GLOBECOM Workshops)*, Jan. 2022, pp. 1425–1430.
- [78] E. Vinogradov, A. V. S. Sai Bhargav Kumar, F. Minucci, S. Pollin, and E. Natalizio, “Remote ID for separation provision and multi-agent navigation,” in *Digit. Av. Sys. Conf. (DASC)*, Nov. 2023, pp. 1–10.
- [79] E. Björnson, J. Hoydis, and L. Sanguinetti, “Massive MIMO networks: Spectral, energy, and hardware efficiency,” *Foundations and Trends® in Signal Processing*, vol. 11, no. 3-4, pp. 154–655, 2017.
- [80] A. A. Khuwaja, Y. Chen, N. Zhao, M.-S. Alouini, and P. Dobbins, “A survey of channel modeling for UAV communications,” *IEEE Commun. Surveys Tuts.*, vol. 20, no. 4, pp. 2804–2821, Jul. 2018.
- [81] C. Yan, L. Fu, J. Zhang, and J. Wang, “A comprehensive survey on UAV communication channel modeling,” *IEEE Access*, vol. 7, pp. 107769–107792, Aug. 2019.
- [82] R. Amorim, H. Nguyen, P. Mogensen, I. Z. Kovács, J. Wigard, and T. B. Sørensen, “Radio channel modeling for UAV communication over cellular networks,” *IEEE Wireless Commun. Lett.*, vol. 6, no. 4, pp. 514–517, May 2017.
- [83] X. Cai and G. Giannakis, “A two-dimensional channel simulation model for shadowing processes,” *IEEE Trans. Veh. Technol.*, vol. 52, no. 6, pp. 1558–1567, Nov. 2003.
- [84] E. Dahlman, S. Parkvall, and J. Skold, *5G NR: The Next Generation Wireless Access Technology*, 2nd ed. USA: Academic Press, Inc., 2021.

- [85] A. P. Cohen, S. A. Shaheen, and E. M. Farrar, "Urban air mobility: History, ecosystem, market potential, and challenges," *IEEE Trans. Intell. Transp. Syst.*, vol. 22, no. 9, pp. 6074–6087, Jun. 2021.
- [86] Y. Zeng, J. Lyu, and R. Zhang, "Cellular-connected uav: Potential, challenges, and promising technologies," *IEEE Wireless Commun.*, vol. 26, no. 1, pp. 120–127, Sep. 2019.
- [87] R. Rumba and A. Nikitenko, "The wild west of drones: a review on autonomous-UAV traffic-management," *Proc. Int. Conf. on U. Air. Syst. (ICUAS)*, pp. 1317–1322, Oct. 2020.
- [88] B. Van Der Bergh, A. Chiumento, and S. Pollin, "LTE in the sky: trading off propagation benefits with interference costs for aerial nodes," *IEEE Commun. Mag.*, vol. 54, no. 5, pp. 44–50, May 2016.
- [89] D. P. Kingma and J. Ba, "Adam: A method for stochastic optimization," *arXiv:1412.6980*, Jan. 2017.
- [90] S. Ruder, "An overview of gradient descent optimization algorithms," Jun. 2017.
- [91] S. J. Reddi, S. Kale, and S. Kumar, "On the convergence of adam and beyond," Apr. 2019.
- [92] S. Bock and M. Weiß, "A proof of local convergence for the adam optimizer," in *Proc. IEEE Int. Joint Conf. on Neural Net. (IJCNN)*, Sep. 2019, pp. 1–8.
- [93] S. Lloyd, "Least squares quantization in pcm," *IRE Trans. Inform. Theory.*, vol. 28, no. 2, pp. 129–137, Mar. 1982.
- [94] D. Bethanabhotla, O. Y. Bursalioglu, H. C. Papadopoulos, and G. Caire, "Optimal user-cell association for massive MIMO wireless networks," *IEEE Trans. Wireless Commun.*, vol. 15, no. 3, pp. 1835–1850, Nov. 2016.
- [95] A. G. Gotsis, S. Stefanatos, and A. Alexiou, "Optimal user association for massive MIMO empowered ultra-dense wireless networks," in *Proc. IEEE Int. Conf. on Comm. Workshops (ICC Workshops)*, 2015, pp. 2238–2244.
- [96] D. A. Belsley, E. Kuh, and R. E. Welsch, *Regression Diagnostics: Identifying Influential Data and Sources of Collinearity*, 1st ed. New York: John Wiley & Sons, 1980.
- [97] J. Kennedy and R. Eberhart, "Particle swarm optimization," in *Proc. IEEE Int. Conf. on Neural Net. (ICNN)*, vol. 4, Aug. 1995, pp. 1942–1948 vol.4.
- [98] Y. Shi and R. Eberhart, "A modified particle swarm optimizer," in *Proc. IEEE Int. Conf. on Evol. Comp. Proc. (ICEC)*, Aug. 1998, pp. 69–73.

- [99] A. P. Engelbrecht, *Computational intelligence: an introduction*, 2nd ed. New York: John Wiley & Sons, 2007.
- [100] J. H. Holland, "Genetic algorithms," *Scientific American*, vol. 267, no. 1, pp. 66–73, Jul. 1992.
- [101] D. E. Goldberg and J. H. Holland, "Genetic algorithms and machine learning," *Machine Learning*, vol. 3, pp. 95–99, Oct. 1988.
- [102] D. Bhandari, C. Murthy, and S. K. Pal, "Genetic algorithm with elitist model and its convergence," *Internat. J. of Pattern Recogn. and A.I.*, vol. 10, no. 06, pp. 731–747, Nov. 1996.
- [103] M. Clerc and J. Kennedy, "The particle swarm - explosion, stability, and convergence in a multidimensional complex space," *IEEE Trans. Evol. Comput.*, vol. 6, no. 1, pp. 58–73, Feb. 2002.
- [104] S. Mirjalili, *Evolutionary Algorithms and Neural Networks: Theory and Applications*, 1st ed. Berlin, Heidelberg: Springer, 2018.
- [105] G. Xu and G. Yu, "On convergence analysis of particle swarm optimization algorithm," *L. of Comp. and Appl. Math.*, vol. 333, pp. 65–73, May 2018.
- [106] Y.-L. Zheng, L.-H. Ma, L.-Y. Zhang, and J.-X. Qian, "On the convergence analysis and parameter selection in particle swarm optimization," in *Proc. Int. Conf. on Commun. Machine Learning and Cybernetics*, vol. 3, 2003, pp. 1802–1807 Vol.3.
- [107] G. Rudolph, "Convergence analysis of canonical genetic algorithms," *IEEE Trans. Neural Netw.*, vol. 5, no. 1, pp. 96–101, Jan. 1994.
- [108] A. E. Eiben, E. H. L. Aarts, and K. M. Van Hee, "Global convergence of genetic algorithms: A markov chain analysis," in *Parallel. Probl. Solv. from Nature*. Berlin, Heidelberg: Springer Berlin Heidelberg, Jun. 1991, pp. 3–12.
- [109] H. Asplund, D. Astely, P. von Butovitsch, T. Chapman, E. Dahlman, M. Frenne, F. Ghasemzadeh, M. Hagström, B. Hogan, G. Jöngren, J. Karlsson, F. Kronstedt, E. Larsson, S. Parkvall, and J. Skold, *Advanced Antenna Systems for 5G Network Deployments: Bridging the Gap Between Theory and Practice*. USA: Academic Press, Inc., 2020.